Protocols and Devices for Scalable Spin-Photon Quantum Networks

by

Kevin C. Chen

B.S., California Institute of Technology (2017)
S.M., Massachusetts Institute of Technology (2019)

Submitted to the Department of Electrical Engineering and Computer Science in partial fulfillment of the requirements for the degree of

Doctor of Philosophy

at the

MASSACHUSETTS INSTITUTE OF TECHNOLOGY

September 2023

©2023 Kevin C. Chen. All rights reserved.
The author hereby grants to MIT a nonexclusive, worldwide, irrevocable, royalty-free license to exercise any and all rights under copyright, including to reproduce, preserve, distribute and publicly display copies of the thesis, or release the thesis under an open-access license.

Authored by: Kevin C. Chen
Department of Electrical Engineering and Computer Science
August 31, 2023

Certified by: Dirk R. Englund
Associate Professor of Electrical Engineering and Computer Science
Thesis Supervisor

Accepted by: Leslie A. Kolodziejski
Professor of Electrical Engineering and Computer Science
Chair, Department Committee on Graduate Students

Protocols and Devices for Scalable Spin-Photon Quantum Networks

by

Kevin C. Chen

Submitted to the Department of Electrical Engineering and Computer Science
on August 31st, 2023, in partial fulfillment of the
requirements for the degree of
Doctor of Philosophy

Abstract

One of the central goals in quantum information science is constructing a quantum network useful for quantum communication, sensing, and computation. Its realization crucially depends on efficient distribution of entanglement. A promising approach entails connecting quantum nodes via photons, which are naturally resilient against decoherence, and storing quantum bits in atomic memories; among which, solid state spin qubits in diamond are particularly promising candidates for memory storage in a quantum repeater network. However, experimental efforts thus far have been mainly stymied by the absence of efficient and scalable spin-photon interfaces.

To address these challenges, we propose a photonic integrated circuit architecture with heterogeneously integrated emitter-nanocavity systems for faithfully transferring photonic qubits onto diamond color centers. This hybrid platform offers arbitrary photonic routing, phase stability, and reconfigurability to achieve high-fidelity and high-efficiency local and remote entanglement generation. Subsequently, we report our experimental efforts in realizing a cavity-enhanced optical interface with tin-vacancy centers in diamond and characterizing a heterogeneously integrated emitter-cavity system in a silicon nitride photonic integrated circuit. The on-chip components allow for additional control over both the spin and optical degrees of freedom necessary for achieving spin-photon entanglement. As an outlook, we discuss how the experimental results in this thesis and ongoing efforts pave the path towards additional quantum network applications, such as realizing a quantum random access memory.

Thesis Supervisor: Dirk R. Englund
Title: Associate Professor of Electrical Engineering and Computer Science

Acknowledgments

This thesis is a culmination of works that I could not have done without the folks I have met at MIT. First off, I want to thank Dirk who welcomed me into his group with open arms. His undying passion towards science has been a source of inspiration throughout my PhD journey. It is without a doubt a humbling experience to have him as my research advisor. I want to thank my thesis committee as well, Professor Karl Berggren and Professor Kevin O'Brien, who have both provided invaluable feedback on my thesis work and advice that will accompany me for the remainder of my career. I want to also express my sincere gratitude for all the administrative and operations staff who are keeping the Quantum Photonics group functional over the years: Janice Balzer, David Barnett, and Andrew Birkel. They have all patiently dealt with my incessant purchasing needs as I struggled on planning out my experiments. Needless to say that none of the demonstrations laid forth in this thesis would have been possible without their help.

Over the past six years, I have the pleasure collaborating with many brilliant minds. Dr. Romain Debroux, Jesus Martinez, Ryan Parker, Dr. Catheryn Michaels, Alexander Stramma, and Professor Dorian Gangloff from Professor Mete Atature's group in University of (original) Cambridge have been fantastic collaborators in pushing the frontiers on anything relating to SnV centers. In our bi-weekly meetings, I have benefited greatly from our discussions surrounding quantum optics and spectroscopy. Additionally, our collaborators at MIT Lincoln Laboratory, Dr. Ben Dixon, Dr. David Starling, Dr. Xingyu Zhang, Dr. Ryan Murphy, Dr. Katia Shtyrkova, Dr. David Kharas, and Dr. Scott Hamilton have been instrumental to our integrated photonics efforts. The heterogeneous integration results are intimately tied to their hard work in producing and designing the low loss silicon nitride platform. I want to also thank Dr. Edward Bielejec and Dr. Michael Titze at Sandia National Laboratory for providing various focused-ion-beam-implanted samples. Despite our unreasonable requests, they have always delivered essential samples that help bolster our understanding in color centers in diamond. Lastly, I have been blessed to be involved in the

MITRE Quantum Moonshot program, in which I interacted with many accomplished scientists, in particular Dr. Genevieve Clark, Dr. Andrew Golter, and Dr. Mark Dong. I have full faith in their capability to bringing the Moonshot project to its fruition.

Much of my time in graduate school has been spent inside the (now-retired) NanoStructures Lab (NSL), which had been a wonderful cleanroom thanks to Jim Daley, Mark Mondol, and Karl. Jim has been paramount to keeping the diamond fabrication process up and running. Whenever any equipment went under the weather, he was immediately on the repair job within the day. I also want to thank the rest of the MIT nano staff, notably Kurt Broderick, Donal Jamieson, Eric Lim, and Yang Yu, who have dedicated a great amount of time training and helping me develop all the relevant processes.

I am grateful to be able to be mentored by many esteemed alumni from the Quantum Photonics group. When I first entered the group, Dr. Sara Mouradian and Dr. Noel Wan taught me everything about diamond fabrication and spectroscopy. Their foundational work in the quasi-isotropic process has truly enabled many experiments covered in this thesis. Noel has especially been a source of wisdom in and out of lab. My many conversations with him about hobbies and being foodies have instilled me a sense of appreciation for maintaining a (somewhat-healthy) work-life balance. Working with him and Dr. Tsung-Ju (Jeff) Lu on the large-scale integration project was an experience I would never forget, e.g. the many nights we spent in Building 13 tinkering with the FIB tool. I want to also thank Dr. Matt Trusheim who, to this day, has still been my go-to quantum optics textbook. In the lead-related defect project, he taught me analyzing data rigorously is just as important, if not more than, as performing the measurements themselves. Dr. Michael Walsh, the software guru that built the entire Command Center infrastructure from scratch, had taught me how to properly write and comment code (though I am guilty to admit I didn't always follow his advice). He also generously bestowed upon me the UHV furnace that has been the workhorse for annealing all the diamonds throughout my PhD. Dr. Eric Bersin, software guru number 2 with whom I also had the pleasure to work on the

PEPSI project, taught me everything ranging from daily optics lab work to writing experiments in Command Center. A big shout out to Dr. Lorenzo de Santis, who had been an immensely knowledgeable person in every SnV-related project. Despite the frequent breakdown of lab equipment (pesky lasers and all), mysterious mishaps with the cryostats, and optics refusing to cooperate, Lorenzo always persevered and "got things done". I learned from him to never be afraid to try the unknown, an attitude which definitely had helped me push through the difficult moments during grad school.

I am also fortunate to have wonderful office mates over the years. Dr. Hyeongrak (Chuck) Choi, the rumorville of QPG (seconded by Noel in his thesis), has been the most knowledgeable person in quantum optics and information theory that I have ever met. His rigor as a theorist has motivated me to always methodically consider every element in my theoretical works, though they may still not be up to his standards. Isaac Harris, our resident Canadian of 36-531, has been an incredibly helpful colleague in everything electronics, DFT, and Group-IV color center related. Whenever there is a coffee hour, I know I can count on Isaac to accompany me. Linsen Li, the diamond boss, has been a great colleague to work with in the cleanroom and in lab. We had many wild adventures etching and pick-n-placing diamonds (in ways that will never be known to the rest of the world) that reminded me what fun is in research. During the 5th floor renovation when several of us were shoved into a windowless mail room on the 3rd floor, I had the pleasure of sharing the same space as Dr. Hyowon Moon and Dr. Saumil Bandyopadhyay. Hyowon's calming attitude towards life had always brought a sense of serenity when I needed it. Saumil, on the other hand, is a source of juicy gossips at a level almost on par with Chuck's. He has been an entertaining colleague to talk to, especially when I receive updates on the whatabouts of the silicon photonics ~~matrix-multiplication~~ subgroup. In a same vein, Yuqin (Sophia) Duan has brought a joyful presence to lab. Since Noel's graduation from the group, Sophia has supplanted the resident foodie role and is a reliable informant of what the hottest boba shop/restaurant is in town. Over the years, I am also thankful to have interacted with other QPG members: Dr. Christopher Panuski who single-handedly

uplifted the social life of the group; Hugo Larocque who generously served as the host of many unforgettable parties at his beautifully gardened backyard; Dr. Carlos Errando-Herranz whom I had the pleasure of working with on the qRAM project and was an irreplaceable role model to a lot of us during his QPG stint; Madison Sutula who was my partner in crime in keeping iQuISE operational and one of the kindest souls I know; Hanfeng Wang who has offered tremendous help on the NV sensing lab in Dirk's course that I TAed.

In the integrated photonics effort, I am blessed to have worked with (soon-to-be-Dr) Ian Christen and Hamza Raniwala. Since day 1, Ian is the prototypical genius that puts out fire everywhere. Despite his already overburdening schedule, he works tirelessly to help ensure everyone's projects go smoothly. It's safe to say that his impact on this thesis (and many others before and after mine) is simply ineffable. It has been a great honor to have worked beside Ian, and seen him from being a person without any phone in the 21st century to becoming a savvy iPhone user[1]. Hamza, the future of the atomic memories subgroup, has been the perfect mentee anyone could ask for. His willingness to learn has inspired me to become a better mentor and often led me to achieve a deeper understanding in anything quantum and photonics. Being a fellow Techer, Hamza is perhaps one of the few people I know who truly loves "the grind". In the contexts of both science and gaming, he chooses the often more difficult yet more rewarding route.

Throughout grad school, I have also been involved in MIT iQuISE, from being just a member who taps everyone's ID at the door to eventually becoming a co-president that runs this weekly seminar series. I feel honored to have seen iQuISE blossom into this organization that now hosts student conferences and hackathons at a scale unimaginable six years ago. I am grateful to have worked with Sara, Michael, Eric, Dr. Benjamin Lienhard, Dr. Guoqing Wang, Ariel Barr, Lamia Ateshian, Jennifer Wang, and Shantanu Jha on this journey.

Lastly, the works I have done over the last six years would not have been possible without the undying support of my family and friends. I am truly blessed to have such

[1]Ian, if you're reading this, this is a gentle reminder for you to take a break.

a loving network throughout the journey, providing me encouragement and comfort during the ebbs and flows. For this, I dedicate this thesis to those I cherish dearly.

Contents

List of Figures

List of Tables

Chapter 1

Introduction

This first chapter introduces the concept of quantum network and the necessary components in building one. Then, we define and provide an example of an entangled quantum state, which can be used to perform quantum teleportation that is key to constructing quantum networks. Section 1.3 discusses color centers in diamond as promising memory qubits, followed by Section 1.4 that highlights the importance of having efficient spin-photon interfaces for teleportation. We end the chapter by giving an outline of the remainder of the thesis.

1.1 Quantum network and its requirements

The internet is essential to everyday operations in the modern era. Computers relay information encoded in bits either within local networks or over long distances. Analogously, in the advent of quantum technologies, the *quantum* internet would be equally paramount [7] to the next era of information processing. In one simple setting, this so-called quantum network consists of memory nodes that retain quantum information in the form of quantum bits (qubits in short), which can be coherently transferred from one place to another via photons. Such a construct is crucial to fundamentally secure quantum communication [8, 9, 10], distributed quantum computation [11, 12, 13] and sensing [14, 15, 16], and applications yet to be explored.

Though there exist many proposals and implementations of quantum networks,

each quantum node generally takes the form of a matter-based *memory* qubit that must be both optically active in order to interact with the photons and has a relatively long coherence time to faithfully retain quantum information during the course of the photon's transit. Importantly, to counteract errors during operations with the quantum network, e.g. decoherence of the matter qubit or photon loss, the quantum node would require having multiple memories. Therefore, a practical implementation must choose a qubit platform that is inherently scalable. Furthermore, the matter qubit must have an efficient optical interface via photonics engineering to reliably transfer quantum information to and from flying photonic qubits. Though promising demonstrations have been made over the years [17, 18, 19, 20], these stringent requirements have thus precluded realizations of large-scale quantum networks with practical quantum advantages. The aim of this thesis is to address these aforementioned issues both theoretically and experimentally, with emphasis on how to *engineer* quantum photonic systems with atomic memories suitable for constructing a near-term quantum network.

1.2 Quantum entanglement and teleportation

Crucial to the construction of quantum networks (and in fact most practical quantum processors) is *entanglement*, which is a purely quantum mechanical phenomenon that exhibits non-classical correlations between two quantum systems. Given a qubit basis of $\{|\downarrow\rangle, |\uparrow\rangle\}$, the prototypical maximally entangled state is a Bell state [21],

$$|\Phi^+\rangle_{AB} = \frac{|\downarrow\rangle_A |\downarrow\rangle_B + |\uparrow\rangle_A |\uparrow\rangle_B}{\sqrt{2}}, \tag{1.1}$$

where subscripts A, B represent Alice and Bob, two fictional characters commonly employed in quantum network experiments. If Alice measures $|\downarrow\rangle$, the measurement itself collapses the Bell state to ${}_A\langle\downarrow|\Phi\rangle \sim |\downarrow\rangle_B$. Similarly, if Alice measures $|\uparrow\rangle$, the projected quantum state that Bob has is ${}_A\langle\uparrow|\Phi\rangle \sim |\uparrow\rangle_B$. Clearly, the measurement results for Alice and Bob are correlated due to the presence of entanglement.

This non-classical correlation is an essential resource for general quantum information processing. One example relevant to construction of quantum networks is quantum teleportation for transferring a qubit from Alice to Bob (and vice versa) by using an already shared Bell state $|\Phi^+\rangle_{AB}$ shown in Eq. 1.1. If Alice wishes to teleport an arbitrary qubit $|\psi\rangle_a = \alpha|\downarrow\rangle_a + \beta|\uparrow\rangle_a$ onto Bob's memory qubit, the initial product state would be

$$|\Psi\rangle_{\text{init}} = |\psi\rangle_a |\Phi^+\rangle_{AB} \tag{1.2}$$

$$= \frac{1}{2}\left[|\Phi^+\rangle_{aA}(\alpha|\downarrow\rangle_B + \beta|\uparrow\rangle_B) + |\Phi^-\rangle_{aA}(\alpha|\downarrow\rangle_B - \beta|\uparrow\rangle_B)\right.$$
$$\left.|\Psi^+\rangle_{aA}(\alpha|\uparrow\rangle_B + \beta|\downarrow\rangle_B) + |\Psi^-\rangle_{aA}(\alpha|\uparrow\rangle_B - \beta|\downarrow\rangle_B)\right], \tag{1.3}$$

where $|\Phi^\pm\rangle$ and $|\Psi^\pm\rangle$ are the four maximally entangled Bell states,

$$|\Phi^\pm\rangle = \frac{|\downarrow\rangle|\downarrow\rangle \pm |\uparrow\rangle|\uparrow\rangle}{\sqrt{2}}, \tag{1.4}$$

$$|\Psi^\pm\rangle = \frac{|\downarrow\rangle|\uparrow\rangle \pm |\downarrow\rangle|\uparrow\rangle}{\sqrt{2}}. \tag{1.5}$$

Measuring in the Bell basis (i.e. a Bell state measurement, or BSM) projects the joint state into one of the four terms in Eq. 1.3. Noting the measurement outcome, Bob can apply a corresponding single qubit rotation (Pauli correction) to recover Alice's qubit: $\alpha|\downarrow\rangle_B + \beta|\uparrow\rangle_B$.

This same procedure can be adapted to teleport a flying qubit onto a memory qubit, and vice versa, for building a quantum network. For an instance, one then transfer entanglement in an entangled photon pair (e.g. generated by spontaneous parametric downconversion (SPDC) sources) to a pair of remote spin qubits [22]. Alternatively, one may also leverage a cavity-reflection-based two-qubit gate to entangle a flying qubit between two remote spin qubits [19], as will be detailed in Section 2.3.

However, these methods require *efficient and high-fidelity* entanglement between the spin and photonic qubits (from here on we will refer the matter qubit as the spin qubit), a central challenge that is critical to constructing quantum networks over long distances. For now, we table the details for achieving spin-photon entanglement to

Section 2.3. As mentioned previously, there are two essential characteristics a useful quantum repeater node must have: (1) an optically active spin qubit whose coherence time is long comparing to the photon transit time; and (2) the efficiency of the spin-photon interface for producing high fidelity spin-photon entanglement. The following two sections in this chapter address both (1) and (2) respectively.

1.3 Diamond color centers as memories

In this section, we introduce the Group-IV emitters in diamond and their differences from the more notable NV center. We discuss in more detail about both their upsides and downsides as memory qubits, and how we select the SnV center as the qubit of choice for the experimental portion of this thesis.

1.3.1 The upside of Group-IV emitters

Many qubit candidates have been explored as atomic memories in a quantum network node. For examples, atomic vapor [17], neutral atoms [19], trapped ions [23], and even superconducting qubits [20] have been presented as potential platforms. In particular, solid-state defects hosted in large band-gap materials are especially promising due to their intrinsic scalability and compatibility with fabrication of micro-scale or even nano-scale structures [24]. Notably, the much-explored nitrogen-vacancy (NV) centers in diamond have demonstrated several hallmark achievements towards constructing quantum networks: > 1 s coherence time [25], deterministic long-distance entanglement [26, 18], construction of a 3-node quantum network [18]. However, presently in the case of NV center, further increase in the size of the quantum network is stymied by its low Debye-Waller (DW) factor of $\sim$0.03, which characterizes the ratio of emission rate into its coherent zero-phonon line (ZPL) relative to the total emission including the incoherent phonon sideband [26, 18]. One solution is to utilize *Purcell enhancement* [27], which boosts its ZPL contribution by placing the NV center inside a photonic cavity. Greater enhancement effect generally entails using smaller photonic cavities down to sub-micron scales. However, presently, NV

center placed in nanostructures suffers from optical dephasing [28]. Due to its crystallographic asymmetry, it experiences spectral diffusion in which its optical transition frequency drifts due to nearby charge fluctuations.

As an alternative, the recently discovered Group-IV emitters (negatively charged SiV, GeV, SnV centers) exhibit crystallographic inversion symmetry (Figure 1-1) that shields them from environmental noises, enabling promising optical and spin properties. In addition to reduced spectral diffusion, they have high quantum efficiencies, which characterize how much emission goes into radiative pathways as opposed to the non-radiative ones. Furthermore, Group-IV emitters have significantly higher ZPL contributions in their emission than NV centers, thus a larger proportion of their emission can be used to encode qubits. Specifically, the corresponding Debye-Waller factors for SiV, GeV, and SnV centers are DW $= 0.76, 0.61$, and 0.41 [29], all are an order of magnitude higher than that of NV center.

1.3.2 Level structure of Group-IV emitters

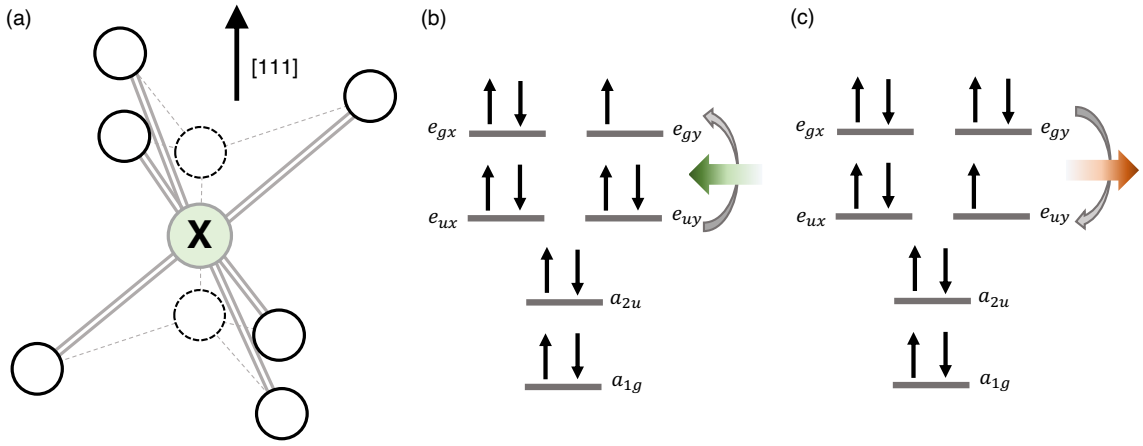

Figure 1-1: Crystallographic and electronic structures of Group-IV emitters in diamond. (a) The crystallographic structure of a negatively charged **X**V center with inversion symmetry, where **X** can be Si, Ge, Sn, or Pb. (b) The ground state configuration of the electronic structure. Upon excitation, the electron spin is promoted to the e_g orbital. (c) The excited state configuration of the electronic structure. Upon relaxation of an electron spin from the e_g to the e_u orbital, the **X**V center emits a photon.

These negatively charged Group-IV emitters have a total of eleven electrons: six from the dangling σ bonds from the carbon atoms, four from the Group-IV atom itself, and one additional electron captured from a nearby donor. Figure 1-1(b,c) display the ground and excited state configurations, which demonstrate an optical transition arising from an electron relaxing from the e_g orbital to the e_u orbital [30].

Under zero applied field, the spin-orbital coupling (SOC) and the dynamic Jahn-Teller (DJT) effect give rise to two doublets, one in the ground state and another in the excited state manifold (Figure 1-2(a)).

The SOC is a relativistic effect coupling spin to the electron's orbital motion under the nucleus' potential. Its Hamiltonian is

$$\mathcal{H}^{\mathrm{SOC}} = \frac{\hbar}{4mc^2} \left(\nabla V \times \hat{\mathbf{p}}\right) \cdot \frac{\hat{\mathbf{S}}}{\hbar} \approx -\frac{\lambda}{2} \hat{\mathbf{L}} \cdot \hat{\mathbf{S}}, \tag{1.6}$$

where V is the electronic potential subjected to the nucleus' magnetic field, m is the electron's mass, $\hat{\mathbf{p}}$ is the electron's momentum operator, and $\hat{\mathbf{S}}$ is the spin operator consisted of Pauli matrices. Importantly, λ represents the spin-orbit coupling strength. The form of $\mathcal{H}^{\mathrm{SOC}}$ indicates that the eigenstates can be written as a tensor product of the orbital and spin components. In the approximated form of the Hamiltonian, the L_z operator has off-diagonal elements that cause orbital mixing. Therefore, spin-orbit coupling transforms the orbital eigenstates $|e_x\rangle, |e_y\rangle$ to a new eigenbasis formed by $|e_+\rangle, |e_-\rangle$.

The DJT effect arises from a spontaneous symmetry breaking that distorts the molecule to a configuration that reduces the equilibrium energy (more details regarding point symmetries can be found in Ref. [31]). In essence, similar to SOC, the DJT effect induces further mixing in the orbital components depending on the characteristic constants Υ [30].

A typical fine structure spectrum is shown in Figure 1-2(b). The spin-orbital splittings for the ground (g) and the excited (e) manifolds are

$$\Delta_{g,e} = \sqrt{\lambda_{g,e}^2 + \Upsilon_{g,e}^2}. \tag{1.7}$$

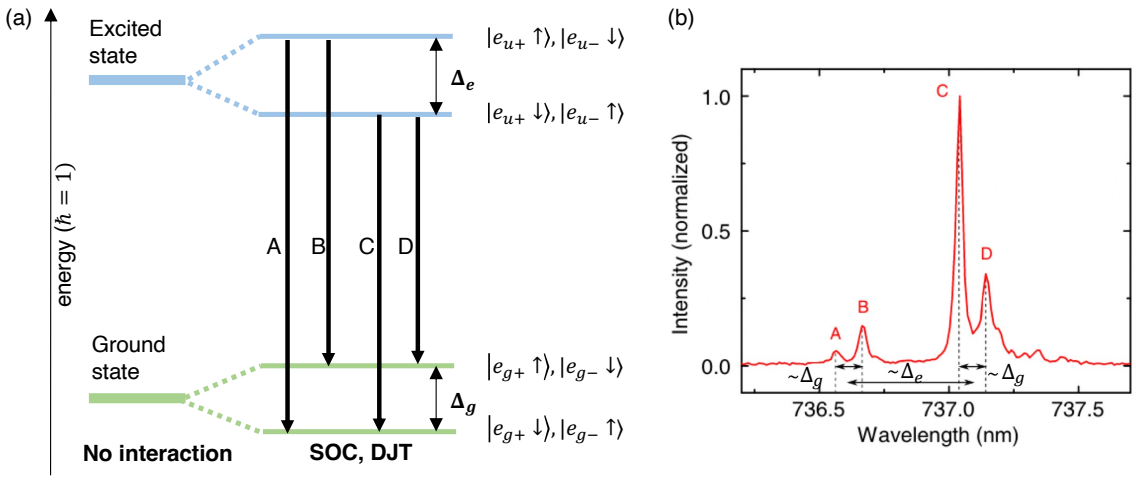

Figure 1-2: Fine structure of a Group-IV emitter. (a) With the orbital degeneracy lifted, four optical transitions (A,B,C,D) exist. The energy difference between C and D (A and B) is the ground (excited) state manifold's spin-orbital splitting Δ_g (Δ_e). (b) A photoluminescence spectrum displaying the SiV center's fine structure (adapted from Ref. [1]).

Since the Group-IV emitters are spin-$\frac{1}{2}$, applying a magnetic field further splits the energy eigenstates into two spin states by the Zeeman effect. The magnetic field couples to both the orbital and spin angular momenta, as shown by the Zeeman Hamiltonian

$$\mathcal{H}^Z = \mathcal{H}^{Z,L} + \mathcal{H}^{Z,S} = \gamma_L \hat{\mathbf{L}} \cdot \hat{\mathbf{B}} + \gamma_S \hat{\mathbf{S}} \cdot \hat{\mathbf{B}} \tag{1.8}$$

$$\approx q\gamma_L \hat{L}_z B_z + \gamma_S \hat{\mathbf{S}} \cdot \hat{\mathbf{B}}, \tag{1.9}$$

where $\gamma_L = \mu_B/\hbar$ and $\gamma_S = 2\mu_B/\hbar$ are the orbital and electron gyromagnetic ratios, respectively, and q is a quenching factor. The orbital Zeeman effect for the Group-IV emitters is strongly quenched by the Jahn-Teller interaction [30], i.e. $q \ll 1$. Hence, we will henceforth neglect contribution from the first term.

The energy separation between the hyperfine sublevels is determined by the strength of the magnetic field along the axial [111] direction. It is important to note that any off-axis projection would induce spin mixing, therefore reducing the cyclicity of the spin conserving transitions, i.e. fewer population cycles can occur before the population is pumped to another ground state.

1.3.3 The downside of Group-IV emitters

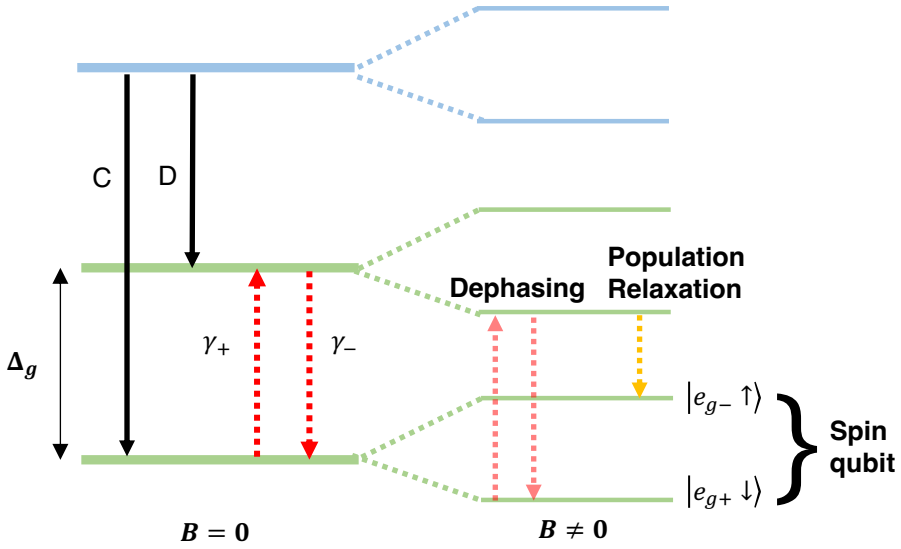

Figure 1-3: Hyperfine structure of a Group-IV emitter. With an externally applied magnetic field, the spin component splits further into two states due to the Zeeman effect. The red arrows indicate the electron phonon scattering processes $\gamma_{+,-}$ that lead to either dephasing or population relaxation (depolarization) errors in the spin qubit.

The two lowest energy states, $|e_{g+},\downarrow\rangle$ and $|e_{g-},\uparrow\rangle$ are typically chosen to form the qubit. There is, however, a fundamental source of decoherence in the level structure of these Group-IV emitters: phononic scattering processes within the ground and excited state manifolds, as indicated by the dotted limes in Figure 1-3. However, since the qubit is encoded in the two lowest energy states, we are only concerned with the ground state scattering processes.

γ_+ in Figure 1-3 represents the rate at which thermal phonons provide sufficient energy to pump the population to the upper orbital state. For the $B \neq 0$ case, as it relaxes back to the qubit sublevels, it can either return to $|g_+,\downarrow\rangle$ and accumulate an additional phase from the round trip, effectively decohering the qubit, or pump the population to the $|g_-,\uparrow\rangle$ state and depolarizes the qubit.

These scattering rates can be derived from the Fermi's golden rule [32],

$$\gamma_+ = 2\pi\chi\rho\Delta_g^3 n_{\text{th}}(T) \tag{1.10}$$

$$\gamma_- = 2\pi\chi\rho\Delta_g^3 (n_{\text{th}}(T) + 1), \tag{1.11}$$

where χ, ρ are proportionality constants and n_{th} is the phonon population governed by the Bose-Einstein distribution. They both consist of a product between the phonon density of states that scales as $\propto \Delta_g^2$ and the electron-phonon coupling strength that scales as $\propto \Delta_g$. Except γ_- includes an additional term that represents spontaneous emission. Ultimately, the transition rates depend on temperature T implicitly through the occupation of phononic modes $n_{\text{th}}(T)$. There are two extremes worth considering: one, when the thermal energy $k_B T$ is greater than the splitting energy $h\Delta_g$, and second, when the thermal energy is much less than the orbital splitting energy. In the first case $k_B T > h\Delta_g$, γ_+ is dominated by the increasing phonon density of states that is dependent on Δ_g. On the other hand, in the second case $k_B T \ll h\Delta_g$, the phonon population can be approximated by the Boltzmann distribution such that $n_{\text{th}} \approx \exp -\frac{h\Delta_g}{k_B T}$.

With decreasing temperature in the latter case, the upward scattering rate γ_+ is exponentially suppressed by the Boltzmann factor, thus reducing spin dephasing. Intuitively, the lower the temperature, the better the qubit's coherence time. However, taking SiV for example, a < 200 mK dilution refrigerator is required to achieve milli-second coherence time in addition to dynamical decoupling pulse sequences [33]. This requirement imposes additional engineering challenges and diminishes the potential of scalability critical for building useful quantum networks. Therefore, there naturally exists a desire to increase Δ_g rather than to decrease $k_B T$ in suppressing decoherence.

Generally, heavier Group-IV elements have greater spin-orbit splitting, with the four candidates, {SiV, GeV, SnV, PbV}, having $\Delta_g = \{48, 169, 846, 5700\}$ GHz [32, 29]. Figure 1-4 shows the normalized electron phonon scattering rate γ_+ as a function of temperature for the four Group-IV emitters. Using the scattering rate for SiV at 100 mK [33] as a reference for sufficiently low γ_+, the corresponding temperatures

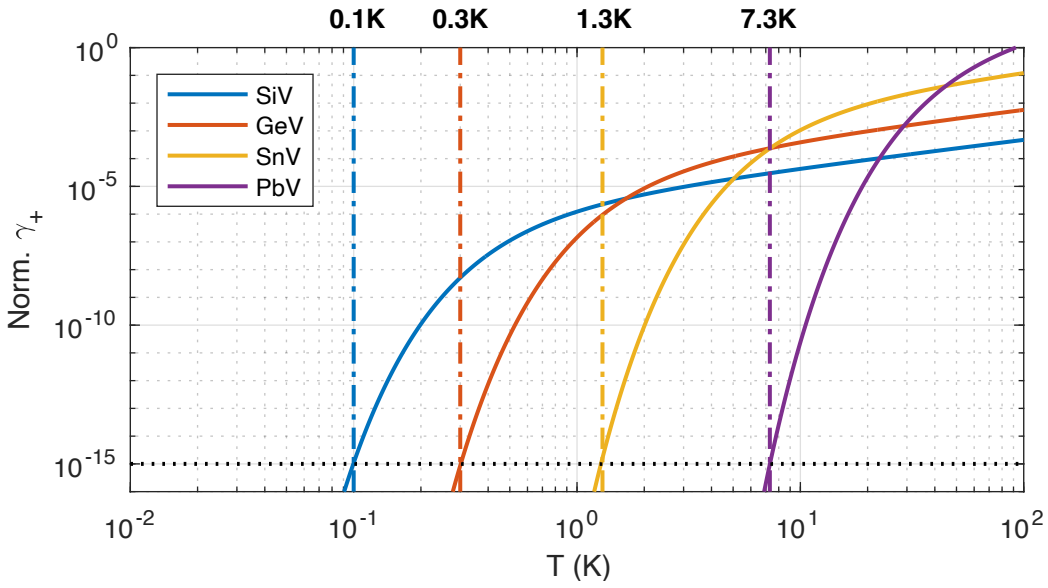

Figure 1-4: Normalized electron phonon scattering rate $\gamma_+ \propto \Delta_g^3 n_{\text{th}}(T)$ as a function of temperature for the four Group-IV emitters: SiV, GeV, SnV, and PbV. Their corresponding spin-orbit splitting in the ground state manifold are $\{48, 169, 846, 5700\}$ GHz, respectively. Black dashed (horizontal) line represents the normalized γ_+ at 100 mK for SiV. The dashed dotted (vertical) lines show the corresponding temperature requirements.

at which the spin coherence time becomes comparably long are $\{0.3, 1.3, 7.3\}$ K for {GeV, SnV, PbV}. Since GeV still requires dilution refrigerator temperature and PbV has yet to be conclusively determined [34], there has been a surging interesting in the heavier SnV center [35, 36, 37, 38]. Its greater ground state splitting $\Delta_g =$ 850 GHz enables spin relaxation time >ms at 4K [36] and spin coherence time > µs at 1.3 K [38]. Moreover, due to its inversion symmetry, the SnV center is compatible with integration into nanostructures without much loss in optical coherence [36, 39]. In a similar pursuit, the experimental portion of this thesis will also address our efforts in exploring the SnV center as a promising spin qubit for quantum networks. Specifically, we aim to not only use the SnV center by itself, but also leverage photonics engineering to improve the efficiency of interaction between a photonic qubit and a SnV-based spin-photon interface.

1.4 Photonics engineering for scalability

High-fidelity spin-photon entanglement depends on having an efficient light-matter interface. That is, how do we efficiently deliver and collect photons that are useful for quantum information, and how do we enhance interaction between a photonic qubit and a spin memory for quantum teleportation. As constructing quantum networks likely requires remote entanglement via flying qubits [17, 40, 41, 42], it is desirable to have control over their many degrees of freedom. One convenient method is to utilize photonic structures to tailor the propagating mode of light. For example, an elementary unit in photonics is a *waveguide*, in which only specific spatial and polarization modes can propagate [43]. Many protocols in building optical-based entanglement requires interfering a pair of *indistinguishable* single photons [44], meaning their spectral, spatial, polarization, and temporal modes all have to match. Therefore, having photonic structures such as a single mode waveguide removes ambiguity over the photon's spatial and polarization degrees of freedom, ensuring high fidelity entanglement barring temporal and spectral mismatch. In contrast, in an entirely free-space approach, the emission of defect centers in bulk diamond may vary from one to another due to their variations in local microscopic environments, thereby causing spatial *distinguishability* between two single photons (whether that is successive in time or coming from two emitters simultaneously) and degrading the entanglement fidelity [45].

Furthermore, building a quantum repeater network requires *scalability*. One platform that supports routing and controlling of thousands of photonic modes takes the form of a *photonic integrated circuit* (PIC), as shown in Figure 1-5. Even more paramount, a PIC in essence is a miniaturized optical setup that intrinsically provides phase stability crucial to many quantum operations [46]. Typically on a PIC, there exist photonic waveguides that can arbitrarily route photons into and out of various photonic components [47]; for examples, directional couplers forming a beam splitter for interference-based measurements, a polarization rotator/splitter for polarization control, ring resonators acting as spectral filters. In addition, active chip-

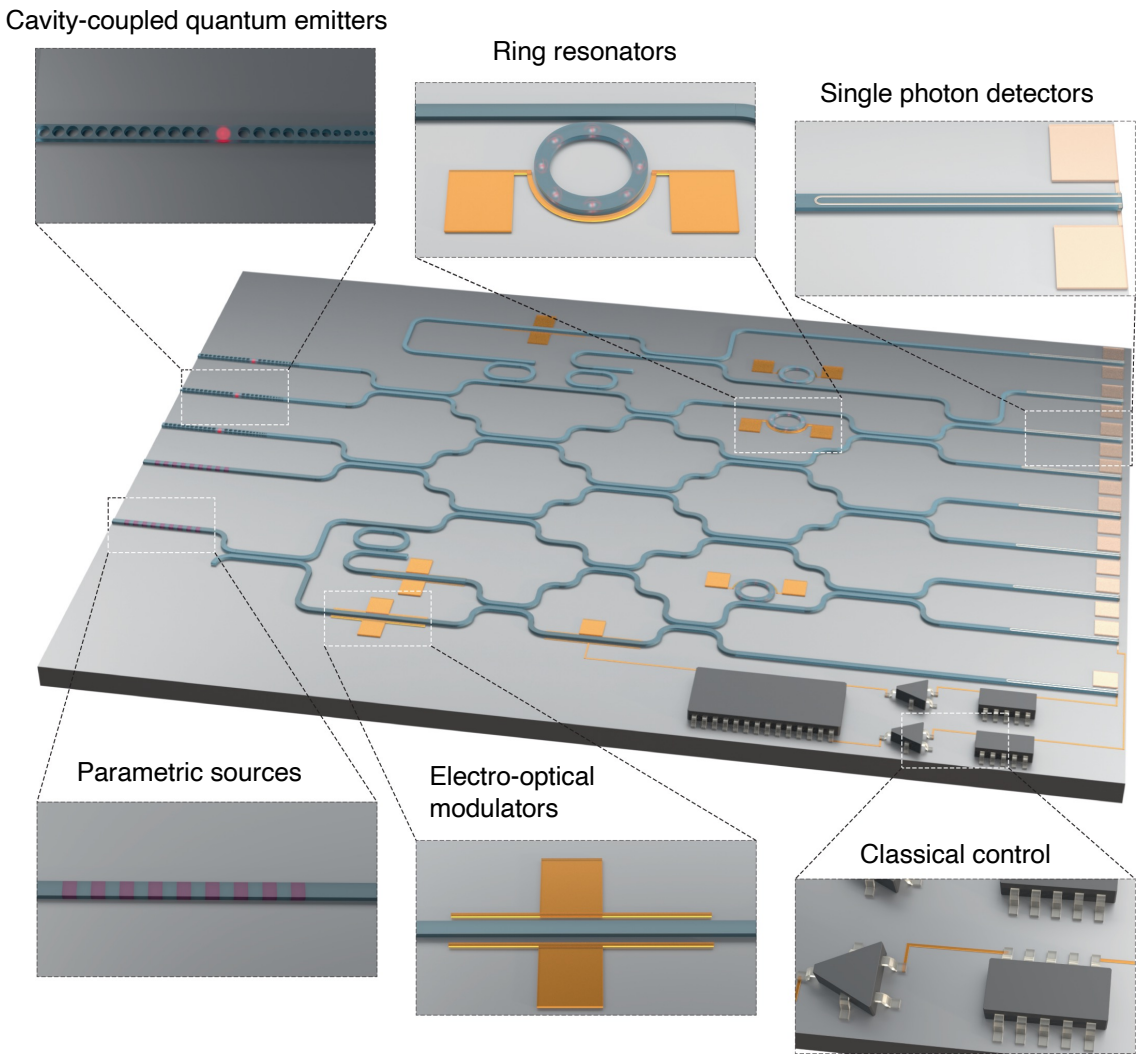

Figure 1-5: A photonic integrated circuit for quantum information processing. The platform contains photonic waveguides connecting cavity-coupled quantum emitters that may act as spin memories for quantum networks, ring resonators for spectral filtering and enhanced light-matter interaction, single photon detectors for on-chip measurements, parametric nonlinear sources for single photon generation, electro-optical modulators for high-bandwidth switching and phase-shifting, and additional classical control components. Figure is adapted from Ref. [2].

integrated components such as microwave striplines and integrated single photon detectors [48, 49] enable the necessary coherent control and measurements of both the spin and photonic qubits. While the material of interest in this thesis, diamond, does permit a monolithic diamond photonic architecture, fabrication constraints on non-wafer-scale single-crystalline diamonds and the absence of active on-chip com-

ponents limit construction of practical quantum network nodes. Hence, this thesis focuses on *heterogeneous integration* of diamond nanophotonic structures [50] into a matured visible PIC platform [51, 52].

Lastly, to engineer strong light-matter interaction, we introduce photonic *cavities* to the picture. When a quantum emitter is placed inside an optical cavity, especially one on the micron-scale, the strong interaction between the photonic and spin qubits provides two key functionalities. First, the single photon generation rate of an emitter-cavity system is Purcell enhanced [27], potentially increasing the emission-based remote entanglement generation rate. Second, the light-matter interaction arising from cavity quantum electrodynamics (QED) enables nonlinear effects that can be engineered to produce spin-photon entanglement [53].

1.5 Overview of the thesis

This thesis presents both theoretical and experimental efforts towards leveraging the aforementioned benefits provided by a PIC and the excellent atomic properties exhibited by color centers in diamond. Chapter 2 reviews the relevant physics in cavity QED and how coherent interaction between the photonic and spin qubits is used to perform cavity-reflection-based quantum teleportation. Then, Chapter 3 presents a scalable photonic architecture to realize high-fidelity teleportation with the aforementioned technique. Chapter 4 delineates our experimental demonstration of coupling between a nanophotonic cavity and a SnV center in diamond at 4 K, entailing: design and fabrication of photonic devices in bulk diamond, spectroscopy of the produced devices and SnV centers, and finally Purcell enhancement measurements exhibiting emitter-cavity coupling. Subsequently, Chapter 5 details our on-going efforts in heterogeneously integrating diamond photonic cavities into a silicon nitride PIC, which is used as an optical interposer for spectroscopy at 1.3 K. Chapter 6 addresses a specific application of spin-photon quantum networks based on PIC in constructing a quantum random access memory integral to distributed quantum computing. Finally, Chapter 7 concludes the thesis and discusses future directions for the diamond-PIC

platform.

Chapter 2

Cavity-based entanglement protocol

This chapter first covers a brief review of the physics in cavity quantum electrodynamics (QED). For more in-depth details regarding this topic, interested readers may consult Ref. [54, 55, 3]. Then, we derive the cavity reflection coefficient using the input-output formalism [56] and see how a reflected photon acquires a spin-state-dependent phase. Lastly, we show how this spin-dependent reflection enables quantum teleportation between a photonic and a spin qubit.

2.1 Cavity quantum electrodynamics

We first discuss the relevant cavity parameters assuming a coupled emitter-cavity system. Then, we give a succinct derivation of the reflectivity of a single photon off the cavity in a semi-classical approach (namely, input-output formalism [56]). Finally, we show how a spin-state-dependent cavity reflectivity can be used to achieve spin-photon entanglement and consequently teleportation.

In essence, a photonic cavity is a structure that confines light in particular propagating modes, each of which occupies a resonance frequency ω_c. Specifically, a *nano*photonic cavity entraps light in geometries whose allowed eigenmodes (i.e. propagating modes in cavities) have spatial extents along certain dimensions on the scale of the cavity-resonance wavelength $\lambda_c = 2\pi c/\omega_c$. For examples, in diamond, these structures may be ring resonators [57, 58], whispering-gallery-mode resonator [59],

photonic crystal cavities [60, 61, 58]. Regardless of their form, they share a common set of intrinsic parameters that we list below.

2.1.1 Quality factor

The *quality* (Q) *factor* characterizes the time duration a particular cavity mode stays confined before leaking out of the structure (note that each mode has its own Q factor). Formally, it is defined as ω_c/κ, where κ is the total cavity decay rate into *all* leakage channels. Often, however, we can only utilize certain leakage channels in experiments. In general, we can divide the Q factor into two types. One, a cavity's intrinsic Q factor, Q_i, accounts for the undesired channels such as scattering loss and material absorption loss. Two, there is a coupling Q factor, Q_c, that represents a specific channel from which we wish to collect light. Together, the geometric mean of Q_i and Q_c gives the total quality factor, also known as the extrinsic or loaded Q factor, Q_{ext}, defined as

$$\frac{1}{Q_{\text{ext}}} = \frac{1}{Q_i} + \frac{1}{Q_c}. \tag{2.1}$$

Each Q factor also has an associated decay rate: $\kappa = \omega_c/Q_{\text{ext}}$, $\kappa_i = \omega_c/Q_i$, and $\kappa_c = \omega_c/Q_c$. A central challenge in engineering and fabricating nanophotonic cavities for quantum information processing is to maximize the ratio κ_c/κ, which represents how strongly coupled the desired leakage channel is to the cavity mode relative to other loss channels. Concretely, there are three regimes of interest: (i) the undercoupled regime where $\kappa_c/\kappa < 0.5$, (ii) the critically coupled regime where $\kappa_c/\kappa = 0.5$, and (iii) the overcoupled regime where $\kappa_c/\kappa > 0.5$. We will revisit the importance of this figure of merit in the following section when addressing creating spin-photon entanglement using cavity-reflection based methods.

2.1.2 Mode volume

Another important parameter is the cavity's *mode volume* V, which is a measure of the spatial confinement of the electric field defining a particular cavity mode. Formally,

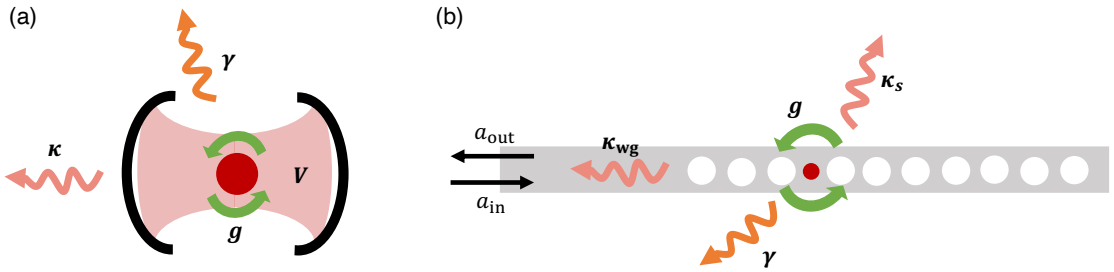

Figure 2-1: Diagram showing the relevant coupling rates of a cavity QED system. (a) A generic Fabry-Perot cavity of mode volume V coupled to a single emitter with interaction strength g. The spontaneous emission rate of the emitter is γ (not specifying into which channel it is emitting). The cavity's total decay rate is κ. (b) A single-sided cavity with the desired input channel whose coupling rate to the cavity mode is κ_{wg}. Note that time-reversal symmetry dictates that the input and output coupling rate must both be equal at κ_{wg}. The cavity mode also suffers from the undesired scattering loss at rate κ_s. a_{in} and a_{out} represent the annihilation operators of the input and output waveguide modes. The defect center may spontaneously emit into the waveguide channel with probability $C/C+1$ [3].

it is defined as [62, 63]

$$V = \frac{\int \epsilon |\mathbf{E}|^2 dV}{\max\left(\epsilon |\mathbf{E}|^2\right)}, \tag{2.2}$$

where ϵ is the dielectric constant of the material, and $\mathbf{E}$ is the cavity mode's electric field profile. For example, a ring resonator with cavity modes circulating around has a mode volume that essentially the size of the structure itself, spanning tens of um. On the other hand, photonic crystal cavities that confine light utilizing photonic bandgaps [63] (see Section 4.1) tend to have small mode volumes on the order of λ^3, crucial for engineering strong light-matter interaction.

2.1.3 Cavity QED parameters

Thus far, the aforementioned parameters (Q and V) are simply intrinsic properties of the photonic cavities. Once they are coupled to a quantum emitter, in our case of interest a defect center in diamond, we need to consider the coupling strength g between the cavity and the spin qubit, as shown in Figure 2-1. This light-matter

interaction can be described by the canonical Jaynes-Cummings (JC) Hamiltonian (with rotating wave approximation [54, 55]),

$$H_{\mathrm{JC}} = \frac{\hbar\omega_a}{2}\sigma_z + \hbar\omega_c\left(a^\dagger a + \frac{1}{2}\right) + i\hbar g\left(a^\dagger\sigma_- - \sigma_+ a\right), \tag{2.3}$$

where ω_a is the emission frequency of the emitter, σ_z is the Pauli-Z operator, $a^\dagger$ (a) is the creation (annihilation) operator for the cavity mode, and σ_+ (σ_-) is the raising (lowering) operator for the spin qubit, which we assume to consist of two levels. The first two terms of the JC Hamiltonian represent the energy terms of the emitter and the cavity mode separately, whereas the third term signifies coupling between the two systems.

The coupling constant g can be derived from quantization of the electric field[1]. For brevity, we will skip the derivation and refer interested readers to Ref. [54, 55]. Instead, we will write down the explicit form of g in terms of other parameters as

$$g(\mathbf{r}) = g_0 \cdot \frac{\mathbf{E}(\mathbf{r})}{|\mathbf{E}(\mathbf{r})|_{\max}} \cdot \cos(\xi), \tag{2.4}$$

where

$$g_0 = \frac{d}{\hbar}\sqrt{\frac{\hbar\omega}{2\epsilon V}} \tag{2.5}$$

is the maximum coupling strength, and d is the electric dipole moment. $\frac{\mathbf{E}(\mathbf{r})}{|\mathbf{E}(\mathbf{r})|_{\max}}$ and $\cos(\xi)$ account for spatial and dipole misalignment, i.e. they both equal to 1 when the emitter is located at the cavity mode field maximum and its dipole moment $\vec{d}$ is perfectly aligned (for example, in-plane for a TE-like cavity mode). The position vector $\mathbf{r}$ indicates the spatial dependence of the emitter-cavity coupling strength.

Importantly, g_0 is inversely proportional to $\sqrt{V}$. Thus, having a photonic cavity with smaller mode volume translates increasingly strong emitter-cavity coupling. That said, boosting $g(\mathbf{r})$ alone is not sufficient. To see this, we must solve for the

[1]The interaction Hamiltonian can be re-written as $H_{\mathrm{int}} = -\mathbf{d}\cdot\mathbf{E}$ where $\mathbf{d}$ is the dipole moment of the emitter.

eigenstates and eigenenergies based on the JC Hamiltonian. To simplify the discussion, we will only consider the so-called *Purcell* regime, in which $\kappa > g \gg \gamma$ [54, 55]. Often in solid-state engineering, optical cavities suffer from fabrication errors, resulting in $\kappa/(2\pi)$ on the order of 10's and 100's of GHz, much greater than the state of the art g coupling strengths [64].

There exist two eigenstates when $\omega_c = \omega_a$, with respective eigenenergies

$$E_\pm = \hbar\left(\frac{\kappa}{2} \pm \sqrt{\frac{\kappa^2}{4} - g^2}\right) = \hbar\frac{\kappa}{2}\left(1 \pm \sqrt{1 - \frac{4g^2}{\kappa^2}}\right) \tag{2.6}$$

$$\approx \hbar\frac{\kappa}{2}\left(1 \pm \left(1 - \frac{2g^2}{\kappa^2}\right)\right) \tag{2.7}$$

$$\Rightarrow E_+/\hbar = \kappa, E_-/\hbar = \frac{g^2}{\kappa}. \tag{2.8}$$

The first eigenenergy E_+ with corresponding decay rate κ represents direct leakage rate of the cavity mode. The second eigenenergy E_-, however, represents modified spontaneous emission rate of the emitter. Essentially, the presence of a coupled cavity increases (or decreases in the spectrally detuned case) the local density of states (LDOS). The ratio between the spontaneous emission rates of the emitter in a cavity and without a cavity defines the Purcell factor

$$F_P = \frac{2g^2}{\kappa\gamma}. \tag{2.9}$$

Using Eq. 2.4 and the fact that $\kappa = \omega_c/Q$, we find that the maximum Purcell factor is

$$F_{P,\max} = \frac{3}{4\pi^2}\left(\frac{\lambda}{n}\right)^3\frac{Q}{V}. \tag{2.10}$$

Accounting for detuning and spatial/dipole misalignment, Purcell factor can be re-written as

$$F_P = F_{P,\max} \cdot \frac{1}{1 + 4Q^2(\omega_c/\omega_a - 1)} \cdot \frac{\mathbf{E}(\mathbf{r})}{|\mathbf{E}(\mathbf{r})|_{\max}} \cdot \cos(\xi). \tag{2.11}$$

The Purcell-enhanced spontaneous emission rate Γ becomes

$$\Gamma = F_P\gamma + \gamma_{\mathrm{nr}} + \gamma_{\mathrm{PSB}}, \tag{2.12}$$

where γ_{nr} and γ_{PSB} are the decay rates into non-radiative channels and the incoherent phonon sideband, respectively. Typically, in experiments, this can be verified by observing a strongly Purcell-enhanced ZPL in the fluorescence spectrum (Figure 2-2(a)) and/or a reduced emitter's lifetime $\tau_P \propto 1/\Gamma$ (Figure 2-2(b)).

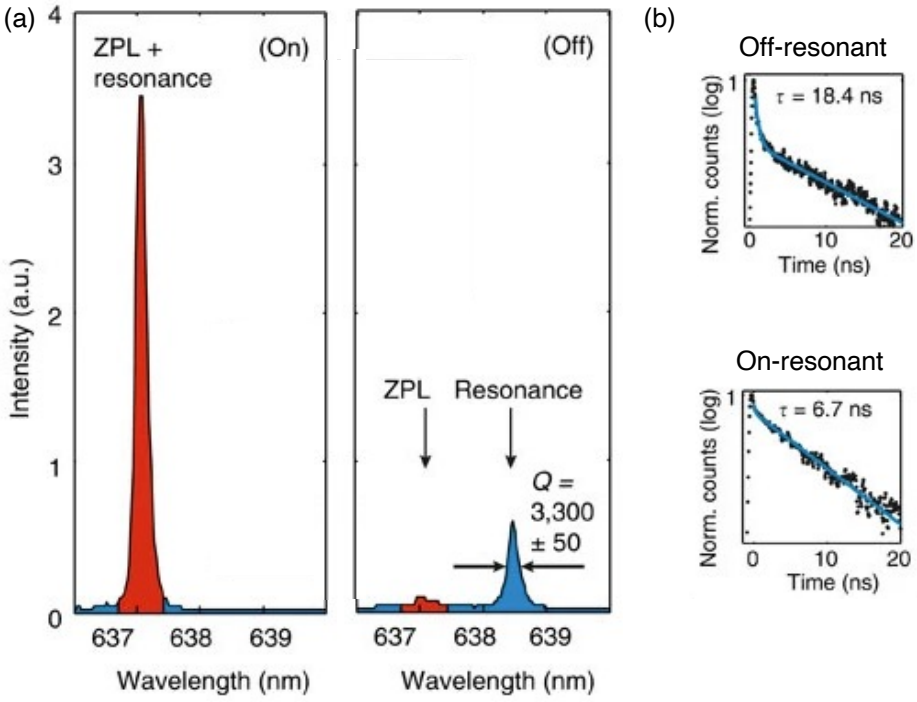

Figure 2-2: Purcell enhancement signatures. (a) When coupled to a cavity, the emitter's ZPL count rate is Purcell-enhanced as observed on the fluorescence spectrum. (b) The lifetime is reduced by a factor of 3 when the emitter is coupled to the cavity. Figures are adapted from Ref. [4].

Purcell factor, however, only describes the change in spontaneous emission rate *out of the excited state*. In using defect centers in diamond for quantum information processing requires addressing specific optical transitions, in which case optical coherence is also warranted. The so-called *cooperativity* C describes the coherent interaction strength between the spin qubit and the cavity mode, and captures both

emitter-cavity coupling and optical coherence in the form

$$C = \frac{4g^2}{\kappa\Gamma}, \tag{2.13}$$

where

$$\frac{\Gamma}{2} = \frac{\gamma}{2} + \gamma^*, \tag{2.14}$$

where γ^* is pure dephasing. Note here we neglect spectral diffusion that happens at a much slower time scale than the spontaneous emission rate. In other words, if there is significant pure dephasing, either stemming from surface effects common to emitters in nanophotonic cavities [65] or lattice damage from ion implantation [28], the emitter-cavity system can have a small cooperativity C but still retain high Purcell factor F_P. Intuitively, increasing F_P only entails sufficient overlap in frequency (barring spatial and dipole misalignment). With κ being significantly larger than the emitter linewidth (typical lifetime limit of SnV is $\leq$ 30 MHz), the overlap likely persists despite frequency jitter caused by dephasing, unless in the extremely unlikely case that γ^* becomes comparable to κ.

For constructing useful quantum gate operations based on emitter-cavity interaction, having a high cooperativity is paramount. In the following section, we will directly show how C affects cavity reflection that is utilized in constructing two-qubit gates between spin and photonic qubits.

2.2 Cavity reflectivity

Here, we conceive a specific scenario [53] in which a photonic cavity is coupled to an input waveguide, as shown in Figure 2-1(b). We can generalize the cavity decay channels to two types, one into the waveguide with decay rate κ_{wg} and another into the environment (scattering loss) $\kappa_s = \kappa - \kappa_{\text{wg}}$. Moreover, the cavity of interest is a single-sided cavity that suppresses transmission. Hence, an incoming single photon from the waveguide can only either (i) reflect off the cavity and return back to the

waveguide or (ii) scatter into free-space.

Using the JC Hamiltonian in Eq. 2.3, we can derive the cavity reflection coefficient by first writing down the equations of motion for the cavity mode and atomic lowering operators, a and σ_-. For the interested readers, Appendix A includes detailed derivations of the input-output formalism and equations of motion. Using Schrödinger's equation, we find

$$\dot{a} = -\left(i(\omega_c - \omega) + \frac{\kappa}{2}\right) a - g\sigma_- - \sqrt{\kappa_{\text{wg}}} a_{\text{in}} \tag{2.15}$$

$$\dot{\sigma}_- = -\left(i(\omega_a - \omega) + \frac{\gamma}{2}\right) \sigma_- + g\sigma_z a. \tag{2.16}$$

Assuming steady state, i.e. $\dot{a} = \dot{\sigma}_- = 0$, and leveraging the input-output relation $a_{\text{out}} - a_{\text{in}} = \sqrt{\kappa_{\text{wg}}} a$ (where a_{in} and a_{out} represent the annihilation operators of the cavity-coupled waveguide mode), the cavity reflection coefficient for a single-sided cavity is

$$r(\omega) = 1 - \frac{\kappa_{\text{wg}}}{i(\omega_c - \omega) + \frac{\kappa}{2} - \frac{g^2}{i(\omega_a - \omega) + \frac{\gamma}{2}}}, \tag{2.17}$$

where ω is the probe frequency. Assuming we send a single photon on-resonance with the cavity and the emitter, and that the cavity is perfectly overcoupled to the waveguide such that $\kappa_{\text{wg}} = \kappa$, the expression simplifies to

$$r(\omega) = \frac{C - 1}{C + 1}, \tag{2.18}$$

where C is again the cooperativity.

Let us use this simplified expression to acquire an intuitive picture on how it may be used to construct a two-qubit gate between the spin and the photonic qubits. As shown in Figure 2-3, if the cavity linewidth κ is sufficiently narrow to cover only one of the two optical transitions, $|\downarrow\rangle \leftrightarrow |\downarrow'\rangle$, then the cavity reflection changes its *phase* depending on the spin state. Explicitly, in the limit of large C, if the spin is in the $|\downarrow\rangle$ state, $r(\omega)$ approaches $+1$. In contrast, if the spin is in the $|\uparrow\rangle$ state, $C = 0$ as

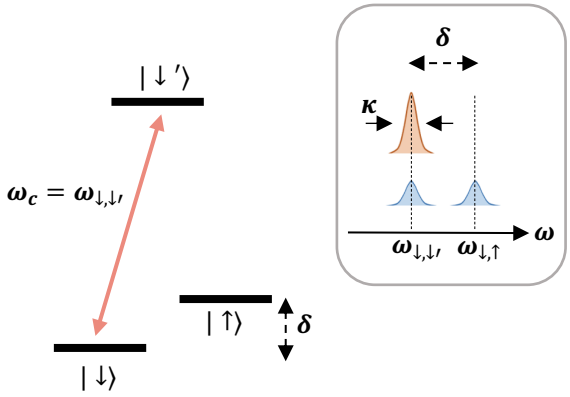

Figure 2-3: A prototypical lambda level structure of a quantum emitter. It consists of two ground spin states separated by δ, $|\downarrow\rangle$ and $|\uparrow\rangle$, both of which can be excited up to $|\downarrow'\rangle$. In the case that only one of the two transitions, $|\downarrow\rangle \leftrightarrow |\downarrow'\rangle$, is resonant with the cavity resonance ω_c, a single photon reflecting off the cavity from the waveguide acquires drastically different phase depending on the spin state. Note that this is satisfied when the cavity linewidth κ is sufficiently narrow.

it is decoupled from the cavity mode, thus $r(\omega)$ approaches -1. It is exactly this π phase difference acquired by the reflected photon that constructs a controlled-phase (CZ) gate between the spin and the photonic qubits.

In reality, however, the cavity linewidth is often large enough to cover both transitions, which have overlapping polarization modes with the cavity mode. In this case, depending on the cavity coupling regime (undercoupled vs critically coupled vs overcoupled), achieving the π phase contrast may require engineering other degrees of freedom, e.g. atomic detuning between ω and ω_a and $\kappa_{\text{wg}}/\kappa$. This will be explicitly demonstrated in the later Section 5.5.

2.3 Spin-photon teleportation

We can leverage the aforementioned controlled-phase gate to perform teleportation between a spin and a photonic qubit, as spelled out by the seminal paper by Duan and Kimble [53]. The setup shown in Figure 2-4 is essentially a Michelson interferometer with a polarizing beam splitter (PBS) that separates out two spatial paths for the two polarization modes. The V polarization mode is routed towards a bare mirror, whereas the H polarization mode is directed to the single-sided cavity. We

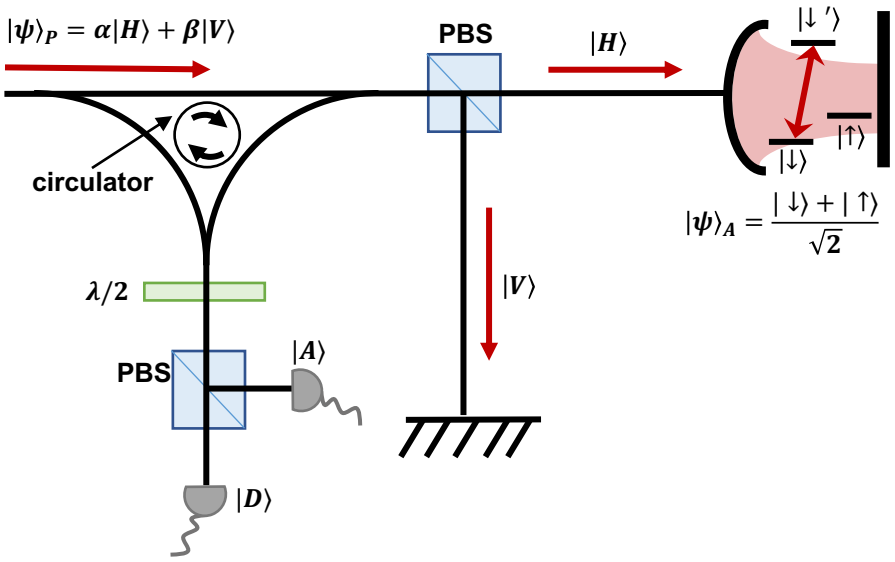

Figure 2-4: The optical setup for spin-photon teleportation. An incoming photonic qubit is dual-rail encoded in polarization: $|\psi\rangle_P = \alpha\,|H\rangle + \beta\,|V\rangle$. It enters a Michelson interferometer with a PBS that routes the V component to a bare mirror and the H component to a single-sided cavity, which couples to an emitter initialized in a superposition state, $|\psi\rangle_A = (|\downarrow\rangle + |\uparrow\rangle)/\sqrt{2}$. Upon reflection, the two polarization modes recombine at the PBS and the photonic qubit (now entangled with the spin qubit) is detected in the diagonal basis. After feedforward, the photonic qubit is teleported onto the spin qubit whose final state is $|\psi\rangle'_A = \alpha\,|\downarrow\rangle + \beta\,|\uparrow\rangle$.

can evaluate how teleportation is constructed by the following Schrödinger picture evolution. Let the initial photonic qubit to be an arbitrary *polarization* state of the form

$$|\psi\rangle_P = \alpha\,|H\rangle + \beta\,|V\rangle\,, \tag{2.19}$$

where $|\alpha|^2 + |\beta|^2 = 1$. Additionally, the spin qubit is initialized in an even superposition state,

$$|\psi\rangle_A = \frac{|\downarrow\rangle + |\uparrow\rangle}{\sqrt{2}}. \tag{2.20}$$

The total system then has an initial product state (neglecting normalization for

now)

$$|\Psi\rangle = |\psi\rangle_P \otimes |\psi\rangle_A \tag{2.21}$$

$$= \alpha\,|H,\downarrow\rangle + \alpha\,|H,\uparrow\rangle + \beta\,|V,\downarrow\rangle + \beta\,|V,\uparrow\rangle\,. \tag{2.22}$$

From electrodynamics, we know that in the V polarization path, reflection off a bare mirror (irregardless of the polarization) imparts a constant π phase shift. As for the H polarization path, reflection off the single-sided cavity that is coupled to an emitter gives only the $|\uparrow\rangle$ state a π phase shift while leaving the $|\downarrow\rangle$ intact. As a result, after reflection off the mirror and the cavity, the composite spin-photon state is now an entangled state

$$|\Psi\rangle = \alpha\,|H,\downarrow\rangle - \alpha\,|H,\uparrow\rangle - \beta\,|V,\downarrow\rangle - \beta\,|V,\uparrow\rangle\,. \tag{2.23}$$

In the detection port after the circulator, the photon is measured in the diagonal basis $\{D, A\}$[2]. In the new basis, the entangled state can be written as

$$|\Psi\rangle = |H\rangle \otimes [(\alpha+\beta)\,|\downarrow\rangle + (-\alpha+\beta)\,|\uparrow\rangle] \tag{2.24}$$

$$|V\rangle \otimes [(\alpha-\beta)\,|\downarrow\rangle + (-\alpha-\beta)\,|\uparrow\rangle]\,. \tag{2.25}$$

Depending on whether the H or the V detector heralds a click, the state is projected to either $(\alpha+\beta)\,|\downarrow\rangle+(-\alpha+\beta)\,|\uparrow\rangle$ or $(\alpha-\beta)\,|\downarrow\rangle+(-\alpha-\beta)\,|\uparrow\rangle$. For illustration, in the former case, we can recover the initial quantum state by first applying a Hadamard gate then a Pauli-Z gate to the spin qubit, resulting in

$$|\psi\rangle'_A \to \alpha\,|\downarrow\rangle - \beta\,|\uparrow\rangle \qquad \text{(after Hadamard)} \tag{2.26}$$

$$\to \alpha\,|\downarrow\rangle + \beta\,|\uparrow\rangle \qquad \text{(after Pauli-Z)} \tag{2.27}$$

In the end, we have faithfully teleported the photonic qubit onto the spin qubit.

[2]This is done by passing the photon through a half wave plate (HWP) that transforms $H \to H+V, V \to V-H$ at rotation angle $\theta = \pi/4$

This is a powerful technique for mapping a flying qubit that propagates long distances onto a long-lived matter qubit for memory storage. More importantly, the gate operation is a *heralded* process, meaning only upon detection of a photon's arrival does the teleportation process complete. As a result, photon loss[3] is a detectable error, rendering the Duan-Kimble scheme conducive to building up distant quantum repeater network in which propagation loss can be significant.

However, the gate operation fidelity crucially depends on the cavity reflection coefficient. If the emitter-cavity system exhibits a lower C, the final state fidelity would inevitably degrade, as computed by the overlap between the teleported and the ideal states,

$$\mathcal{F} = \frac{1}{6}\sum_i \mathcal{F}_i = \frac{1}{6}\sum_i |_i\langle\phi|\psi\rangle'_{A,i}|^2, \tag{2.28}$$

where $|\phi\rangle_i$ ($|\psi\rangle'_{A,i}$) represents the ideal (teleported) spin state and each i indicates a basis state (along X,Y,and Z axes) on the Bloch sphere. More details about the effect of imperfect cavity reflection and ways to counteract this will be covered in the following chapters.

Finally, we note that using a phase difference for performing teleportation is only one of many methods. For an instance, one may also utilize *amplitude* difference and time bin-encoded photonic qubits to achieve the same goal, in which case critical coupling would be preferred, as shown by Ref. [64, 66][4]. The only subtle difference is that the latter is by definition a two-photon protocol that relies on detection of two subsequent photons, which may lead to lower success probability relative to the former case. Therefore, for the analysis covered in Sections 3.4 and 5.5, we only concern with phase-based methods and polarization-encoded qubits. However, a similar treatment can be easily applied to the time bin-encoding case.

[3]Loss of a photonic qubit is essentially a leakage error out of the qubit subspace.

[4]The reason that the critically coupled regime works better is there is intrinsically a maximized amplitude difference due to destructive interference based on coupled-mode theory [67].

Chapter 3

A polarization-encoded photon-to-spin interface (PEPSI)

The research outcomes of this chapter have been published as a journal article entitled "A polarization encoded photon-to-spin interface" *in* npj Quant. Info. **7**, 2 (2021) [46].

One subtlety about the Duan-Kimble scheme in the previous chapter is its phase sensitivity. Since the two polarization modes are separated into two spatial paths in the Michelson interferometer, any introduction of a varying relative phase $\Delta\phi(t)$ (as shown in Figure 3-1(a)) would lead to infidelity in the teleported state. This is especially problematic to a free-space optical setup in which the two polarization paths may span 10's of centimeters, over which any environmental fluctuation (thermal, mechanical,...etc.) may induce a non-zero $\Delta\phi(t)$. Therefore, we propose a monolithic, micron-scale photonic structure that combines the H and V paths into one phase-stable architecture (Figure 3-1(b)). This Polarization-Encoded Photon-to-Spin Interface (PEPSI) greatly simplifies quantum networking with polarization-encoded photons coupled to atomic memories [46].

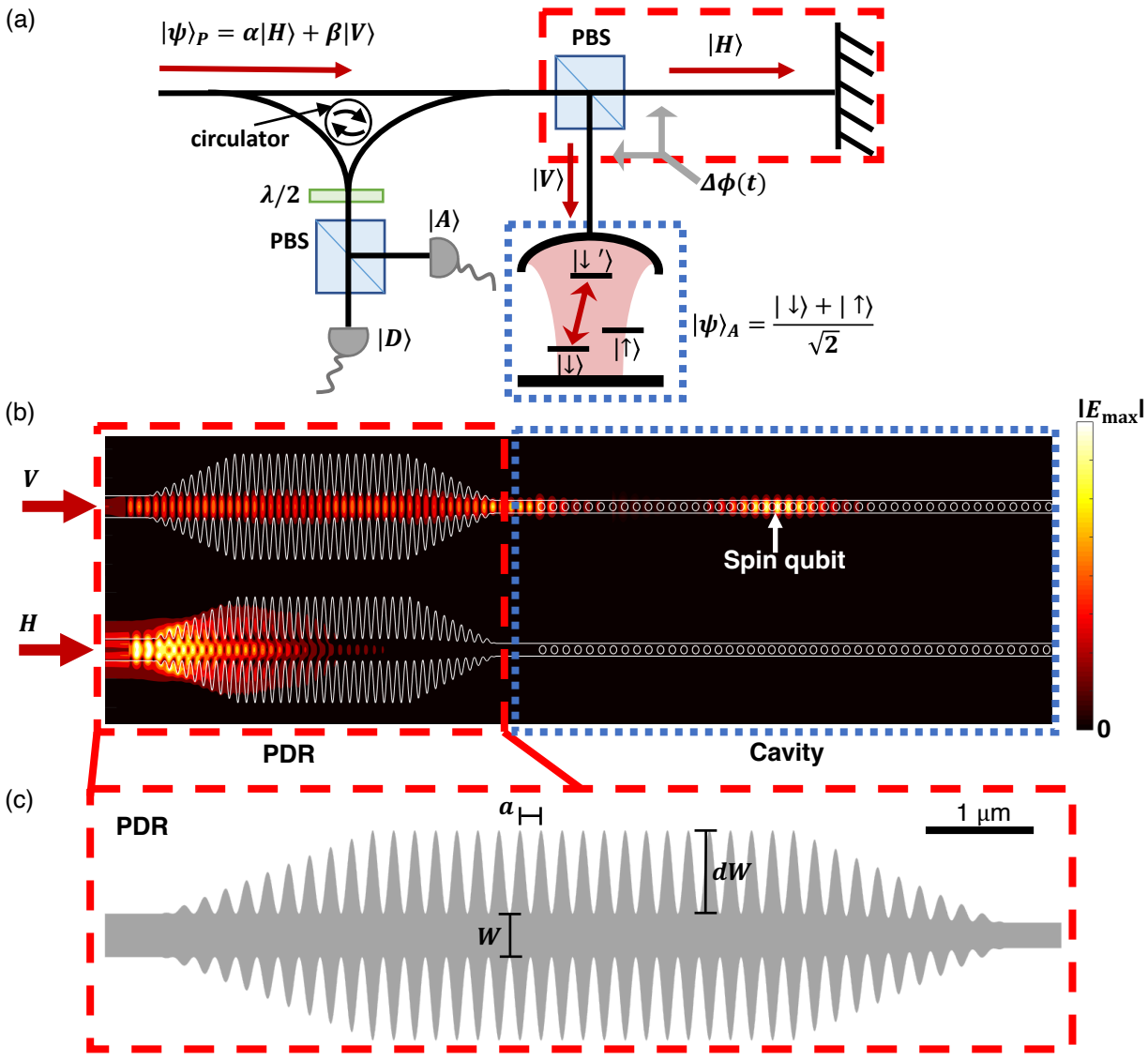

Figure 3-1: (a) The Duan-Kimble scheme for polarization-spin mapping. The requirements of a high extinction polarizing beam splitter (PBS), strong cavity-atom coupling, and stabilization of the phase mismatch between arms $\Delta\phi(t)$ all make implementation with bulk optics challenging. (b) Our proposal for a phase-stable monolithic device (PEPSI) that implements the protocol in (a). A polarization-dependent reflector (PDR, red dashed lines) then reflects H light while passing V light through to interact with the cavity-emitter system (blue dashed lines). (c) A zoom-in depiction of the PDR with geometry parameters a (periodicity), W (width), and dW (modulation amplitude). The scale bar corresponds to 1 micron.

3.1 Device design

As illustrated in Figure 3-1(b), the structure comprises i) a polarization-dependent reflector (PDR) for the H (TE) mode, and ii) an over-coupled single sided cavity

for the V (TM) mode. As opposed to what was shown in Section 2.3, the reason the cavity is designed to be resonant with a TM mode as opposed to TE mode is to comply with the thickness constraint posed by the corrugated photonic crystal PDR. Nevertheless, the working principle remains the same. The PEPSI collapses both interferometric arms into one co-propagating path that greatly suppresses phase instability stemming from environmental noise. In contrast, bulk optics suffer from thermal and vibrational fluctuations that incur phase noise, which requires phase stabilization costly in operation time [66].

The PDR shown in Figure 3-1(c) uses a corrugated photonic crystal design with periodicity $a = 184$ nm, width $W = 2.07a$, modulation amplitude $dW = 3.97a$. An adiabatic taper transfers photons to a 1D photonic crystal nanocavity coupled to the SiV center. The following sections analyze the performance of this phase-stable device. Specifically, we investigate the impact of PEPSI device parameters on teleportation fidelity, the rate-fidelity trade-off in a quantum network link, and extensions to a scalable photonic integrated circuit platform.

3.2 Effects of device imperfections

To analyze the state transfer (aka teleportation) process, we use the same definition for the final state fidelity $\mathcal{F}$ spelled out in Eq. 2.28. However, the final state would have additional coefficients after considering the effects of imperfect devices. Specifically, the photonic qubit interacts with an imperfect PDR with field reflection (transmission) coefficients r_i (t_i) for the polarization mode $i \in \{H, V\}$. The transmitted output is incident on a nanophotonic cavity coupled to a spin qubit. Since only the $|\downarrow\rangle \leftrightarrow |\downarrow'\rangle$ (see Figure 3-1(a)) transition is resonant with the cavity mode (assuming a sufficiently narrow cavity linewidth), the photon experiences a spin-dependent cavity reflection: $r_{cav} \in \{r_{i,uncoupled}, r_{i,coupled}\}$. The output joint photon-spin system

after the HWP (that transform $H \to H+V, V \to V-H$) is in the state

$$\begin{aligned}|\psi\rangle'_A = |H\rangle \otimes [(\alpha r_{H,\text{on}} - \beta r_{V,\text{on}})\,|\downarrow\rangle + (\alpha r_{H,\text{off}} - \beta r_{V,\text{off}})\,|\uparrow\rangle] \\ + |V\rangle \otimes [(\alpha r_{H,\text{on}} + \beta r_{V,\text{on}})\,|\downarrow\rangle + (\alpha r_{H,\text{off}} + \beta r_{V,\text{off}})\,|\uparrow\rangle],\end{aligned} \tag{3.1}$$

where

$$r_{H,\text{on(off)}} = r_H + \frac{r_{H,\text{(un)coupled}} t_H^2}{1 - r_{H,\text{(un)coupled}} r_H} \tag{3.2}$$

$$r_{V,\text{on(off)}} = r_V + \frac{r_{V,\text{(un)coupled}} t_V^2}{1 - r_{V,\text{(un)coupled}} r_V}. \tag{3.3}$$

When a device is perfect such that a lossless PDR has infinite polarization extinction ratios and a nanocavity has perfect waveguide-cavity coupling ($\kappa_{\text{wg}}/\kappa = 1$), the cavity reflection solely determines the fidelity that scales as $(C-1)/(C+1)$ in the large cooperativity limit [68]. However, when the PDR has finite extinction ratios and scattering losses, and the single sided cavity has a reduced waveguide-cavity coupling efficiency $\kappa_{\text{wg}}/\kappa < 1$, the need to balance losses becomes especially important to achieving high fidelity. For example, considering the desired state $|\phi_1\rangle$ where $\alpha = \beta = 1$, balancing losses entails matching the two coefficients by satisfying

$$|r_{H,\text{on}} - r_{V,\text{on}}| = |r_{H,\text{off}} + r_{V,\text{off}}|, \tag{3.4}$$

which are both functions of PDR transmissivity/reflectivity and the cavity reflectivity.

Figure 3-2(a) shows $\mathcal{F}$ as a function of the PDR's width and modulation amplitude given a low scattering loss and fixed cavity parameters corresponding to our design: waveguide-cavity coupling $\kappa_{\text{wg}}/\kappa \approx 0.83$ and cooperativity $C = 100$, which has already been experimentally demonstrated in Ref. [66]. We find the upper bound of the fidelity is maximized at 99.978% (assuming perfect gate and detection fidelities) when $W = 380$ nm and $dW = 730$ nm, corresponding to transmission and reflection extinction ratios of 17.72 dB and 18.93 dB for 20 periodicities. In order to controllably balance losses to maximize the state transfer fidelity, we also include

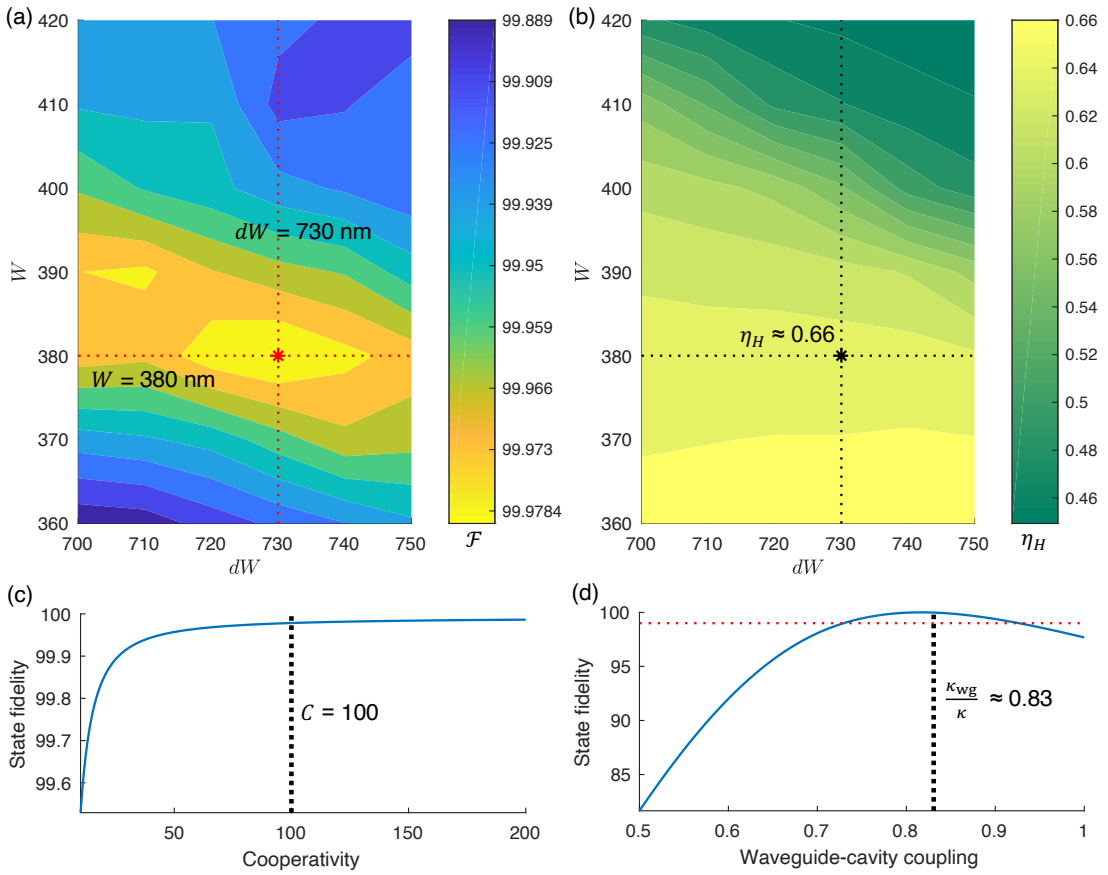

Figure 3-2: (a) $\mathcal{F}$ is plotted as a function of the two PDR geometry parameters: the width W and the modulation amplitude dW. $W = 380$ nm and $dW = 730$ nm are chosen for our particular device with an optimum $\mathcal{F} = 99.978\%$. (b) The optimal H polarization attenuation factor for balancing losses as a function of W and dW. (c,d) The state fidelity as functions of the atom-cavity cooperativity and waveguide-cavity coupling. The atom-cavity cooperativity is calculated using Eq. 2.17. The PDR is designed specifically for a single sided cavity with $C = 100$. The waveguide-cavity coupling is tuned to $\kappa_{\mathrm{wg}}/\kappa \approx 0.83$ to maximize fidelity within the allowable design space. The red dashed line indicates the threshold $\mathcal{F} = 99\%$, which is satisfied in the range $\kappa_{\mathrm{wg}}/\kappa = [0.73, 0.93]$.

an H attenuator that only diminishes the incoming H light (see Appendix B.1). For each set of parameter values $\{dW, W\}$, we calculate the H attenuation factor η_H that maximizes $\mathcal{F}$ in Figure 3-2(b). For the particular design with $W = 380$ nm and $dW = 730$ nm, the optimal upper bound $\mathcal{F} = 99.978\%$ is reached when $\eta_H = 66\%$. In fact, by tuning η_H appropriately, we observe that $\mathcal{F}$ well exceeds 99% for any dW between 700 nm and 750 nm and similarly for any W between 360 nm and 420 nm, providing the PEPSI tolerance to fabrication errors.

Additionally, the state transfer fidelity intimately relates to the cavity parameters. Figure 3-2(c) shows that the state fidelity monotonically improves with the atom-cavity cooperativity since the cavity reflectivity $r \propto (C-1)/(C+1)$ approaches $+1$. For our device, the atom-cavity cooperativity of $C = 100$ gives $\mathcal{F} = 99.978\%$. We also analyze the fidelity's dependence on the waveguide-cavity coupling strength. As a result of balanced losses, Figure 3-2(d) indicates that the fidelity is maximized when $\kappa_{\text{wg}}/\kappa = 0.82$ and decreases as the waveguide-cavity coupling deviates from the optimal point. An undercoupled or critically coupled cavity would result in a severely degraded state transfer due to insufficient cavity reflection. On the other hand, overcoupling past $\kappa_{\text{wg}}/\kappa = 0.82$ would curtail the atom-cavity interaction and consequently lowers the fidelity. However, our calculation shows that the fidelity can still exceed 99% as long as $\kappa_{\text{wg}}/\kappa$ falls between 0.73 and 0.93, granting again partial immunity to errors.

3.3 Teleportation rate-fidelity trade-off

We now analyze the performance of the PEPSI in facilitating quantum state transfer across a lossy network link by assessing the rate-fidelity trade-off for a device realized in simulation. We denote the probability of a photon entering and returning through the PDR as $\eta_H \eta_{\text{PDR}}^2 R_{\text{cav}}$, where R_{cav} is the cavity reflection coefficient and $1 - R_{\text{cav}}$ is the cavity decay rate into the environment (assume negligible transmission through the single sided cavity). η_{PDR} is the transmission efficiency of the PDR. As shown in Figure 3-3(a), the protocol begins by initializing the spin qubit in a superposition

state $(|\uparrow\rangle+|\downarrow\rangle)/\sqrt{2}$ in a time $\tau_{\text{reset}} = 30\mu\text{s}$ [66]. A photonic qubit $|\psi_P\rangle$ launched across the link with transmissivity η_{link} reaches the PDR shown in Fig 3-3(b). If the reflected photon is detected as described above with probability $p_{\text{det}} = \eta_{\text{link}}\eta_H\eta_{\text{PDR}}^2 R_{\text{cav}}\eta_{\text{det}}$, the spin qubit is projected to the state $\alpha|\downarrow\rangle+\beta|\uparrow\rangle$. If no photon is detected, the protocol is repeated.

However, when $\eta_{\text{link}} \ll 1$, most transmission attempts do not interact with the spin, and time can be saved by not re-initializing on every transmission attempt. In particular, we consider a series of N photons injected into the link after spin re-initialization. These photons are interspersed by dynamical decoupling pulses (π-pulses in Figure 3-3(a)) to maintain memory coherence. If the detector registers a click for the mth attempt, the receiver blocks the subsequent $N-m$ pulses. The complication is that any photon that reaches the cavity but is subsequently lost produces an unheralded error with probability $p_e = \eta_{\text{link}}\eta_H\eta_{\text{PDR}}(1-R_{\text{cav}})$, since the environment projects the spin to a mixed state $\rho_{\text{mixed}} = \frac{1}{2}\mathbb{I}$. Thus, the optimum fidelity for a given device is achieved by re-initializing the spin qubit in advance of every photon transmission. However, the photon can also be either lost in the link before reaching the spin with probability $p_{\text{lost}} = 1-p_e-p_{\text{det}}$ or heralded by the detector with probability p_{det}. Conditioned on not detecting a click, the probability of photon loss without contaminating the spin is $p_{\text{lost}}/(1-p_{\text{det}})$, and therefore the probability of photon never reaching the spin after $m-1 \leq N$ channel uses is $(p_{\text{lost}}/(1-p_{\text{det}}))^{m-1}$.

Explicitly, for calculating p_{det} and p_{lost}, we consider the transmission efficiency $\eta_{A,V/H}$ through the H attenuator to be 79.8% for the V polarization and 52.6% for the H polarization (see Section 3.3.3). We denote the power transmission and reflection coefficients of the PDR as $T_{V/H}$ and $R_{V/H}$. The cavity reflectivity $R_{\text{cav},V}/R_{\text{cav},H}$ is the average reflectivity between on- and off-resonance cases for the V/H polarization, respectively: $R_{\text{cav},V} = (|r_{\text{cavity-}V}|^2 + |r_{\text{coup-}V}|^2)/2 = 82.2\%, R_{\text{cav},H} = 95.8\%$ basing on our simulated device and $C = 100$.

In order to detect a V (H) photon, it has to either undergo a round-trip as denoted by Fig. 3-3(b) with probability $\eta_{\text{link}}\eta_{a,V}T_V R_{\text{cav},V} T_V \eta_{\text{det}}$ ($\eta_{\text{link}}\eta_{a,H}T_H R_{\text{cav},H} T_H \eta_{\text{det}}$) or reflect off the PDR upon the first pass with probability $\eta_{\text{link}}\eta_{a,V}R_V\eta_{\text{det}}$ ($\eta_{\text{link}}\eta_{a,H}R_H\eta_{\text{det}}$),

where $\eta_{\text{det}} = 93.6\%$ is the detection efficiency accounting for the PBS, the HWP, and the photon detector (see Section 3.3.3). The average detection probability is then

$$p_{\text{det}} = \frac{\eta_{\text{link}}}{2}\left(\eta_{a,V}T_V^2 R_{\text{cav},V} + R_V + \eta_{a,H}T_H^2 R_{\text{cav},H} + R_H\right)\eta_{\text{det}} \tag{3.5}$$

The photon can also scatter off en route to the PDR with probability $1-\eta_{\text{link}}$, or by the PDR, contributing to the probability of photon loss *without* error defined as

$$p_{\text{lost}} = 1 - \eta_{\text{link}} + \eta_{\text{link}}\left(1 - \frac{\eta_{a,V}+\eta_{a,H}}{2}\right) + \frac{\eta_{\text{link}}}{2}\left(\zeta_V + \zeta_H\right), \tag{3.6}$$

where $\zeta_V = 1 - T_V - R_V$ and $\zeta_H = 1 - T_H - R_H$.

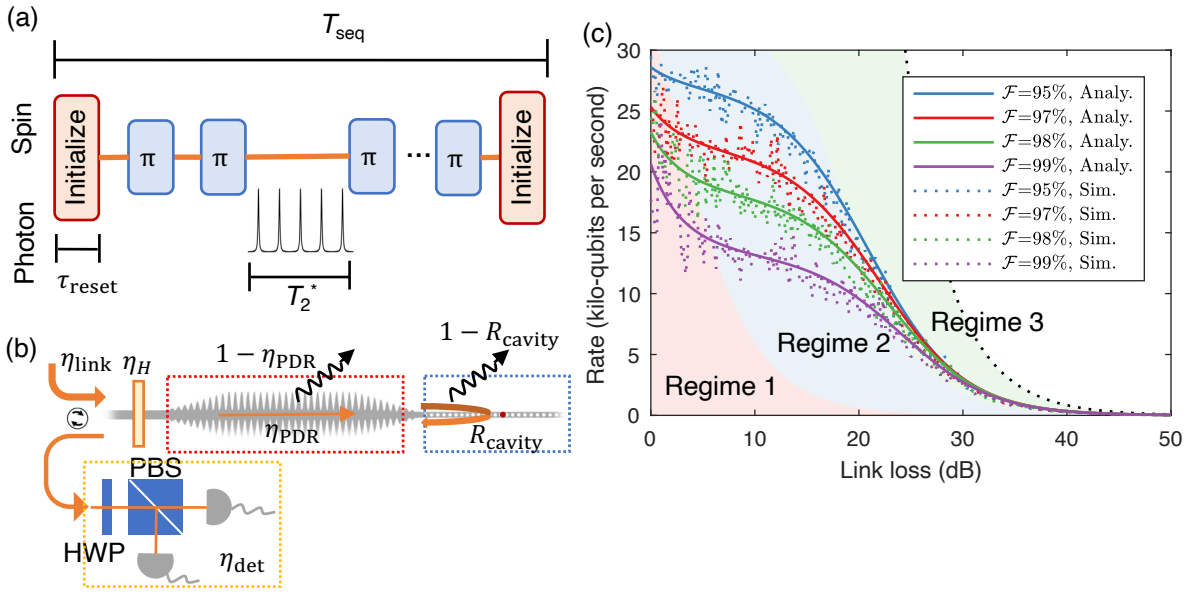

Figure 3-3: (a) Pulse sequences for conducting quantum state transfer between a polarization qubit and a spin qubit. (b) A diagram depicting where scattering losses occur. (c) Transfer rate (kilo-qubits per second, operated at 5.81 MHz clock rate) as a function of link loss $1-\eta_{\text{link}}$ for four fidelity constraints: $\mathcal{F} = 95, 97, 98, 99\%$. We plot both the analytical solutions (solid) and the Monte Carlo simulations (dashed). We categorize the rate as a function of link loss into Regime 1 (red), Regime 2 (blue), and Regime 3 (green). The black dashed line denotes the repeater-less bound for quantum key distribution protocols [5].

Given a detector click on the m^{th} attempt, the probability that at least one error

has occurred in the preceding $m-1$ bins is

$$P_{\text{error}}(m) = 1 - \left(\frac{p_{\text{lost}}}{1-p_{\text{det}}}\right)^{m-1}. \tag{3.7}$$

The average error probability P_{error} is found by summing over all possible sequences up to a total of N attempts, each sequence weighted by $P\left(m^{\text{th}} \text{ click}\right)$, which is the probability of detecting a click on the m^{th} attempt. P_{error} is then defined as

$$P_{\text{error}} = \sum_{m=1}^{N} P_{\text{error}}(m) P(m^{\text{th}} \text{ click}) = 1 - (1-p_{\text{det}})^N - p_{\text{det}} \frac{1-p_{\text{lost}}^N}{1-p_{\text{lost}}}. \tag{3.8}$$

The average state fidelity after the protocol that uses sequences of length N before resetting the memory is then

$$\mathcal{F} = \langle \psi_{\text{ideal}} | \left(1 - P_{\text{error}}\right) \rho_{0,\text{eff}} + P_{\text{error}} \rho_{\text{mixed}} | \psi_{\text{ideal}} \rangle, \tag{3.9}$$

where $|\psi_{\text{ideal}}\rangle$ is the ideal transferred quantum state and $\rho_{0,\text{eff}}$ is the effective density matrix incorporating device imperfections and detection error. We can solve Eq. 3.9 for the maximum number of channel uses before spin re-initialization N_{max} under a given fidelity constraint, e.g. $\mathcal{F} = 99\%$.

Each sequence (duration T_{seq} as denoted in Figure 3-3(a)) of N_{max} transmission attempts has a probability $P_{\text{success}} = 1 - (1-p_{\text{det}})^{N_{\text{max}}}$ to detect at least one click. The number of failed sequences (i.e. each sequence of N_{max} attempts without clicks followed by a memory reset) before a successful one is given by the geometric distribution. Thus, the average time of failed sequences per detector click is

$$T_{\text{failures}} = \frac{(1-p_{\text{det}})^{N_{\text{max}}}}{1-(1-p_{\text{det}})^{N_{\text{max}}}} \left[N_{\text{max}} \tau_{\text{pulse}} + \tau_{\text{reset}}\right], \tag{3.10}$$

where $4\tau_{\text{pulse}}$ is an effective pulse time accounting for repetition rate and dynamical decoupling π pulses.

After these failures, there is a successful sequence where the m^{th} bin yields a click,

which takes an average time of

$$T_{\text{success}} = \tau_{\text{reset}} + \sum_{m=1}^{N_{\max}} P(m^{\text{th}} \text{ click}) m\tau_{\text{pulse}}$$
$$= \tau_{\text{reset}} + \tau_{\text{pulse}} \left(\frac{P_{\text{success}}}{p_{\text{det}}} - N_{\max}(1-p_{\text{det}})^{N_{\max}} \right). \tag{3.11}$$

The average quantum state transfer rate is then the inverse of the time per success

$$\bar{\Gamma} = \frac{1}{T_{\text{failures}} + T_{\text{success}}}. \tag{3.12}$$

In Figure 3-3(c), we explore the trade-off between the heralded state fidelity $\mathcal{F}$ and the average rate accounting for both polarization modes. We verify our analytical solutions with Monte Carlo simulations, and show that the PEPSI can achieve transfer rate exceeding 1 kilo-qubits per second even at high link loss ~ 30 dB.

We divide the rate into three regimes. In Regime 1 (shaded red) where $N_{\max}$ is low, high-fidelity state transfer prohibits increasing $N_{\max}$ to offset losses in the channel, causing an exponential rate loss that intensifies for higher fidelity constraint, e.g. $\mathcal{F} = 99\%$. On the other hand, for a more relaxed fidelity constraint, e.g. $\mathcal{F} = 95\%$, the spin does not need to be re-initialized as frequently and the rate does not fall off as drastically. As the link loss increases in Regime 2 (shaded blue), the number of transmission attempts per memory reset also increases. However, the time per success is still dominated by memory reset time in this regime where $\tau_{\text{reset}} > N_{\max}\tau_{\text{pulse}}$. As a result, the rate of increase for the number of sequences prior to detecting a click stays constant, and the rate consequently remains relatively flat. However, in Regime 3 (shaded green) when the number of transmission attempts per sequence increases such that $N_{\max}\tau_{\text{pulse}} > \tau_{\text{reset}}$, η_{link} becomes the rate-limiting factor. In this Regime, the rate thus approaches the channel-limited bound (black dashed) given by $\propto \eta_{\text{link}}/\tau_{\text{pulse}}$ [5].

3.3.1 Monte Carlo simulations

Numerical simulations were performed in MATLAB (MathWorks Inc.). For each attempt, a probability value p_{random} is chosen out of a uniform distribution $U(0,1)$. p_{random} then determines if the photon is lost in the device before reaching the spin (p_{lost}), lost in the device *after* the spin (p_e), or detected (p_{det}). Each simulation trial terminates once the photon is detected, and the total experimental time is recorded. A trial can consist of multiple sequences, and each sequence has the number of attempts up to N_{max}, which depends on the fidelity constraint and the link loss. Each Monte Carlo data point presented in Fig. 3-3(c) is the average rate of 100 simulation trials.

The oscillation in the Monte Carlo simulations (dashed lines in Fig. 3-3(c)) is an artifact from discretizing the number of attempts required to achieve a certain fidelity constraint given a fixed link loss (see Section 3.3.2). The allowable N_{max} is first analytically calculated assuming a continuous variable, then fed into the Monte Carlo simulations to validate the transfer rate calculations. The origin of the artifact can be understood by considering the trade-off between fidelity and the number of attempts. Recall that every undetected photon can be scattered before reaching the emitter-cavity system. Hence, time can be saved by not re-initializing the spin qubit as N_{attempts} increases. In other words, as link loss increases, it is advantageous to increase the number of attempts. If an integer number of attempts Z is fixed, increasing the link loss consequently lowers the transfer rate *until the number of attempts increases to the next integer* $Z+1$. After which, the rate increases suddenly and manifests in a sinusoidal behavior in simulations.

3.3.2 Fidelity lower and upper bounds

Figure 3-4 shows representative curves for four selected link losses: 5,10,15,20 dB. For low loss at 5 dB, the fidelity rapidly drops off with increasing N_{attempt} since the photon would likely be lost from scattering off the device after reaching the spin. In contrast, the fidelity decreases relatively slowly at a higher link loss, e.g. 20 dB. Regardless of link losses, there exists a lower bound for the state fidelity determined

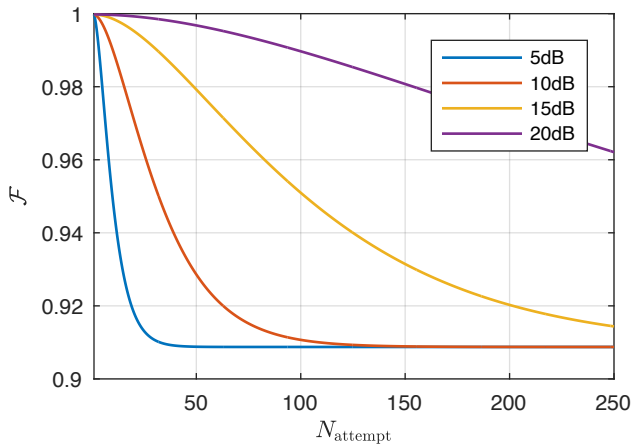

Figure 3-4: Mean fidelity as a function of N_{attempt} photons at link losses 5 dB, 10 dB, 15 dB, and 20 dB. There exist a lower bound of $\mathcal{F}_{\text{lower}} = 90.874\%$ and an upper bound $\mathcal{F}_{\text{upper}} = 99.978\%$.

purely by PDR scattering loss. If we take the limit of large N (Eq. 3.7), the equation simplifies to

$$\lim_{N\to\infty} P_{\text{error}} = 1 - \frac{p_{\text{det}}}{1 - p_{\text{lost}}}. \tag{3.13}$$

The resulted lower bound for fidelity is then

$$\mathcal{F}_{\text{lower}} = \langle\rho_0\rangle - \left(\langle\rho_0\rangle - \frac{1}{2}\right)\frac{p_{\text{det}}}{1 - p_{\text{lost}}}, \tag{3.14}$$

where $\langle\rho_0\rangle$ is $\mathcal{F}$'s upper bound is set by the single-attempt fidelity, which is $\mathcal{F}_{\text{upper}} = 99.978\%$. On the other hand, our particular device gives a lower bound $\mathcal{F}_{\text{lower}} = 90.874\%$, which stems from defining a mean fidelity conditioned on detecting a click. After a large number of attempts, at least one photon is guaranteed to arrive at PEPSI. It is either detected or lost determined by the device's efficiency. Therefore, in the $N \to \infty$ limit, $\mathcal{F}$ is purely subjected to $p_{\text{det}}/(1 - p_{\text{lost}})$.

3.3.3 System parameters

- **Pulse times**: τ_{pulse} is an effective pulse time that includes the fractional number of dynamical decoupling π pulses. Each π-pulse follows immediately after a

series of pulses within T_2^*: $\tau_{\text{pulse}} = (1 + t_\pi/T_2^*)\, T_1 \times 100$, where $t_\pi = 32$ ns, $T_1 = 1.72$ ns is the optical lifetime, and $T_2^* = 0.2$ ms is the spin coherence time [66, 33].

- H **attenuator**: We assume a transmission efficiency of 89.3% for each of the beam displacers (see Appendix B.1) for both polarization modes. Additionally, given the specific PDR design, we set $\eta_H = 66\%$ to balance losses and maximize the transfer fidelity.

- **Detection system**: $\eta_{\text{det}} = 93.6\%$ is the product of efficiencies of the PBS, the HWP, and the photon detector: 95%, 99.5%, and 99%, respectively. The numbers for the PBS and the HWP are based on commercially available components. We take the number reported in Ref. [66] for a superconducting nanowire single photon detector (SNSPD) optimized for 737 nm.

3.4 Discussion and extension to PIC

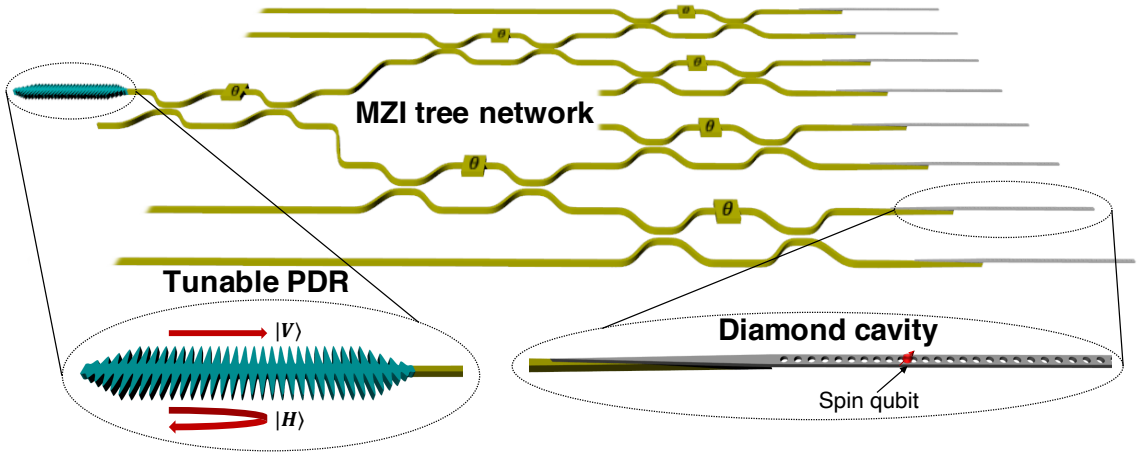

Figure 3-5: A PIC incorporating diamond nanocavities. The V polarization passes through a tunable PDR (a combination of a PDR, active on-chip waveplates and polarizers) and enters an MZI tree network, which routes the photon to an atom-coupled cavity for quantum state transfer.

Practical quantum repeater nodes will likely require multiplexing over a large

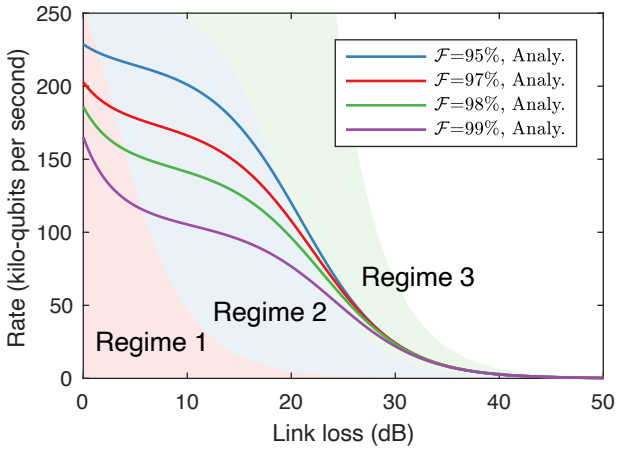

Figure 3-6: State transfer rate as a function of link loss $1 - \eta_{\text{link}}$ for the integration platform.

number of qubits. To this end, we consider the PEPSI photonic integrated circuit (PIC) illustrated in Fig. 3-5. An incoming photonic qubit $|\psi_P\rangle$ enters through a PDR followed by a Mach-Zehnder interferometer (MZI) tree network, which routes the photon to a quantum memory. The PIC with >GHz modulation of the MZIs [69] can perform state mapping across the memory array simultaneously by sending multiplexed photons to different atom-coupled cavities. As a result, the transfer rate improves by a factor of N_{cav} equivalent to the number of memories connected to the tree network, as shown by Figure 3-6. The architecture can also produce heralded entanglement by sending a photon that enters an MZI 50:50 beam splitter immediately before entering any two neighboring memories. Repeated heralding then produces a cluster of entangled nodes useful for quantum key distribution protocols.

Furthermore, an active PIC provides tunability essential for efficient quantum state transfer. For example, aluminum nitride photonic circuits have integrated 128 diamond waveguide-coupled color centers [50] and can enable piezoelectric spectral tuning of photonic crystal cavities [60] and diamond color center emission [70, 71]. Integration by pick-and-placing allows post-selecting high-performing devices, and additional on-chip waveplates and polarizers in conjunction with the PDR (collectively termed as a tunable PDR in Fig. 3-5) can then optimally balance losses to achieve high transfer fidelity. Multiple emitters may also be implanted [72] to in-

crease the number of devices containing SiV^- oriented along the applied magnetic field's direction.

In summary, we introduced a phase-stable architecture for high-fidelity quantum state transfer between photonic polarization and spin qubits: the fundamental elements of a quantum repeater network. Our simulations and calculations show that the PEPSI can achieve state fidelity exceeding 99% at kilo-qubits per second transfer rate by carefully balancing losses. We note that the source of infidelity considered in the analyses addresses only the mode-mismatch error. Namely, the loss imbalance that arises from non-optimal transmissivities and reflectivities of the PDR and the nanocavity. Additional qubit errors concerning dephasing, spectral diffusion, and charge-state instability will require further investigation [73, 74]. Therefore, the calculated fidelity of 99.978% is realistically an upper bound. Nevertheless, beyond color centers in diamond, our scheme applies to other quantum memories including rare-earth ions [75, 76, 77] and neutral atoms [78] that may exhibit lower qubit errors. Lastly, we proposed a multiplexing PIC platform for state mappings across a quantum memory array via an MZI tree network. As PIC platforms have scaled beyond tens of individually controllable components [79], our nanophotonic spin-photon interface should extend these gains to large-scale multiplexed quantum repeaters [80] and even photonic cluster states [81].

Chapter 4

Experimental realization of a cavity-enhanced spin-photon interface

In PEPSI, a crucial component is the emitter-cavity coupled system that enables spin-photon entanglement via cavity reflection. This chapter presents our experimental realization of a cavity-enhanced photonic interface with SnV center in diamond. In Section 4.1, we will begin with discussing the design of a 1-dimensional photonic crystal cavity in diamond. Then, we will explain the diamond nanofabrication process based on quasi-isotropic etching to produce the designed devices in Section 4.2. Section 4.3 will provide cavity characterization results using a cross-polarization setup. Section 4.4 details spectroscopic characterization of SnV centers at 4 K. With the in-situ gas tuning technique explained in Section 4.5, we will present measurement results demonstrating Purcell enhancement of emitter-cavity coupled systems in Section 4.6.

4.1 1D PhC cavity design

For simplicity of discussion, we will only consider 1-dimensional structures, e.g. a suspended nanobeam, due to fabrication constraints (see Section 4.2). Readers interested in other types of photonic crystals and their applications should consult Ref. [63].

The photonic cavity employed in the experiment is based on photonic crystals

(PhC), which are periodic structures, e.g. a nanobeam with air holes separated by a constant spacing as shown in Figure 4-1(a), which form a *photonic bandgap*. Similar to the electronic bandgap in which no electronic states can exist, a photonic bandgap disallows certain frequencies of light to propagate inside a PhC structure. Effectively, a PhC structure functions as a Bragg mirror that suppresses transmission of these frequencies. In this case, for our target wavelength of $\lambda_{\text{Snv}} \sim 619$ nm corresponding to the SnV center's ZPL, we parameterize the nanobeam width W, thickness H, the air hole radius r, and the periodicity a to maximize the size of the photonic bandgap centered at λ_{Snv}[1]. Figure 4-1(b) shows the photonic bandstructure[2] containing a photonic bandgap obtained from finite-difference time-domain (FDTD) simulations (Lumerical).

In order to engineer an optical *cavity*, one naive approach is to sandwich a nanobeam without holes by two PhC Bragg mirrors. However, these mirrors cannot support resonant modes as effectively as a free-space Fabry-Perot cavity whose mirrors are shaped to sustain a standing wave. Hence, the resultant cavity Q would be low due to scattering loss at the junctions with the PhC. A more prudent approach would be to *adiabatically* modulate the geometries, e.g. hole size and/or periodicity, to engineer a defect state within the photonic bandgap [63, 82]. Since consistently producing small air holes down to 10's of nm can be challenging in fabrication, we focus on a design that only modulates the periodicity. Specifically, our 1D PhC cavity has hole spacing that grows exponentially from the center based on the following formula,

$$a_j = a - (a - a_0)\exp\left(-j^2/(2\sigma^2)\right) \qquad \text{for } j \in \{0, ..., N_{\text{holes}}\}, \tag{4.1}$$

where $a_0 = d + 2r$ and d is the separation distance between the middle two holes. Note that the fundamental cavity mode is a *dielectric mode* in this case, such that the electric field maximum is in diamond ($n = 2.4$) instead of air.

[1] A simple way is to find a geometry that minimizes (maximizes) the transmission (reflection) signal through the PhC.

[2] The bandstructure can be computed by solving for the eigenmodes at each k_x, with Bloch (periodic) boundary condition applied to one period of the PhC with a single air hole.

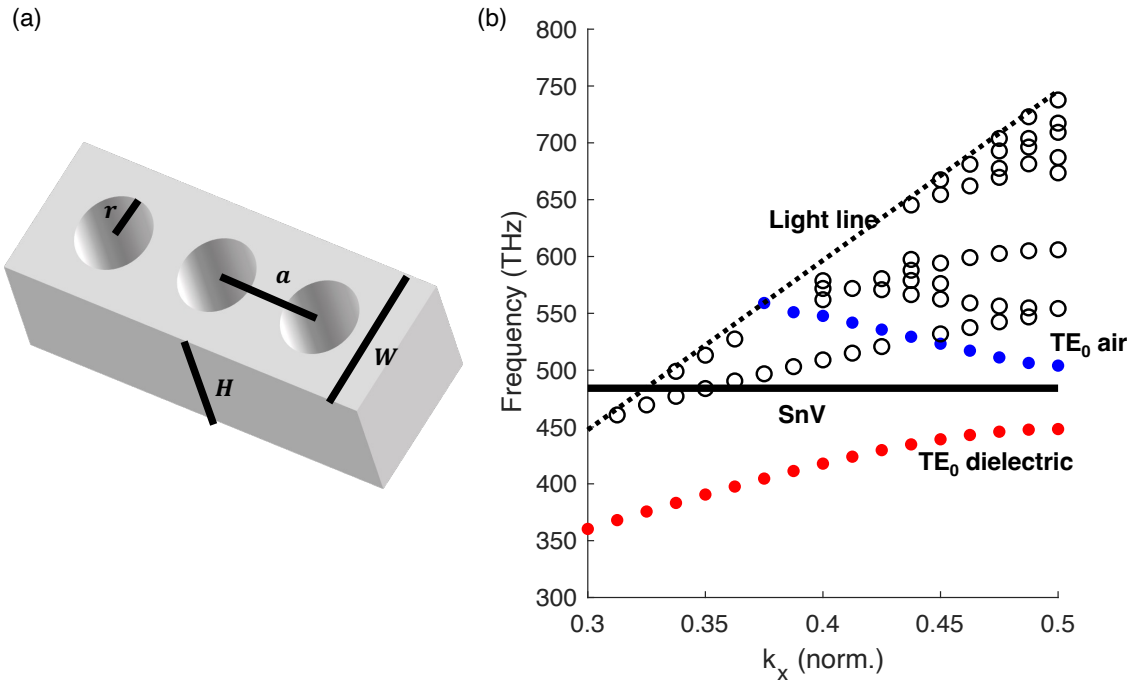

Figure 4-1: (a) An example of a photonic crystal Bragg mirror defined by four parameters: thickness H, width W, radius of the air hole r, and periodicity a. (b) A photonic bandstructure with frequency plotted against the Bloch vector (x component in the case of a 1D PhC). The PhC is optimized to have a photonic bandgap for the TE-like mode centered at λ_{SnV} indicated by the thicker white line. The dashed white line represents the light line, above which exist leakage modes. The parameters are $H = 202$ nm, $W = 269$ nm, $r = 58$ nm, and $a = 201$ nm.

By optimizing over the parameters $\{d, \sigma\}$ in FDTD and fixing $\{H, W, r, a\}$, we find $\{d \approx 59 \text{ nm}, \sigma \approx 3.96\}$ maximize the simulated cavity's intrinsic Q factor[3] at $Q_i \sim 3 \times 10^6$. Its cavity mode profile is shown in Figure 4-2. The mode volume is computed to be $V \approx 0.8\,(\lambda_{\mathrm{SnV}}/n)^3$. Hence, the theoretical maximum Purcell factor can reach $> 10^5$, barring any imperfections in the dipole (quantum emitter) itself.

In the experiment covered in Section 4.6, we focus on maximizing the Q factor and therefore intentionally make the cavity mode undercoupled to all channels, including the adjacent diamond waveguides, with $\kappa_{\mathrm{wg}}/\kappa \sim 5 \times 10^{-3}$. Specifically, the Bragg mirror strength is maximized by padding $N_{\mathrm{mir}} = 25$ air holes on each side. For devices more conducive for transmission/reflection-based measurements via the

[3]To find the intrinsic Q factor, we run a FDTD simulation with "infinitely" many holes on both sides of the 1D PhC cavity.

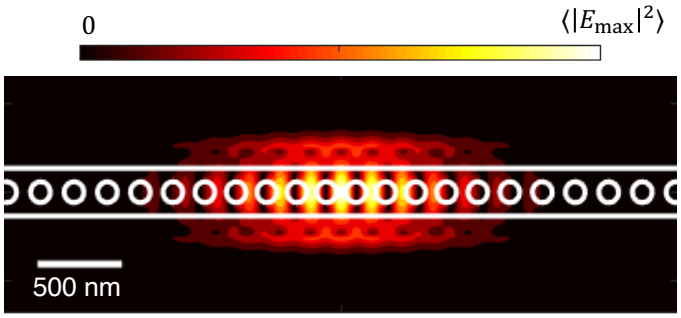

Figure 4-2: FDTD simulation of the fundamental (TE-like) mode profile of the optimized 1D PhC cavity by modulating the periodicity based on Eq. 4.1.

coupled waveguide, we propose an alternative design covered in a later Section 5.6.

4.2 Diamond device fabrication

The fabrication method laid forth in this section is improved upon based on processes spelled out in Ref. [59, 60, 61]. Here, we review the diamond nanofabrication process step-by-step.

4.2.1 Sample preparation

The diamonds are type-IIa substrates synthesized via chemically vapor deposition (CVD)[4]. There are typically two varieties used in our fabrication runs, one with higher nitrogen defect concentration < 1 ppm (which we term "IIa") and another with lower nitrogen defect concentration < 5 ppb (which we term "EG" standing for electronic-grade). The latter is generally preserved for quantum experiments given its low defect environment conducive to emitter spectroscopy with minimal decoherence (optical or spin), while the former is commonly used for testing/calibrating fabrication processes.

We first mechanically polish the diamond surfaces to ∼nm root mean square (rms) surface roughness. Then, the diamond is solvent-cleaned (with acetone and isopropyl alcohol (IPA)) under sonication, followed by a 5-min. soak in piranha

[4]Element Six, Inc.

(3:1 sulfuirc acid to hydrogen peroxide). After removing residual impurities from the surface resultant from mechanical polishing, we conduct an Ar/Cl_2 ICP RIE step that isotropically etches away the top 4 μm of the surface. Crucially, this step removes the strained layer stemming from mechanical polishing. It is important to maintain surface cleanliness before the Ar/Cl_2 etch since any impurity can act as a micromask that induces formation of micropits [83, 84].

Subsequently, we perform an O_2 ICP RIE that removes another 3 μm of diamond. The O_2 etch step ensures the top surface is not contaminated by Cl that penetrates into the diamond from Ar/Cl_2 ICP RIE, which is purported to quench[5] the emission of color centers in diamond [85]. This two-step RIE polishing process smooths the surface down to sub-nm rms roughness.

4.2.2 Ion implantation

After planarizing the surface, the diamond is implanted with ions[6] with specified ion dosage, energy, and sample tilt (e.g. 7 degrees) to avoid channeling into the diamond lattice. Specifically, we implant Sn ions at the maximum energy of 350 keV allowed by the ion implanter, corresponding to ~ 86 nm based on Stopping and Range of Ions in Matter (SRIM) simulations. From prior test runs, we have found dosage of 5×10^{10} ions/cm^2 yielding approximately 1 SnV center per μm^2. However, for the experiment, we perform an additional blanket implantation over the entirety of the surface at a dose of 5×10^{11} ions/cm^2 to improve the emitter-cavity coupling yield. However, high energy ion implantation at high dosage likely produces lattice damage, resulting in vacancy complexes that may optically decohere the defect center. Hence, a better approach for future experiments would be employing either (i) targeted focused-ion beam (FIB) implantation (see Appendix C) as was done in Ref. [50] to minimize area of ion bombardment or (ii) low-energy ion implantation with masking followed by diamond overgrowth by an amount of half the target thickness $H/2$ [86].

[5]Emission of NV centers in diamond is found to be suppressed under the influence of chlorine being nearby.

[6]Companies such as Innovion Inc. and Cutting Edge Ions, Inc. provide ion implantation services.

4.2.3 High-temperature annealing

After ion implantation, we conduct high-temperature annealing in a home-built ultra-high vacuum furnace (Figure 4-3) at $< 10^{-8}$ mbar. The annealing sequence consists of: a 120 min. linear ramp from room temperature to 400°C and holding for 400 min., a 120 min. linear ramp from 400°C to 800°C and holding for 400 min., a 120 min. linear ramp from 800°C to 1200°C and holding for 300 min., and finally a linear ramp down to room temperature. The 800°C step enables single vacancy mobility such that vacancies diffuse and bind to the defect (Sn) to form the interstitial SnV center [87, 88]. Higher temperatures are found empirically to remove an absorption peak at 595 nm [35]. After high-temperature annealing, we submerge the sample in a boiling tri-acid (1:1:1 nitric:sulfuric:perchloric acid) solution at 345°C for 2 hours to remove graphite formed on the surface [83].

4.2.4 Fabrication of devices in bulk diamond

After annealing and yielding of color centers in diamond, the sample is deposited with a 180 nm thick Si_3N_4 hard mask via plasma-enhanced CVD (PECVD)[7]. In order to transfer patterns defined in our CAD file (GDSII produced via Python), we perform electron beam lithography (EBL). We first spin coat a 300 nm thick positive-tone EBL resist (ZEP520A, spun at 6k for 1 min.), pre-bake the sample for 2 min. at 180°C, and finally spin coat another 20 nm thin conductive layer (Espacer, spun at 4k for 1 min.) for charge dissipation, particularly important for an insulating material such as diamond. We then proceed with EBL[8] with proximity effect correction (PEC) applied to our write file[9]. The base dosage for an EG (IIA) sample is set at 550 $\mu C/cm^2$ (500 $\mu C/cm^2$) at 1.6 nA.

After EBL, the sample undergoes a deionized (DI) water soak to remove the conductive polymer, and subsequently cold development at 0°C for $\sim$ 75 s. The sample is descumed in oxygen plasma at 100 W for 15 s. A CF_4 RIE then transfers

[7] A low-stress film is found to have better selectivity against O_2 ICP RIE for the subsequent steps.
[8] Elionix F125.
[9] BEAMER software, GenISys GmbH.

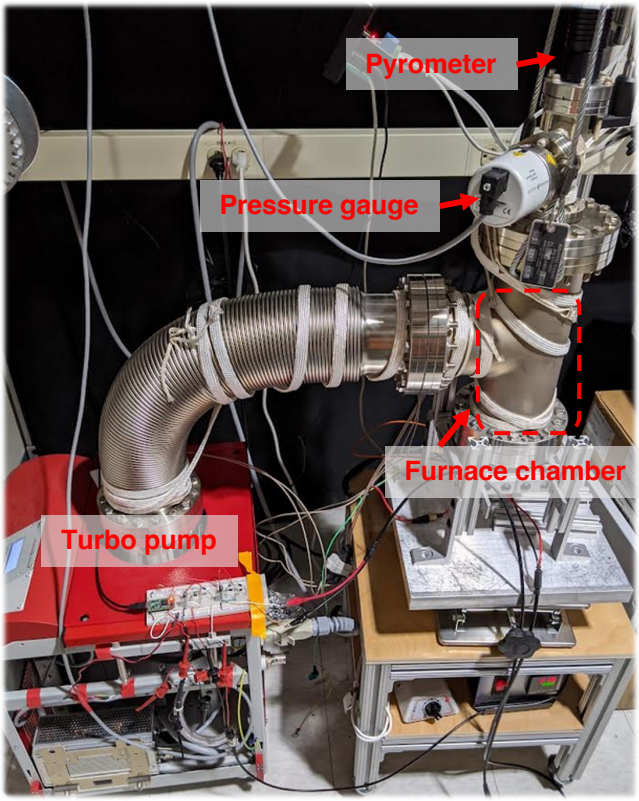

Figure 4-3: A home-built annealing furnace. A turbo pump (Pfeiffer HiCube) lowers the pressure to ultra-high vacuum level at $< 10^{-8}$ mbar. Inside the furnace chamber, the diamond samples sit inside an alumina crucible, which contacts a resistive pyrolytic boron nitride (PBN) heating element (HTR-1001 from Momentive Tech). A type-K thermocouple is used to directly measure the temperature of the PBN. Atop the furnace chamber are a pressure gauge (Pfeiffer IKR270) and an infrared pyrometer (Omega OS550a) for pressure and additional temperature readout.

the pattern defined in the resist into the nitride hard mask[10]. Finally, the resist is removed by soaking the sample in NMP-1165[11].

The pattern in the nitride mask is transferred into the diamond substrate via an anisotropic O_2 ICP RIE at 32°C, resulting in Step (i) in Figure 4-4. Specifically, we etch a micron into the diamond to have sufficient depth for the later quasi-isotropic etch step. Note that the nitride mask thickness must not be too small, otherwise the subsequent O_2 ICP RIE would break down the Si_3N_4 layer (30:1 selectivity with respect to diamond).

[10]Bias power set at 200 W with 15 sccm of CF_4 at 1.3 mTorr gives $\sim$ 70 nm/min. Si_3N_4 etch rate (Plasma-Therm RIE).

[11]MICROPOSIT Remover 1165.

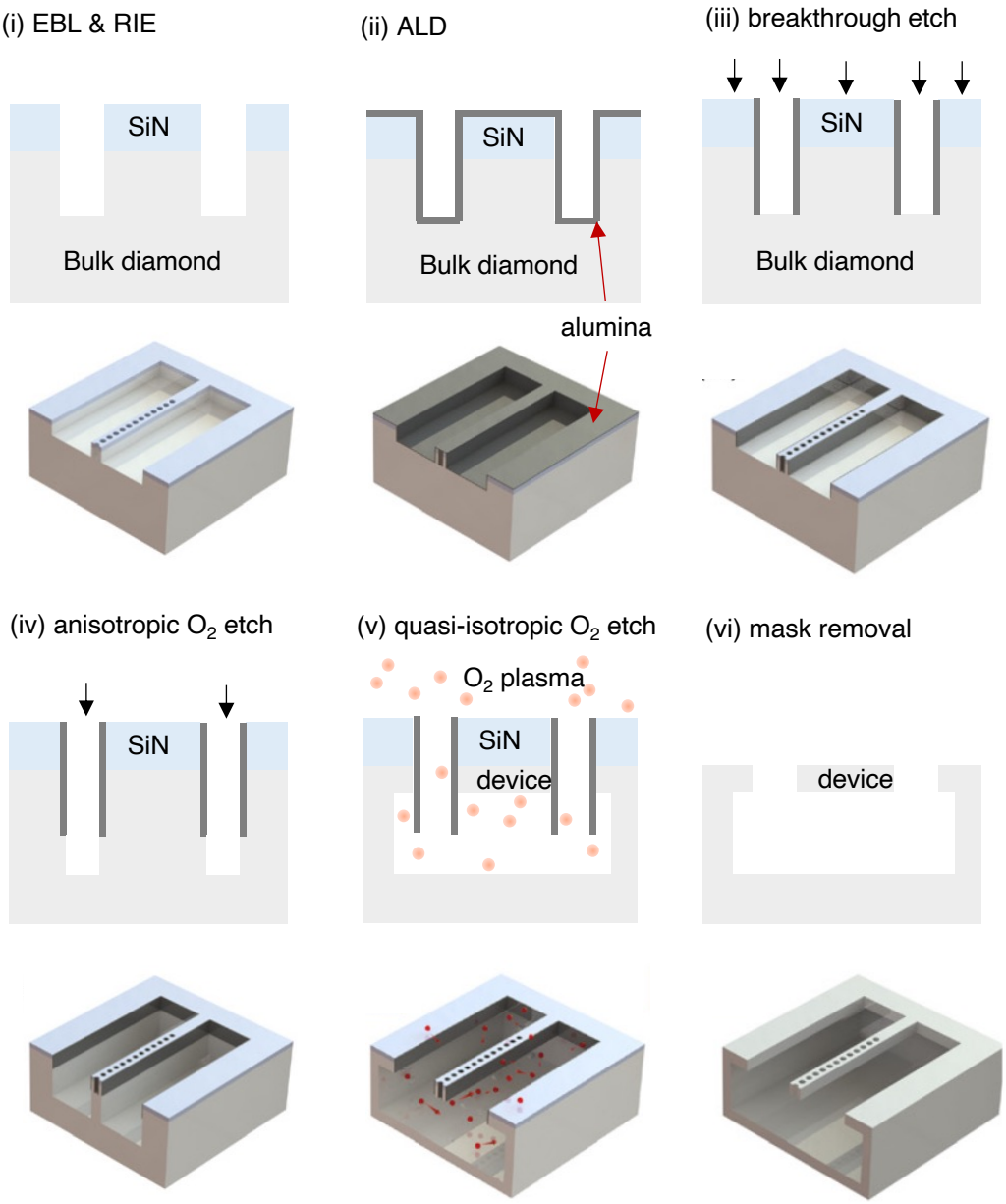

Figure 4-4: Diamond fabrication process flow. (i) The nitride mask pattern is defined in EBL and transferred into the bulk diamond via an anisotropic O_2 ICP RIE. (ii) A thin layer of alumina is ALD-coated on the diamond surface, followed by (iv) an anisotropic CF_4 etch that removes the top-facing alumina layer. With the sidewalls still protected, another anisotropic O_2 ICP RIE step enlarges the diamond trench, allowing for (v) bias-free O_2 plasma to etch along the $\{111, 100\}$ diamond facets for undercutting. (vi) Finally, the sample is submerged in HF to remove the nitride and alumina layers, releasing suspended diamond devices.

In Step (ii), we conformally coat the diamond surface with $\sim$ 20 nm of alumina via atomic layer deposition (ALD). Then, in Step (iii), CF_4 RIE is again used to etch

away any top-facing alumina layer, leaving the sidewalls still protected. Critically, we time the etch such that CF_4 does not degrade the nitride layer and lead to mask breakdown during the quasi-isotropic etch. Afterwards, we do a short anisotropic O_2 ICP RIE to open the diamond trench, as shown in Step (iv) in Figure 4-4. At this point, we turn off the bias power to remove any preferential ion directionality. Instead, the O_2 plasma etches along the diamond {111} ($\sim$ 35 degrees with respect to the diamond {100} surface) and {100} facets [59]. Hence, for effective undercutting, the nanostructures' longitudinal axes should be aligned parallel to the {110} facet, which incorporates both the vertical etching along {100} [12] and angled etching along {111} [89, 60]. Additionally, we elevate the chamber temperature to 200 °C to improve the etch rate of the quasi-isotropic etch step, as pictured in Step (v) in Figure 4-4. As opposed to methods based on Faraday cages [90] or angular directional etching [91], this undercutting technique allows for fabrication of devices with *rectangular* cross-sections and enables realization of more complex photonic structures suitable for heterogeneous integration [50].

We note that since the quasi-isotropic etching rate differs from sample to sample[13], we measure the device thickness through the alumina sidewall intermittently during the undercut step via scanning electron microscopy (SEM)[14]. Finally, once the desired thickness is reached, we submerge the sample ($\geq$ 5 min.) in 49% hydrofluoric (HF) acid to remove both nitride and alumina, releasing suspended nanostructures in diamond as illustrated by Step (vi).

Immediately after fabrication, we perform another round of high-temperature annealing to strain relieve the devices, followed by boiling tri-acid clean to ensure an ordered surface for minimizing decoherence effects from surface defects [83].

Figure 4-5 shows SEM images of suspended diamond devices fabricated using the aforementioned process. In particular, the designed structure is in the form of a quantum micro-chiplet (QMC) detailed in Ref. [50]. Each QMC contains an array

[12]For Element 6's diamonds, the top face is usually [100].

[13]EG diamonds are found to have slower undercutting rate than IIA.

[14]It is important to not dwell too long when imaging the sidewalls since electrons' interaction with the alumina may cause it to bend and close up, inhibiting further undercutting in the imaged region.

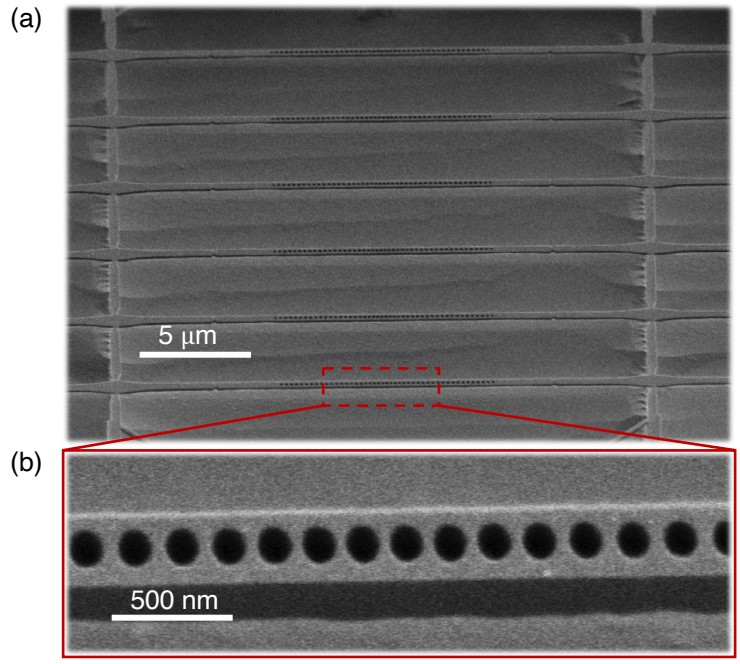

Figure 4-5: SEM images of a fabricated suspended diamond device acquired at a 30-degree tilt of the sample stage. (a) A QMC contains an array of six 1D PhC cavities, with each connected to adjacent cavities via support beams. (b) A close-up image of the center region of a cavity, whose defect mode is produced from modulating the hole periodicity.

of six 1D PhC cavities as shown in Figure 4-5(a), with supporting beams connecting adjacent channels set at $\sim$ 3 μm apart. Figure 4-5(b) shows the center of the PhC cavity with modulated spacing between adjacent air holes. The device exhibits non-uniform thickness in the hole regions due to variation in the local quasi-isotropic etching rate. The non-planar underside degrades the experimental Q factor, which will be detailed in the following Section 4.3. One avenue to ameliorate this issue is to etch deeper into bulk diamond in Step (i), allowing for the O_2 plasma during quasi-isotropic etching to have sufficient time to smooth the underside [59, 61]. This would also enable smoother undersides of devices with widths greater than $\sim$ 500 nm, as they require even longer undercutting time to planarize the underside. However, in order to prevent the hard mask from breaking down, alternative mask materials (e.g. metals, oxides, Si) with higher selectivity against O_2 ICP RIE [92] should be used instead. Another approach would entail doing another CVD of additional hard mask

material after undercutting has begun. This re-deposition "heals" the partially etched hard mask, allowing for potentially longer subsequent quasi-isotropic etching limited only by the alumina sidewall as opposed to the nitride layer, as detailed in Ref. [93]. Separately, the distance between adjacent cavities (i.e. the trench width currently set at ~ 3 μm) also influences the amount of RIE lag for the quasi-isotropic etch step. Thus, increasing the distance may help with smoothing the underside at the cost of increasing the QMC footprint and mechanical instability[15]. The aforementioned approaches in potentially improving in the quasi-isotropic process warrant further studies in the future.

4.3 Cavity characterization

In order to measure the fabricated cavities' Q factors, we can either (1) off-resonantly excite the SnV centers in the devices and use their photoluminescence to pump the cavity modes, or (2) measure reflection/transmission signals using a broadband light source[16]. Since the latter approach collects the laser signal *directly*, the required integration time is generally $\ll 1$ s, allowing for high-throughput characterization of arrays of devices. Therefore, we perform cavity reflectivity measurements using a room temperature cross-polarization confocal setup, as shown in Figure 4-6.

Crucially, we leverage the fact that the cavity mode of interest is TE-like (H) and orient the cavity along the diagonal axis ($H \pm V$). Hence, interference between the cavity mode and the bare reflection occurs at the device interface [67, 94]. As a result, after the PBS, the transmitted H component inherits a frequency dependent coefficient $1 - r(\omega)$ [95], as demonstrated by the schematic in Figure 4-7(a). With appropriate spatial filtering, the measured cavity reflectivity spectrum consequently exhibits Fano lineshapes indicative of cavity resonances [67, 94].

We find that the characteristics of the Fano lineshapes crucially depend on the excitation/collection position. Figure 4-8(a) shows an automated cavity spectrum

[15] Devices longer than 100 μm may start to bend down due to their own weights.
[16] SuperK Extreme, NKT Photonics.

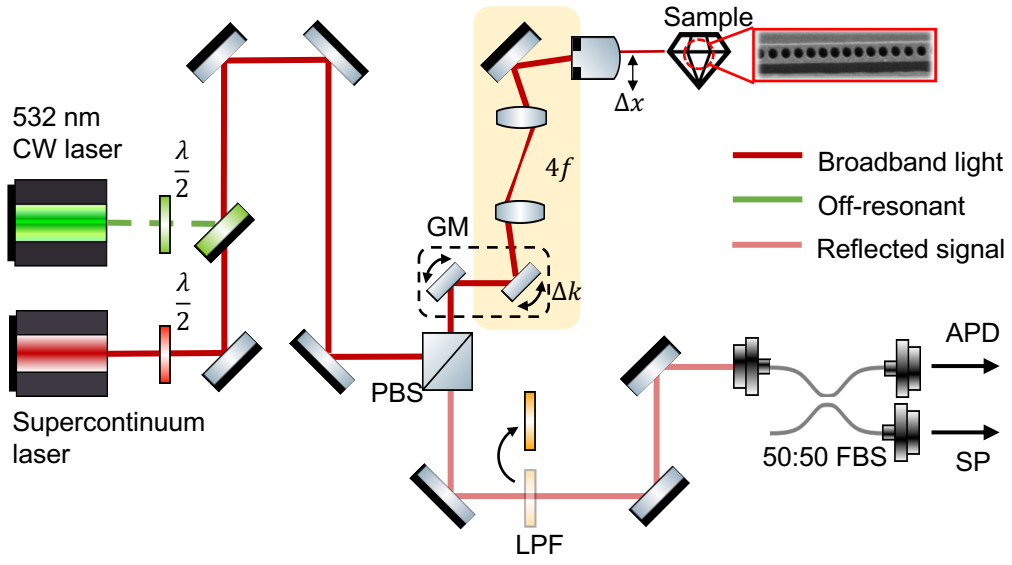

Figure 4-6: Schematic representing the confocal microscopy setup. A 532 nm CW laser (Coherent Verdi 8W) is used to off-resonantly excite the SnV centers, whereas a broadband supercontinuum laser is used to directly excite the cavity mode. A dichroic mirror (shown in green) intercepts their common path, allowing for both lasers to be used simultaneously. Notably, each source has a HWP ($\lambda/2$) to ensure cross-polarization. The excitation path enters a PBS, which reflects the V component to a 4-f system that maps an angular-steered excitation beam (via a galvanometer (GM)) to the back-plane of the objective. In the Fourier plane at which the sample resides, the angular change Δk is mapped to a spatial change Δx, enabling the GM to raster scan through the field of view. The collected emitter fluorescence (with a longpass filter (LPF) at 550 nm in the collection path) or cavity mode is directed to a fiber beam splitter (FBS), which directs to an avalanche photon detector (APD, PerkinElmer SPDC-AQRH-14) or a spectrometer (SP, Princeton Instruments Acton SP-2500i).

measurement, in which a grid of positions ($i \in \{1, ..., 7\}$ per cavity $j \in \{1, ..., 6\}$) is defined around the cavity centers for six PhC cavities. Figure 4-8(b) indicates how the Fano lineshape's asymmetry and signal contrast vary as the position changes. We expect that exciting at precisely the cavity center can most efficiently pump the cavity mode, allowing for maximal collection (with 0.9 NA) of the cavity photons. However, due to local variations from fabrication imperfections, the position at which Fano lineshape is most pronounced may deviate from the purported center. Hence, reliable characterization of the cavities with strong signal contrast necessitates a procedure that spatially sweeps over their central regions in an automated fashion.

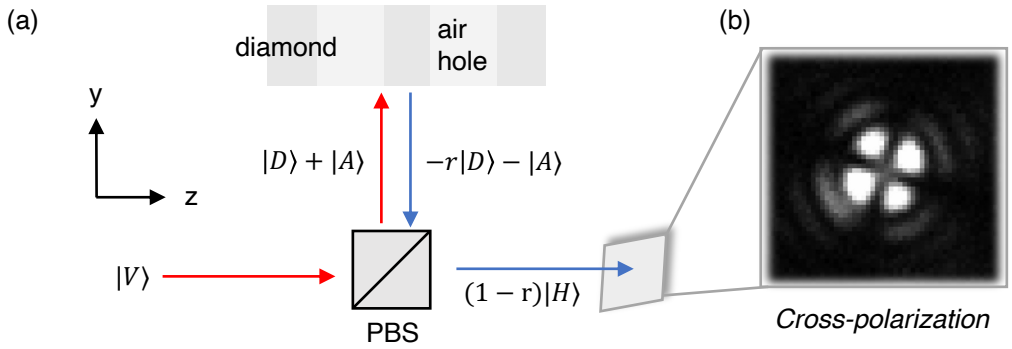

Figure 4-7: (a) A diagram showing the working principle of cross-polarization spectroscopy. The excitation enters $|V\rangle$, which can be rewritten as $|D\rangle + |A\rangle = (|V\rangle + |H\rangle) + (|V\rangle - |H\rangle)$. Since the device is oriented 45 degrees, only $|V + H\rangle$ acquires a dispersive reflectivity coefficient $r = r(\omega)$, while the $|A\rangle = |V - H\rangle$ obtains a constant phase. The transmitted $|H\rangle$ mode is left with frequency-dependent term $1 - r(\omega)$ that gives rise to the Fano lineshape. (b) A CCD image of the excitation beam reflecting off a planar surface in cross-polarization, as signified by the "clover-leaf" pattern.

We can fit each Fano lineshape to obtain the device Q factor and resonance wavelength. Specifically, we use a generalized asymmetric lineshape based on a weighted Fano-Lorentz function [94]

$$I(\lambda) = A\left(\frac{\eta(\Delta\lambda + \delta\kappa/2)^2}{\Delta\lambda^2 + \kappa^2/4} + \frac{(1-\eta)\kappa^2/4}{\Delta\lambda^2 + \kappa^2/4}\right), \tag{4.2}$$

where $\Delta\lambda = \lambda - \lambda_c$ is the detuning from the cavity resonance and κ represents again the cavity linewidth. δ is the Fano asymmetry factor that dictates the lineshape, and η is the weighting factor between Fano and Lorentz lineshapes. Lastly, A is a normalization constant. From the spectra taken from the optimal positions determined by the automated measurements, we fit each cavity's fundamental TE-like mode (highest energy) based on Eq. 4.2 and obtain Q on average exceeding 10^2. Figure 4-9 shows the chosen spectra, with the inset indicating a Fano-Lorentz model fit to the fundamental mode of cavity $j = 5$. The fitted resonance wavelength and Q factor are 621.53 nm and $(7.98 \pm 0.10) \times 10^2$, respectively. We notice that the cavity Q also improves as the sample temperature decreases. The highest observed Q at 4 K is about 2×10^3 (before gas-tuning, see Section 4.5). The large discrepancy with the

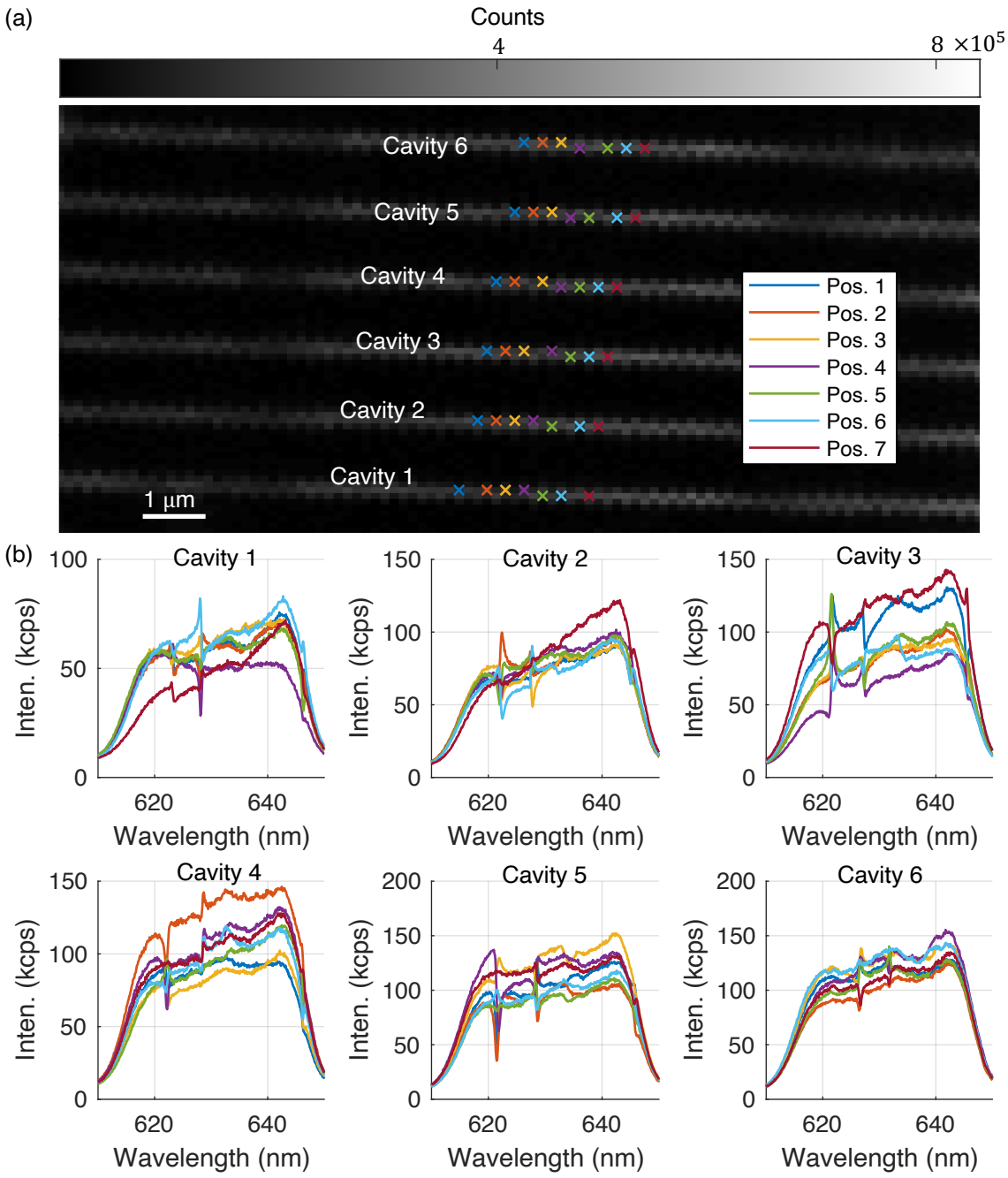

Figure 4-8: (a) A confocal reflection map using a supercontinuum laser. An automated experiment surveys the reflected spectra positions defined in an array, covering the central regions of all six PhC cavities. (b) The acquired reflected spectra show Fano lineshapes indicative of cavity resonances. The Fano asymmetry and signal contrast are highly spatially dependent due to local geometry variations caused by fabrication.

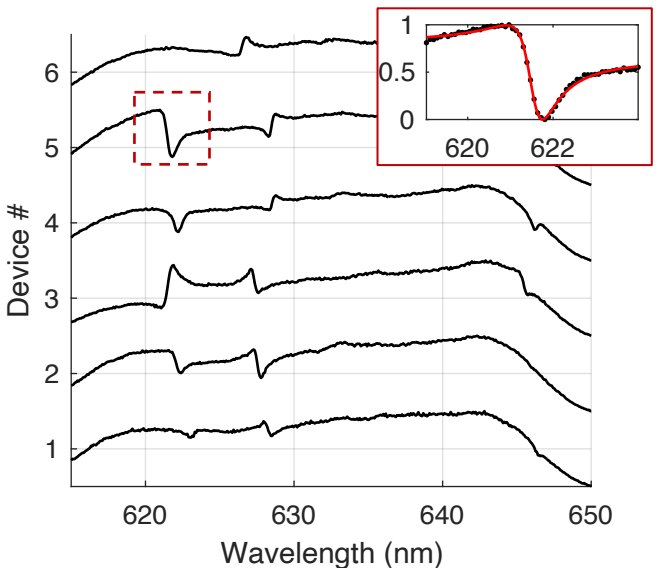

Figure 4-9: Spectra acquired at the optimal excitation/collection positions based on cavity reflectivity signal contrast. The inset shows a Fano-Lorentz fit based on Eq. 4.2 on the fundamental mode of cavity $j = 5$, giving a fitted resonance wavelength of 621.52 ± 0.01 nm and a Q factor of $(7.98 \pm 0.10) \times 10^2$.

simulated Q factor could attribute to slight deviation from the target geometry by ~ 30 nm[17] and mainly underside/sidewall roughness. In FDTD, with rms roughness of 10 nm for the underside, 1 nm for the sidewall, and 5 nm for the inner wall inside the holes (correlation lengths of 10 nm parallel to and 50 nm orthogonal to the device longitudinal axis), we simulate a degraded cavity Q to be $\sim 6 \times 10^3$. Further improvement in the Q requires materials engineering to smooth the underside and sidewalls (see discussion at the end of Section 4.2).

4.4 Spectroscopy of SnV centers at 4 K

In addition to cavity measurements, we also perform spectroscopy of the SnV centers at 4 K using a closed-loop Helium cryostat[18]. The optical setup surrounding the cryostat is shown in Figure 4-10. Similar to the setup described in Section 4.3, the

[17]This is caused by error in measuring the device thickness via SEM-imaging during the quasi-isotropic etch step. To compensate for drift in one geometry parameter, we typically sweep over a large range of H, W, and r in design to ensure a subset of cavities have resonances close to λ_{SnV}.

[18]Montana Instruments CR-579.

4 K setup is in cross-polarization with an above-band excitation source (515 nm[19]) and a tunable resonant laser (around 619 nm[20]). The latter can operate either in CW or pulsed regime via an electro-optical modulator (EOM[21]). The two sources converge at a non-polarizing beam splitter (NPBS) and are directed to the sample via the V-port of the PBS. The collected fluorescence can be detected by either an electron-multiplying CCD (EMCCD) for wide-field spectroscopy (not used in this experiment) or a set of free-space APDs. A flip mirror in the collection path is used to couple signal into a single mode fiber that feeds into a spectrometer. Configured with a time-correlated single photon counter (TCSPC[22]), the setup enables both time-resolved autocorrelation and lifetime measurements, as described later.

Figure 4-11(a) shows a fluorescence map of a QMC containing six PhC cavities, obtained by off-resonantly exciting the device confocally. The spectrum of the fluorescence collected from the cavity region reveals both C and D transitions separated by SnV center's ground state spin-orbital splitting $\Delta_g \sim 820$ GHz, as depicted by Figure 4-11(b). However, since the emitter's optical linewidth is on the order of 10's to low 100's of MHz, the frequency resolution provided by the spectrometer (0.06 nm) is insufficient. Therefore, we perform *photoluminescence excitation* (PLE) spectroscopy, in which a narrowband (linewidth < 50 kHz) tunable laser is swept across the C transition and the PSB emission (with a 628 nm longpass filter) is collected. In the pulse sequence, we apply a $\tau_{\text{repump}} = 1$ μs long off-resonant *repump* pulse at 300 nW for charge stabilizing [96, 97] SnV^-, followed by $\tau_{\text{delay}} = 1$ μs for compensating timing errors, and finally $\tau_{\text{res}} = 10$ μs long resonant pulse at 110 nW time-synchronized to the APD readout. The pulse sequence is cycled 5×10^3 times for each selected frequency point to build up a PLE curve shown in Figure 4-11(c). Importantly, both the repump and resonant powers must be kept sufficiently low to avoid spectral diffusion and power broadening for accurate measurement of the emitter's optical linewidth, while maintaining high enough counts for PLE. The acquired curve is then fitted

[19]Hubner Photonics Cobolt 80 mW.
[20]Msquared SolStis+EMM.
[21]EOspace 20 GHz intensity modulator.
[22]PicoQuant PicoHarp 300 (4 ps resolution).

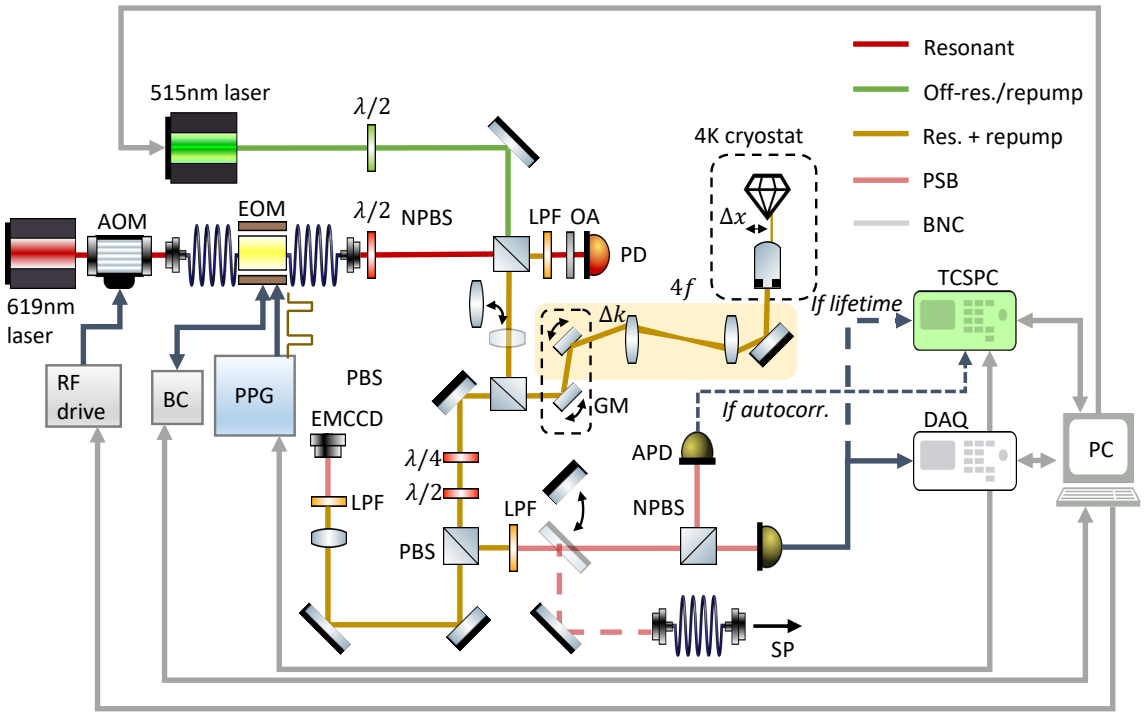

Figure 4-10: A schematic of the optical setup for measurements done at 4 K. The TTL-controlled off-resonant (515 nm) laser is free-spaced coupled into the excitation path with a HWP controlling its polarization axis. The on-resonant ($\sim$ 619 nm) laser is modulated by both an acoustic-optical modulator (AOM) and an amplitude EOM, which is driven by a pulse-pattern generator (Anritsu MP1763B). A commercial bias controller (ixBlue MBC-DG-LAB) maintains the null point of the amplitude EOM, whose output is constantly monitor by a photodiode (PD) after filtering by a LPF and an optical attenuator (OA). Both sources are directed to the 4-f via the V-port of the PBS. Fluorescence from the emitter is collected by a cryogenic objective (NA=0.9) and routed to a PBS. It can be measured by either an EMCCD for wide-field imaging (requiring an additional lens in the excitation path to focus onto the objective's back aperture), or a set of free-space APDs. A flip mirror can be inserted in the collection path for acquiring spectra on the spectrometer. The APDs are BNC-connected to a TCSPC for time-correlated measurements such as autocorrelation and lifetime. Pulsing sequences for photoluminescence excitation (PLE) spectroscopy are produced by a programmable TTL generator (PulseBlaster).

to a Lorentzian[23]. The fitted linewidth is $\sim 204 \pm 71$ MHz whereas the transform limit is $\sim$30 MHz (based on the lifetime data in Figure 4-16 and Figure 4-17), suggesting presence of pure dephasing that homogeneously broadens the linewidth by a

[23]Given an exponentially decaying excited state population of a two-level system, the corresponding frequency width in Fourier space is a Lorentzian [98]: $I(\omega) = A\left[\Gamma/2\right)/((\omega-\omega_a)^2 + (\Gamma/2)^2] + b$, where Γ is the optical linewidth, A is a normalization constant, and b accounts for background.

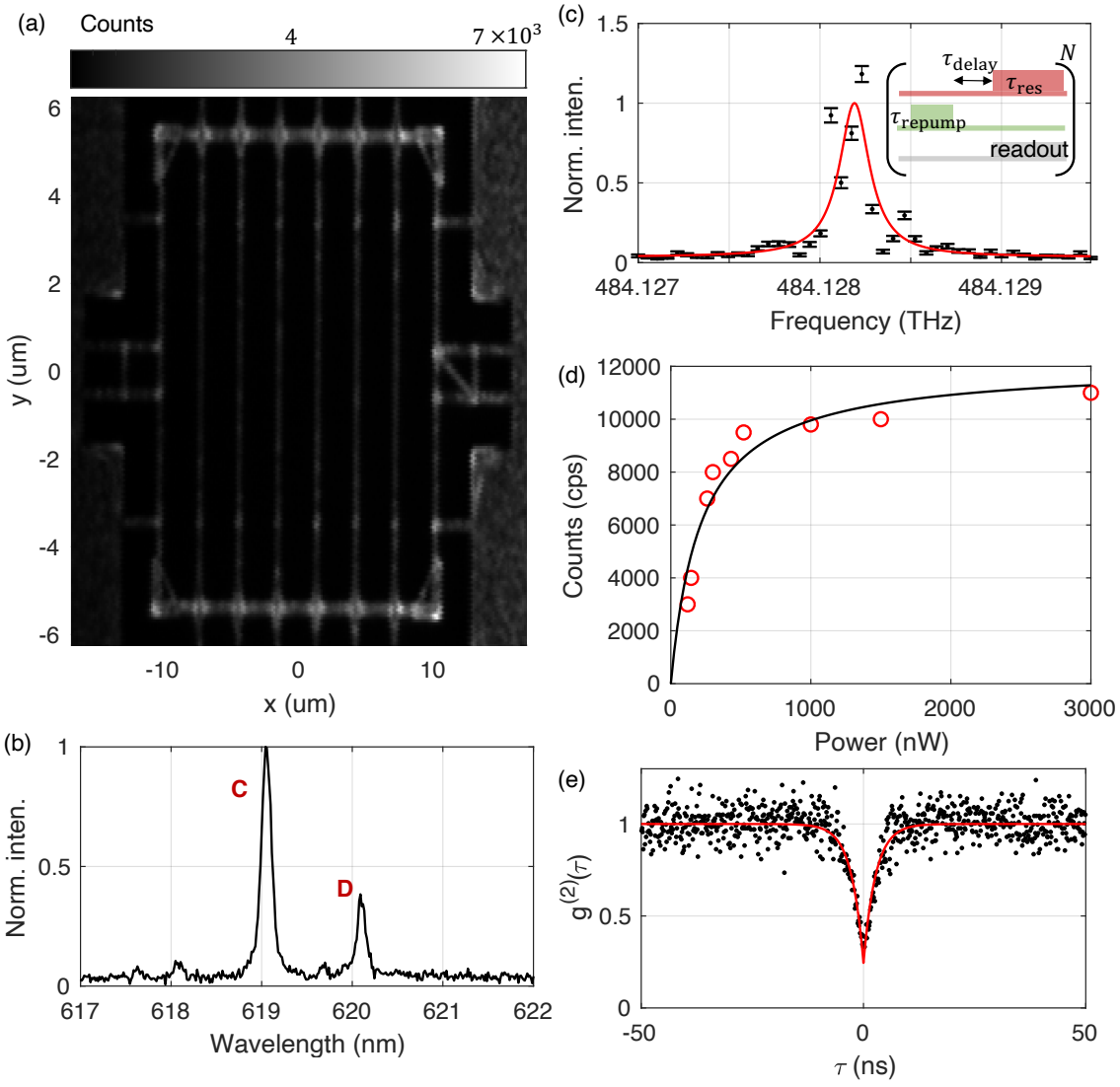

Figure 4-11: Spectroscopy of SnV centers at 4 K. (a) A confocal fluorescence image of a QMC containing six PhC cavities, encapsulated in a support frame that is connected to the bulk. (b) A representative PL spectrum of SnV center shows both C and D transitions. (c) A representative PLE curve of a SnV center in a cavity region fitted with a Lorentzian. The fitted optical linewidth is $\sim 204 \pm 71$ MHz. (d) A saturation curve (resonant excitation at the fitted ZPL frequency from (c)) indicates a saturation power of (215 ± 109) nW. (e) An autocorrelation measurement shows a $g^{(2)}(0) = 0.25 \pm 0.01$ at zero time-delay.

factor of ~ 7. Additionally, the emitters tend to "blink" during the scan, resulting in sub-optimal SNR for the PLE curve.

Nevertheless, using the fitted resonance frequency, we perform an on-resonant power saturation measurement, in which the PSB count rate I_{PSB} is monitored against

the resonant excitation power P (with weak CW repump on), as shown in Figure 4-11(d). The data points are fitted to the model

$$I_{\mathrm{PSB}}(P) = \frac{I_{\mathrm{sat}} P}{P + P_{\mathrm{sat}}}. \tag{4.3}$$

We estimate the saturation power to be $P_{\mathrm{sat}} = 215 \pm 109$ nW. Finally, the Hanbury-Brown-Twiss (HBT) setup in the collection depicted in Figure 4-10 allows us to perform an autocorrelation $g^{(2)}$ measurement. Figure 4-11(e) shows a histogram of correlated photon counts, with $g^{(2)}(\tau)$ plotted against the time delay τ. We fit the data to the model

$$g^{(2)}(\tau) \propto 1 - \exp\left(-|\tau|/\tau_0\right), \tag{4.4}$$

where $\tau_0 = 2.74 \pm 0.17$ ns is a convolved time scale between the emitter's lifetime and the resonantly-driven Rabi oscillation rate [99]. The fitted dip at $\tau = 0$ gives $g^{(2)}(\tau = 0) = 0.25 \pm 0.01$, below the classical limit of $g^{(2)}(\tau = 0) = 0.5$, affirming the presence of a single SnV center as opposed to an ensemble. We attribute the deviation from the ideal limit of $g^{(2)}(\tau = 0) = 0$ to detector dark counts ($\sim$500 cps) and the detector's timing jitter ($\sim$550 ps based on fit in Figure 4-16) [99].

4.5 In-situ gas tuning

Inevitably, the fabricated cavities would be detuned from the SnV center's resonance by more than $\kappa \sim 300$ GHz. Therefore, a tuning mechanism to shift the cavity resonance in a cryogenic environment must be employed to achieve emitter-cavity coupling. To do so, we rely on an in-situ *gas tuning* technique [4, 64, 100]. We modify the cryostat base port to include an inlet gas line, which is externally connected to an argon gas tank. Inside, as illustrated in Figure 4-12(a,b), a copper gas line is wrapped around the piezoelectric positioner stack[24], pointing upwards at the objective's radiation shield (not shown) near the sample mount. Due to the small working

[24] Attocube ANC300 positioners.

distance of 200 µm set by the objective, the gas line cannot be positioned to be right above the mounted sample.

Upon opening the gas needle valve, the gas molecules would ballistically exit the gas line, ricochet off the radiation shield, and deposit onto the diamond devices. The adsorbed gas molecules would modify the effective refractive index of the cavity and waveguide modes, thereby shifting the cavity resonance. Specifically, decreasing the air hole size leads to an overall higher permittivity ϵ value in an unit volume, hence red-shifting the cavity resonance $\lambda_c \propto 1/\epsilon$ (Rayleigh quotient [63]), as shown in Figure 4-12(c). By locally applying high optical power, we can also vaporize the adsorbed gas molecules and blue-shift the cavity resonance back to its starting point. Since this gas tuning only permits shifting wavelengths greater than the starting point (as opposed methods combining cavity trimming), we target devices with resonance wavelengths $\lambda_c < \lambda_{\mathrm{SnV}}$.

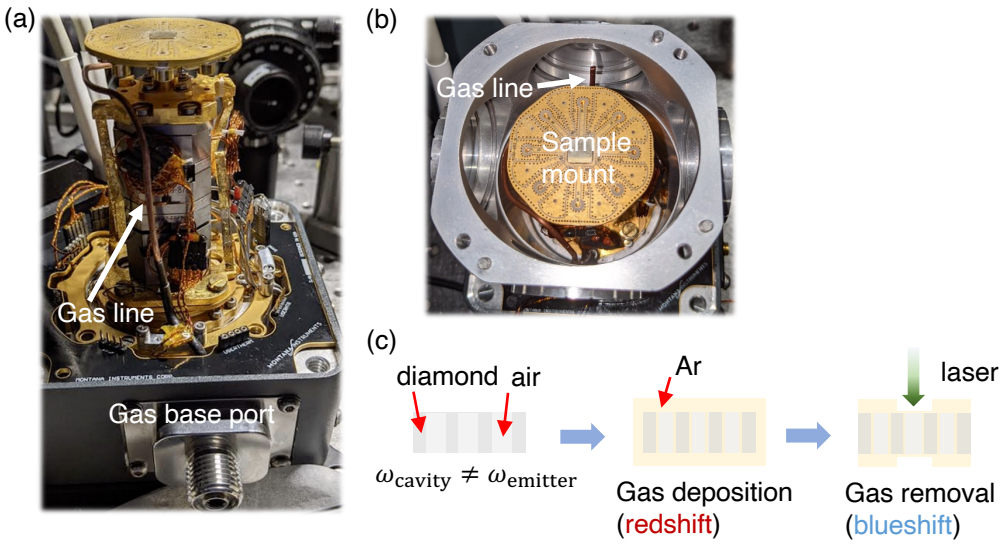

Figure 4-12: (a) A copper gas line wrapping around the piezoelectric positioner stack is attached to the base port, which is externally connected to an argon gas tank. (b) The gas line points upwards towards the cryo-objective's radiation shield near the sample mount. (c) A diagram illustrates how the in-situ gas tuning technique red-shifts the cavity resonance. By applying high optical power, gas molecules can also be removed to blue-shift the cavity resonance back to its starting point.

Figure 4-13 shows experimental data of an actively tuned cavity resonance via cross-polarization reflectivity. In Figure 4-13(a), the cavity resonance is red-shifted

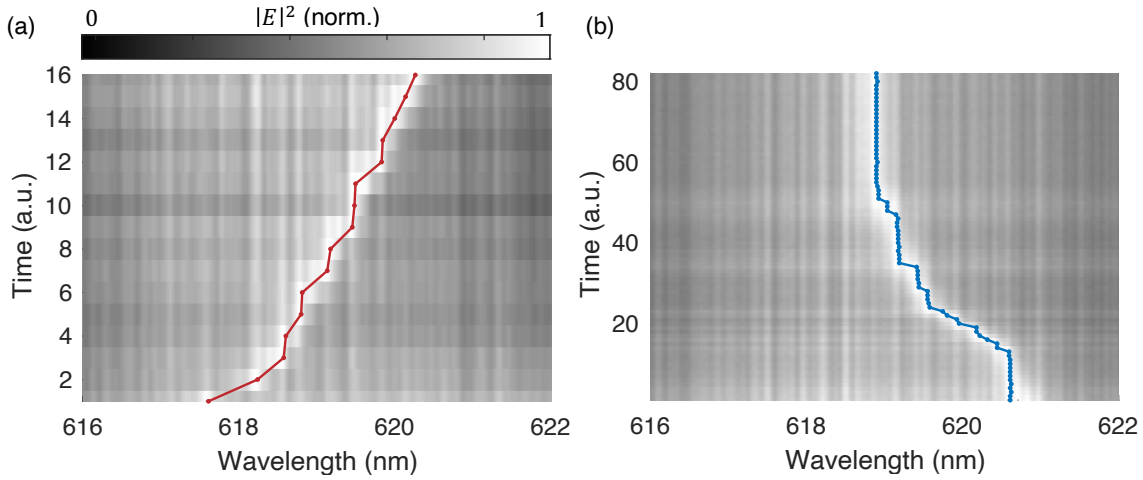

Figure 4-13: (a) Upon opening the gas valve, we acquire a cavity reflectivity spectrum every 5 s, integrated for 0.5 s. The cavity resonance is red-shifted from ∼618 nm to ∼620 nm. (b) We then close the gas valve and apply 515 nm CW laser light at the cavity center and observe a blue-shift of cavity resonance, from ∼621 nm to ∼619 nm.

from $\sim$ 618 nm to $>$ 620 nm, and subsequently blue-shifted down to the target at 619 nm in Figure 4-13(b). Interestingly, during our Purcell enhancement measurements (in the following Section 4.6), we have noticed an *improvement* in cavity Q as we red-shift via gas tuning. We conjecture that this is due to the cavity resonance being shifted closer to the center of the photonic bandgap and the layer of gas molecules smoothing the surface roughness. Figure 4-14 shows the Q of two investigated devices, "d1.0.77.4" and "d1.0.77.2", vary as we introduce the gas-tuning. Figure 4-14(a,d) show the Fano model fits to the cavity reflectivity measurements before any gas is introduced, with $Q = (1.51 \pm 0.04) \times 10^3$ $(j = 4)$ and $Q = (9.4 \pm 0.2) \times 10^2$ $(j = 2)$. Immediately after gas tuning to shift the cavities to resonances with their respective SnV centers, at which point the thickest layer of gas is present, Figure 4-14(b,e) indicate higher Q's at $Q = (2.28 \pm 0.05) \times 10^3$ $(j = 4)$ and $Q = (2.09 \pm 0.08) \times 10^3$ $(j = 2)$. After further blue-shifting via removing part of the gas layers, Figure 4-14(c,f) show that the Q factors drop to $Q = (1.77 \pm 0.07) \times 10^3$ $(j = 4)$ and $Q = (1.56 \pm 0.10) \times 10^3$ $(j = 2)$, which are still higher than the pre-gas tuning Q's perhaps due to residual gas molecules lessening surface roughness. A more methodical study in the future is warranted to delineate the effect of in-situ gas tuning on cavity Q.

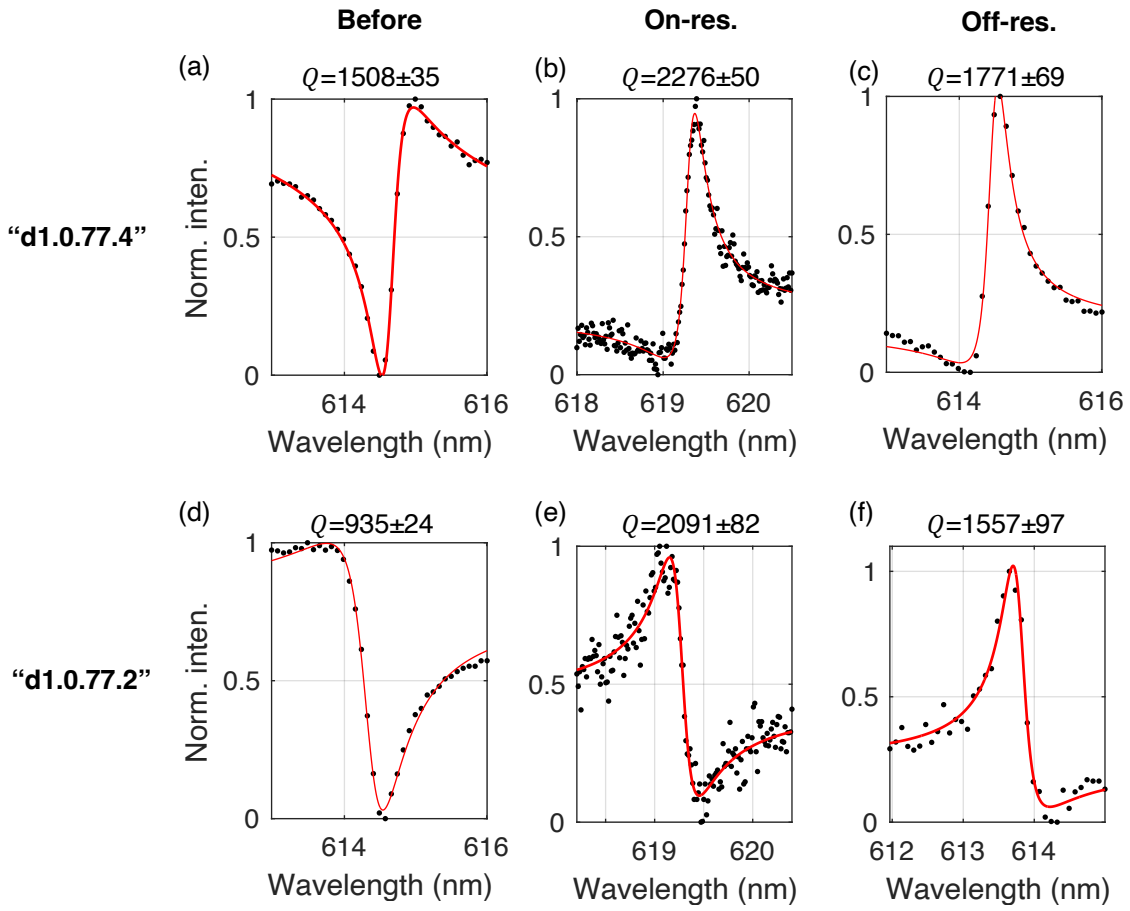

Figure 4-14: The cavity Q at various stages during gas tuning for Purcell enhancement measurements, evaluated for two devices: "d1.0.77.4" and "d1.0.77.2". The Q is measured (a,d) before any introduction of gas molecules, (b,e) after red-shifting via deposition of the gas layer, and finally (c,f) after blue-shifting as part of the gas layer is removed.

4.6 Purcell enhancement measurements

As mentioned in Section 2.1.3, when an emitter is coupled to a photonic cavity, its spontaneous emission rate is Purcell enhanced. Correspondingly, its lifetime is reduced. In the experiment, by gas tuning and shifting λ_c, we can change the detuning $\Delta = \lambda_c - \lambda_{\mathrm{SnV}}$ and measure the lifetime of the SnV center. Critically, the excitation must be pulsed with a duration that is shorter than the lifetime, which may span several ns without cavity enhancement. The supercontinuum laser used in cavity reflectivity measurements can generate ∼5 ps pulses to off-resonantly excite the SnV centers. However, we found that the required off-resonant power centered at 532 nm

to have sufficient PL counts *leads to removal of gas molecules*[25]. Consequently, the cavity resonance cannot be stabilized during lifetime measurements. We surmise that the QMC structure may lead to trapping of heat generated by optical excitation, as the heat packet generated at the cavity center must first route through the support frame then to the bulk connections [50]. Hence, heat cannot be dissipated as effectively as a PhC cavity that is directly connected to the thermally anchored bulk. Specifically, we find ~ 40 μW power is enough to blue-shift the cavity resonance, suggesting burning of gas molecules, while ~ 80 μW is needed to initiate blue-shifting for the outermost devices, which have shorter path lengths to the bulk. We use an estimated thermal conductivity of $k \sim 100$ W/(m·K) for diamond at 4 K [101] and assume unity absorbance at 532 nm to simulate the thermal gradient with a 40 μW heat source at the center of the QMC. Figure 4-15 shows that upon optical excitation, the effective heat-trapping due to the QMC geometry causes a temperature rise up to 70 K. There have also been studies suggesting the thermal conductivity of diamond further decreases with increasing concentration of vacancy and lattice defects in diamond [102, 103]. Given that our sample has undergone high-dosage ion implantation, the consequent lattice damage could contribute to $k \leq 100$ W/(m·K), hence leading to even higher temperature buildup exceeding the boiling point of argon (~ 87 K).

Since off-resonant excitation requires pumping with saturation power on the order of mW [35, 36, 38] and is not compatible with gas tuning, we resort to *resonant* excitation. In order to generate sufficiently short pulses with the CW tunable laser, we use a fiber-coupled amplitude EOM (see Figure 4-10) whose bandwidth can reach up to 20 GHz. However, the pulse pattern generator (PPG) used only reaches a bandwidth of 2 GHz. As a result, we generate approximately 500 ps long pulses, with a time-average power of ~ 40 nW (repetition rate set at 62.5 MHz by the PPG). In order to efficiently excite the SnV center per pulse, the bias voltage applied to the EOM is optimized with respect to the acquired PSB counts at approximately $V_{\mathrm{pp}} = 2$ V[26]. Immediately after pulsing, we collect the PSB photons to probe the

[25]Fortunately, ~ 10 μW of broadband laser power is enough to perform cavity reflectivity measurements, below the threshold of required optical power to burn off the gas molecules.

[26]V_π for the amplitude EOM is 3.8 V.

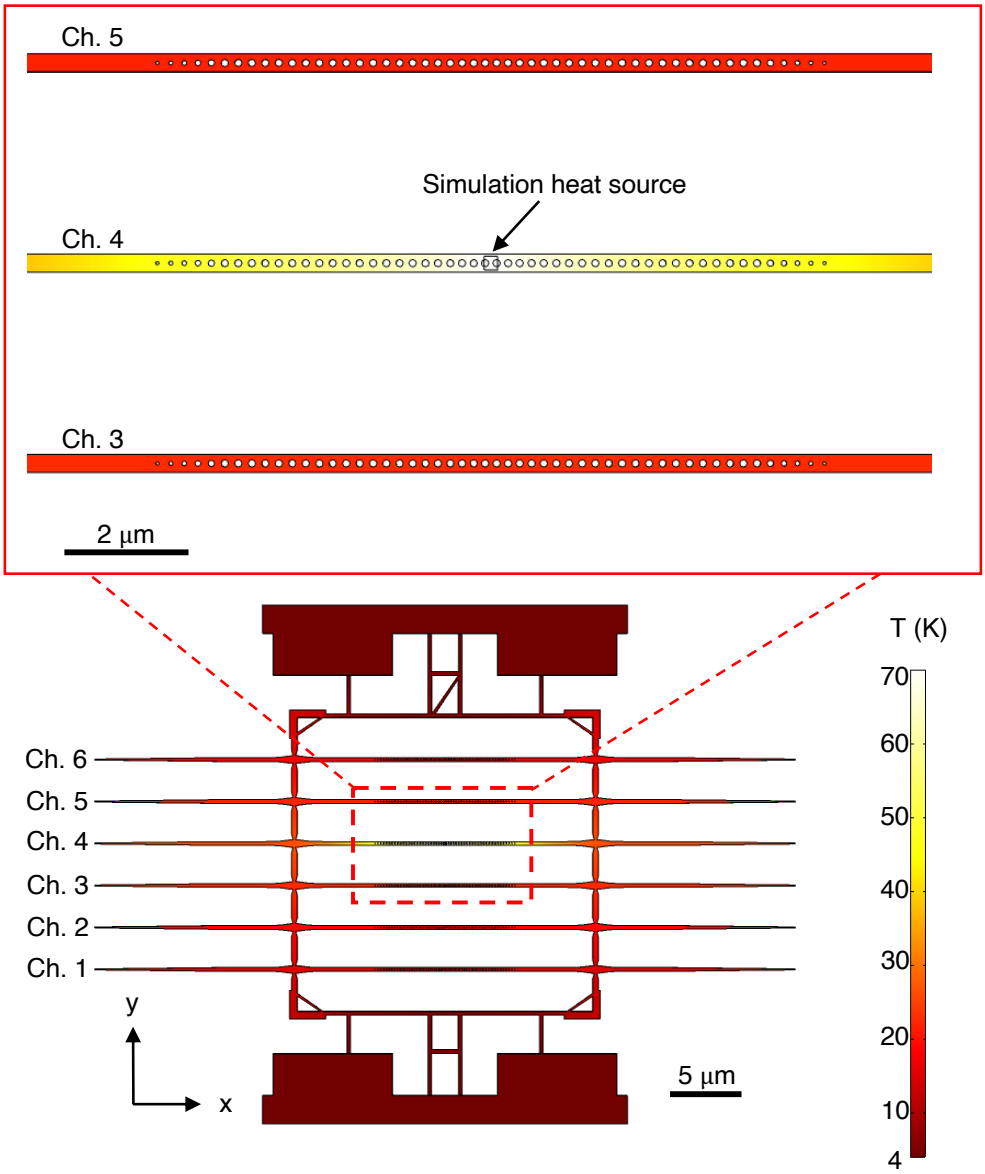

Figure 4-15: A thermal gradient in a diamond QMC caused by optical excitation at 532 nm, simulated using the heat transfer module in COMSOL. A heat source at 40 μW is placed at the center of the $j = 3$ channel, close to the center of the QMC. Fourier's law is used to simulate the steady-state thermal gradient across the device. The anchored regions (top and bottom) act as thermal sinks fixed at 4 K.

excited state population as a function of time t. All the while, a weak CW 515 nm light at 300 nW is used to repump the SnV center. The pulse sequence is repeated over N cycles, integrated over 300 s for each lifetime measurement.

Figure 4-16 shows lifetime τ versus cavity detuning Δ of one particular SnV center

in cavity $j = 6$ in QMC "d1.0.77" (different from what was presented in Section 4.3), with ZPL at 619.22 nm. Each lifetime curve is fitted with a single exponential convolved with a Gaussian that represents the instrument response function (IRF) [104], mainly determined by the timing jitter of the APD. Specifically, the convolution takes the form

$$f(t;\mu,\sigma,\tau) = \frac{1}{2\tau}\exp\left(2\mu + \sigma^2/\tau - 2t\right)\operatorname{erfc}\left(\frac{\mu + \sigma^2/\tau - t}{\sqrt{2}\sigma}\right), \tag{4.5}$$

where μ and σ represent the mean and standard deviation of the Gaussian, and τ is the inverse exponential decay rate corresponding to the SnV center's lifetime. After fitting, at large detuning, i.e. $\Delta = 7.45$ nm, the measured lifetime is 5.89 ± 0.25 ns. As Δ decreases, the lifetime monotonically decreases. At close to zero detuning, i.e. $\Delta = 0.05$ nm, the lifetime is shortened to 1.12 ± 0.04 ns. The observed lifetime reduction signifies Purcell enhancement of the SnV center's spontaneous emission rate due to emitter-cavity coupling (see Section 2.1.3).

In order to estimate the maximum Purcell factor F_P realized in experiments, we use the following formula that accounts for the modified local density of states when placing a SnV center in nanostructure and non-radiative decay pathways out of the excited state,

$$F_P = \frac{\tau_{\text{bulk}}\left(\frac{1}{\tau_{\text{on}}} - \frac{1}{\tau_{\text{off}}}\right)}{\xi}, \tag{4.6}$$

where $\xi = 0.456$ is a product of the SnV center's quantum efficiency QE=0.8 [35] and the Debye-Waller factor DW=0.57 [37]. τ_{on} and τ_{off} are the (nearly-)on-resonance and off-resonance lifetimes. We take one representative SnV center in bulk and use its lifetime for the following calculations, with $\tau_{\text{bulk}} = 5.10 \pm 0.22$ ns. The estimated Purcell factor for the measured SnV center in Figure 4-16 is $F_P = 8.07 \pm 0.55$. We can further estimate the β-factor, which is the probability of the SnV center emitting

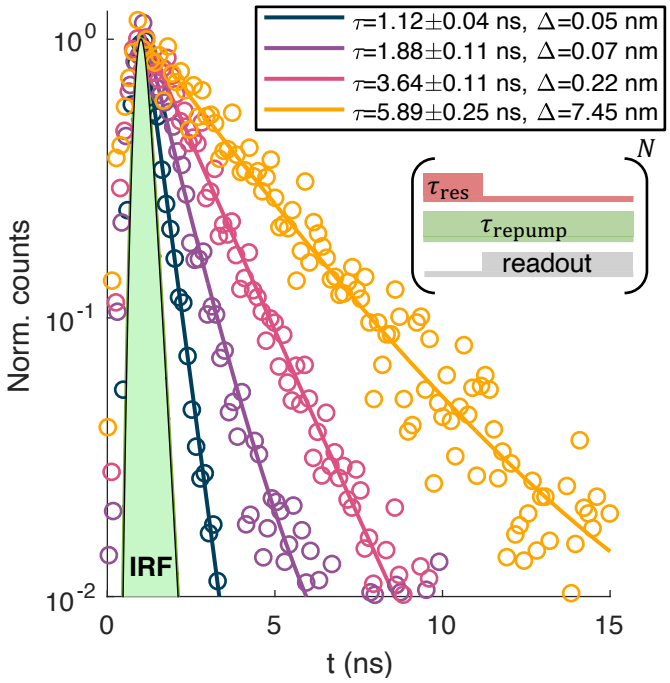

Figure 4-16: Lifetime τ versus emitter-cavity detuning Δ, fitted with a convolution between a single exponential and a Gaussian that represents the IRF (shaded in green). The emitter's lifetime expectedly reduces as detuning decreases due to Purcell enhancement. The pulse sequence consists of a short resonant pulse with weak CW repump light on at all times, and APD readout of the PSB fluorescence is triggered by the PPG. The sequence is repeated over N cycles.

into the cavity mode, defined as

$$\beta = \frac{\kappa}{\kappa + \gamma} \frac{F_P}{F_P + 1} \tag{4.7}$$

$$\approx \frac{F_P}{F_P + 1} \tag{4.8}$$

in the Purcell regime ($\kappa \gg \gamma$). The corresponding β-factor is $\beta = 89 \pm 9\%$.

Importantly, we achieve *multi-channel* Purcell enhancement within a single QMC. We find four coupled emitter-cavity systems in channels 2, 4, 5 and 6 (channels 1 and 3 do not contain SnV centers within the cavities). Figure 4-17 presents lifetime data for the remaining channels 2, 4, and 5. Table 4.1 shows a summary of each coupled emitter-cavity system's Purcell factor F_P, β-factor, and lifetime reduction ratios $\tau_{\text{off}}/\tau_{\text{on}}$. On average, the Purcell factors and β-factors acquired from this single QMC are 6.98 ± 0.26 and $86 \pm 5\%$, respectively.

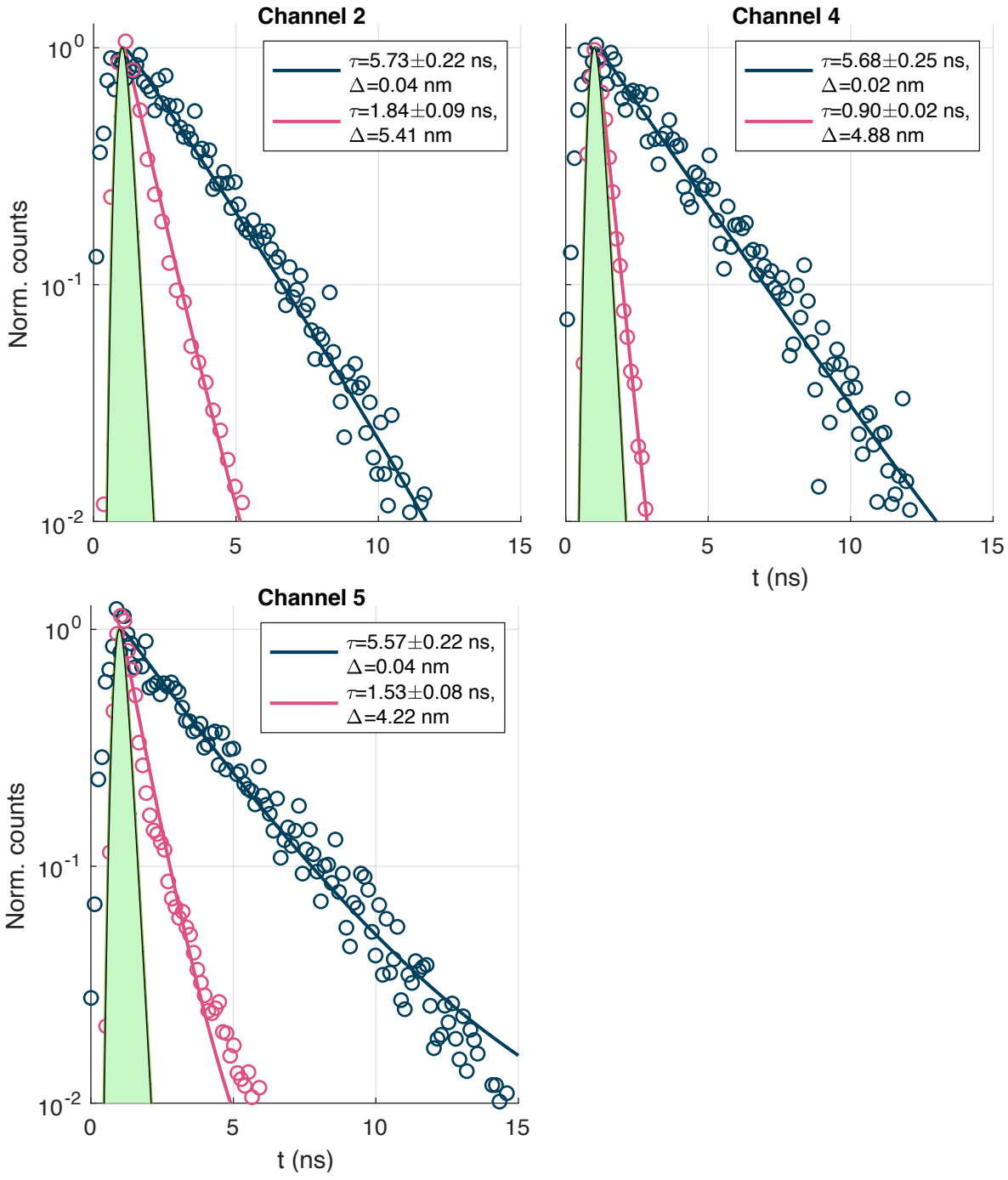

Figure 4-17: Lifetime data for the remaining channels 2,4,and 5. Similar to Figure 4-16, each curve is fitted with a convolution between a single exponential and a Gaussian representing the instrument response function (IRF, shaded in green). The reductions in lifetimes at close to resonance between SnV centers and cavities signify Purcell enhancement in all three channels.

Channel	ZPL (nm)	Max. observed F_p	β-factor	Lifetime ratios
2	619.2821	4.13 ± 0.40	$81 \pm 11\%$	3.12 ± 0.19
4	619.2560	10.40 ± 0.62	$91 \pm 8\%$	6.28 ± 0.32
5	619.2965	5.32 ± 0.49	$84 \pm 11\%$	3.65 ± 0.23
6	619.2220	8.07 ± 0.55	$89 \pm 9\%$	5.25 ± 0.28

Table 4.1: A summary table of the lifetime results. Lifetime ratio is defined as the closest on-resonance lifetime divided by the far-detuned lifetime. ZPL of the SnV center is read off the wavemeter (HighFinesse) connected to the tunable 620 nm resonant laser.

In particular, one emitter-cavity coupled system in cavity $j = 4$ in QMC "d1.0.77" exhibits ten-fold Purcell enhancement at $F_P = 10.40 \pm 0.62$. Its cavity Q factor at close to resonance $\Delta = 0.14$ nm is $Q \approx (2.28 \pm 0.05) \times 10^3$ (Figure 4-14). Accounting for detuning that reduces the measured Purcell factor by a factor of $1 + 4Q^2(\lambda_{\mathrm{SnV}}/\lambda_c - 1)$ [57, 105], we estimate the maximum experimental Purcell factor at $\Delta = 0$ improves slightly to $F_P = 10.63 \pm 0.14$. The theoretical maximum Purcell factor $F_{P,\mathrm{max}} = \frac{3}{4\pi^2}\left(\frac{\lambda_c}{n}\right)^3 \frac{Q}{V}$ is $F_{P,\mathrm{max}} = 216.2 \pm 0.4$ (assuming the simulated mode volume). Accounting for dipole misalignment (angular difference between the [111] and [100] crystal axes) reduces the maximum Purcell factor to $F_{P,\mathrm{max}} = 124.9 \pm 0.3$. We attribute the difference between the theoretical and experimental maxima of a factor of $F_{P,\mathrm{max}}/F_P \sim 11.37 \pm 0.04$ to the SnV center being spatially off-centered from the cavity field maximum, an issue which can be resolved by employing focused ion beam implantation [106] or masked implantation [107] in future efforts.

Chapter 5

Heterogeneous integration into PIC

In the previous chapter, we demonstrate coupling between SnV centers and 1D PhC cavities contained in a QMC. In the following sections, we show hybrid integration of these cavity-enhanced spin-photon interfaces into a silicon nitride PIC [51, 52]. Based on the measured experimental parameters, we estimate the theoretical photon-to-spin quantum state transfer fidelity and success probability in Section 5.5 based on scalable photonic platforms, and discuss potential improvements.

5.1 Silicon nitride PIC

The silicon nitride photonic integrated circuit (PIC) is primarily designed by my colleague, Ian Christen.

The PIC we use is fabricated by MIT Lincoln Laboratory in a silicon CMOS foundry (90-nm node) with silicon nitride (SiN) waveguides cladded in silicon dioxide (SiO_2). The on-chip waveguide has been measured to exhibit low propagation loss at $\sim$ 0.3 dB/cm [51, 52] at visible wavelengths. Furthermore, the oxide cladding in conjunction with adiabatic tapering[1] of the SiN waveguide at the PIC's facet is optimal for edge-based optical coupling to a single-mode fiber, e.g. 630HP. However, we note that the PIC is originally designed to be operating at 737 nm. Therefore, at

[1]From an initial waveguide width of 600 nm down to 300 nm at the facet.

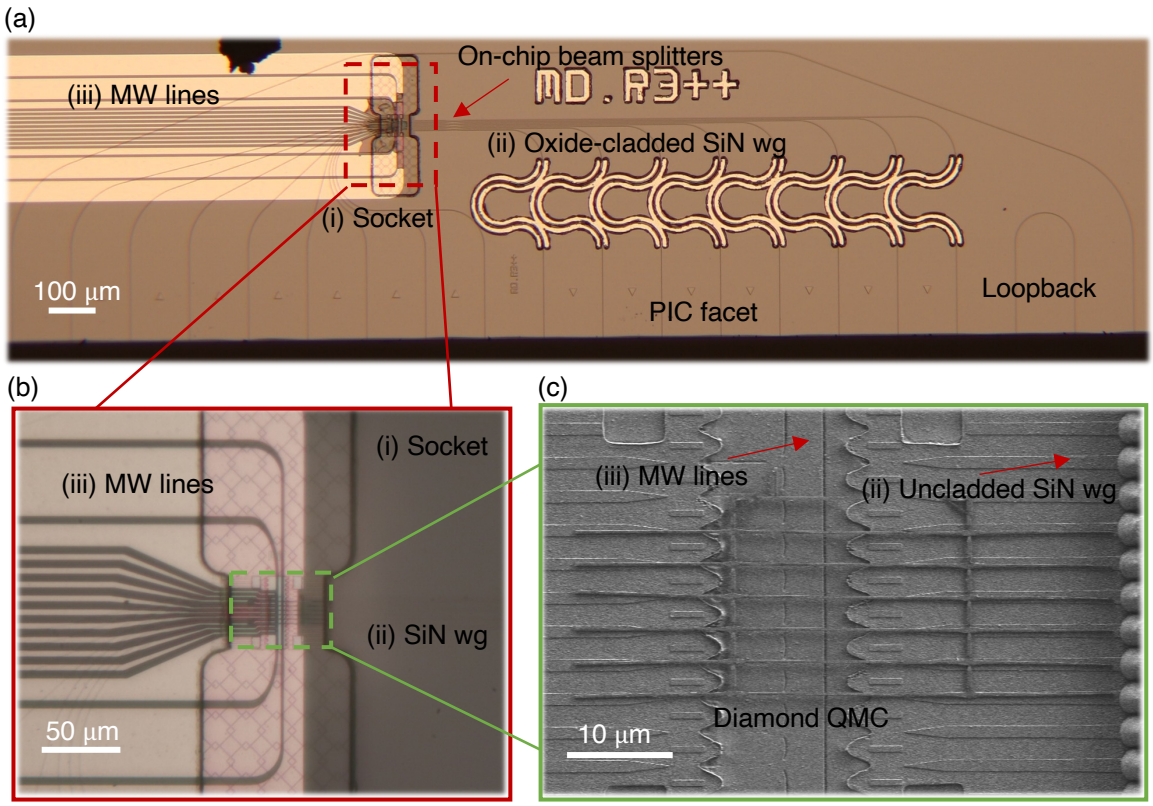

Figure 5-1: Layout of the SiN PIC for diamond QMC experiments. (a) An optical micrograph of (i) a socket where oxide is removed for integration of diamond QMCs, (ii) SiN waveguides routing from the socket to the PIC facet, and (iii) gold MW lines running through the middle of the socket for coherent control. There are also directional couplers that construct passive on-chip beam splitters. (b) A close-up image of the inside of the socket. (c) A SEM image of a transferred diamond QMC evanescently coupled to the uncladded SiN waveguides.

our SnV center's wavelength of ∼620 nm, the PIC-fiber coupling efficiency may not be optimal with a single-mode fiber (see Section 5.3.2).

As shown in Figure 5-1(a,b), part of the PIC layout includes (i) a socket opening in the cladded oxide layer for diamond QMC integration, (ii) SiN waveguides routing to the edge of the chip, and (iii) gold microwave lines for coherent control of spin qubits (bonding pads located near other facets not shown). Figure 5-1(c) shows a SEM image of a diamond QMC placed inside the socket, with diamond waveguides evanescently coupled to the uncladded SiN waveguide.

The reported results in the following only utilize components (i) and (ii), though we have also used (iii) to perform optically detected magnetic resonance (ODMR) of

SnV centers in a separate experiment [108]. For more details about the PIC design and its material stack, interested readers may consult Ref. [52].

5.2 Transfer printing

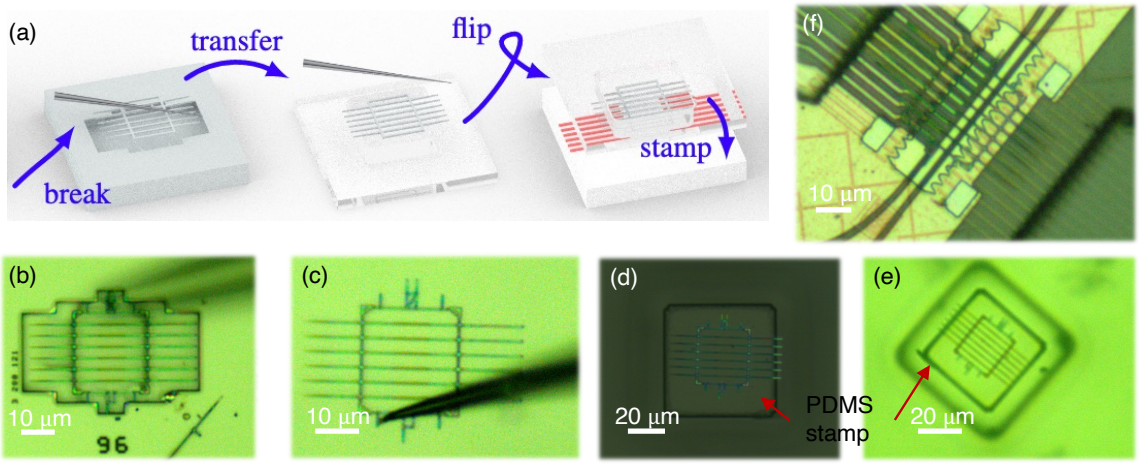

Figure 5-2: A step-by-step diagram of the transfer printing process for heterogeneously integrating a diamond QMC into a SiN PIC. (a) A general process flow involving breaking the QMC from the diamond substrate, transferring it onto a PDMS stamp, flipping the stamp over, then stamping the QMC onto the PIC. (b) A fine-tipped tungsten probe is used to break the connections to the bulk to detach the QMC from the parent diamond substrate. (c) After detaching from the substrate, the QMC is attached to the probe via van der Waals. (d) The QMC is subsequently placed onto the PDMS stamp, (e) which is then flipped and positioned to align to the SiN waveguides on PIC. (f) The transferred QMC, with the smooth side facing downwards, is in contact with the underlying SiN waveguide.

To heterogeneously integrate the diamond QMCs into the SiN PIC, we adapt a transfer printing process [109, 110] as illustrated in Figure 5-2. First, we use a tungsten probe with 500 nm tip radius[2] to detach the diamond QMC from its parent substrate (Figure 5-2(b)). Then, the detached QMC is adhered to the probe via van der Waals (Figure 5-2(c)). Recall from Section 4.2 that the top side of our fabricated diamond devices is much smoother than the rough underside due to the quasi-isotropic etch step. Therefore, for optimal evanescent coupling to the PIC waveguide, it is paramount to have the smoother topside in contact with the SiN waveguide. Since

[2]Standard W Probe Tips for AutoProbe 100 & 200.

the probe is already in contact with the smooth top side, we first transfer the QMC onto a PDMS stamp[3] that contacts the QMC's rough backside (Figure 5-2(d)). We then flip the stamp over and position it to align to the PIC by imaging through the PDMS (Figure 5-2(e)). Finally, we stamp the diamond QMC onto the PIC socket (Figure 5-2(f)). As opposed to the approach conducted in Ref. [50], in which either a second tungsten probe is used to flip the diamond QMC or the initial probe is weakly adhered to the rough backside and needs axial rotation, this "pick-n-stamp" method minimizes risks of losing/destroying devices during the transfer process.

5.3 A PIC-based optical interposer

Using the aforementioned transfer printing process, we heterogeneously integrated a QMC containing 1D PhC cavities into the SiN PIC. The PIC serves as an optical interposer that enables us to perform cavity characterization and spectroscopy on SnV centers via both free-space and fiber excitation/collection.

5.3.1 Diamond and SiN waveguide mode coupling

Crucial to our measurements is coupling between the photonic modes supported by the diamond QMC and the SiN waveguide mode. Since we have already assessed the cavity-waveguide coupling efficiency ($\sim 5 \times 10^{-3}$ due to a design focused on under-coupling to the waveguide to maximize extrinsic Q) in Section 4.1, here we perform FDTD and eigenmode-solver simulations to evaluate the efficiency of transferring a diamond *waveguide* mode to the PIC SiN waveguide mode.

Figure 5-3(a) shows an optical micrograph of an integrated diamond QMC in the PIC socket. Figure 5-3(b) shows a SEM image of the socket containing the integrated QMC. Due to a pitch mismatch between the QMC and the SiN waveguides, only channels 2-5 are optically coupled for measurements. We estimate roughly a $\sim$21 μm overlap in length between diamond and SiN waveguides, both of which are

[3]This is custom-designed to have a 50 μm by 50 μm plateau. The stamp is produced by X-Celeprint.

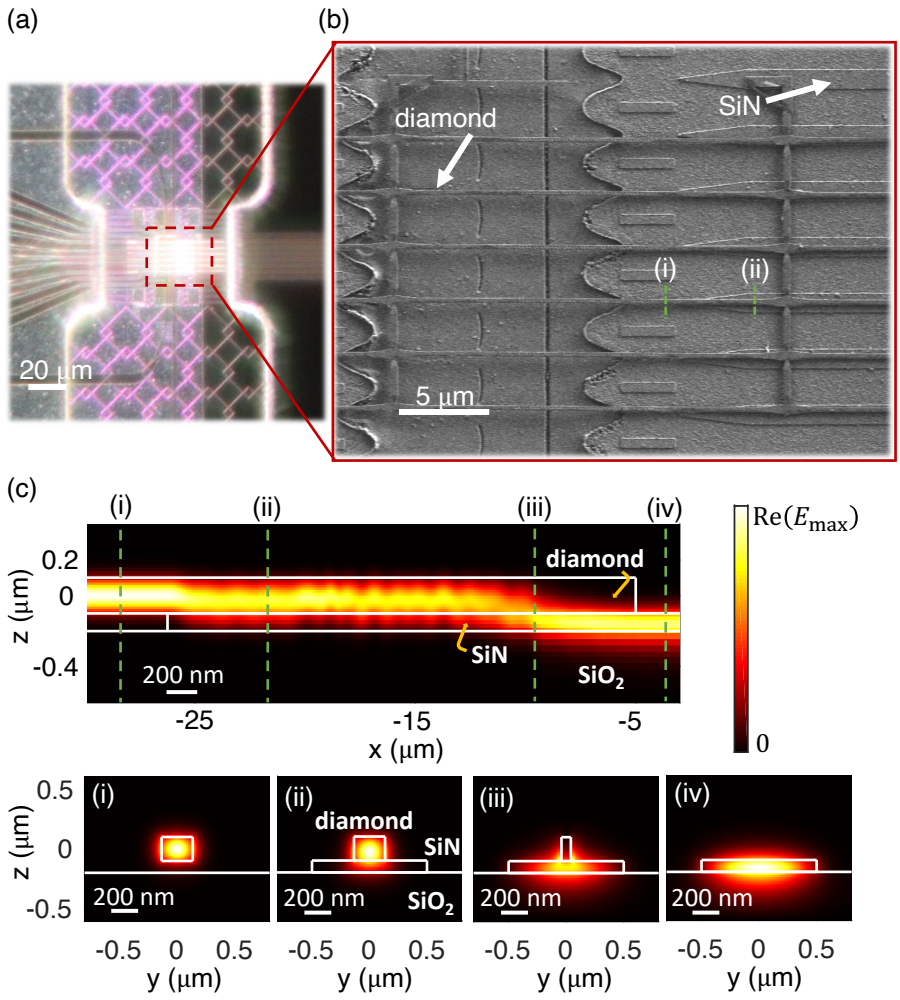

Figure 5-3: Integration of a diamond QMC into a SiN PIC. (a) An optical image of the integrated device. (b) A SEM image of the diamond QMC in the socket. (c) The TE mode propagates from diamond waveguide to the evanescently coupled SiN waveguide (100 nm thick) on oxide. The waveguide modes for the integrated QMC on SiN PIC: (i) diamond waveguide before contact with SiN, (ii) in the overlapped region at 10 μm and (iii) at 2.25 μm from the diamond tip, and (iv) SiN waveguide on oxide. Positions (i) and (ii) are also indicated in (b).

adiabatically tapered to minimize scattering loss.

We estimate roughly a $\sim$ 21 μm overlap in length between diamond and SiN waveguides, both of which are adiabatically tapered to minimize scattering loss. With the diamond (SiN) waveguide tapering down from 260 nm (1 μm) to 50 nm (0 nm) in width over 9 μm (4 μm) in length, the transmission efficiency is simulated to be 94.4% at 619 nm in FDTD at zero angular offset. Figure 5-3(c) shows the propagating TE

mode out of the cavity from the diamond waveguide (left) to the evanescently coupled SiN waveguide (right) on oxide, with mode profiles evaluated at four selected points: (i) suspended diamond waveguide before overlapping with SiN, (ii) in the overlapped region at 10 μm and (iii) at 2.25 μm from the diamond tip, and (iv) SiN waveguide on oxide. The SiN waveguide mode for each channel is then routed to an inversely tapered waveguide at the chip's edge for optimal optical coupling to a single-mode fiber [52].

In FDTD, we also analyze the change in transmission efficiency as a function of angular offset. Figure 5-4 shows the decrease in transmission from $\sim 94\%$ at perfect angular alignment to $\sim 84\%$ at 2 degrees offset. Based on the SEM shown in Figure 5-3(b), we estimate an angular offset $\sim$0.5 degree with a corresponding transmission efficiency $\sim$91%.

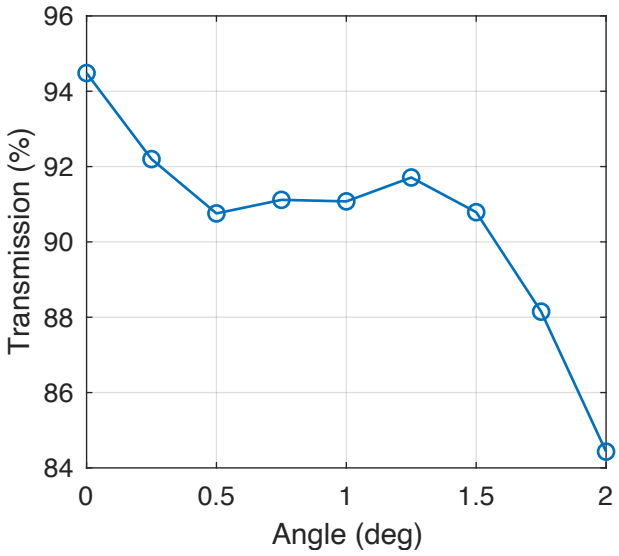

Figure 5-4: Transmission efficiency from diamond to SiN waveguide as a function of angular offset.

5.3.2 Fiber edge-coupling efficiency

After transferring the QMC "s1.0.77" containing PhC cavities into the SiN PIC, we load the sample onto the same room-temperature confocal setup described in Section 4.3. Additionally, we include a 3-axis NanoMax translation stage attached with

either a single-mode fiber (e.g. cleaved 630HP shown in Figure 5-5) or a 8-channel fiber array[4]. In the free space portion of the setup, a CCD camera allows imaging of the diamond socket. By sending in laser signal, for example the supercontinuum laser used in cavity characterization, we can monitor the transmission from the edge-coupled SiN waveguide into the diamond QMC. We then optimize fiber coupling to the PIC facet by maximizing the scattered laser signal by the QMC observed on the live CCD image.

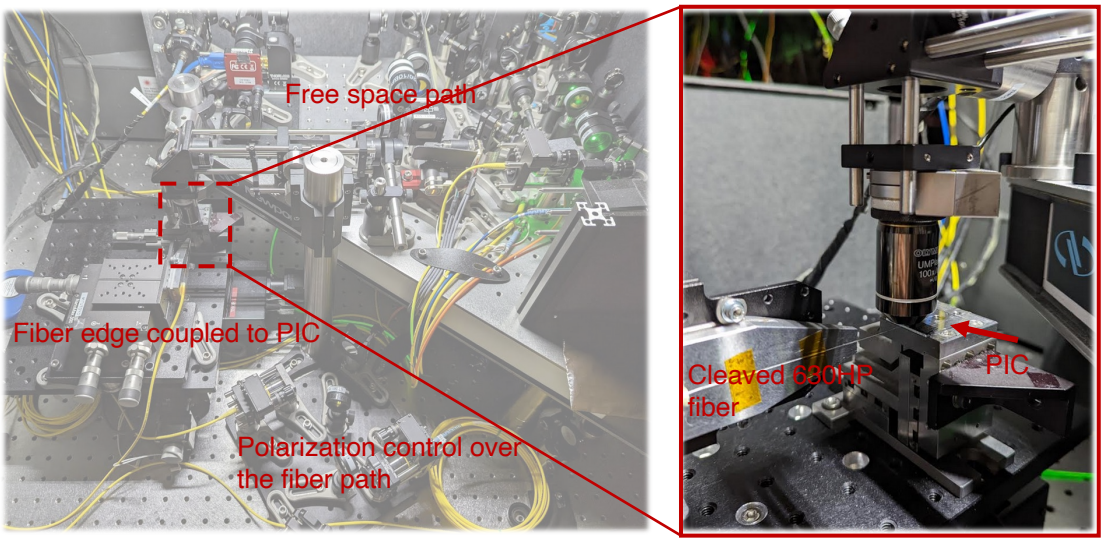

Figure 5-5: An optical setup consisting of free-space optics and a translation stage that permits edge-coupling of single-mode fibers to the PIC. There is an additional optical breadboard containing polarization control optics for the fiber path, in which a single-mode fiber is out-coupled into free-space then back into another single-mode fiber.

Using a 8-channel fiber array, we simultaneously edge-couple to two SiN waveguides forming the loopback structure (bottom right of Figure 5-1(a)). By measuring the input power before one SiN waveguide and the transmitted power at the other channel, we extract the fiber-to-PIC edge-coupling efficiency at various wavelengths, which are set by a variable bandpass filter (10 nm wide) of the supercontinuum laser. As shown in Figure 5-6, the coupling efficiency per fiber-to-PIC interface is $\sim 30\%$ at 620 nm. Expectedly, the coupling efficiency is higher at 737 nm, which is the targeted wavelength. However, the measured efficiency is still about 10% lower than what is

[4]8ch 127P SMFA-FC/APC, Precision Micro-Optics.

reported in Ref. [52]. We attribute the discrepancy to angular misalignment (yaw and pitch) and mechanical instability in our setup.

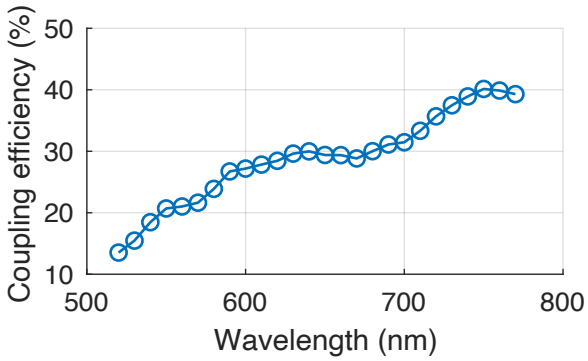

Figure 5-6: Measured fiber-to-PIC edge-coupling efficiency as a function of wavelength.

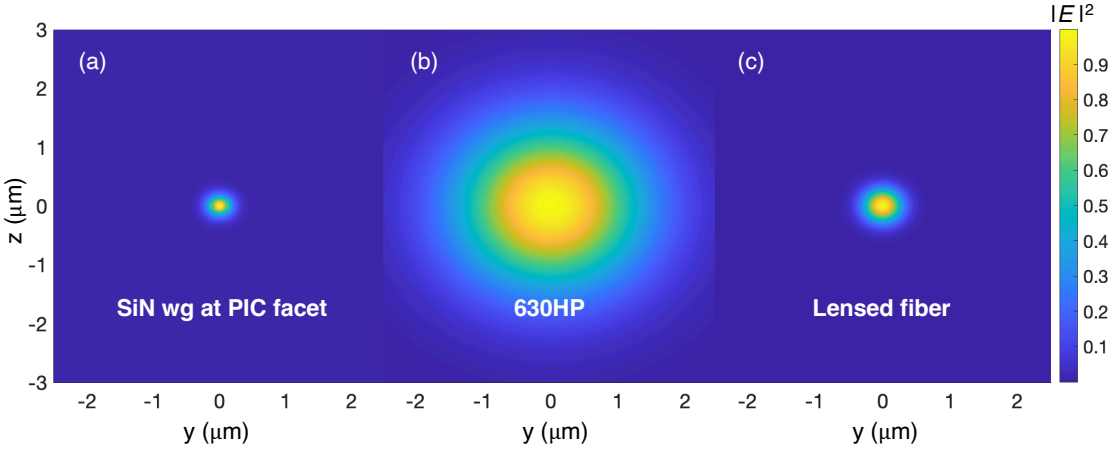

Figure 5-7: Mode coupling efficiency with an oxide-cladded SiN waveguide at the PIC facet. Its width and thickness are 300 nm and 100 nm, respectively. With a 630HP (lensed) fiber, the coupling efficiency is calculated to be $\sim 23\%$ ($\sim 91\%$).

We also simulate the oxide-cladded SiN waveguide mode at the facet and compute the coupling efficiency at 620 nm. Interestingly, the simulation result shown in Figure 5-7 suggests $\sim 23\%$ edge-coupling efficiency with a single-mode 630HP fiber (mode field diameter of 4 μm). We surmise the 7% offset could stem from having different fiber and SiN waveguide modes in experiments than those in simulations. Nevertheless, we compare with using a lensed fiber (spot size diameter 0.8 μm) and find a simulated edge-coupling efficiency of $\sim 91\%$. Given the drastic improvement

in simulations, we proceed our room temperature characterization experiments with a lensed fiber to improve fiber collection efficiency.

5.3.3 Cavity characterization via the PIC

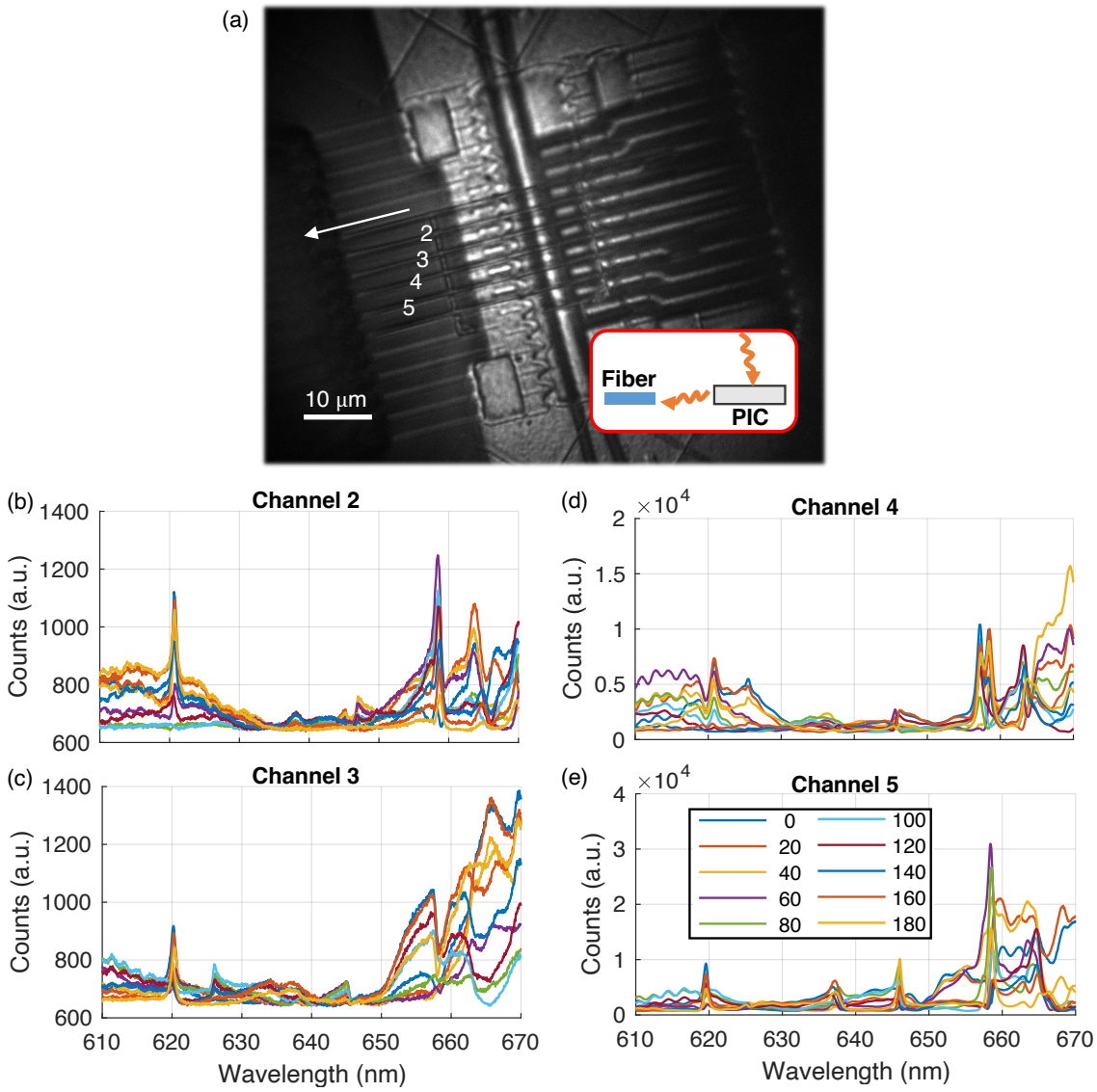

Figure 5-8: (a) A white light image of an integrated diamond QMC containing six PhC cavities. (b-e) Cavity transmission spectra for channels $j = \{2, 3, 4, 5\}$ with swept linear polarization.

With the same setup described in the previous section, we characterize our cavities via transmission through the PIC as an optical interposer. As opposed to the

cavity reflectivity measurement described in Section 4.3, we excite the cavity modes confocally from the top with the supercontinuum laser and monitor the spectrum of the transmitted photons collected by the edge-coupled lensed fiber.

Figure 5-8(a) shows a white light image of the diamond QMC containing six 1D PhC cavities. Due to the offset in pitch, i.e. channel separation distance, between the SiN waveguide at 3 μm and the diamond cavities at 2.6 μm[5], we only survey channels $j = \{2, 3, 4, 5\}$ as the outer channels are laterally displaced.

Figure 5-8(b-e) show the cavity spectra for the four channels swept with different linearly polarized input light from the top. The polarization axis is determined by a HWP, set from 0 to 180 degrees in increments of 20. All four sets of spectra indicate resonance peaks representing both fundamental resonances near 620 nm and higher-order modes > 640 nm. Note that the cavity signals still exhibit Fano lineshapes due to frequency dependence of cavity absorption and transmission through the diamond-PIC. Fitting them to Eq. 4.2 gives Q factors for channels 2-5: 900±15, 767±18, 631±11, 840±7.

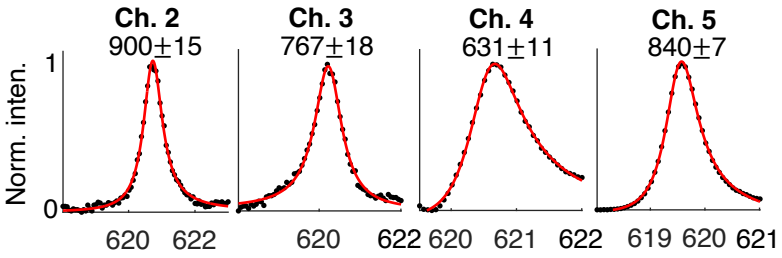

Figure 5-9: The fitted Q factors of channels 2-5 based on the measured cavity transmission spectra. Each cavity resonance is fitted with the Fano-Lorentz function (Eq. 4.2), with fitted Q factors: 900±15, 767±18, 631±11, 840±7.

We also try applying 532 nm green excitation from the fiber at above saturation > 10 mW to excite the SnV centers present in the diamond devices, and collect the cavity mode's photons from the top, as illustrated in Figure 5-10(a). The ZPL and PSB fluorescence from the emitters are used to pump the cavity modes, which we observe in the spectra of the top-collected signal shown in Figure 5-10(b). Note that

[5]This is a result of sweeping the pitch in our CAD for diamond fabrication to compensate for uncertainty in the final device thickness, dictated by the pitch that sets the quasi-isotropic etch rate.

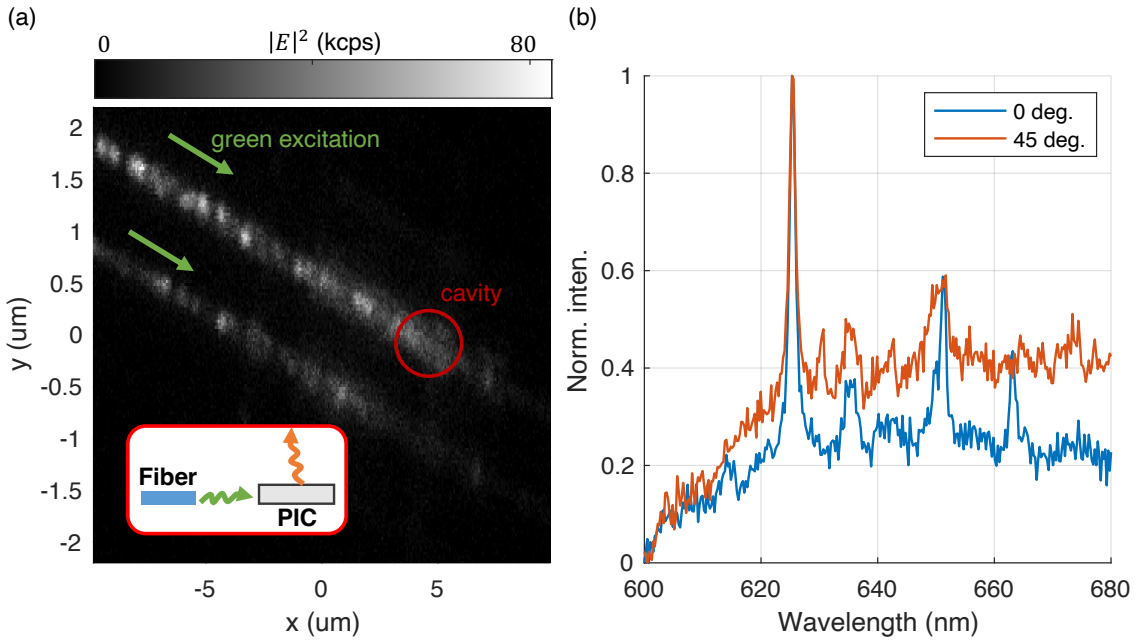

Figure 5-10: (a) A fluorescence image acquired by rastering the top-collection confocal spot. Two channels, $j = \{3, 4\}$, are simultaneously excited via an on-chip beam splitter. The circled spot in red marks where the cavity mode is observed. (b) Spectra acquired at two different HWP rotation angles, 0 and 45 degrees. Both spectra show a strong peak at ∼625 nm, which may result from having a non-linearly polarized higher order cavity mode.

two adjacent channels ($j = \{3, 4\}$) are simultaneously excited via a passive on-chip beam splitter (see Figure 5-1(a)).

During our measurements, we have discovered additional scattering loss ∼ 7 dB [52] at the junction where oxide is removed, likely caused by a non-adiabatic change in the SiN waveguide mode's effective index. As a result, when probing the cavity resonance in a fiber-only approach, we observe etalon-ing signal on the spectrometer that obscures any Fano features. For example, Figure 5-11 shows an image indicating scattering at the oxide junction and an etalon-ing spectrum obscuring the resonance of SiN ring resonators[6]. We surmise scattering at the oxide junction and at the diamond PhC cavity itself form an etalon. Therefore, for all the PIC-related measurements, we focus only on transmission-type measurements in which excitation and collection

[6]The observed etalon-ing's FSR is ∼ 0.5 nm, corresponding to a path length of ∼ 400 µm (SiN thin film index $n_{\mathrm{SiN}} \approx 2.03$ [51]). This length matches the path distance between the two oxide junctions.

channels are from the top and fibers, respectively, or vice versa.

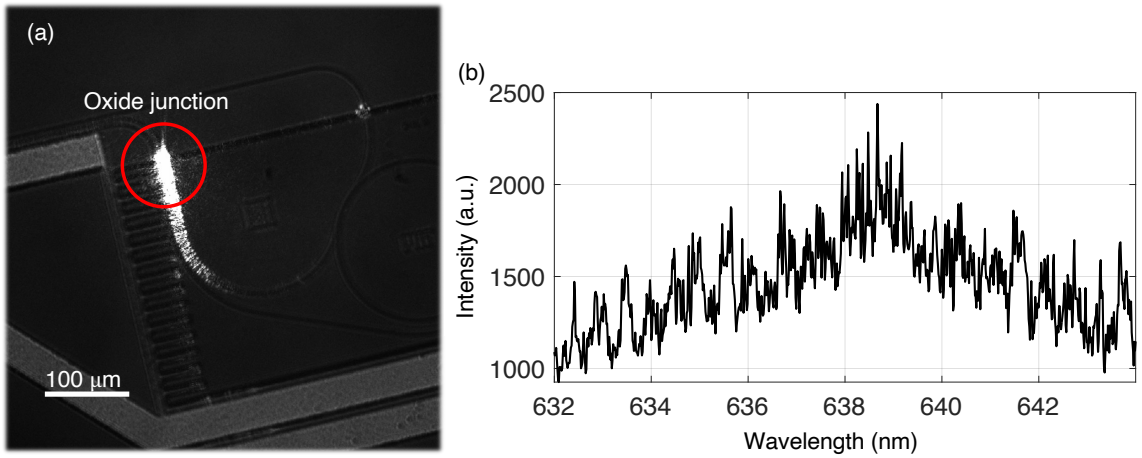

Figure 5-11: (a) A white light image showing severe scattering loss (circled in red) at the junction of the oxide window. (b) An example spectrum indicating etalonning between two junction points, obscuring the resonance signal of the probed ring resonators.

5.4 Spectroscopy of SnV centers in PIC at 1.3 K

The measurements described in this section are taken in the facility belonging to Prof. Karl Berggren, with the help of Dr. Marco Colangelo on operating the cryostat.

After characterizing the cavities integrated into the PIC at room temperature, we proceed to performing cryogenic measurements with a 1.3 K ICE Oxford cryostat. Illustrated in Figure 5-12, the SiN PIC is attached to a machined copper (Cu) mount fixed in position. On the other hand, the fiber array (630HP) is attached to an Attocube positioner stack for alignment. Moreover, GE varnish is applied to the corners of the PIC to provide further mechanical stability and cushioning when the fiber array block physically contacts the PIC for edge-coupling.

The single-mode fibers exit out of the top of the cryostat and are routed to an external setup, as shown in Figure 5-13. Similar to the setup described in Section 4.4, it includes the same supercontinuum laser for cavity characterization, a tunable 620 nm laser for PLE, and a 515 nm laser for off-resonant excitation and charge repump.

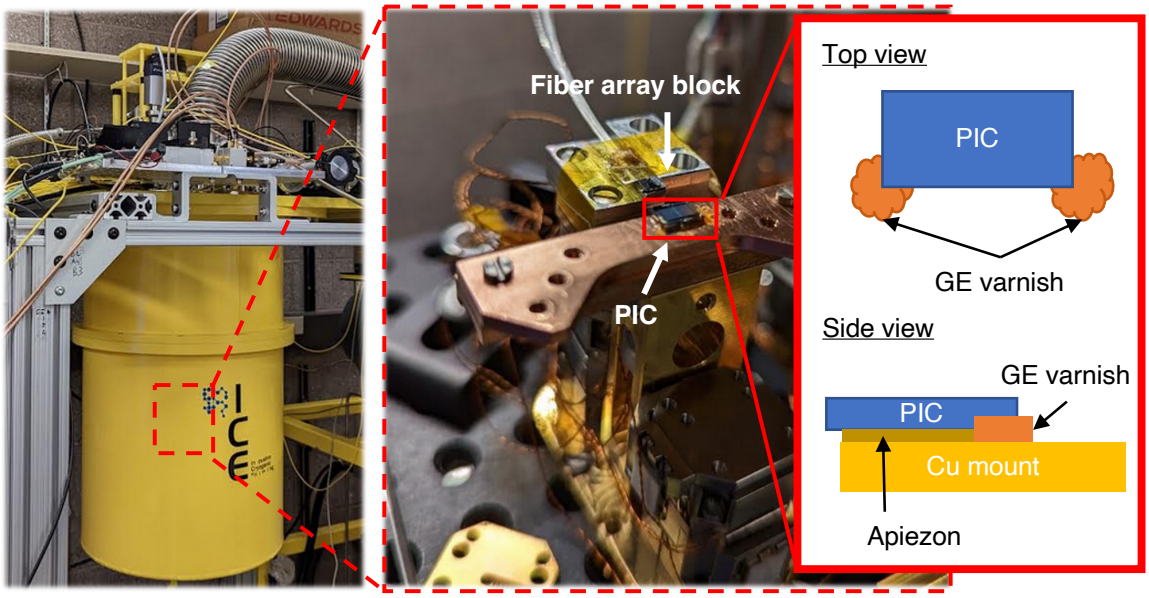

Figure 5-12: Diagram showing inside the ICE Oxford cryostat. The PIC is glued onto a machined Cu mount, and a fiber array block attached to an Attocube positioner stack for edge-coupling.

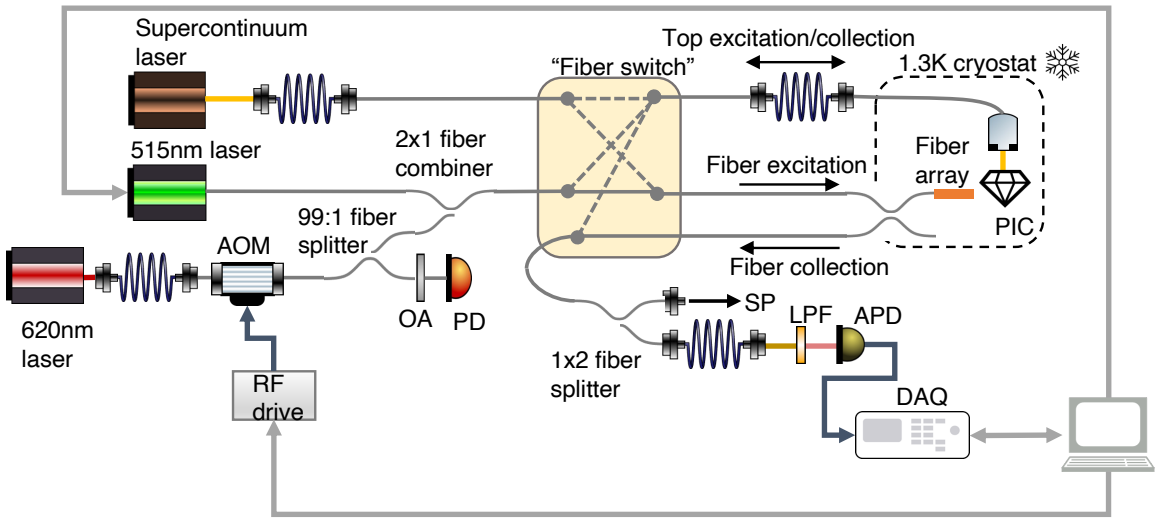

Figure 5-13: A schematic of the setup for the ICE Oxford cryostat. A 515 nm laser and a free-spaced coupled 620 nm laser are combined in a 2x1 fiber combiner, which is routed to one of the fiber array channels. The tunable 620 nm is modulated by a fiber AOM (TEM-150-9-60-633-2FP, Brimrose), and its output is constantly monitored by a photodiode (PD) attenuated by an optical attenuator (OA). A supercontinuum laser is also used for top excitation/reflection and cavity transmission measurements via a cryo-objective. The "fiber switch" is done manually. The collected signals from an adjacent fiber channel to the excitation port is sent to either a free-space APD or a spectrometer (SP).

However, as mentioned in the previous section, due to the cavities being under-coupled to the waveguides, we cannot efficiently excite the SnV centers located at the cavity centers resonantly from fiber. As a result, we employ top excitation in the same spirit as stated in Section 5.3.3. We install a cryo-compatible objective[7] that is attached to its own Attocube positioner stack. Importantly, we ensure the objective to have a long working distance at 1.5 mm to avoid collision with the fiber array[8] when focusing on the PIC's top plane.

With a spot size of about 0.5 μm (objective NA=0.68 with 3.1 mm focal length), we first perform top imaging of the PIC by collecting the reflected laser signal in a cross-polarization setup[9]. Figure 5-14(a) shows a reflectivity map of the socket containing a diamond QMC above the gold lines, which have higher reflectivity contrast. The scan is acquired using 0.5 μm step size corresponding to the focused spot size. Once we localize the position of the QMC, we then switch to a transmission-type measurement by top excitation and fiber collection. Figure 5-14(b) shows the transmission map using the supercontinuum laser, with fiber channel's $j = 5$ transmission measured by the APD. We then adjust the position of excitation spot around the cavity center to maximize the Fano signal at $\sim$ 620 nm, as shown in Figure 5-14(c), which matches the observed cavity resonances shown in Figure 5-8.

5.4.1 PLE measurement via the PIC

At 1.3 K, we perform spectroscopy on the SnV centers residing at the cavity center. By exciting the same location that exhibits cavity resonance signal (Figure 5-14(c)) with 515 nm at 21 mW[10], we observe C and D transitions typical of SnV centers, as shown in Figure 5-15(a), with spin-orbital splitting of $\sim$820 GHz. However, off-resonant light may easily scatter to regions outside of the cavity center and lead to collection of fluorescence from SnV centers that would not be coupled to the PhC

[7]LT-IWDO/0.68 CFM II, Attocube.

[8]The distance from the fiber channels to the top of block is about 1 mm.

[9]Cross-polarization is used to filter direct reflection from the collimators to improve signal contrast.

[10]Power is measured after the 2x1 fiber combiner.

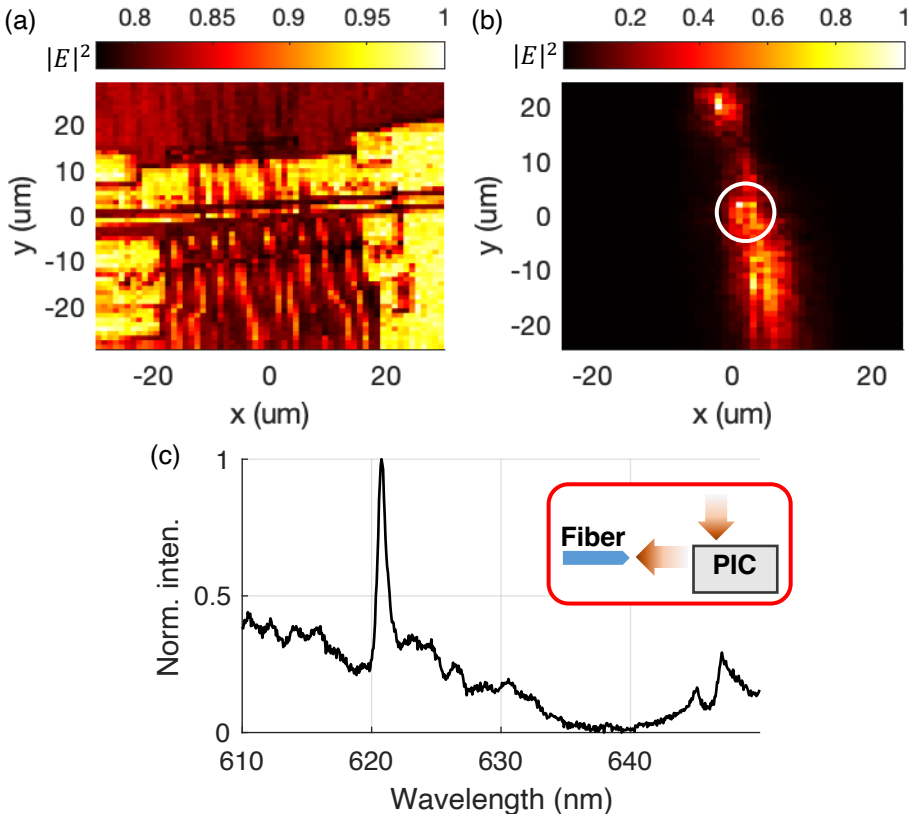

Figure 5-14: (a) A reflectivity map of the socket with top excitation and collection that is cross-polarized. The highly reflective parts indicate the underlying metal lines, with the silhouette of the diamond QMC centered about $x = y = 0$. (b) A transmission map with top excitation and fiber (channel $j = 5$) collection. The white circle indicates where the cavity resonance signal contrast is maximized. (c) A transmission spectrum acquired at close to the cavity center, indicating the same resonance at ~ 620 nm as was observed in Figure 5-8.

cavity. Therefore, we also perform PLE via the tunable 620 nm laser, and sweep a large frequency range to spectrally locate the SnV centers. The weak resonant light at ~ 900 nW should only excite emitters close to the focused spot. We confirm this by comparing the count rate difference between exciting on and off the cavity center, and find that the latter is essentially at the level of dark counts ~ 100 counts per second (cps).

For our PLE measurement, we execute the same pulse sequence as detailed in Section 4.4. However, since transmission from the cavity region to the waveguide mode is low $\sim 5 \times 10^{-3}$, the collected PSB count rate is only on order of 10^2 cps.

Hence, for each frequency point in our PLE measurement, we repeat the following pulse sequence 10^5 times to improve the signal-to-noise ratio (SNR): $\tau_{\text{repump}} = 1$ μs at 760 μW for charge repump [96, 97], followed by $\tau_{\text{delay}} = 5$ μs of timing delay, and $\tau_{\text{res}} = 10$ μs for the resonant pulse and the APD readout window.

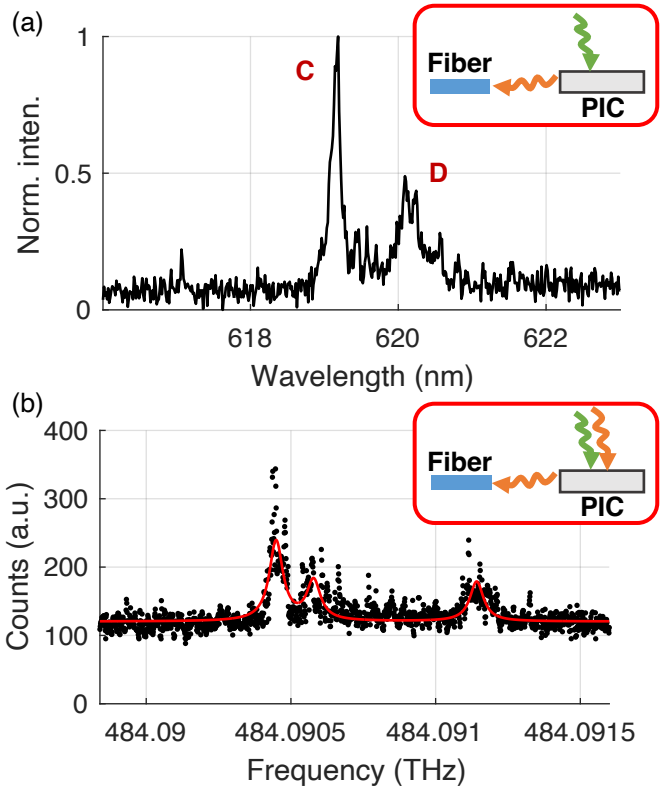

Figure 5-15: Spectroscopic measurements of SnV centers in a 1D PhC cavity via a PIC-based optical interposer. (a) PL spectrum using off-resonant excitation reveals the C and D transitions representative of SnV center in diamond. (b) PLE curve showing three peaks that could stem from zero-field hyperfine transitions in our Sn-117 sample. The presence of a third peak suggests static strain induced by nanofabrication and transfer printing. The fitted linewidth, hyperfine splitting, and strain-induced splitting are 66.4 ± 5.3 MHz, 437.8 ± 4.9 MHz, and 305.7 ± 6.2 MHz, respectively.

Figure 5-15(b) shows the acquired PLE curve indicating the presence of three peaks, which may stem from nuclear-electro hyperfine transitions. Recent results from Parker *et al.* and Harris *et al.* have found that the large hyperfine coupling between the Sn-117 nuclear and electron spins exceeds its optical linewidth [111, 112]. As a result, even under zero applied field, they can still observe twin peaks representing the two spin-1/2 hyperfine transitions. During the scan, we also notice that the emitters

would stop fluoresce intermittently. Since our applied repump power at 760 μW[11] should be more than sufficient to charge repump the SnV centers, it is unlikely the "blinking" is caused by charge state instability alone. Therefore, we surmise the investigated SnV center, which has a Sn-117 nuclear isotope, is optically pumped to other hyperfine states, in addition to any spectral diffusion. To counteract this phenomenon, we repeat the PLE scan in forward (increasing frequency) and backward (decreasing frequency) directions, and average over the curves to produce Figure 5-15(b). In contrast, the SnV center shown in Figure 4-11(c) exhibits a single peak, implying that it was a Sn-120 isotope with spin-0.

Assuming the three peaks result from the hyperfine transitions, we fit the peaks to three Lorentzian with the same linewidth and amplitude ratios of 2:1:1 [112]. The fitted ZPL positions are 484.0904 THz, 484.0906 THz, and 484.0912 THz, with linewidth 66.4 ± 5.3 MHz. We estimate a hyperfine splitting of 437.8 ± 4.9 MHz, which agrees closely with what was observed in Ref. [111, 112]. Furthermore, the presence of the third peak suggests additional splitting due to strain, which may be introduced by nanofabrication and/or transfer printing. Based on the fit, we estimate strain-induced splitting corresponding to 305.7 ± 6.2 MHz.

However, to truly verify the three peaks are indeed stemming from a single SnV center with three hyperfine transitions requires autocorrelation measurements. Specifically, using the sidebands of an EOM to simultaneously excite two transitions at a time, hence requiring $\binom{3}{2} = 3$ separate measurements. At our current count rate $< 10^3$ cps, this would require acquisition time on the order of days, over which mechanical instability from vibrations of the cryostat would inevitably lead to misalignment between the PIC and the fiber array. Therefore, we table a $g^{(2)}$ measurement for future experiments with better waveguide-coupled devices, as will be addressed in Section 5.6, and packaged solution detailed in Ref. [52].

[11] This is more than three orders of magnitude higher than what was used for effective repumping in the 4 K experiments (Section 4.4) at 300 nW. The transmission efficiency from the 2x1 fiber splitter to the sample is measured to be 31% (due to fiber splicing imperfection). Even accounting for the larger spot size at 0.5 μm, the effective power incident on the device is at most reduced by a factor of ~ 2 (fraction of the focal spot covered by the diamond device), we still estimate repump power > 100 μW.

5.5 Theoretical spin-photon entanglement fidelity and efficiency

In this section, we analyze the theoretical photon-to-spin quantum state transfer, i.e. teleportation, fidelity $\mathcal{F}$ and success probability p_{succ} via spin-photon entanglement based on the obtained results. In particular, we consider the polarization-encoding protocol described in Sections 2.3 and 3.4.

5.5.1 System analysis

Cavity QED parameters

For estimating the fidelity, we need to assess the cavity QED parameters obtained in the optical linewidth and Purcell enhancement measurements shown in Section 4.4 and 4.6. Computing the cavity reflectivity specifically requires estimating how much pure dephasing (optical decoherence) γ^* is present and the emitter-cavity coupling strength g (see Section 2.1.3).

We make the following assumptions: (1) the SnV center (specifically "d1.0.77.4") investigated in the Purcell enhancement measurement experiences the same amount of pure dephasing as the one shown in Figure 4-11(c); (2) no additional pure dephasing is introduced with an applied magnetic field that is needed for Zeeman splitting; (3) the probed SnV center has Sn-120 nuclear isotope so no hyperfine states at zero field.

Given a lifetime of $\tau_{\text{off}} \sim 5.68$ ns at large detuning (off-resonance), the corresponding transform limit is $1/\tau_{\text{off}} \approx 2\pi \times 28$ MHz. With the measured optical linewidth of ~ 204 MHz, we then estimate pure dephasing $\gamma^* = 204\text{ MHz} - 28\text{ MHz} = 176$ MHz.

Estimating g requires knowing both the Purcell broadened linewidth Γ and the total cavity decay rate. Γ is first calculated to be

$$\Gamma = \frac{1}{\tau_{\text{on}}} - \frac{1}{\tau_{\text{off}}} \approx 2\pi \times 148\text{ MHz}. \tag{5.1}$$

With the fitted cavity Q of 2.3×10^3 centered at $\lambda_{\text{cav}} = 619.28$ nm, the corre-

sponding total cavity decay rate is $\kappa \approx 2\pi \times 213$ GHz. As a result, the emitter-cavity coupling strength [113] is

$$g = \sqrt{\frac{\Gamma\kappa}{4}} \approx 2\pi \times 2.8 \text{ GHz}. \tag{5.2}$$

Correspondingly, the cooperativity is approximated to be

$$C = \frac{4g^2}{\kappa\Gamma} \approx 0.73. \tag{5.3}$$

Component efficiencies

Next, to estimate the success probability, we extract the relevant efficiencies of all the relevant components. We break the system into three parts: (i) device including the diamond QMC and the SiN PIC, (ii) fiber setup, and (iii) free-space setup. For (i), we account for waveguide-cavity coupling ($\kappa_{\text{wg}}/\kappa \sim 5 \times 10^{-3}$ based on FDTD), transmission efficiency from diamond waveguide to the SiN waveguide in the uncladded socket (~ 0.91 based on FDTD), on-chip beam splitter (0.5), scattering loss at the oxide junction (3.3 dB [52]), propagation loss in the PIC (~ 0.99 using loss metric 0.2 dB/cm [51]), fiber edge-coupling efficiency (0.3, experimentally measured at 620 nm). The estimated efficiency is $\eta_{(i)} \approx 3.2 \times 10^{-4}$, largely dictated by the low waveguide-cavity coupling $\kappa_{\text{wg}}/\kappa$. For (ii), given the measured fiber transmission loss from inside the cryostat to the external setup (~ 0.61) and fiber insertion loss (conservative estimate of 0.5 dB per fiber-to-fiber connection), the estimated efficiency in the fiber setup is $\eta_{(ii)} \approx 0.48$. Lastly, for (iii), we account for mirror reflection (0.99 per mirror), collimator transmission (0.995), and transmission through the lens (0.99). The estimated efficiency for the free-space setup is $\eta_{(iii)} \approx 0.96$. Prior to detection, the overall collection efficiency is $\eta_{(i)} \cdot \eta_{(ii)} \cdot \eta_{(iii)} \approx 1.5 \times 10^{-4}$. Assuming a detection efficiency of 0.65 (PerkinsElmer), the overall detection efficiency is then 9.6×10^{-5}.

We verify our estimations using the measured count rate based on our PLE measurement shown in Figure 5-15(b). With a background count of ~ 100, the collected

PSB count rate is $\sim$ 250 cps. On the other hand, using the un-enhanced lifetime of 5.68 ns (see Section 4.6), the raw PSB count rate (accounting for quantum efficiency 0.8 and using Debye-Waller of 0.57) should be 7.3×10^7 cps. With the above estimate of overall collection efficiency, and accounting for the zero-field hyperfine states (a factor 4 reduction), the nominal count rate is then 1.7×10^3. The observed count rate is about 14% of the nominal count rate, whose discrepancy we attribute to underestimating the transmission loss on-chip (namely diamond waveguide-cavity coupling and the oxide junction) and sub-optimal fiber edge-coupling efficiency due to vibrations.

In the following sections, we treat $\kappa_{\mathrm{wg}}/\kappa$ as a variable degree of freedom and use an overall detection efficiency that abstracts out waveguide-cavity coupling: $\eta_{\mathrm{det}} = 1.9 \times 10^{-2}$. Furthermore, we take the product of device and fiber setup efficiencies without $\kappa_{\mathrm{wg}}/\kappa$ as the excitation efficiency, i.e. probability of the probe photon arriving at the diamond cavity without loss: $\eta_{\mathrm{exc}} = 3.4 \times 10^{-2}$. The success probability is then defined as $p_{\mathrm{succ}} = \eta_{\mathrm{det}}\eta_{\mathrm{exc}}|r|^2$, where r is the cavity reflection.

5.5.2 Optimization of atomic detuning and mirror amplitude

With the estimated values for g and γ^*, we first proceed with calculating the theoretical photon-to-spin teleportation fidelity based on the Duan-Kimble scheme [53]. Crucially, in our simulations, the probe frequency ω is set midpoint between the two atomic transitions $\{\omega_{\downarrow,\downarrow'}, \omega_{\uparrow,\downarrow'}\}$. This is to ensure their reflection amplitudes are equivalent and minimize reflection loss, where we assume all leakage channels besides reflecting back to the waveguide mode constitute scattering loss. For the protocol that uses polarization-encoded photonic qubits as described in Section 3.4, the teleportation fidelity largely depends on (1) the phase difference between the two spin states for the H-polarization path, whose reflection coefficients we denote as $r_\downarrow$ and $r_\uparrow$, and (2) the amplitude difference between $|r_\downarrow - r_m|$ and $|r_\uparrow + r_m|$ (see Section 3.2), where r_m is the bare mirror reflection in the V-polarization path. For (1), recall from Section 2.3, the ideal phase difference between $r_\downarrow(\omega)$ and $r_\uparrow(\omega)$ is π, which can be optimized over by changing the atomic detuning $\omega - \omega_{\downarrow(\uparrow),\downarrow'}$ via Zeeman splitting Δ_Z,

since experimentally we have control over the applied field strength. As for (2), we want to balance losses by matching $|r_\downarrow - r_m|$ and $|r_\uparrow + r_m|$ as closely as possible. In this case, we assume adjustability of the bare mirror reflection coefficient r_m via an on-chip Sagnac loop reflector and a MZI in the V path, as pointed out in Section 3.4[12].

5.5.3 Fidelity and success probability evaluations based on current parameters

For simplicity in the simulations, we assume we have a perfect on-chip polarization beam splitter with unity extinction ratio between H and V. Additionally, we fix g, γ^*, and κ based on the experimental values estimated in Section 5.5.1. We first compute the reflection coefficients at $\kappa_{\text{wg}}/\kappa = \{0.1, 0.3, 0.5, 0.7, 0.9\}$ to gain intuition about the spin-dependent amplitude and phase profiles. Starting with the undercoupling regime at $\kappa_{\text{wg}}/\kappa = 0.1$, Figure 5-16(a) shows reflectivity at $\omega = 0$ exceeding 0.5 yet with nearly zero phase difference, hence a correspondingly abysmal fidelity at the classical limit of $\mathcal{F} = 0.5$. As $\kappa_{\text{wg}}/\kappa$ increases to 0.3, the phase difference begins to grow at the cost of diminishing reflectivity, as indicated in Figure 5-16(b). At critical coupling (Figure 5-16(c)), reflectivity is essentially zero, corresponding to a vanishingly small success probability. On the other hand, the phase difference is constant across the cavity linewidth at π, leading to near unity fidelity. As $\kappa_{\text{wg}}/\kappa$ enters the overcoupling regime at 0.7 (Figure 5-16(d)), the cavity reflectivity begins to increase. Additionally, the phase profile of $r_{\downarrow,\uparrow}$ spans 2π, enabling an appropriate atomic detuning such that the phase difference at $\omega = 0$ can be exactly π. As a result, $|r_\downarrow - r_m|$ and $|r_\uparrow + r_m|$ can be perfectly satisfied and the fidelity can reach unity. However, as $\kappa_{\text{wg}}/\kappa$ increases further to 0.9 (Figure 5-16(e)), the change in phase becomes increasingly sharp, rendering a phase difference of π more difficult to obtain. Correspondingly, the fidelity begins to drop. This is ultimately limited by the *emitter's* optical linewidth, specifically pure dephasing of $\gamma^* \approx 2\pi \times 176$ MHz. In contrast, the higher reflectivity now contributes to a greater success probability.

[12]In the PEPSI case, the bare mirror was in the H path due to the design constraint imposed by the PDR.

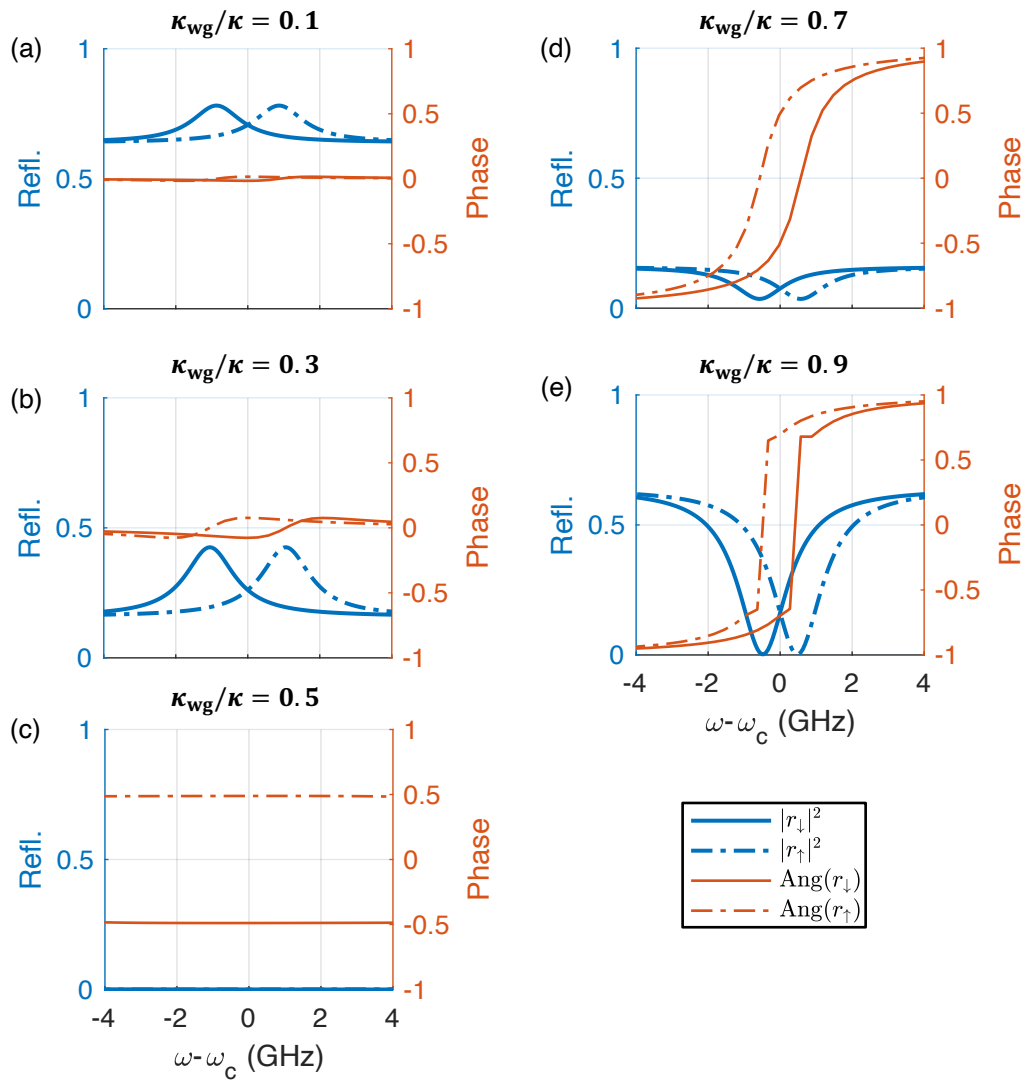

Figure 5-16: Spin-dependent cavity reflection coefficients evaluated at waveguide-cavity coupling $\kappa_{wg}/\kappa = \{0.1, 0.3, 0.5, 0.7, 0.9\}$. The reflectivities of the two spin states, $|r_\downarrow|^2$ (solid blue) and $|r_\uparrow|^2$ (dash-dotted blue), and their phase profiles, Ang($r_\downarrow$|) (solid orange) and Ang($r_\uparrow$) (dash-dotted orange) are shown in (a-e).

We find that a trade-off between $\mathcal{F}$ and success probability p_{succ} arises when pure dephasing is present. To illustrate this, we evaluate $\mathcal{F}$ and p_{succ} by sweeping both κ_{wg}/κ and γ^*, as shown in Fig. 5-17(a,b). For pure dephasing less than 0.5 MHz, $\mathcal{F}$ increases sharply close to critical coupling $\kappa_{wg}/\kappa = 0.5$. Intuitively, in the undercoupling regime $\kappa_{wg}/\kappa < 0.5$, the phase contrast between $r_\downarrow(\omega)$ and $r_\uparrow(\omega)$ is much less than π, hence limiting the spin-photon entanglement fidelity. As κ_{wg}/κ increases past $\kappa_{wg}/\kappa = 0.5$, $\mathcal{F}$ increases to unity and eventually rolls off with finite pure dephasing.

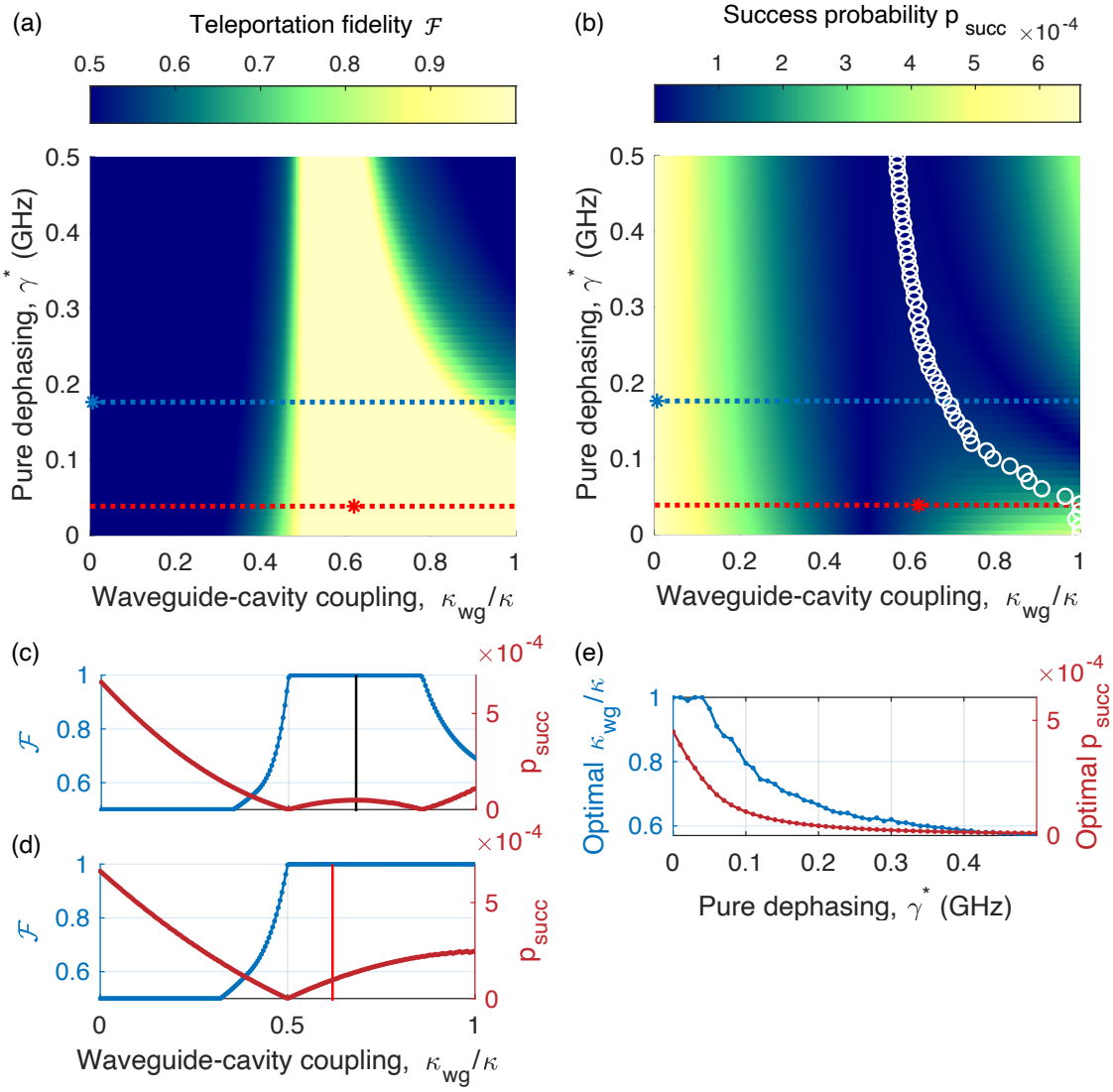

Figure 5-17: The photon-to-spin teleportation fidelity and success probability based on the Duan-Kimble scheme. The (a) teleportation fidelity $\mathcal{F}$ and success probability p_{succ} (b) are numerically computed as functions of both pure dephasing γ^* and waveguide-cavity coupling $\kappa_{\text{wg}}/\kappa$. The blue (red) dotted line indicates a 1D slice at $\gamma^* = 176$ MHz ($\gamma^* = 38$ MHz) based on the linewidth in the 4 K (1.3 K) experiment. The blue (red) star marker represents where the current (ideal) parameters stand, with $\kappa_{\text{wg}}/\kappa = 5 \times 10^{-3}$ based on FDTD ($\kappa_{\text{wg}}/\kappa = 0.62$ [6]) and $\gamma^* = 176$ MHz ($\gamma^* = 38$ MHz). The corresponding fidelity is unity and $p_{\text{succ}} \approx 10^{-4}$. (c) At $\gamma^* = 176$ MHz, $\mathcal{F}$ and p_{succ} exhibit a trade-off as $\kappa_{\text{wg}}/\kappa$ increases past $\kappa_{\text{wg}}/\kappa = 0.85$. The black vertical line shows where the optimal $\kappa_{\text{wg}}/\kappa$ is for maximizing both $\mathcal{F}$ and p_{succ}. (d) At $\gamma^* = 38$ MHz, both $\mathcal{F}$ and p_{succ} monotonically increase with increasing $\kappa_{\text{wg}}/\kappa$. The red vertical line indicates the current state of the art $\kappa_{\text{wg}}/\kappa = 0.62$ [6] where $p_{\text{succ}} \approx 10^{-4}$. (e) The optimal $\kappa_{\text{wg}}/\kappa$ values and corresponding p_{succ} selected for each γ^*, where $\mathcal{F}$ and p_{succ} are maximized.

At $\gamma^* = 176$ MHz (based on the 4 K PLE), Figure 5-17(c) illustrates a trade-off between $\mathcal{F}$ and p_{succ} after $\kappa_{\text{wg}}/\kappa = 0.85$. On the other hand, as shown in Fig. 5-17(d), with smaller dephasing at $\gamma^* = 38$ MHz on par with the transform-limit (based on the 1.3 K PLE), the trade-off vanishes, and both $\mathcal{F}$ and p_{succ} monotonically increase with increasing $\kappa_{\text{wg}}/\kappa$, suggesting high-fidelity cavity-based teleportation protocol [53] necessitates having optically coherent emitters.

We also calculate the optimal $\kappa_{\text{wg}}/\kappa$ values under the presence of pure dephasing by maximizing both $\mathcal{F}$ and p_{succ}. For example, as shown by the black solid line in Fig. 5-17(c), we find $\kappa_{\text{wg}}/\kappa = 0.68$ maintains $\mathcal{F} \approx 1$ with a local maximum of $p_{\text{succ}} \approx 5 \times 10^{-5}$. We plot the optimal $\kappa_{\text{wg}}/\kappa$ as a function of γ^* in Fig. 5-17(e) (also represented by the white circles in Fig. 5-17(b)). Expectedly, with decreasing pure dephasing, the preferred $\kappa_{\text{wg}}/\kappa$ increases with correspondingly higher p_{succ}. Our current waveguide-cavity coupling is estimated to be $\kappa_{\text{wg}}/\kappa = 5 \times 10^{-3}$, which leads to a fidelity at the classical limit $\mathcal{F} = 0.5$. However, using the state of the art $\kappa_{\text{wg}}/\kappa = 0.62$ demonstrated in Ref. [6] (red star marker in Fig. 5-17(a,b)), our calculation shows that the fidelity improves significantly to $\mathcal{F} \approx 1$ with $p_{\text{succ}} \approx 10^{-4}$.

5.6 Potential system improvements and alternative cavity designs

Here we consider improvements on several key components. First, the large scattering loss at the oxide junction can be reduced by employing inter-layer SiN waveguide coupling. Based on Ref. [114], the loss can be potentially minimized to 0.5 dB as opposed to the current 7 dB per junction. As opposed to using a fiber array with 630HP, a single lensed fiber can be used to maximize edge coupling efficiency to 91% based on simulations, as shown in Figure 5-7. Additionally, using a single photon detector with higher quantum efficiency, e.g. SNSPD, can boost the detection efficiency to 99% [66]. As a result, the overall detection efficiency without considering diamond waveguide-cavity coupling can be improved to 0.19, which is about an order of magni-

tude higher than what our current setup achieves. Lastly, Ref. [6] has shown diamond waveguide-cavity coupling in the overcoupling regime, with $\kappa_{\mathrm{wg}}/\kappa = 0.62$. With the aforementioned numbers, again assuming optimization of Δ_Z and r_m, the photon-to-spin teleportation fidelity and success probability can be improved to $\mathcal{F} \approx 1$ and $p_{\mathrm{succ}} \approx 1.6 \times 10^{-3}$. Hence, operating at a clock rate of 1 MHz, the emitter-cavity system can achieve a teleportation rate exceeding kHz.

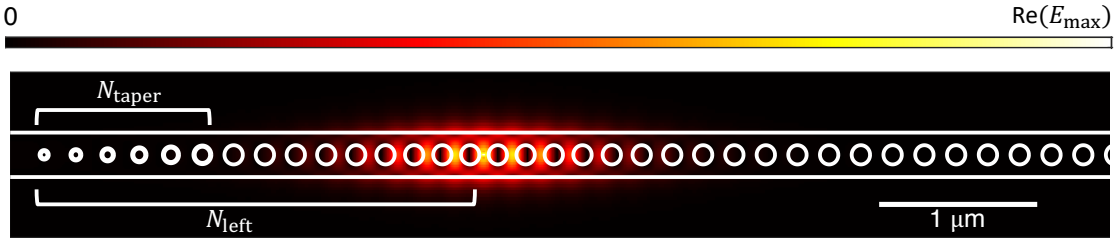

Figure 5-18: The electric field profile of an example single-sided cavity that is strongly coupled to the waveguide mode on the left. With $N_{\mathrm{taper}} = 6$ and $N_{\mathrm{left}} = 14$, the simulated waveguide-cavity coupling is $\kappa_{\mathrm{wg}}/\kappa = 0.918$ with an extrinsic quality factor of $Q_{\mathrm{ext}} \approx 2 \times 10^5$ at $\lambda_{\mathrm{SnV}} \sim 619.7$ nm.

As for improving $\kappa_{\mathrm{wg}}/\kappa$ to what has been demonstrated by Ref. [6] and beyond, we propose modifying the 1D PhC cavity design introduced in Section 4.1 by having (1) weaker mirror strength on the waveguide-coupled side in conjunction with (2) adiabatic tapering of the hole size. In FDTD simulation, we fix the smallest hole diameter to 50 nm limited by fabrication, and sweep both the number of holes defining the Bragg mirror N_{left} and the number of linearly tapered holes within N_{taper}. Figure 5-18 shows an example "single-sided" cavity in which the left side has a weaker Bragg mirror with $N_{\mathrm{left}} = 14$ holes and linear tapering over $N_{\mathrm{taper}} = 6$ holes. The right side is padded with 25 holes to ensure only the left side is strongly coupled to the waveguide mode, from which an incoming polarization-encoded photonic qubit is sent and reflected.

We perform a 2D sweep over both parameters, $\{N_{\mathrm{left}}, N_{\mathrm{taper}}\}$, and evaluate both the waveguide-cavity coupling $\kappa_{\mathrm{wg}}/\kappa$ and the extrinsic quality factor Q_{ext}. As illustrated in Figure 5-19, $\kappa_{\mathrm{wg}}/\kappa$ expectedly increases with weakening of the Bragg mirror via increasing N_{taper} and decreasing N_{left}. Correspondingly, Q_{ext} decreases as the cav-

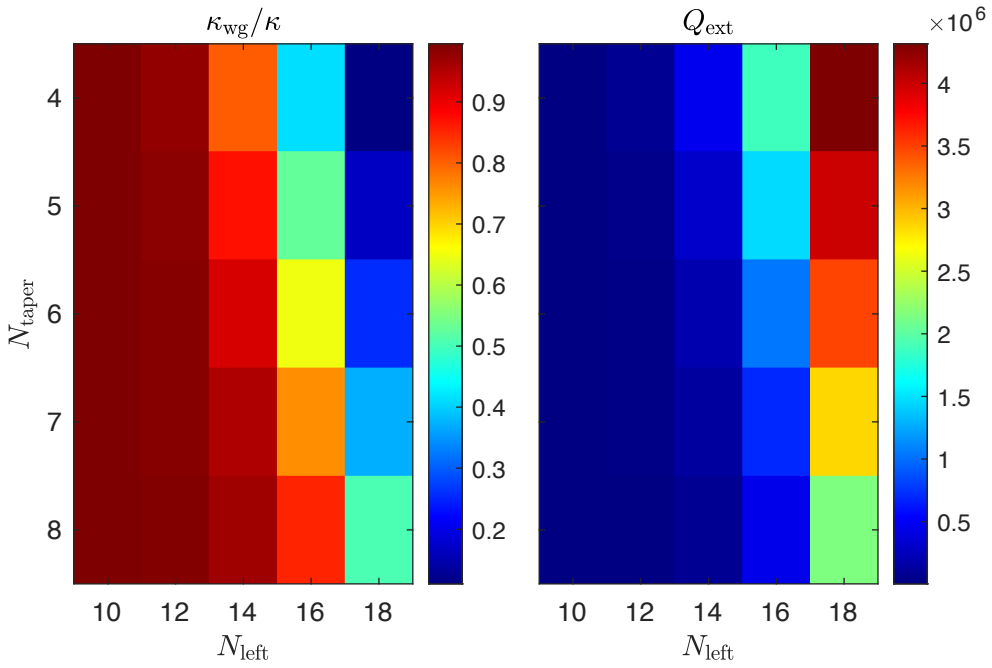

Figure 5-19: The waveguide-cavity coupling κ_{wg}/κ and the extrinsic quality factor Q_{ext} evaluated at $N_{left} = \{10, 12, 14, 16, 18\}$ and $N_{taper} = \{4, 5, 6, 7, 8\}$. With decreasing N_{left} and increasing N_{taper}, κ_{wg}/κ expectedly increases with Q_{ext} lowering, and vice versa.

ity mode becomes increasingly coupled to the waveguide mode that acts as a "leakage" channel. Since the teleportation fidelity crucially depends on the waveguide-cavity coupling and exhibits a sharp increase past the critical coupling regime ($\kappa_{wg}/\kappa = 0.5$), the single-sided cavity must have $N_{left} \leq 16$ with at least $N_{taper} \geq 5$. Considering the Q factor of the cavity is likely constrained by surface roughness (see Section 4.3), and that the state of the art diamond 1D PhC cavities have been limited to $Q \sim 2 \times 10^4$ [66], we impose an upper-bound to Q at 10^5. Based on Figure 5-19, FDTD simulations suggest $N_{left} = 14$ and $N_{taper} = 7$ may serve as a better design for photon-to-spin teleportation, with $\kappa_{wg}/\kappa \approx 0.95$ and $Q_{ext} \approx 10^5$ (in the limit of no pure dephasing). Further reduction in N_{left} and increase in N_{taper} would lead to greater κ_{wg}/κ at the cost of degraded Q_{ext}.

Lastly, further reducing the emitter's optical linewidth would require careful materials engineering. Low energy ion implantation to minimize lattice damage has shown to improve optical coherence [86]. Studies of high-pressure and high-temperature

(HPHT) treatment [35, 37] have also suggested potential improvements in narrowing the inhomogeneous distribution of defect centers in diamond. This could suggest HPHT healing the diamond lattice from implantation damage, and may potentially contribute to reduction of pure dephasing caused by vacancy defects nearby. Additionally, the linewidth obtained in Figure 5-15(b) is ~ 3 times lower than that from Figure 4-11(c), suggesting that the same thermal issue experienced by the QMC still attached to bulk diamond may cause optical decoherence. Finally, despite inversion symmetry, SnV centers placed near surface of diamond nanostructures may still be subjected to surface charge fluctuations. Therefore, modifying the cavity design to maximize the distance between the cavity center and sidewalls [115, 116], at the cost of increasing V, may help lower γ^*.

Chapter 6

A quantum random access memory based on spin-photon networks in PIC

The research outcomes of this chapter have been published as a journal article entitled "Scalable and High-Fidelity Quantum Random Access Memory in Spin-Photon Networks" *in* PRX Quantum **2**, 030319 (2021) [117].

In this chapter, we discuss a specific application of quantum networks in distributed quantum computing. We present a theoretical proposal for using the previously discussed platform of a PIC integrated with diamond color centers for constructing a *quantum random access memory* (qRAM) [117], which is considered an essential computing unit to enable polynomial speedups in quantum information processing. Proposed implementations thus far include using neutral atoms and superconducting circuits to construct a binary tree, but these systems still require demonstrations of the elementary components. In Section 6.2, we explain how a quantum PIC architecture integrated with solid-state memories can implement the two key qRAM operations, (1) quantum state transfer and (2) quantum routing, with already demonstrated components: electro-optic modulators, a Mach-Zehnder interferometer (MZI) network, and nanocavities coupled to artificial atoms for spin-based memory writing and retrieval. Our approaches furthermore benefit from built-in error-detection based on photon heralding. We present detailed theoretical analysis of the qRAM query fi-

delity and efficiency in Sections 6.2.3 and 6.2.4, showing that our proposal presents viable near-term designs for a general qRAM. Lastly, we propose an alternative form of building a qRAM using teleportation based on quantum networks in Section 6.3.

6.1 Introduction to qRAM

Random access memory (RAM) is a fundamental computing unit that allows on-demand storing and retrieving data. While a classical RAM addresses one memory cell in the database per operation, a quantum RAM permits querying a superposition of multiple memories [118]. Given a superposition of addresses j, the 'qRAM' returns a correlated set of data D_j, described by

$$|\psi\rangle_{\text{in}} = \sum_{j=1}^{N} \alpha_j |j\rangle_a |\emptyset\rangle_b \xrightarrow{\text{qRAM}} |\psi\rangle_{\text{out}} = \sum_{j=1}^{N} \alpha_j |j\rangle_a |D_j\rangle_b , \tag{6.1}$$

where N is the number of memory cells and the subscripts a and b denote the address and bus qubits, respectively. One efficient implementation of qRAM proposed by Giovannetti, Lloyd, and Maccone (GLM) [118, 119] is the 'bucket-brigade model': a binary tree of memory nodes that direct the bus qubit to the data layer. A tree of depth $n > 1$ contains a total of $2^n - 1$ nodes, with the last layer containing $N = 2^{n-1}$ memory cells. Each preceding layer i represents the register k_i of the address $|j\rangle = |k_1 k_2 ... k_{n-1} k_n\rangle$, which sets the path leading to the corresponding memory cell D_j (Figure 6-1(a)).

Principally, these memory nodes must (1) store an address register qubit that (2) routes ensuing qubits for addressing and retrieval. The register $|k_i\rangle$ sets layer i's internal state that governs routing of the subsequent registers $\{|k_{i+1}\rangle, |k_{i+2}\rangle, ...\}$. A qRAM query thus performs a sequence of alternating state transfer and routing operations, with each register qubit determining how the node routes the subsequent register. Once the binary tree has been programmed by the state of address qubits, $\sum_j \alpha_j |j\rangle_a$, it is traversed by the bus photon $|\downarrow\rangle_b$ to access the memory cells $\{D_j\}$ in superposition. The bus qubit travels back up the tree and addresses are mapped onto

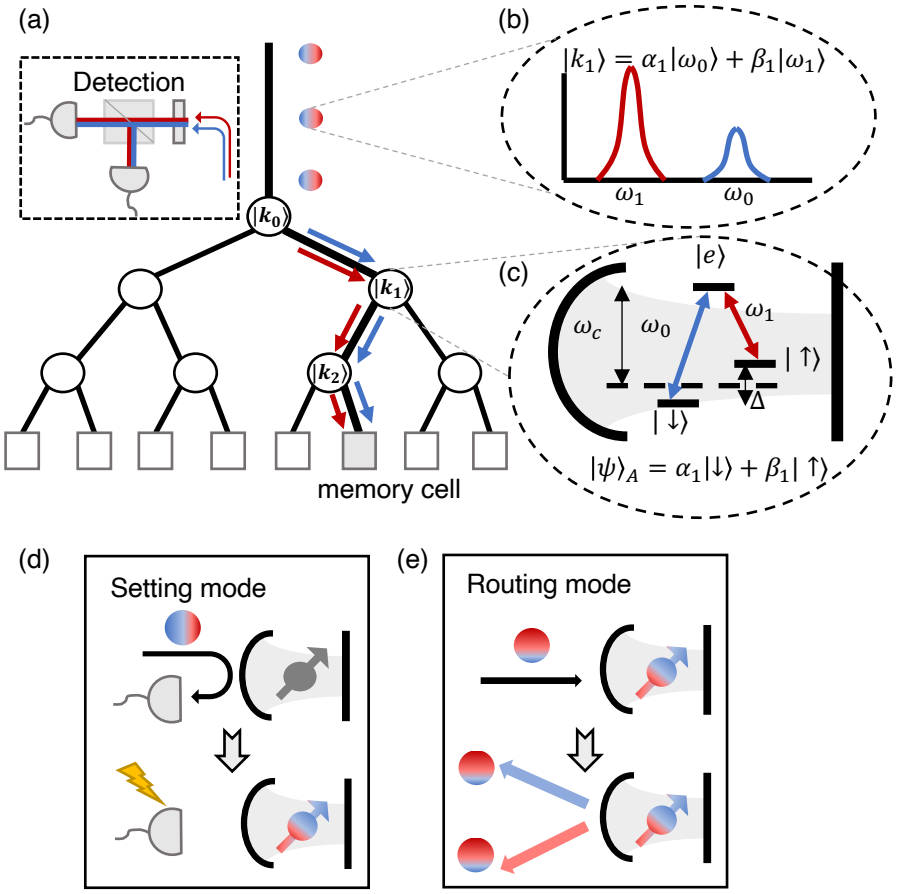

Figure 6-1: An illustrative bucket-brigade model with a cavity-coupled Λ-level atom at each tree node. (a) The address $|j\rangle$ consisting the register qubits $|k_0\rangle\,|k_1\rangle\,|k_2\rangle$ arrives at the 3-level binary tree containing $N = 2^3$ memory cells. (b) Each register is a frequency-encoded photonic qubit in the $\{\omega_0, \omega_1\}$ basis. (c) For our implementation, each tree node is a Λ-atom coupled to a single-sided nanocavity whose resonant frequency ω_c is tuned to the average of the two atomic transition frequencies, ω_0 and ω_1, which are separated by a Zeeman splitting Δ. For layer 1, the register $|k_1\rangle$ sets the node's internal state to $|\psi_A\rangle = \alpha_1\,|\downarrow\rangle + \beta_1\,|\uparrow\rangle$ that routes the successive register $|k_2\rangle$. Two essential operations are (d) the setting mode via cavity reflection and (e) the routing mode.

the returning register qubits to disentangle themselves from the nodes, producing the qRAM output state $|\psi\rangle_{\text{out}}$. The ability to perform this operation in $\log(N)$ time steps highlights the advantage of quantum parallelism and offers polynomial speedups in quantum algorithms for applications such as quantum machine learning [120], matrix inversion [121], quantum imaging [122], and quantum searching [123].

Despite its mathematical elegance, no qRAM proposals have been experimentally

demonstrated. The existing proposals are based on neutral atoms [119, 124, 125] and superconducting circuits [126], but still require elementary components to be realized. Here, we introduce a scheme that assembles separately demonstrated technologies into a PIC architecture integrated with artificial atoms. Namely, the system contains a high-fidelity frequency beam splitter [127, 128, 129], nanocavities strongly coupled to long-lived spin memories [107, 66], and a scalable nanophotonic Mach-Zehnder interferometer (MZI) array [130]. Importantly, the protocol relies on a cavity-assisted controlled-phase (CZ) gate [53] whose heralding inherently provides the ability to detect qubit loss. The protocol's framework applies to quantum networks that require no additional modifications.

6.2 Bucket-Brigade Scheme in a quantum PIC

In our PIC implementation, the address register and the bus qubits are frequency-encoded photons $|\psi_P\rangle = \alpha\,|\omega_0\rangle + \beta\,|\omega_1\rangle$ shown in Figure 6-1(b) prepared by electro-optic modulators, which together act as a frequency beam splitter [127, 128, 129]. They arrive at each node in the binary tree and interact with a cavity-coupled atom, which has two spin states $|\downarrow\rangle$ and $|\uparrow\rangle$. Both states are coupled to an excited state $|e\rangle$ with respective transition frequencies ω_0 and ω_1 shown in Figure 6-1(c). In this proposal, we specifically consider diamond's negatively charged silicon-vacancy (SiV^-) center strongly coupled to a single-sided cavity [107, 66]. By having the cavity resonance ω_c equally detuned from the two transitions, i.e. $\omega_{0,1} = \omega_c \pm \Delta/2$ where Δ is the Zeeman splitting between the spin states, the resulting Fano interference satisfies the following conditions: upon a cavity reflection, the photon acquires no phase shift when it is resonant with the atomic transition; otherwise, it receives a π phase shift.

Specifically, by appropriately choosing the atomic and cavity detuning, the resultant Fano interference can satisfy the following truth table, whose entry represents the probe's acquired phase from reflecting off the nanocavity:

This can be satisfied by demanding the reflection to be $+1$ when the spin state is

	$\|\downarrow\rangle$	$\|\uparrow\rangle$
$\|\omega_0\rangle$	0	π
$\|\omega_1\rangle$	π	0

Table 6.1: Table showing the acquired phase by the probe photon depending on its frequency and the spin qubit's state.

on-resonance and -1 when it is off-resonance. Using Equation 2.17, we arrive at

$$\mathrm{Re}\left\{\frac{\kappa_{\mathrm{wg}}\left(i\Delta_a+\frac{\gamma}{2}\right)}{\left(i\Delta_c+\frac{\kappa}{2}\right)\left(i\Delta_a+\frac{\gamma}{2}\right)+g^2}\right\}=2. \tag{6.2}$$

We center the cavity resonance between the two transition frequencies: $\omega_c = (\omega_0+\omega_1)/2$. Therefore, given the Zeeman splitting Δ, the cavity detuning would be half of the spin driving frequency: $\Delta_c = \frac{\Delta}{2}$. Similarly, the atomic detuning would exactly equal the splitting: $\Delta_a = \Delta$. In the Purcell regime, Eq. 6.2 leads to

$$\Delta \approx \sqrt{2g^2+\frac{\kappa}{4}\left(\kappa-\kappa_{\mathrm{wg}}\right)-\frac{\gamma^2}{4}}. \tag{6.3}$$

Therefore, given a fixed set of atom-cavity parameters $\{g,\gamma,\kappa,\kappa_{\mathrm{wg}}\}$, we may set the corresponding magnetic field B_{opt} that satisfies the appropriate Zeeman splitting $\Delta \sim \mu g B_{\mathrm{opt}}/\hbar$ where $\mu = q\hbar/2m_e$ is the Bohr magneton and g$\approx$ 2 is the Lande g-factor.

As an illustrative example, we plot the reflection r of a perfectly over-coupled cavity ($\kappa_{\mathrm{wg}}/\kappa = 1$) against the probe frequency ω/κ. Figure 6-2(a) shows $r = +1$ at the probe frequency $\omega = \omega_c + \Delta/2$ whereas $r = -1$ at $\omega = \omega_c - \Delta/2$ when the spin population resides in state $|\downarrow\rangle$, and vice versa as shown in Figure 6-2(b).

6.2.1 Implementations of setting and routing

This spin-dependent phase shift enables the two operation modes necessitated by the bucket-brigade model: the photonic qubit "setting" the spin state (Figure 6-1(d)) and the spin qubit routing the subsequent register qubits (Figure 6-1(e)). The cavity interaction enables a CZ gate for heralding a quantum state transfer between

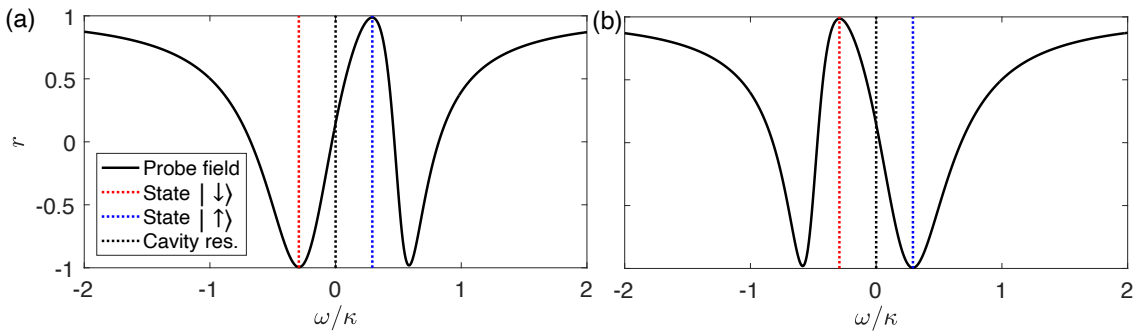

Figure 6-2: Cavity reflection as a function of probe frequency. The normalized probe frequency ω/κ is centered at the cavity resonance (black dashed line) ω_c. The magnetic field is appropriately chosen such that the two atomic transition frequencies ω_0 and ω_1 coincide with the cavity reflection maximum $r = +1$ and minimum $r = -1$. The reflection when (a) the spin is in the $|\downarrow\rangle$ state is the mirror of when (b) the spin is in the $|\uparrow\rangle$ state.

the photonic and the spin qubits, as shown in Figure 6-3(a). The very same phase dependence on the atomic state also allows quantum routing by leveraging the cavity system as an interferometer.

Explicitly in the PIC platform, each node comprises an MZI, an add-drop filter resonant with the ω_0 component, and a single-sided nanocavity coupled to an SiV^- center. First, in the setting mode, the atom is initialized in a superposition state $|\psi_A\rangle = (|\downarrow\rangle + |\uparrow\rangle)/\sqrt{2}$ by a Hadamard operation. Figure 6-3(b) shows the register qubit $|\psi_P\rangle = \alpha\,|\omega_0\rangle + \beta\,|\omega_1\rangle$ arriving at the MZI and exiting out of the top output port. An add-drop filter then directs the ω_0 component to a mirror (e.g. Sagnac loop reflector) such that $|\omega_0\rangle$ acquires a π phase shift upon reflection regardless of the spin state. On the other hand, the ω_1 component continues down the path and reflects off the atom-cavity system, acquiring a spin-dependent phase shift. Finally, the ω_0 and ω_1 components recombine and undergo a Hadamard transformation by a frequency beam splitter before heralding the completion of quantum state transfer. While heralding conveniently provides detection of photon loss error, it is essential for the detection system to be shared by all the qRAM layers at the root of the tree. A local detection would otherwise reveal the path information and thereby collapse the superposition of addresses. Therefore, all the register qubits must reflect off the

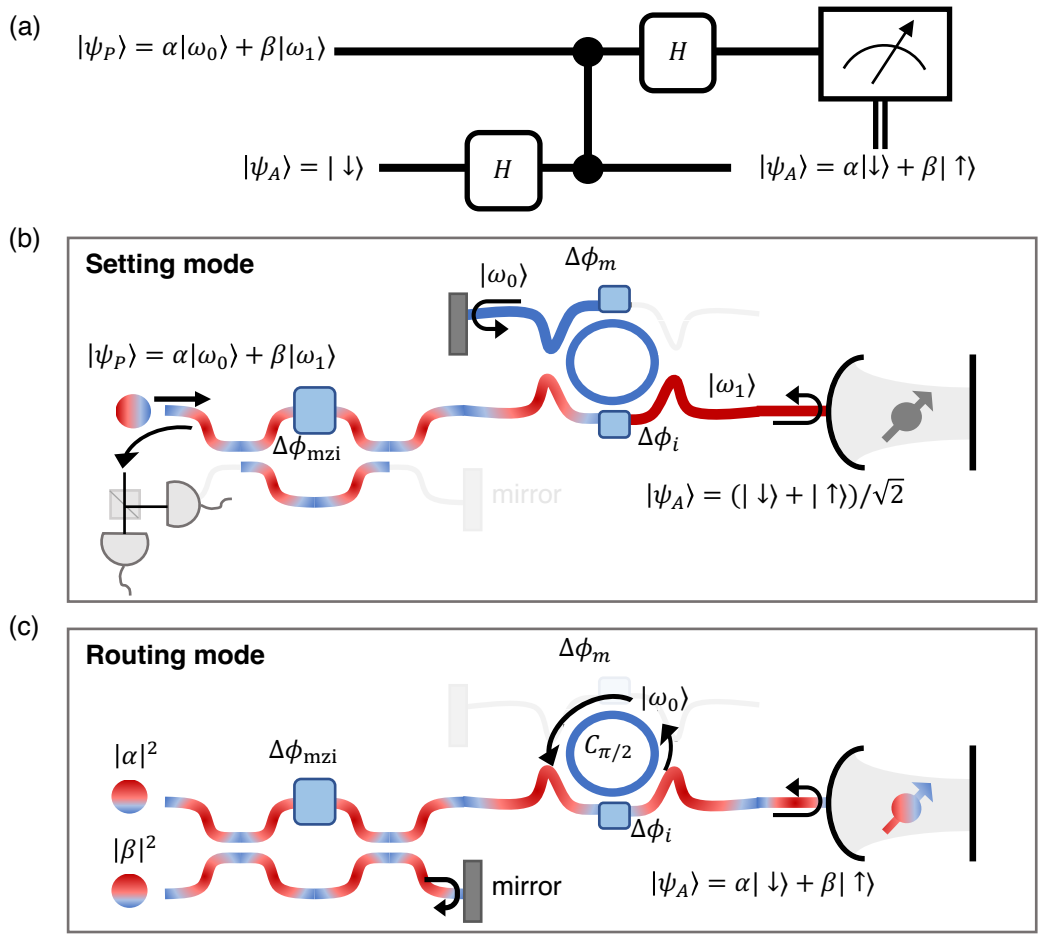

Figure 6-3: PIC implementation of qRAM. (a) The circuit representation of a quantum state transfer operation that maps the register qubit $|\psi_P\rangle$ onto the atomic qubit $|\psi_A\rangle$. (b) In the setting mode, the photon undergoes a CZ operation to complete quantum state transfer. After passing through the MZI, the $|\omega_0\rangle$ component resonantly couples to the add-drop filter that imparts a π phase shift upon reflection off the mirror, while the $|\omega_1\rangle$ component interacts with the atom-cavity system and acquires a spin-dependent phase shift. (c) In the routing mode, the MZI is set to a 50:50 beam splitter, and the top waveguide of the add-drop filter is decoupled such that the ring resonator imparts a $\pi/2$ phase shift to the $|\omega_0\rangle$ component upon a single pass. After cavity reflection, the returning photon re-interferes with itself and is routed to either the $|\downarrow\rangle$ path with probability $|\alpha|^2$ or the $|\uparrow\rangle$ path with probability $|\beta|^2$.

qRAM nodes and *return to the root* to preserve entanglement between the spin qubits and the address paths. This path erasure also ensures the same conditional Z gate applies to all the active nodes in layer i during the setting operation.

After the photon detection, the MZI is switched to a 50:50 beam splitter and the tunable add-drop filter is turned "off" such that the ring resonator only imparts a

$\pi/2$ phase shift to the ω_0 component upon a single pass (see Section 6.2.2). Hence, the photon acquires a spin-dependent phase shift *independent* of the frequency component. Illustrated in Figure 6-3(c), the subsequent register qubit $|k_1\rangle$ arrives at the 50:50 beam splitter. One of the MZI output ports connects to the same path as before, while the other leads to a mirror. As a result, the photon taking the former route acquires a spin-dependent phase shift from interacting with the cavity while one taking the latter route always acquires a π phase from reflecting off the mirror. The returning photon then interferes with itself at the beam splitter and is routed to an exit port depending on the spin state. With $|\alpha|^2$ probability, the photon exits out of the top path corresponding to the $|\downarrow\rangle$ spin state; and with $|\beta|^2$ probability, it travels down the bottom path corresponding to the $|\uparrow\rangle$ spin state. Effectively, the beam splitter in conjunction with the atom-cavity system constitute an MZI with the spin-cavity system acting as a phase shifter.

Both the setting and routing operations are repeated alternatingly, carving out the path for the bus qubit to arrive at the desired memory cells. The data can be transferred onto the bus qubit with the same cavity reflection scheme by reversing the role of the photonic and the spin qubits, followed by a projective measurement on the atom via single-shot readouts [33]. Finally, the sequence is run backwards to disentangle the binary tree from the address qubits, leaving the data qubits $|D_j\rangle$ correlated with their respective addresses $|j\rangle$.

6.2.2 Frequency-dependent add-drop filter

To perform both the (1) setting and (2) routing operations, the add-drop filter must resonantly couple to only the ω_0 component to impart (1) a π phase shift upon reflection off a mirror and (2) a $\pi/2$ phase shift through a single pass after decoupling the resonator from the mirror waveguide. The system can be modeled by tracking the evolution of the field propagating through the MZI (or interferometric) couplers [131].

As illustrated in Figure 6-4(a), the outputs of the MZI couplers are

$$\begin{bmatrix} s_{\text{out}} \\ s_{ci-} \end{bmatrix} = \mathcal{T}^{(i)} \begin{bmatrix} s_{\text{in}} \\ s_{ci+} \end{bmatrix}, \quad \begin{bmatrix} s_{m+} \\ s_{cm+} \end{bmatrix} = \mathcal{T}^{(m)} \begin{bmatrix} s_{m-} \\ s_{cm-} \end{bmatrix}, \tag{6.4}$$

where $\mathcal{T}^{(n)} = C^{(n)} Z^{(n)} C^{(n)}$ for $n = \{m, i\}$. The matrices $C^{(n)}$ and $Z^{(n)}$ are transfer matrices that describe the beam splitter and the interferometer arms in the forms

$$C^{(n)} = \begin{bmatrix} \nu_n & i\sqrt{1-\nu_n^2} \\ i\sqrt{1-\nu_n^2} & \nu_n \end{bmatrix}, \quad Z^{(n)} = \begin{bmatrix} e^{i\Psi_{nT}} & 0 \\ 0 & e^{i\Psi_{nB}} \end{bmatrix}, \tag{6.5}$$

where ν_n represents the coupling to the through-waveguide, Ψ_{nT} and Ψ_{nB} are the phases accumulated in the phase shifter and the resonator arms, respectively. For the remainder of the section, we assume a balanced interferometric coupler such that $\nu_n = 1/\sqrt{2}$.

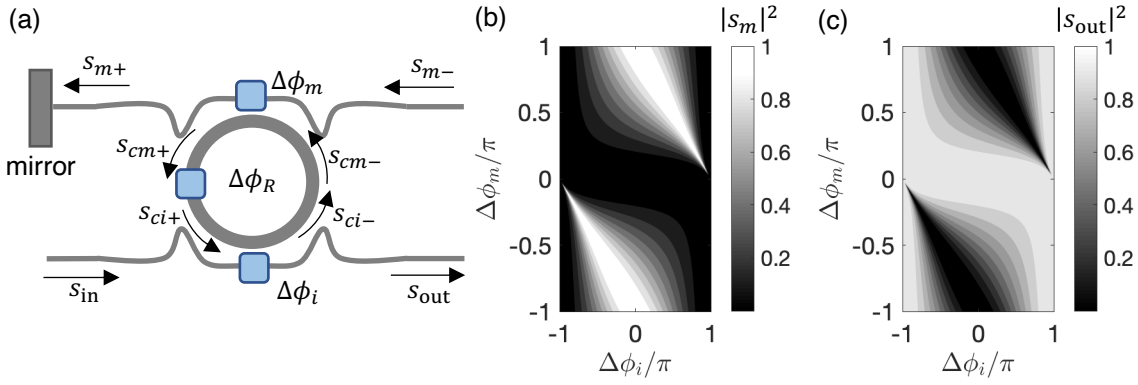

Figure 6-4: Add-drop filter schematic. (a) Each of the propagating fields in the add-drop filter is labeled for deriving the transfer matrices. The ring resonator (whose resonance can be tuned by $\Delta\phi_R$) is coupled to the waveguides via balanced MZI, or interferometric, couplers, each containing a phase shifter $\Delta\phi_{i,m}$. When the top waveguide is coupled to the resonator, the ω_0 component is routed to reflect off a Sagnac loop reflector (mirror). (b) The output intensity towards the mirror $|s_m|^2$ as a function of $\Delta\phi_i$ and $\Delta\phi_m$. (c) The output intensity of the through-component $|s_{\text{out}}|^2$.

Explicitly, we can write the MZI transfer matrix as

$$\mathcal{T} = e^{i\Psi_{nR}} \begin{bmatrix} (1+e^{i\phi_n})\nu_n^2 - 1 & i(1+e^{i\phi_n})\nu_n\sqrt{1-\nu_n^2} \\ i(1+e^{i\phi_n})\nu_n\sqrt{1-\nu_n^2} & \nu_n^2 - e^{i\phi_n}(1-\nu_n^2) \end{bmatrix} \quad \forall n \in \{m, i\}, \tag{6.6}$$

where $\phi_n(\omega) = k(\omega)\Delta L_n + \Delta\phi_n$ and $k(\omega) = (n_{\text{eff}}/c)\omega_0 + (n_{g,\text{PIC}}/c)(\omega - \omega_0)$. Here, ΔL_n is the path length difference between the two arms and $k(\omega)$ is the propagation constant governed by the effective and group indices in the PIC, n_{eff} and $n_{g,\text{PIC}}$, respectively.

For the interest of our operations, we can set $s_{\text{in}} = 1$ and $s_{m-} = 0$. The resultant system of equations consists

$$s_{\text{out}} = T_{1,1}^{(i)} s_{\text{in}} + T_{1,2}^{(i)} s_{ci+} \tag{6.7}$$

$$s_{ci-} = T_{2,1}^{(i)} s_{\text{in}} + T_{2,2}^{(i)} s_{ci+}. \tag{6.8}$$

From which, after solving for s_{out} and $s_{m+} = T_{1,2}^{(m)} s_{cm-}$, we get

$$s_{\text{out}} = e^{i\Psi_{iR}} \left(T_{1,1}^{\prime(i)} + \frac{e^{i\phi_c}\zeta_m T_{1,2}^{\prime(i)} T_{2,1}^{\prime(i)}}{1 - e^{i\phi_c}\zeta_i\zeta_m} \right) \tag{6.9}$$

$$s_{m+} = \frac{e^{i\phi_{im}} T_{1,2}^{(m)} T_{2,1}^{(i)}}{1 - e^{i\phi_c}\zeta_i\zeta_m}, \tag{6.10}$$

where $\phi_c(\omega) = \psi_{iR} + \phi_{im} + \psi_{mR} + \phi_{mi} = k(\omega)L_c$ is the phase acquired in the resonator, and $\zeta_n = \nu_n^2 - e^{i\phi_n}(1-\nu_n^2)$. For the routing operation, we wish to have $s_m = s_{m+} = 1$ (correspondingly $s_{\text{out}} = 0$) such that the ω_0 component is entirely directed to the mirror. In Figure 6-4(b,c), we plot the output intensity $|s_m|^2$ and $|s_{\text{out}}|^2$ as a function of $\Delta\phi_i$ and $\Delta\phi_m$ set by the phase shifters in the MZI couplers. In order to maximize $|s_m|^2$, we find that the phases must satisfy the condition: $\Delta\phi_i + \Delta\phi_m = \pi$.

It is equally essential for the resonator to have a sufficiently high quality factor (Q) such that the linewidth is narrow enough to only couple to the ω_0 instead of both frequencies. For the simulations presented in the main text, the Zeeman splitting is assumed to be $\sim$ 12 GHz, which implies that the Q must be $> 10^4$ to resolve

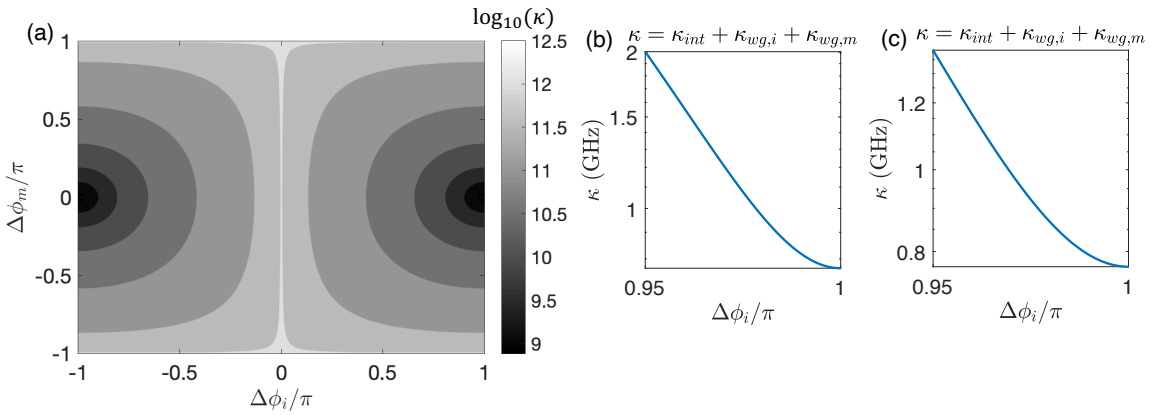

Figure 6-5: Decay rate of the ring resonator. (a) The resonator's total decay rate (linewidth) is plotted as a function of $\Delta\phi_i$ and $\Delta\phi_m$ on a log scale. κ reaches its minimum near $\Delta\phi_i = \pm\pi$ and $\Delta\phi_m = 0$ at which the resonator is decoupled from the waveguides. κ (GHz) is plotted against $\Delta\phi_i$ for (b) the setting mode and (c) the routing mode.

between ω_0 and ω_1. In Figure 6-5(a), we find that κ is smallest at $\Delta\phi_i = \pm\pi$, which corresponds to the resonator completely decoupled from the input waveguide (source) and cavity leakage is maximally suppressed. Similarly, when $\Delta\phi_m = 0$, the ring (source) is completely decoupled from the mirror waveguide. As long as $\Delta\phi_i$ is sufficiently close to π, Figure 6-5(b) indicates that the resonator linewidth is sufficiently smaller than the Zeeman splitting of $\sim$ 12 GHz. For example, at $\Delta\phi_i = 0.95\pi$ such that $\Delta\phi_m = 0.05\pi$, $|s_m|^2$ is approximately unity and hence satisfies the setting mode. In the routing mode, we only need to minimally shift $\Delta\phi_m$ to 0 such that $|s_{\text{out}}|^2 = 1$ and $|s_m|^2 = 0$, as indicated by the drastically varying region near $\Delta\phi_i = \pi$ and $\Delta\phi_m = 0$, as shown in Figure 6-4(b,c). With $\Delta\phi_m = 0$ fixed, we validate that the narrowness of the resonator linewidth as illustrated by Figure 6-5(c). κ is expectedly smaller in the routing mode than the setting mode since the resonator is decoupled from the mirror waveguide, thereby having one fewer leakage channel.

Lastly, we can appropriately choose $\Delta\phi_R$, which is the phase shifter within the resonator, such that traversing through the resonator imparts a $\pi/2$ phase to the ω_0 component upon a single pass. In a round-trip, $|\omega_0\rangle$ effectively undergoes a Pauli X gate, rendering the truth table shown in Table 6.2.

	$\|\downarrow\rangle$	$\|\uparrow\rangle$	$\xrightarrow[X \text{ on } \omega_0]{}$		$\|\downarrow\rangle$	$\|\uparrow\rangle$
$\|\omega_0\rangle$	0	π		$\|\omega_0\rangle$	π	0
$\|\omega_1\rangle$	π	0		$\|\omega_1\rangle$	π	0

Table 6.2: Modifying the probe frequency's acquired phase by a Pauli X gate.

6.2.3 Setting fidelity per node

In our cavity-assisted scheme, qubit loss is a heralded error. Therefore, a sequence of successful photon detection guarantees the absence of infidelity stemming from photon loss in the qRAM output. Here, we analyze imperfections in the atom-cavity system that critically affects quantum state transfer as the primary sources of infidelity in our protocol, since any inexact mapping from the register qubit to the spin qubit would result in faulty routing of the subsequent registers. To characterize the setting fidelity given an input register $|\psi\rangle_P = \alpha\,|\omega_0\rangle + \beta\,|\omega_1\rangle$, we calculate the resultant spin state $|\psi\rangle_A$ after heralding via a Schrodinger picture evolution to be

$$|\psi\rangle_A = (2\alpha r_m \pm \beta(r_{\text{on}} + r_{\text{off}}))\,|\downarrow\rangle \pm \beta(-r_{\text{on}} + r_{\text{off}})\,|\uparrow\rangle\,, \tag{6.11}$$

where r_{on} (r_{off}) is the on-resonance (off-resonance) cavity reflection and r_m is the mirror reflection. Note that β is positive (negative) if the photon is detected in the ω_0 (ω_1) port. (see Section D.1).

After a controlled-Z gate (see Section D.1), the overlap between the heralded spin state $|\psi_{s,f}(i)\rangle$ and the target state $|\psi\rangle_A = \alpha\,|\downarrow\rangle + \beta\,|\uparrow\rangle$ defines the state transfer fidelity $\mathcal{F}$, of which we take the average over six representative states $|\phi_i\rangle$ (axes of a Bloch sphere) [21, 132]

$$\mathcal{F} = \frac{1}{6}\sum_i \mathcal{F}_i = \frac{1}{6}\sum_i |\langle\phi_i|\psi_{s,f}(i)\rangle|^2\,, \tag{6.12}$$

where $|\phi_1\rangle = |\downarrow\rangle\,, |\phi_2\rangle = |\uparrow\rangle\,, |\phi_{3,4}\rangle = (|\downarrow\rangle \pm |\uparrow\rangle)/\sqrt{2}, |\phi_{5,6}\rangle = (|\downarrow\rangle \pm i\,|\uparrow\rangle)/\sqrt{2}$ in the $\{|\downarrow\rangle\,, |\uparrow\rangle\}$ basis.

Due to the sub-ns travel times of photonic qubits and conditional gate time on the atoms (∼30 ns based on Ref. [66]) being short relative to the SiV^- spin coherence

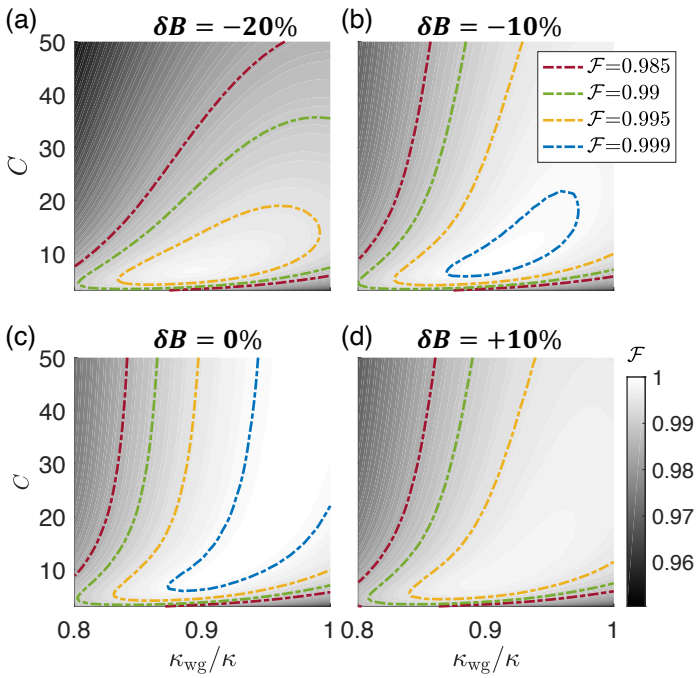

Figure 6-6: Quantum state transfer fidelities. The transferred state fidelity for a single setting operation is plotted against the atom-cavity cooperativity C and the waveguide-cavity coupling strength κ_{wg}/κ for magnetic field deviations (a) $\delta B = -20\%$, (b) -10%, (c) 0%, and (d) 10%. The contour lines denote the fidelity thresholds at $\mathcal{F} = 0.985, 0.99, 0.995, 0.999$.

time $T_2 > 10$ ms [33], we will neglect errors caused by spin decoherence. Instead, the setting mode's performance relies on the cavity's coupling strength to the output waveguide mode. When the waveguide-cavity coupling is unity, i.e. $\kappa_{wg}/\kappa = 1$, the cavity reflection solely determines the transfer fidelity that scales as $(C-1)/(C+1)$ in the large cooperativity limit [133, 68]. However, for any reduced $\kappa_{wg}/\kappa < 1$, the need to balance losses becomes especially important. For example, for a desired state $|\phi_3\rangle$ where $\alpha = \beta = 1/\sqrt{2}$, balancing losses entails matching the moduli of the on- and off-resonance cavity reflections $r_{on} \propto \kappa_{wg}(C-1)/(C+1)$ and $r_{off} \propto \kappa_{wg}/\kappa$ (see Section D.1).

In Figure 6-6, we analyze $\mathcal{F}$ as a function of κ_{wg}/κ, C, and δB, which is the deviation from the optimal magnetic field $B_{opt} \propto \sqrt{\gamma\kappa\left(2C + \kappa\left(\kappa - \kappa_{wg}\right)/4 - \gamma^2/4\right)}$ for the suitable Fano line-shape. For each point in the fidelity contour, a particular value of r_m is chosen to optimize the fidelity assuming the mirror is tunable. When

$\delta B = -20\%$, Figure 6-6(a) indicates that only a selective range of $C \lessapprox 20$ and $\kappa_{\text{wg}}/\kappa \in \{0.83, 0.98\}$ result in $\mathcal{F} > 0.995$. However, as the magnetic field deviation reduces to -10% from the optimum, the transferred state fidelity can exceed 0.999 for a selected range of C and $\kappa_{\text{wg}}/\kappa$. Figure 6-6(c) shows that at the optimal magnetic field, i.e. $\delta B = 0\%$, the transfer fidelity well exceeds 0.999 for any $C > 20$ and $\kappa_{\text{wg}}/\kappa > 0.94$. Interestingly, a small region of cooperativities $C < 20$ and $\kappa_{\text{wg}}/\kappa < 0.94$ can still achieve $\mathcal{F} > 0.999$ by carefully balancing losses. However, the tolerance to a varying C diminishes as $\kappa_{\text{wg}}/\kappa$ decreases. As δB approaches 10%, however, the setting fidelity can no longer reach 0.999. Its disparity with $\delta B = -10\%$ stems from the asymmetry exhibited by Fano interference.

The fidelity considered here is the state transfer fidelity *per node*, which consequently determines the node's routing fidelity.. If we consider the probability of routing erroneously to be $\epsilon = 1 - \mathcal{F}$ per node, then the query infidelity $1 - \mathcal{F}_{\text{query}}$ scales polylogarithmically with the memory size: $1 - \mathcal{F}_{\text{query}} \sim \epsilon \log(N_{\text{memories}})^3$ [134]. Hence, the qRAM query can be performed with high fidelity as long as $\epsilon \ll 1/\log(N_{\text{memories}})^3$. We estimate that our qRAM architecture with state transfer infidelity $\epsilon = 10^{-4}$ per node permits querying up to $N_{\text{memories}} \sim 10^4$.

6.2.4 Efficiency

Next, we analyze the qRAM query efficiency by first calculating the success probability of heralding each register qubit $|k_i\rangle$ and then the average rate of completing a single query call. Recall that for the bus qubit to reach the memory layer in an n-level qRAM, each register photon $|k_i\rangle$ must travel to the node in layer $i \in \{1, ..., n\}$ and return to the detector after cavity reflection. Given a propagation loss η_p, the probability of completing the round-trip without loss is $e^{-\eta_p L(i)}$, where $L(i)$ is twice the distance between the layer i and the root node. However, since the photon can scatter off the single-sided cavity and the mirror into non-waveguide modes, interaction at each layer further reduces the probability of detecting the returning register qubit by R_{cav} and R_m, which represent the cavity and mirror reflection coefficients, respectively. We take their mean reflection coefficient and define the setting efficiency

as $\eta_s = \eta_{\text{det}}(R_m + R_{\text{cav}})/2$, where η_{det} is the detection efficiency. Similarly, the routing efficiency for each layer i would be $\eta_r = R_{\text{cav}}$ assuming lossless transmission through the interferometric coupler. As a result, the probability of successfully heralding each register $|k_i\rangle$ is

$$p_i = e^{-\eta_p L(i)} \eta_r^{i-1} \eta_s \quad \text{for } i \in \{1, ..., n\}. \tag{6.13}$$

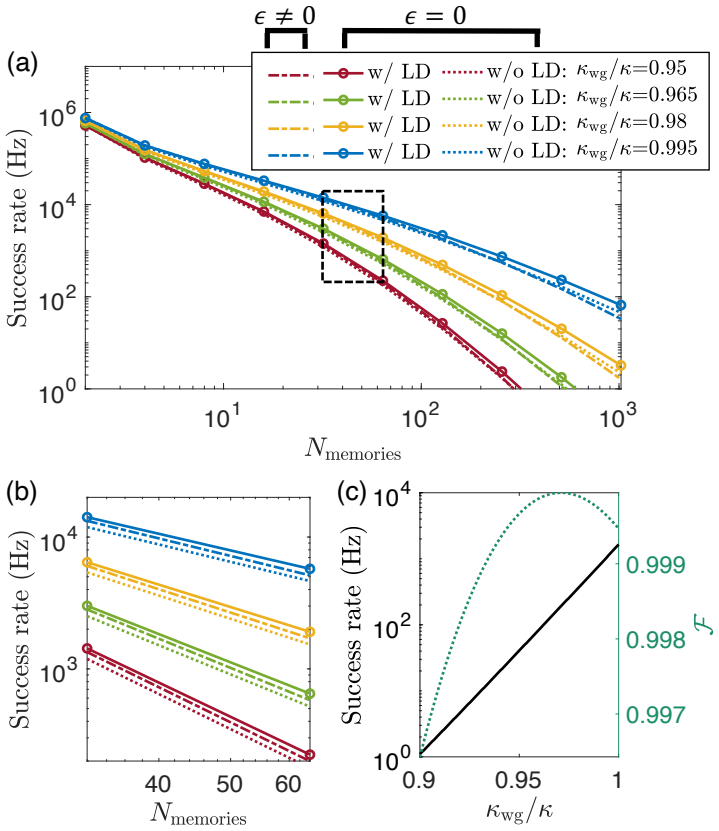

Figure 6-7: Efficiency of the PIC qRAM. (a) The success rate (Hz) is plotted against $N_{\text{memories}} = 2^n$ for a n-level qRAM for $\kappa_{\text{wg}}/\kappa = 0.95, 0.965, 0.98, 0.995$ for schemes with (solid) and without (dashed) qubit loss detection (LD) with perfect routing operation ($\epsilon = 0$), as well as one with loss detection but with routing error probability $\epsilon = 5\times10^{-4} \neq 0$ (dashed dotted). On a log-log scale, the success rate rolls off polynomially with increasing $N_{\text{memories}} = 2^n$ due to an exponentially decreasing success probability of setting each layer i. (b) A zoom-in plot of the black box in (a), highlighting the slight gain in efficiency for the cavity-assisted scheme with LD. (c) Both the success rate and transfer fidelity vary as a function of $\kappa_{\text{wg}}/\kappa$ for $\epsilon = 0$. For a 6-level qRAM with $C = 100$, there exists a trade-off between $\bar{\Gamma}$ and $\mathcal{F}$ after $\kappa_{\text{wg}}/\kappa \approx 0.97$ where $\mathcal{F}$ is maximized by perfectly balancing losses.

To calculate the success rate, we must now include both the round-trip travel time to each layer i denoted as $t_i = L_{\mathrm{PIC}}(i)/v_{g,\mathrm{PIC}} + L_{\mathrm{dmd}}(i)/v_{g,\mathrm{dmd}}$, where L_{PIC} (L_{dmd}) and $v_{g,\mathrm{PIC}}$ ($v_{g,\mathrm{dmd}}$) are the travel distance and group velocity in the PIC (diamond) waveguide. The average time until a successful query call can be found by using the linearity of expectation value. For example, the expected time for a 2-level qRAM is

$$\begin{aligned}\bar{T}_{n=2} = {} & p_1 p_2 (t_1 + t_2) + (1 - p_1)(\bar{T}_{n=2} + t_1 + \tau_{\mathrm{reset}}) \\ & + p_1 (1 - p_2)(\bar{T}_{n=2} + t_1 + t_2 + \tau_{\mathrm{reset}}),\end{aligned} \tag{6.14}$$

where $\tau_{\mathrm{reset}} = 5$ μs is the spin reset time. The first term on the right-hand side is the case of no photons being lost, thus its expected time is simply the product between the success probability of two consecutive heralds $p_1 p_2$ and the total travel time $t_1 + t_2$. The next term represents the case of the k_1 register photon being lost before detection with probability $1 - p_1$. Consequently, the average query time $\bar{T}_{n=2}$ is penalized by the additional time $t_1 + \tau_{\mathrm{reset}}$. Similarly, if the k_1 photon is heralded but the subsequent register k_2 is lost with probability $p_1(1 - p_2)$, $\bar{T}_{n=2}$ is lengthened by $t_1 + t_2 + \tau_{\mathrm{reset}}$. Solving for $\bar{T}_{n=2}$ yields

$$\bar{T}_{n=2} = \frac{t_1 + \tau_{\mathrm{reset}}}{p_1 p_2} + \frac{t_2}{p_2} - \tau_{\mathrm{reset}}. \tag{6.15}$$

The expression can be treated as a summation of each layer's round-trip time weighted by its correspond geometric mean, subtracted by τ_{reset} since the final trial is a successful run without the need to reset.

We can generalize the average time for a n-level qRAM to be

$$\bar{T} = \left(\prod_i p_i\right)\left(\sum_i t_i\right) + (1-p_1)(\bar{T} + t_1 + \tau_{\text{reset}}) \\ + p_1(1-p_2)(\bar{T} + t_1 + t_2 + \tau_{\text{reset}}) + ... + \left(\prod_i^{n-1}(1-p_n)\right)\left(\bar{T} + \sum_i t_i + \tau_{\text{reset}}\right) \tag{6.16}$$

$$\Rightarrow \bar{T} = \left(\sum_{i=1}^{n} \frac{t_i}{\prod_{j=i}^{n} p_j}\right) + \frac{\tau_{\text{reset}}}{\prod_{j=1}^{n} p_j} - \tau_{\text{reset}}. \tag{6.17}$$

Finally, the success rate is then

$$\bar{\Gamma} = \frac{1}{\bar{T}}. \tag{6.18}$$

Figure 6-7(a) shows the qRAM success rate as a function of the number of memories $N_{\text{memories}} = 2^n$ for different waveguide-cavity coupling $\kappa_{\text{wg}}/\kappa = 0.95, 0.965, 0.98, 0.995$. As N_{memories} increases, the rates roll off polynomially on the log-log scale since the success probability p_{succ} diminishes super-exponentially with increasing n. Furthermore, p_{succ} intimately depends on the cavity reflection coefficient $R_{\text{cav}} \propto \kappa_{\text{wg}}/\kappa$, causing $\bar{\Gamma}$ to vary drastically with the waveguide-cavity coupling. For example, the difference between $\kappa_{\text{wg}}/\kappa = 0.95$ and $\kappa_{\text{wg}}/\kappa = 0.995$ exceeds more than an order of magnitude for $N_{\text{memories}} > 10^2$, and the disparity grows exponentially as the circuit depth n increases. The unforgiving drop-off in the success rate emphasizes the need for a highly over-coupled single-sided cavity in our protocol.

Additionally, we consider the efficiency for the cases of having perfect ($\epsilon = 0$) and imperfect ($\epsilon = 5 \times 10^{-4}$) routing operation, represented by the solid and the dashed dotted lines respectively. Recall that if each node has a routing error ϵ, the query error scales as $1 - \mathcal{F}_{\text{query}} \sim \epsilon \log(N_{\text{memories}})^3$ [134]. Hence, the success rate with imperfect routing operations would reduce by an additional factor of $1 - \epsilon \log(N_{\text{memories}})^3$.

On the other hand, our cavity-assisted scheme's built-in loss detection (LD) enables a slight boost in success rate. For a scheme without such loss detection, the qRAM must complete the entire sequence of setting and routing all n register qubits

before needing to reset, assuming qubit loss has occurred and been detected after the query. The corresponding success rate would be

$$\bar{\Gamma}_{\text{no LD}} = \bar{T}^{-1}_{\text{no LD}} = \left(\frac{\sum_i t_i + \tau_{\text{reset}}}{\prod_i p_i} - \tau_{\text{reset}} \right)^{-1}. \tag{6.19}$$

In contrast, our protocol periodically checks for register losses via photon detection. Therefore, time can be saved by halting and immediately resetting the spins as soon as quantum state transfer fails to herald. Note that the gain in rate, however, depends on the ratio between travel time t_i and τ_{reset}. Figure 6-7(b) shows a modest increase in success rate for our scheme with $t_i < 1$ μs and $\tau_{\text{reset}} = 5$ μs relative to one without loss detection. If $\tau_{\text{reset}} \gg t_i$, the slight improvement in efficiency would dwindle as $\bar{\Gamma}$ converges to $\bar{\Gamma}_{\text{no LD}}$.

Lastly, due to the need to balance losses to achieve high transfer fidelity as noted in Sec. 6.2.3, there exists an inevitable fidelity-rate trade-off. Given a qRAM containing 2^6 memory cells, Figure 6-7(c) shows that $\mathcal{F}$ reaches its maximum at $\kappa_{\text{wg}}/\kappa \approx 0.97$ for the assumed cooperativity $C = 100$. However, the success rate still increases monotonically with $\kappa_{\text{wg}}/\kappa$ even past this optimum fidelity point. The waveguide-cavity coupling regime in which the trade-off exists narrows with higher atom-cavity cooperativity, since both $|r_{\text{on}}|$ and $|r_{\text{off}}|$ increase with C and $\kappa_{\text{wg}}/\kappa$. Nonetheless, at $C = 100$ (which has been experimentally demonstrated in Ref. [107, 66]), the success rate can already exceed 1 kHz while maintaining high fidelity $\mathcal{F} > 0.999$.

6.3 Teleportation scheme

While the aforementioned scheme is viable for a low-depth qRAM, the need to *sequentially* set each address register via cavity reflection inhibits scaling up to 10^6 memories due to photon loss from cavity interaction. Here, we present an alternative approach that writes the address registers onto all the layers *simultaneously* via quantum teleportation. Crucial to this step is the ability to perform high-fidelity two-qubit gate operation locally between an electron spin (broker qubit) and its neighboring nuclear

spin (memory qubit). Considering gate fidelity > 0.99 was already achieved experimentally via composite pulses and optimal classical control [135], we assume unity gate fidelity and success probability for the following calculations and consider the general case.

The protocol assumes two physically separated entities, a quantum computer (QC) and a qRAM, both of which contain nodes that each includes a memory and a broker qubit. The QC contains n nodes that hold the query addresses $\sum_j \alpha_j |j\rangle_a$ stored in the memory qubits. While the memory qubit can only interact with the broker qubit locally, the broker qubit can directly interact with photons to generate spin-photon entanglement via cavity reflection (see Section D.1). Hence, any two nodes can be remotely entangled by having their broker qubits to sequentially interact with a single photon (see Section D.3.1). Subsequently, the two entangled broker qubits undergo a SWAP operation with their memory qubits via hyperfine interaction to preserve coherence (see Section D.3.2). In the same manner, two neighboring Bell states can then be entangled to form a 4-qubit GHZ state. Prior to each query operation, all the nodes across each i^{th} qRAM layer are entangled to generate a 2^i-qubit GHZ state: $|\Psi_i\rangle = (|00...0\rangle + |11...1\rangle)/\sqrt{2}$. At the same time, the QC and the qRAM are remotely entangled via the same photon-assisted procedure, leaving the QC and the qRAM in the configuration depicted in Figure 6-8(a).

Now, each QC node undergoes a local Bell state measurement (BSM) between its memory and broker qubits as illustrated in Figure 6-8(b). As a result, the query addresses are teleported onto all the qRAM layers *in parallel*. However, since the routing operation depends on the photon interacting with the cavity-coupled broker qubits, each qRAM node undergoes a local SWAP operation immediately before data retrieval (Figure 6-8(c)). The photonic bus qubit then arrives at the binary tree prepared in the state shown in Figure 6-8(d).

The data retrieval process remains the same as before. Starting from the root node, the bus photon propagates down the binary tree and is routed based on the state-dependent cavity reflection at each layer. After which, the addresses are swapped onto the memory qubits in the qRAM ((Figure 6-8(e)), followed by remote entanglement

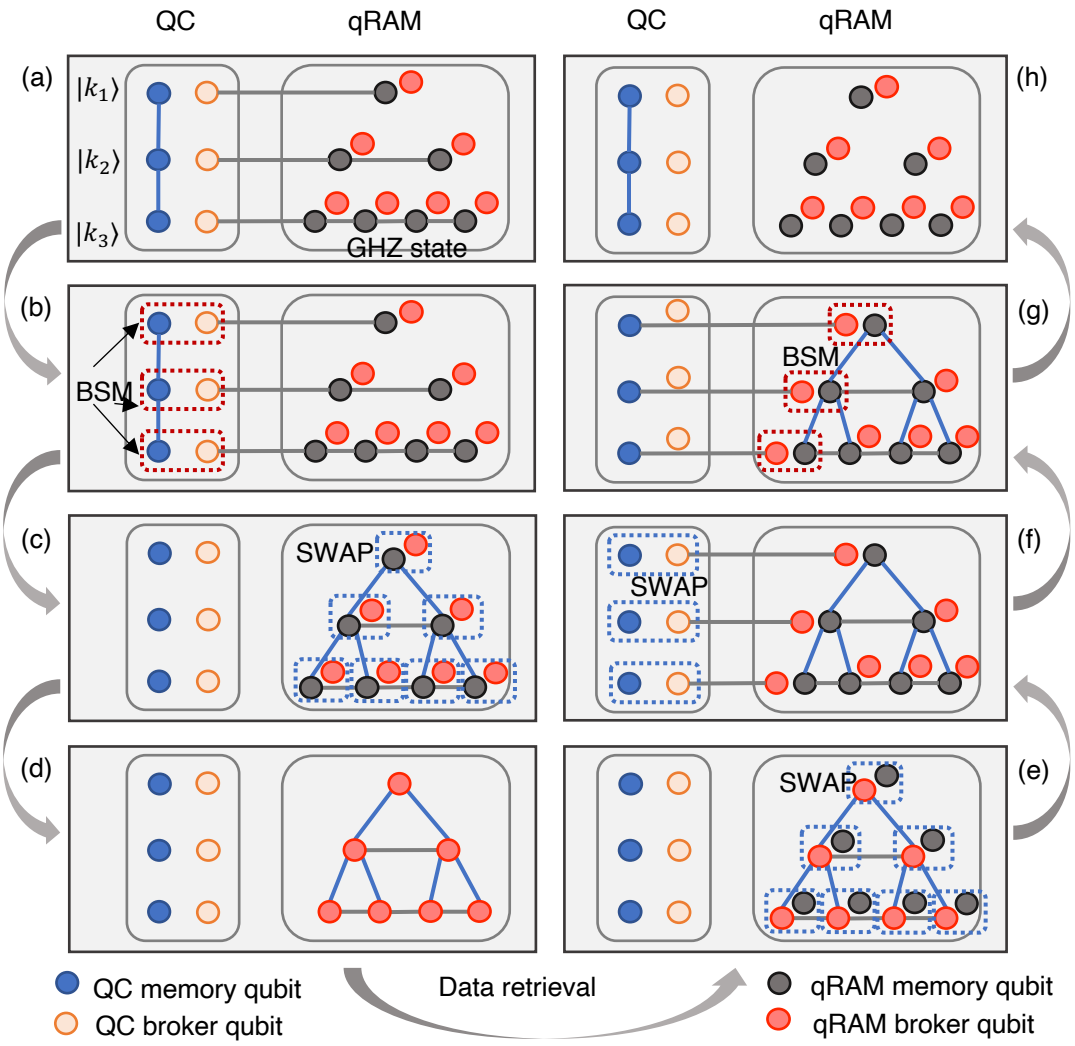

Figure 6-8: A step-by-step procedure of the teleportation scheme. A quantum computer (QC) holds the query addresses that would be mapped onto a qRAM. (a) The QC and qRAM are remotely entangled (as represented by connecting gray lines), and each qRAM layer's nodes are entangled in a GHZ state. (b) Local bell state measurements (BSM) and subsequent Pauli transformations teleport the query addresses onto the binary tree (c) Then, in each node, the memory (red circle) and the broker (gray circle) qubits undergo a SWAP operation, leaving (d) the qRAM ready for the data retrieval process. (e) After the bus qubit has completed querying, the registers are swapped back onto the memory qubits to maintain coherence. (f) The QC and the qRAM are then remotely entangled again via their broker qubits. A subsequent local SWAP operation in the QC then result in entanglement between QC's memory qubits and the qRAM's broker qubits. (g) Local BSMs in the qRAM then teleport the query addresses back onto the QC, returning (h) the binary tree to its original state.

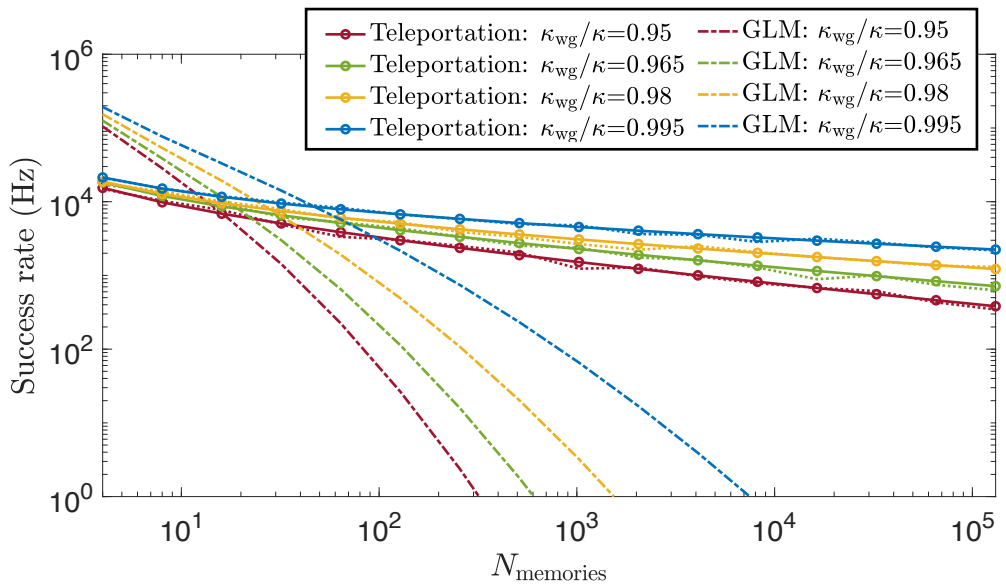

Figure 6-9: Efficiency comparison between the conventional GLM scheme (dashed dot) and the teleportation scheme. For the teleportation scheme, the solid lines are analytical fits to the simulation data represented by the dashed lines (see Section 6.3.1). Each scheme is evaluated at different cavity-waveguide coupling strengths $\kappa_{wg}/\kappa = 0.95, 0.965, 0.98, 0.995$.

between the QC's and the qRAM's broker qubits ((Figure 6-8(f)). Then, a local SWAP operation in the QC entangles the QC's memory qubits with the qRAM's broker qubits. Finally, local BSMs in the qRAM teleport the query addresses back onto the QC ((Figure 6-8(g)), returning the binary tree in its waiting state for future queries ((Figure 6-8(h)).

Importantly, the proposed architecture extends beyond a PIC platform and can be run on a *quantum network*, in which each network node represents a tree node in the qRAM. Distillation can be used to generate high-fidelity Bell states [136], which are then joined to form the GHZ states in the same fashion as heralding entanglement links in a quantum repeater. The protocol's modularity effectively allows the qRAM query to act as a subroutine for distributed quantum computing.

6.3.1 Efficiency comparison

Here, we compare the efficiency of the two proposed schemes assuming perfect spin-photon gate fidelity ($\epsilon = 0$) via optimally balancing losses. The teleportation ap-

proach, similar to the GLM scheme, still requires restarting the query procedure if the bus photon is lost during the retrieval step since the path information is revealed by the environment. Despite which, the rate of success for the teleportation scheme still scales much more favorably than the GLM approach. Figure 6-9 compares the query efficiency between the two approaches. For small circuit sizes $< 10^2$ memories, the GLM scheme achieves higher success rates since the process of generating GHZ states and remote entanglement links is more costly in time than directly transferring the registers sequentially (see Figure 6-10). However, as the qRAM depth increases past the crossover region with $\sim 10^2 - 10^3$ memories, the GLM scheme's efficiency rolls off rapidly.

On the other hand, the teleportation scheme's success rate decreases relatively slowly. Its efficiency is primarily constrained by the retrieval step that succeeds with probability $\propto \eta_r^n$, as opposed to $\propto \eta_r^{n(n-1)/2}\eta_s^n$ in the GLM scheme. Its favorable scaling is conducive to increasing the circuit size for general-purpose applications such as quantum machine learning [120]. Our efficiency simulations in the following Section 6.3.1 show that the teleportation-based approach can theoretically achieve an average >kHz success rate for a qRAM containing 10^5 memories.

Efficiency simulations

The teleportation scheme includes 4 steps: (1) initializing the entanglement links, (2) teleporting the addresses to the qRAM, (3) querying, and (4) teleporting the addresses back to the QC. We perform event-based simulations to estimate the time of completing all four steps.

In step (1), all the nodes except the leftmost node within each qRAM layer are entangled to form a GHZ state. It is created by heralded entanglement between nearest neighbor pairs with success probability $p_{\text{ep}} = \eta_{\text{path}}\eta_s^2\eta_{\text{det}}$. If the entanglement attempt fails, the spins undergo re-initialization for $\tau_{\text{reset}} = 5$ µs. If it succeeds, the electron spins (broker qubits) are swapped with their respective nuclear spins (memory qubits), an operation which we assume to take $t_{e\to n} = 16$ µs. Then, the unlinked neighbors are subsequently entangled in the same fashion. To reduce computational

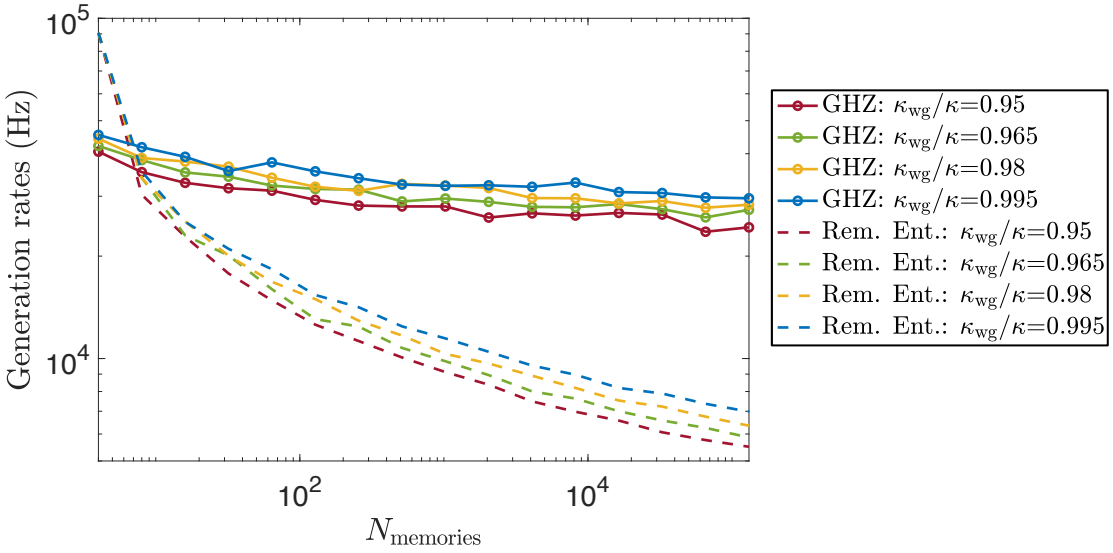

Figure 6-10: The generation rates for the GHZ state and the remote entanglement link are evaluated at different cavity-waveguide coupling strengths $\kappa_{\text{wg}}/\kappa = 0.95, 0.965, 0.98, 0.995$.

costs, we assume the rate is limited by the largest layer and only simulate its GHZ state creation process.

Simultaneously in step (2), we attempt to generate entanglement between the QC's broker qubit and the qRAM's leftmost node for each layer. Once the entanglement link is generated, the electron and nuclear spins are again swapped. In simulation, we take the maximum between the time to generate a GHZ state and the time to produce QC-qRAM Bell state. The generation rates for both the GHZ state and the remote entanglement link are plotted in Figure 6-10. Once both states are constructed, the leftmost node is entangled with the GHZ state composed of the remaining nodes within the same layer. Then, a local BSM is made between the address register and the QC ancillary qubits. To fairly compare the teleportation scheme's efficiency with the GLM scheme, we neglect the physical distance between the QC and the qRAM in Figure 6-9.

In step (3), a bus photon arrives at the root node of the binary tree and is routed to the memory layer with the query success probability p_i for an i-level qRAM. Finally, in step (4), a QC-qRAM Bell state is constructed again for each layer with probability

p_{ep}, followed by local BSMs on the leftmost nodes in the qRAM.

In Figure 6-9, the simulation data are plotted along with their analytical fits. Recall that the GHZ states are produced by linking multiples of Bell pairs. If each Bell pair creation succeeds with probability p, it would take a geometric mean of $1/p$ attempts. In the case of $p = 1$, the GHZ state creation process would merely be a two-step process. For example, for a layer with 4 nodes, nodes 1 and 2 as well as nodes 3 and 4 are entangled in the first time step. Then, nodes 2 and 3 are entangled to complete the GHZ state creation. However, with a non-unity p, the GHZ state creation is ultimately limited by the pair that fails the most number of times. In other words, the rate is mainly determined by the *outlier*. We fit the guessed model $f(N) = aN^{-b}$ multiplied with the analytical rate (based on geometric mean) to the simulation data, where N is the number of nodes within the largest layer. The coefficients a, b capture the outlier's scaling with the circuit depth. Their fitted values averaged over the considered $\kappa_{\text{wg}}/\kappa$ ratios are summarized in Table 6.3.

ω_c	406.774 THz
κ	20.34 GHz [66]
γ	94 MHz
τ_{reset}	5 μs
η_{str}	2.7 dB [69]
η_{bend}	9.3 dB [69]
η_{det}	1.3 dB [128]
$R_{\text{resonator}}$	50 μm [137]
n_{eff}	2.2645
$n_{g,\text{PIC}}$	2.3862
$n_{g,\text{dmd}}$	2.4513
$t_{e\to n}$	16 μs
$t_{n\to e}$	30 ns
a	1.7094
b	0.79386

Table 6.3: Table listing the parameters used in the qRAM simulations based on literature results.

6.3.2 Query fidelity

One drawback of the teleportation approach is decoherence lowering its query fidelity. This is especially problematic for the teleportation scheme because the protocol requires the spin qubits to wait until remote entanglement links are generated between the QC and the qRAM. Specifically, its requirement to prepare a GHZ state whose decoherence rate increases linearly with its size could further worsen the query fidelity. On the other hand, the GLM scheme that sequentially writes the addresses is not constrained by decoherence. As noted previously, the time scales at which the photon traverses through the PIC and the conditional Z gate is applied are much shorter than the electron spin coherence time. In essence, the teleportation scheme trades fidelity off for a substantial gain in efficiency (see Figure 6-9).

Let us consider the worst case where the entirety of the binary tree is active, meaning all possible addresses are used. Assuming the coherence times of the electron [33] and nuclear spins [25] to be 10^{-2} s and 10 s, respectively, we estimate the infidelity caused by decoherence to be $< 10^{-1}$ for $N_{\text{memories}} = 10^3$, as shown in Figure 6-11. Engineering a ^{12}C-rich environment [138] could further improve the coherence times and thereby reduce the infidelity.

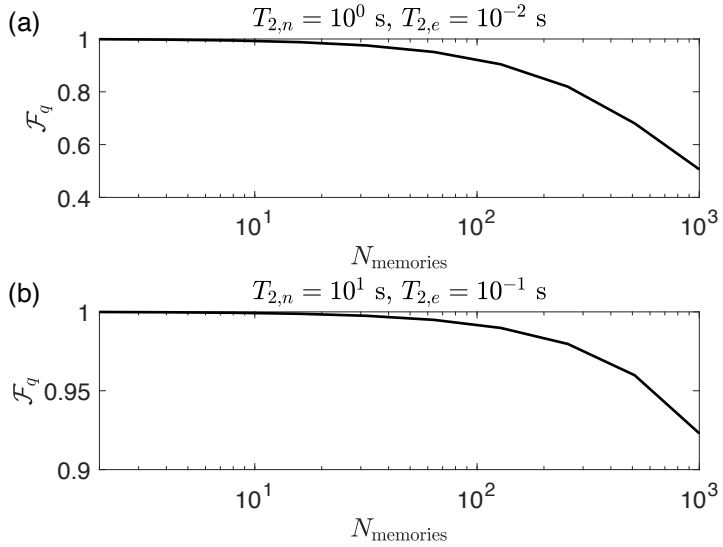

Figure 6-11: Query fidelity as a function of qRAM size. The nuclear and electron spin coherence times are respectively assumed to be: (a) $T_{2,n} = 10^0$ s and $T_{2,e} = 10^{-2}$ s, (b) $T_{2,n} = 10^1$ s and $T_{2,e} = 10^{-1}$ s.

Other sources of infidelity include depolarization, measurement errors, and imperfect two-qubit interaction between nuclear and electron spins. To simplify the discussion, we combine all types of errors into one collective "physical error rate" ϵ. We propose having interconnects interspersed between the layers that allow for arbitrary routing (see Section 6.3.2). As a result, for applications that require querying a small subset of possible addresses sparsely spanning the binary tree, only the necessary number of nodes are activated to minimize infidelity caused by physical errors.

However, for applications that require querying most addresses, the physical error rate could quickly decohere the qRAM since the infidelity rapidly grows as $1 - \mathcal{F}_q \propto (1-\epsilon)^{2^n-1}$ for a circuit depth of n. Assuming a physical error rate of $\epsilon = 10^{-4}$ and $n = 10$, the query infidelity is already $\sim 10^{-1}$. Therefore, scaling up the qRAM necessitates further exploration in converting each tree node to a logical qubit and adapting quantum error correction [139, 74].

PIC interconnect

In contrast with the GLM scheme, the teleportation scheme requires greater connectivity in the qRAM. Each node is not only connected to two children nodes in the next layer, but also to the rest of the nodes *in the same layer*. Here, we detail its PIC construct. Importantly, as shown in Figure 6-12(a), the architecture requires interconnect layers interspersed between the binary tree layers. Additionally, a photon detection system resides between each neighboring pair. Assuming the single photons are propagating in one direction, i.e. incoming from the right of each layer, the detector would register photons after they interact with the cavities to its right.

Within each interconnect layer, MZI switches are classically controlled to enable routing the single photons to individual cavities. The cavity depicted in Figure 6-12(b) is the same construct shown in Figure 6-3. To entangle two neighboring nodes, each tree node first operates in the setting mode. A single photon reflects off the first cavity and is directed to the second cavity via a circulator. After entering the second node through the MZI and reflecting off the cavity, the photon is again routed

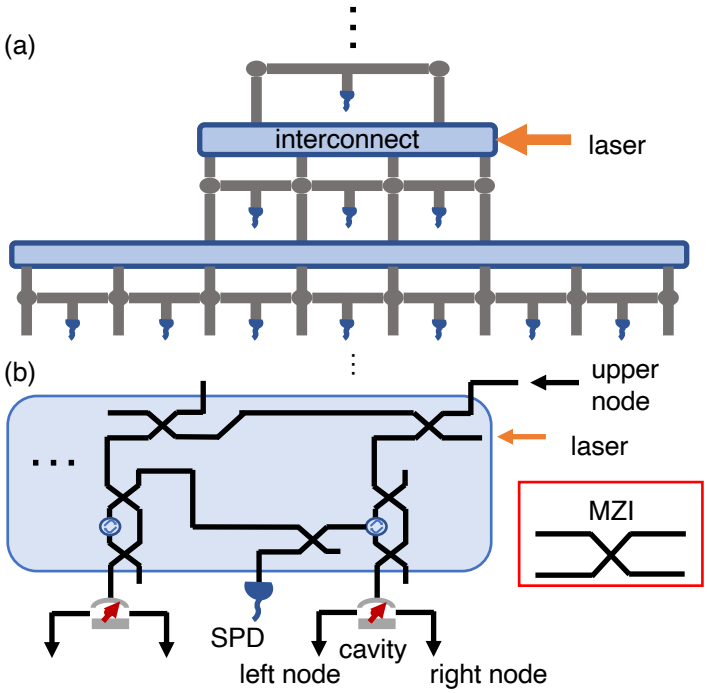

Figure 6-12: Proposed PIC architecture for the teleportation scheme. (a) The qRAM binary tree contains interspersed interconnect layers that enable intra-layer connectivity. (b) Within each interconnect layer, a network of MZIs is classically controlled to direct the single photons to either the subsequent cavity or the detection system for heralding during GHZ state creation. It is then switched to a transparent state during the data retrieval step.

to an MZI switch via a circulator. Except now, the switch directs the photon to the detector for heralding a Bell state creation. We stress here that the interconnect layer enables beyond nearest neighbor connection. Therefore, given prior knowledge of the query addresses, the architecture provides the ability to only entangle the necessary nodes and reduces state infidelity.

After the addresses are teleported from the QC to the qRAM, the cavity nodes are changed to the routing mode to direct the bus qubit to the memory layer at the bottom of the binary tree. In this step, the interconnect layer is essentially transparent by having the photon bypassing the circulators.

6.4 Experimental considerations

Here we address several experimental considerations concerning inhomogeneity in the solid-state defects.

1. **Spectral diffusion**, i.e. slow fluctuation in the emitter's optical transitions (ω_0, ω_1) can make it difficult to maintain the the cavity resonance at the target $\omega_c = (\omega_0 + \omega_1)/2$ Fortunately, recent experiments on group IV-vacancy centers (including the SiV^- center considered here) have shown spectral diffusion far below the radiative linewidth in nanophotonic waveguides and cavities [50, 66]. This stability is due in part to the atomic inversion symmetry of group IV-vacancy centers in diamond, which makes optical transitions first-order insensitive to stray electric fields [29]. In particular, recent demonstrations of SiV^- centers coupled to cavities achieved cooperativities $C > 100$ [66], which bounds spin-photon gate errors $\propto 1/C$. Further gains in cooperativity are possible with improved cavity designs and reduced environment noise through improved surfaces [83].

2. **Inhomogeneous distribution** in the optical transitions (ω_0, ω_1) (caused by variations in the microscopic environments) would detune the spin-based nodes across the network. Fortunately, these detunings can be corrected by strain tuning, which has been shown to align emitters across nearly the full inhomogeneous distribution < 50 GHz [140, 50].

6.5 Outlooks

In summary, we introduced a qRAM implementation in a PIC platform integrated with solid-state spin memories. Our numerical simulations show that our architecture can achieve > 0.99 fidelity with >kHz success rate for a qRAM containing 10^2 memory cells. Moreover, our cavity-assisted scheme relies on heralding the requisite operations, thereby providing built-in qubit loss detection that further improves the query efficiency. Although high success rates demand a sufficiently over-coupled cav-

ity to the waveguide, existing photonic crystal cavity designs [141, 142, 143] already show that they can reach near-unity coupling. We stress that our architecture is technologically feasible given rapidly advancing electro-optic platforms [137, 69] and experimentally shown large-scale integration of artificial atoms in PICs [50].

Additionally, we proposed an alternative scheme based on quantum teleportation that allows for efficiency scaling favorably with the circuit size. With sufficiently strong cavity-waveguide coupling, the teleportation approach enables >kHz success rate for a qRAM containing 10^5 memories, a size unattainable by the conventional approach. We emphasize that the protocol is modular and can be applied to a quantum network, in which each network node acts as a tree node in the qRAM. The nodes would again be entangled via heralding, which removes qubit loss as a potential error.

The architecture also extends to other atomic memories: quantum dots [144] and rare-earth ions [145] strongly coupled to nanocavities, and even trapped-ions [146] and neutral atoms [147] suitable for creating large GHZ states. With rapid advancements in constructing high-fidelity atom-photon interfaces, our proposal presents a scalable design of a general qRAM in the NISQ era.

Chapter 7

Conclusion and future directions

"Nature isn't classical, dammit, and if you want to make a simulation of nature, you'd better make it quantum mechanical, and by golly it's a wonderful problem, because it doesn't look so easy." – Richard Feynman, 1982.

Since the advent of quantum technologies with Richard Feynman's renowned quote [148], the discipline of quantum information processing has blossomed into an active field of research and advanced tremendously. In fact, the 2022 Nobel Prize in physics was awarded to Alain Aspect, John F. Clauser and Anton Zeilinger for their pioneering works in quantum information [149, 150], one of which was the first experimental realization of quantum teleportation for building a quantum network [151]. While many hallmark experiments have been demonstrated since then [8, 9, 10, 17, 18, 19, 20, 66, 152], the formidable engineering challenges in scaling up quantum systems have thus precluded construction of practical quantum networks.

This thesis, among many others, is an attempt at bridging the gap between Feynman's vision and reality. In particular, the theoretical and experiment works laid forth here address the central challenge of efficiently distributing entanglement with high fidelity. Chapter 3 proposes a scalable architecture consisting of a photonic integrated circuit heterogeneously integrated with defect centers in diamond. Moreover, the use of nanophotonic cavities strongly coupled to the quantum emitters enables an effective spin-photon interface for teleporting a photonic qubit onto a spin qubit, a task which

is essential for building quantum repeater network nodes. Then, in Chapter 4, we experimentally demonstrate nanofabrication of diamond photonic crystal cavities and subsequently Purcell enhancement of cavity-coupled SnV centers. In Chapter 5, we present on-going efforts in heterogeneously integrating these emitter-cavity systems into low-loss silicon nitride photonic integrated circuit, which acts as an optical interposer for spectroscopic studies at 1.3 K. Lastly, a quantum network is structurally equivalent to a quantum computer, except it implies entanglement over distances. As Chapter 6 has pointed out, spin-photon quantum networks may prove valuable to other pillars in information processing, such as constructing a quantum random access memory necessary for quantum machine learning [120]. It is not inconceivable that there exist many other applications of quantum networks with advantages over their classical counterparts.

However, the engineering efforts highlighted in this thesis only constitute the tip of an iceberg. This thesis should motivate using these chip-integrated spin-cavity systems to perform on-chip spin-photon entanglement and teleportation. This entails using the microwave lines to perform coherent control over individual spin qubits [108] and integrating single photon detectors for more efficient optical measurements [49]. Furthermore, directional couplers that conveniently construct phase-stable interferometers open the path to producing local entanglement among qubits in different channels. One may envision constructing cluster states crucial for measurement-based quantum computation [153] and error-corrected quantum communication [154].

The integration approach may also be applied to active PIC platforms such as aluminum nitride [50, 155], lithium niobate [69], and silicon carbide [156], all of which permit high-bandwidth switching networks for improving entanglement generation rates. We also note that the discussed physics and engineering platform extend beyond the use of color centers in diamond. Other promising solid-state qubits such as quantum dots [157], color centers in silicon carbide [156], rare-earth ions [75, 158], and defects in silicon [159, 160] may also benefit from the many functionalities bestowed by PICs.

As Feynman keenly noted, tackling this wonderful problem of building quantum

networks and computers is certainly not easy. I hope this thesis, as many others before me have done, paves a step towards unlocking the potential of quantum technologies.

Appendix A

Input-output formalism

Here, we follow the derivations detailed in the seminal paper by Gardiner and Collett [56], and derive the input-output formalism relation.

A.1 Quantum Langevin equations

We begin with a generic system interacting with a heat bath. Together, the total Hamiltonian is

$$H = H_{\text{sys}} + H_B + H_{\text{int}}, \tag{A.1}$$

where

$$H_B = \hbar \int_{-\infty}^{\infty} d\omega \ \omega \ b^\dagger(\omega) b(\omega) \tag{A.2}$$

$$H_{\text{int}} = i\hbar \int_{-\infty}^{\infty} d\omega \ \kappa(\omega)(b^\dagger(\omega)c - c^\dagger b(\omega)) \tag{A.3}$$

are the bath and interaction Hamiltonians, respectively. c is one of many annihilation operators for the unspecified system, and the bath bosonic operator b obeys the commutation relation, $[b(\omega), b^\dagger(\omega')] = \delta(\omega - \omega')$.

From the Schrödinger's equation, we can derive the Heisenberg equations of motion for $b(\omega)$ and an arbitrary system operator a (among the many c's). The equation of

motion for $b(\omega)$ is

$$\begin{aligned}\dot{b}(\omega') &= -\frac{i}{\hbar}\left[b(\omega'), H\right] \\ &= -i\int_{-\infty}^{\infty} d\omega\ \omega\ [b(\omega'), b^\dagger(\omega, b(\omega)] + \int_{-\infty}^{\infty} d\omega\ \kappa(\omega)[b(\omega'), b^\dagger(\omega)c(\omega) - c^\dagger(\omega)b(\omega)] \\ &= -i\omega' b(\omega') + \kappa(\omega')c(\omega'), \end{aligned} \tag{A.4}$$

where we used the commutator identity $[b, b^\dagger b] = [b, b^\dagger]b = b(\omega')\delta(\omega' - \omega)$.

Similarly,

$$\dot{a}(\omega') = -\frac{i}{\hbar}\left[a(\omega'), H\right] \tag{A.5}$$

$$= -\frac{i}{\hbar}\left[a(\omega'), H_{\text{sys}}\right] + \int_{-\infty}^{\infty} d\omega\ \kappa(\omega)\left[b^\dagger[a, c] - [a, c^\dagger]b\right]. \tag{A.6}$$

One can integrate Eq. A.4 to obtain

$$b(\omega) = e^{-i\omega(t-t_0)}b_0(\omega) + \kappa(\omega)\int_{t_0}^{t} e^{-i\omega(t-t')}c(t')\ dt', \tag{A.7}$$

where we replaced $\omega' \to \omega$, and $b_0(\omega)$ is $b(\omega)$ evaluated at $t = t_0$. One can check the validity of the above equation by taking the derivative with respect to t and evaluating at $t = t_0$, using the Leibniz rule[1].

Inserting the result from Eq. A.7 into the equation of motion for $a(\omega)$ yields

$$\begin{aligned}\dot{a} = &-\frac{i}{\hbar}\left[a, H_{\text{sys}}\right] + \int_{-\infty}^{\infty} d\omega\ \kappa(\omega)\left\{\left(e^{i\omega(t-t_0)}b_0^\dagger(\omega) + \kappa(\omega)\int_{t_0}^{t} e^{i\omega(t-t')}c^\dagger(t')dt'\right)[a, c]\right. \\ &\left.-[a, c^\dagger]\left(e^{-i\omega(t-t_0)}b_0(\omega) + \kappa(\omega)\int_{t_0}^{t} e^{-i\omega(t-t')}c(t')dt'\right)\right\} \\ = &-\frac{i}{\hbar}\left[a, H_{\text{sys}}\right] + \int_{-\infty}^{\infty} d\omega\ \kappa(\omega)\left\{e^{i\omega(t-t_0)}b_0^\dagger(\omega)[a, c] - [a, c^\dagger]e^{-i\omega(t-t_0)}b_0(\omega)\right\} \\ &+ \int_{-\infty}^{\infty} d\omega\ \kappa(\omega)^2\int_{t_0}^{t}\left\{e^{i\omega(t-t')}c^\dagger(t')[a, c] - [a, c^\dagger]e^{-i\omega(t-t')}c(t')\right\}. \end{aligned} \tag{A.8}$$

Note that similar to the derivation of quantum master equation, we assumed

[1] $\frac{d}{dx}\left(\int_{a(x)}^{b(x)} f(x,t)\right)\ dt = f(x, b(x))\cdot\frac{d}{dx}b(x) - f(x, a(x))\cdot\frac{d}{dx}a(x) + \int_{a(x)}^{b(x)}\frac{\partial}{\partial x}f(x,t)dt$

the first Markov approximation that the coupling constant is frequency-independent (equivalently, no dependence on previous times because of having no memory), i.e.

$$\kappa(\omega) = \sqrt{\frac{\kappa}{2\pi}} \tag{A.9}$$

For the following, we will use two properties

$$\int_{-\infty}^{\infty} d\omega \; e^{-i\omega(t-t')} = 2\pi\delta(t-t'), \tag{A.10}$$

$$\int_{t_0}^{t} dt' \; c(t')\delta(t-t') = \frac{1}{2}c(t). \tag{A.11}$$

Let us define an operator

$$b_{\rm in}(t) = \frac{1}{\sqrt{2\pi}} \int_{-\infty}^{\infty} d\omega \; e^{-i\omega(t-t_0)} b_0(\omega), \tag{A.12}$$

which obeys the commutator relation $[b_{\rm in}(t), b_{\rm in}^\dagger(t')] = \delta(t-t')$, and insert it into the equation of motion for a,

$$\begin{aligned}
\dot{a} &= -\frac{i}{\hbar}\,[a, H_{\rm sys}] + \sqrt{\frac{\kappa}{2\pi}} \left(\sqrt{2\pi} b_{\rm in}^\dagger(t)[a,c] - [a,c^\dagger]\sqrt{2\pi} b_{\rm in}(t) \right) \\
&\quad + \frac{\kappa}{2\pi} \int_{t_0}^{t} dt \;\; \left\{ 2\pi\delta(t-t')c^\dagger(t')[a,c] - [a,c^\dagger] 2\pi\delta(t-t')c(t') \right\} \\
&= -\frac{i}{\hbar}\,[a, H_{\rm sys}] - [a,c^\dagger] \left(\frac{\kappa}{2} c + \sqrt{\kappa} b_{\rm in}(t) \right) + \left(\frac{\kappa}{2} c^\dagger + \sqrt{\kappa} b_{\rm in}^\dagger(t) \right) [a,c].
\end{aligned} \tag{A.13}$$

Note that from Eq. A.7, we can apply a frequency integral on both sides and obtain

$$\begin{aligned}
\int_{-\infty}^{\infty} d\omega \; b(\omega) &= \int_{-\infty}^{\infty} \left\{ e^{-i\omega(t-t_0)} b_0(\omega) + \kappa(\omega) \int_{t_0}^{t} e^{-i\omega(t-t')} c(t') \; dt' \right\} \\
&= \sqrt{2\pi} b_{\rm in}(t) + \sqrt{\frac{\kappa}{2\pi}} \int_{t_0}^{t} dt' \; 2\pi\delta(t-t')c(t') \\
&= \sqrt{2\pi} b_{\rm in}(t) + \sqrt{2\pi}\frac{\sqrt{\kappa}}{2} c(t)
\end{aligned} \tag{A.14}$$

$$\rightarrow \frac{1}{\sqrt{2\pi}} \int_{-\infty}^{\infty} d\omega \; b(\omega) = b_{\rm in}(t) + \frac{\sqrt{\kappa}}{2} c(t). \tag{A.15}$$

The above derivation began with an *input* field at $t = t_0$. We can repeat the same procedure for an *outgoing* field with $t_1 > t$. The integral solution of b can be similarly written as

$$b(\omega) = e^{-i\omega(t-t_1)}b_1(\omega) + \kappa(\omega)\int_t^{t_1} e^{-i\omega(t-t')}c(t')\ dt'. \tag{A.16}$$

Let us define

$$b_{\text{out}}(t) = \frac{1}{\sqrt{2\pi}}\int_{-\infty}^{\infty} d\omega\ e^{-i\omega(t-t')}b_1(\omega). \tag{A.17}$$

Given the time directionality (time-reversed), κ should now be changed to $-\kappa$. The Langevin equation becomes

$$\dot{a} = -\frac{i}{\hbar}\left[a, H_{\text{sys}}\right] - \left[a, c^\dagger\right]\left(-\frac{\kappa}{2}c + \sqrt{\kappa}b_{\text{out}}(t)\right) + \left(-\frac{\kappa}{2}c^\dagger + \sqrt{\kappa}b_{\text{out}}^\dagger(t)\right)\left[a, c\right]. \tag{A.18}$$

Again, applying the frequency integral over $b(\omega)$ gives us

$$\frac{1}{\sqrt{2\pi}}\int_{-\infty}^{\infty} d\omega\ b(\omega) = b_{\text{out}}(t) - \frac{\sqrt{\kappa}}{2}c(t). \tag{A.19}$$

Combining Eq. A.15 and Eq. A.19, we have the input-output identity

$$b_{\text{out}}(t) - b_{\text{in}}(t) = \sqrt{\kappa}c(t). \tag{A.20}$$

A.2 Single-sided cavity reflection

Now, with the derived input-output formalism, we may apply the typical Jaynes-Cummings Hamiltonian to the (time-forwarding) Langevin equation and evaluate the evolution of the cavity ladder operator $c = a$. The Hamiltonian takes the form

$$H_{\text{sys}} = (\omega_c - \omega)a^\dagger a + (\omega_a - \omega)\sigma_z + ig(\sigma_+ a - a^\dagger\sigma_-), \tag{A.21}$$

where ω_c and ω_a are the cavity resonance and atomic emission frequencies, respectively, and $\sigma_{z,+,-}$ are the atomic operators.

Using Eq. A.13, the equation of motion for a is

$$\begin{aligned}\dot{a} &= -i[a, H_{\text{sys}}] - \frac{\kappa}{2}a - \sqrt{\kappa_{\text{wg}}}a_{\text{in}} \\ &= -i\left((\omega_c - \omega)a - ig\sigma_-\right) - \frac{\kappa}{2}a - \sqrt{\kappa_{\text{wg}}}a_{\text{in}} \\ &= -\left(i(\omega_c - \omega) + \frac{\kappa}{2}\right)a - g\sigma_- - \sqrt{\kappa_{\text{wg}}}a_{\text{in}}, \end{aligned} \tag{A.22}$$

where we take the convention of setting $\hbar = 1$. Note that the coupling rate of the cavity to the input/output channel (e.g. waveguide) is labeled as $\kappa_{\text{wg}} \propto Q_c$ (see Sec. 2.1.3), as opposed to the cavity's total decay rate $\kappa \propto Q_e$.

Similarly, we derive the equation of motion for σ_-,

$$\begin{aligned}\dot{\sigma}_- &= -i[\sigma_-, H_{\text{sys}}] - \frac{\gamma}{2}\sigma_- \\ &= -i\left((\omega_a - \omega)[\sigma_-, \sigma_z] + ig[\sigma_-, \sigma_+]a\right) - \frac{\gamma}{2}\sigma_- \\ &= -i(\omega_a - \omega)\sigma_- + g\sigma_z a - \frac{\gamma}{2}\sigma_- \\ &= -\left(i(\omega_a - \omega) + \frac{\gamma}{2}\right)\sigma_- + g\sigma_z a, \end{aligned} \tag{A.23}$$

where $\gamma/2 = \gamma_\parallel/2 + \gamma^*$ is the total atomic decay rate, composed of the spontaneous emission rate $\gamma_\parallel/2$ and pure dephasing γ^*. Note that Γ and γ used in Chapter 2 equate γ and $\gamma_\parallel$, respectively.

In the following, we adapt the semi-classical treatment and assume the evolution of the single photon interacting with the cavity can be described by the steady-state solution of the operators, i.e. when $\langle\dot{a}\rangle = \langle\dot{\sigma}_-\rangle = 0$. The equations of motion for a and σ_- are then

$$0 = -\alpha\langle a\rangle - g\langle\sigma_-\rangle - \sqrt{\kappa_{\text{wg}}}\langle a_{\text{in}}\rangle, \tag{A.24}$$

$$0 = -\beta\langle\sigma_-\rangle + g\langle\sigma_z a\rangle, \tag{A.25}$$

where we define $\alpha = i(\omega_c - \omega) + \kappa/2$ and $\beta = i(\omega_a - \omega) + \gamma/2$.

In the weak excitation regime, also known as the linear regime in which the atom is not driven to saturation, we can assume $\langle \sigma_z a \rangle \approx -\langle a \rangle$. From the above equations, we can derive an expression for $\langle a \rangle$ in terms of $\langle a_{\text{in}} \rangle$,

$$\langle a \rangle = -\frac{\sqrt{\kappa_{\text{wg}}}}{\alpha - \frac{g^2}{\beta}} \langle a_{\text{in}} \rangle. \tag{A.26}$$

Recall we have the input-output relation

$$a_{\text{out}} - a_{\text{in}} = \sqrt{\kappa_{\text{wg}}} a \tag{A.27}$$

$$\begin{aligned} \Rightarrow \langle a_{\text{out}} \rangle &= \langle a_{\text{in}} \rangle + \sqrt{\kappa_{\text{wg}}} \langle a \rangle \\ &= \langle a_{\text{in}} \rangle - \frac{\kappa_{\text{wg}}}{\alpha - \frac{g^2}{\beta}} \langle a_{\text{in}} \rangle \end{aligned} \tag{A.28}$$

Finally, we have the cavity reflection coefficient for a single-sided cavity defined as

$$\begin{aligned} r(\omega) = \frac{\langle a_{\text{out}} \rangle}{\langle a_{\text{in}} \rangle} &= 1 - \frac{\kappa_{\text{wg}}}{\alpha - \frac{g^2}{\beta}} \\ &= 1 - \frac{\kappa_{\text{wg}}}{i(\omega_c - \omega) + \frac{\kappa}{2} - \frac{g^2}{i(\omega_a - \omega) + \frac{\gamma}{2}}} \end{aligned} \tag{A.29}$$

Appendix B

PEPSI: details about tunable H attenuator and alternative PDR designs

This appendix includes more details about the tunable H attenuator for balancing losses in the PEPSI protocol explained in Chapter 3. It also covers an alternative PDR design based on air holes as opposed to corrugation shown in Section 3.2.

B.1 Tunable H attenuator

To balance losses controllably, we propose adding a tunable H attenuator before the PDR. Figure B-1 shows the implementations with both free-space optics and photonics components. Figure B-1(a) illustrates using a beam displacer to separate out the H and V polarization modes and attenuating only the H component with a continuous variable optical filter. The two paths are subsequently recombined by a second beam displacer. Above, we denote the transmission efficiency of H passing through the tunable attenuator as η_H. Despite the use of free-space optics, the two polarization modes are still effectively co-propagating, thereby maintaining the relative phase stability. Similarly, Figure B-1(b) presents an analogous setup in a photonics platform, in which a polarization splitter diverts the H mode and a Mach-Zehnder

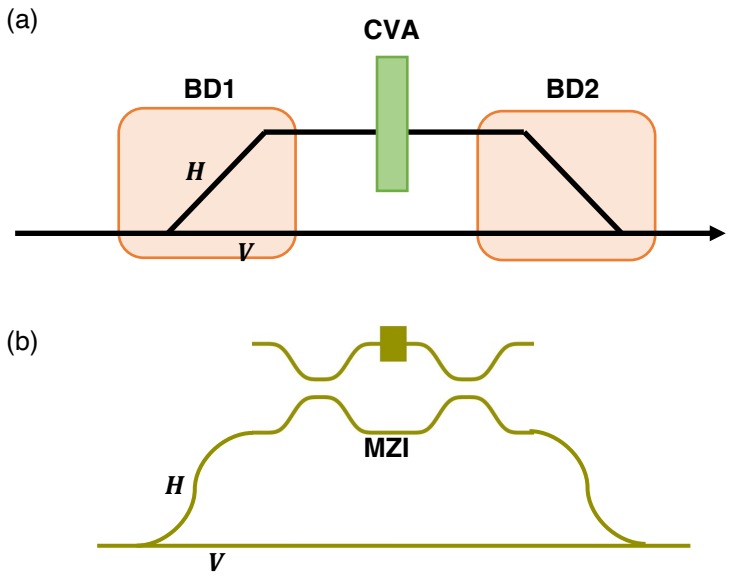

Figure B-1: Implementations of the tunable H attenuator with (a) free-space optics and (b) photonics components. (a) A beam displacer (BD1) first separates out the two polarization modes, and a subsequent continuous variable attenuator (CVA) reduces the amount of H light passing through to optimally balance losses. A second beam displacer (BD2) then recombines the two paths. (b) Analogously, in a photonics platform, a polarization splitter diverts the H polarization mode to a Mach-Zehnder interferometer (MZI), which controllably attenuates the H transmission efficiency.

interferometer controls the amount of H (η_H) that recombines with the V mode.

B.2 Alternative PDR design based on hole-y PhC

In addition to the alligator geometry, we also explored a PhC mirror comprising a straight waveguide and air holes shown in Figure B-2(a). The transfer fidelity is maximized at unity when the periodicity $a = 226$ nm, the air hole radius $r = 0.173a$, and the waveguide width $W = 1.06a$. While this alternative design is more feasible in fabrication than the alligator PDR, the hole-y PDR suffers from fabrication intolerance. Figure B-2(b) indicates that the transfer fidelity worsens drastically as the air hole radius deviates only by a few nanometers, well within the margin of fabrication errors. For example, an increase in r by 2 nm from $r = 39$ nm to $r = 41$ nm lowers the fidelity to 97.3%.

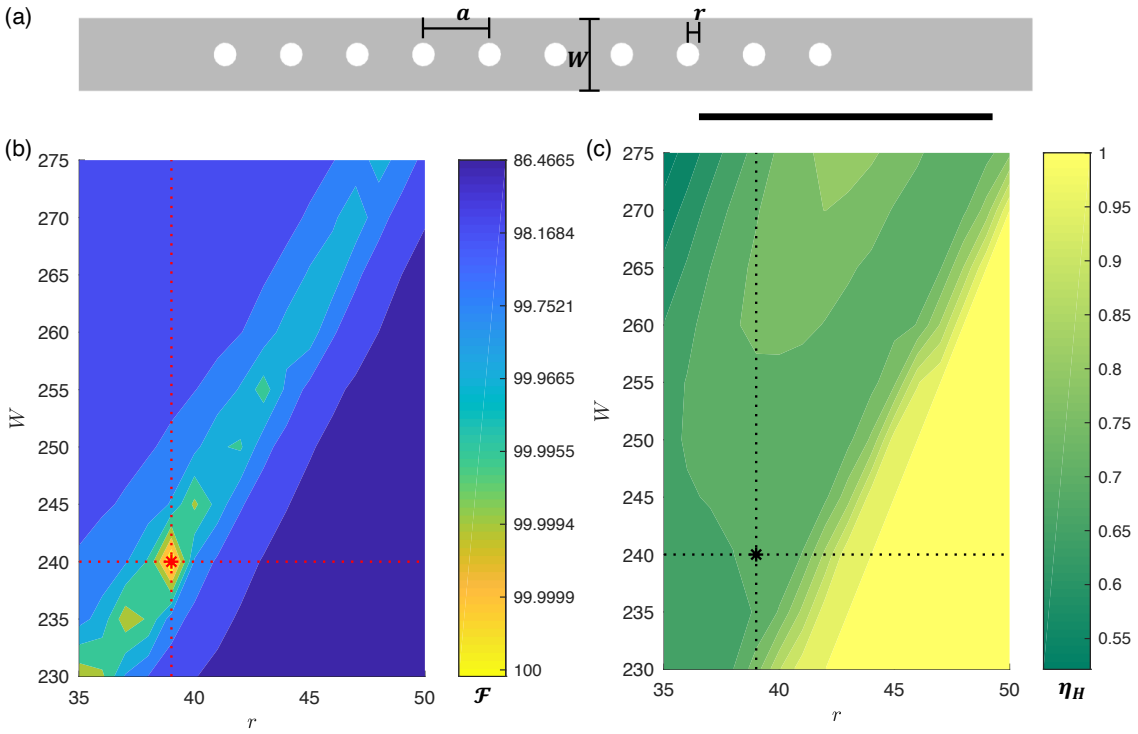

Figure B-2: (a) A PDR consisting of a straight waveguide with air holes. The geometry is defined by the periodicity $a = 226$ nm, the air hole radius $r = 0.173a$, and the waveguide width $W = 1.06a$. Scale bar is 1 um. (b) The state transfer fidelity as a function of r and W. The fidelity is maximized when $r = 39$ nm and $W = 240$ nm. (c) The corresponding H attenuation factors to optimize fidelity. At the optimal point, $\eta_H = 0.71$.

Appendix C

Targeted focused ion-beam implantation

Alternative to blanket implantation with or without mask apertures, we have also pursued targeted focused ion-beam (FIB) implantation in collaboration with Sandia National Laboratory. Devices shown in Ref. [50] are fabricated on such a diamond sample FIB-implanted with Si and Ge ions. We note that the sample undergoing diamond fabrication shown in Section 4.2 does not have targeted FIB implanted SnV centers, as the FIB metal alloy [161] tip for Sn was not ready at the time of sample preparation. Our recent work with investigation of Sn isotopes [112], however, is implanted with the newly developed Sn metal alloy sources. For future experiments involving emitter-cavity systems requiring accurate spatial alignment, targeted implantation via FIB may be a more suitable approach.

Below, we provide a brief overview of of the design and fabrication of alignment markers essential for FIB implantation used in Ref. [50].

C.1 QR + alignment markers

The markers we employ consist of two types: QR codes and FIB alignment markers. The former define a global coordinate system that we may use to navigate across the sample for automated spectroscopy, as detailed in Ref. [162, 163], while the latter is

used for aligning the FIB implantation spots to the desired locations.

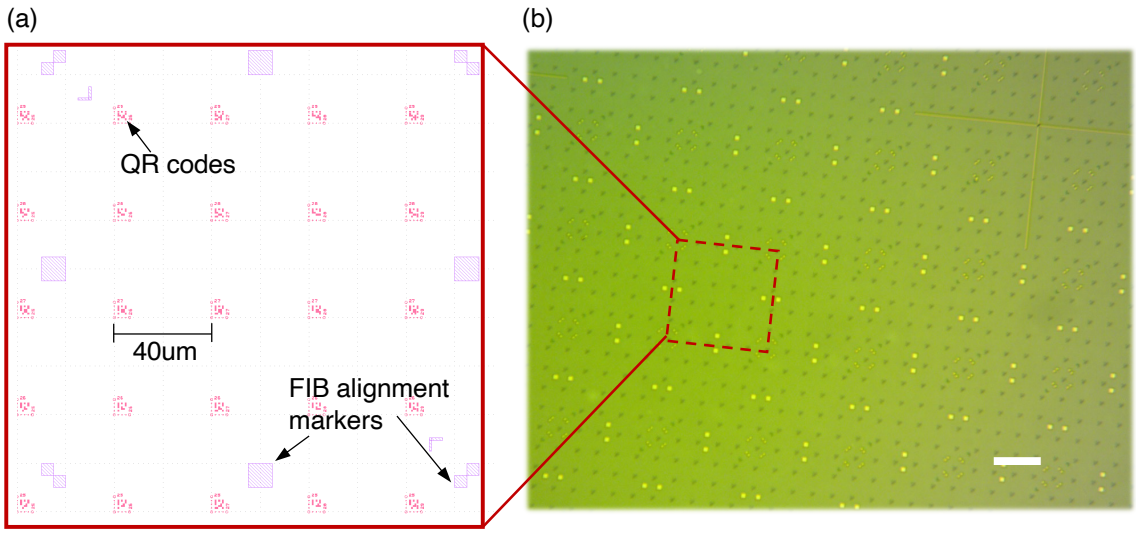

Figure C-1: (a) A 200 μm by 200 μm cell containing both QR codes (pink) and FIB alignment markers (purple). The QR codes are separated by 40 μm. (b) An optical microscope image of a prepared EG diamond's surface with defined QR codes and FIB alignment markers, each etched 1 μm into the diamond and covered with a 50 nm thick gold layer. Scale bar is 100 μm.

Figure C-1(a) shows a 200 μm by 200 μm "cell" tessellating across an EG diamond surface. The FIB alignment markers (purple) include square doublets (5 μm by 5 μm in size) in each of the four corners, and four additional backup square alignment markers in between. Interspersed throughout each cell are individual QR codes [162] (pink) with 40 μm pitch, defining the x, y coordinates that may be used to localized the implanted defect centers after FIB implantation and perform automated spectroscopy [163].

C.2 HF liftoff

To prepare a diamond EG sample for targeted FIB implantation, we first perform the same surface preparation and etching steps detailed in Section 4.2, specifically up to Step (i). However, instead of submerging it in HF to remove the nitride mask, we first deposit a 50 nm thick gold layer via electron beam evaporation across the surface, then subsequently perform liftoff in HF. This ensures the etched markers are

also covered in gold to improve imaging contrast, crucial to accurate FIB alignment especially on insulating materials such as diamond. Figure C-1(b) shows an optical microscope image of a prepared sample surface.

Appendix D

qRAM operations

This appendix details operations critical for implementing a qRAM based on spin-photon networks.

D.0.1 Quantum routing

In the routing mode, the MZI in Figure 6-3(c) is tuned to operate as a 50:50 beam splitter whose unitary matrix is denoted as B. Let a, b be the annihilation operators for the top and bottom spatial modes such that $a^\dagger \left|0\right\rangle_a \left|0\right\rangle_b = \left|1\right\rangle_a \left|0\right\rangle_b$ represents one photon present in the top waveguide and no photon in the bottom waveguide. The MZI provides the unitary transformation on the operators,

$$BaB^\dagger = \frac{1}{\sqrt{2}}(a + ib), \quad BbB^\dagger = \frac{1}{\sqrt{2}}(b + ia). \tag{D.1}$$

Assuming input from strictly the top waveguide, our initial state is $\left|\phi_0\right\rangle = \left|1\right\rangle_a \left|0\right\rangle_b = a^\dagger \left|0\right\rangle_a \left|0\right\rangle_b$. After passing through the MZI, the state becomes

$$\begin{aligned} \left|\phi_1\right\rangle &= B\left|\phi_0\right\rangle = Ba^\dagger \left|0\right\rangle_a \left|0\right\rangle_b = Ba^\dagger B^\dagger B \left|0\right\rangle_a \left|0\right\rangle_b \\ &= \frac{1}{\sqrt{2}}(a^\dagger - ib^\dagger)\left|0\right\rangle_a \left|0\right\rangle_b . \end{aligned} \tag{D.2}$$

We can denote the unitary transformation of the atom-coupled cavity system (in conjunction with the resonator) as $PaP^\dagger = ae^{i\phi}$. Note that it is only acting on the

top waveguide and has no effect on b. As a result, the photonic qubit after reflection off the mirror and the cavity system becomes

$$\begin{aligned}|\phi_2\rangle = P\,|\phi_1\rangle &= \frac{1}{\sqrt{2}}(Pa^\dagger - ib^\dagger)P^\dagger P\,|0\rangle_a\,|0\rangle_b \\ &= \frac{1}{\sqrt{2}}(e^{i\phi}a^\dagger - ib^\dagger)\,|0\rangle_a\,|0\rangle_b\,. \end{aligned} \tag{D.3}$$

Lastly, the photon returns to and interacts with the MZI once again, with the state

$$\begin{aligned}|\phi_3\rangle = B^\dagger\,|\phi_2\rangle &= \frac{1}{\sqrt{2}}B^\dagger(e^{i\phi}a^\dagger - ib^\dagger)BB^\dagger\,|0\rangle_a\,|0\rangle_b \\ &= \frac{1}{2}\left(e^{i\phi}(a^\dagger + ib^\dagger) - i(b^\dagger + ia^\dagger)\right)|0\rangle_a\,|0\rangle_b \\ &= e^{i\phi/2}\left[\left(\frac{e^{i\phi/2}+e^{-i\phi/2}}{2}\right)a^\dagger\right. \\ &\quad \left. +i\left(\frac{e^{i\phi/2}-e^{-i\phi/2}}{2}\right)b^\dagger\right]|0\rangle_a\,|0\rangle_b \\ &= e^{i\phi/2}\left[\cos\left(\frac{\phi}{2}\right)|1\rangle_a\,|0\rangle_b - \sin\left(\frac{\phi}{2}\right)|0\rangle_a\,|1\rangle_b\right]. \end{aligned} \tag{D.4}$$

In summary, the photon exiting the MZI output a (Figure 6-3(c)) has a constant π phase shift upon reflection off the mirror, whereas one exiting the MZI output b has a spin-dependent $\{0, \pi\}$ phase shift. Together, the MZI-cavity-spin system functions as a spin-dependent router, mapping $(\alpha\,|\downarrow\rangle + \beta\,|\uparrow\rangle) \otimes |0\rangle_a\,|0\rangle_b$ to $\alpha\,|\downarrow\rangle\,|1\rangle_a\,|0\rangle_b + \beta\,|\uparrow\rangle\,|0\rangle_a\,|1\rangle_b$.

D.1 Quantum state transfer: photon-to-spin

The procedure described here is similar to the polarization encoding case spelled out in Section 2-4, but instead in frequency-encoded qubits. The atom is first initialized in a superposition of the two ground states: $|\psi_A\rangle = (|\downarrow\rangle + |\uparrow\rangle)/\sqrt{2}$. With the incoming frequency-encoded photonic qubit, $|\psi_P\rangle = \alpha\,|\omega_0\rangle + \beta\,|\omega_1\rangle$, the joint (un-normalized)

photon-atom state is

$$|\psi\rangle = |\psi_P\rangle \otimes |\psi_A\rangle = (\alpha\,|\omega_0\rangle + \beta\,|\omega_1\rangle)(|\downarrow\rangle + |\uparrow\rangle). \tag{D.5}$$

The add-drop filter resonantly couples to only the ω_0 component that then reflects off a mirror, acquiring π phase shift regardless of the atomic state. On the other hand, the ω_1 component interacts with the atom-cavity system and acquires a spin-dependence phase shift. After the CZ operation, the photon and the atom are entangled in a state

$$|\psi\rangle = -\alpha\,|\omega_0,\downarrow\rangle - \alpha\,|\omega_0,\uparrow\rangle - \beta\,|\omega_1,\downarrow\rangle + \beta\,|\omega_1,\uparrow\rangle\,. \tag{D.6}$$

The returning photon then goes through a frequency beam splitter that performs a Hadamard gate. After which, the two frequency components are routed to different photon detectors, resulting in the state

$$\begin{aligned}|\psi\rangle &= -\alpha(|\omega_0\rangle + |\omega_1\rangle)(|\downarrow\rangle + |\uparrow\rangle) - \beta(|\omega_0\rangle - |\omega_1\rangle)(|\downarrow\rangle - |\uparrow\rangle) \\ &= |\omega_0\rangle \otimes [-(\alpha+\beta)\,|\downarrow\rangle - (\alpha-\beta)\,|\uparrow\rangle] + |\omega_1\rangle \otimes [-(\alpha-\beta)\,|\downarrow\rangle - (\alpha+\beta)\,|\uparrow\rangle]\,.\end{aligned} \tag{D.7}$$

Upon heralding, the atom undergoes another Hadamard gate to complete quantum teleportation. The joint state becomes

$$\begin{aligned}|\psi\rangle &= |\omega_0\rangle \otimes [-(\alpha+\beta)(|\downarrow\rangle + |\uparrow\rangle) - (\alpha-\beta)(|\downarrow\rangle - |\uparrow\rangle)] \\ &\quad + |\omega_1\rangle \otimes [-(\alpha-\beta)(|\downarrow\rangle + |\uparrow\rangle) - (\alpha+\beta)(|\downarrow\rangle - |\uparrow\rangle)] \\ &= -\,|\omega_0\rangle \otimes (\alpha\,|\downarrow\rangle + \beta\,|\uparrow\rangle) + |\omega_1\rangle \otimes (-\alpha\,|\downarrow\rangle + \beta\,|\uparrow\rangle).\end{aligned} \tag{D.8}$$

The end result is

$$\begin{aligned}|\psi\rangle = \alpha\,|\downarrow\rangle + \beta\,|\uparrow\rangle \quad &\text{if } \omega_0 \text{ is detected} \\ \text{or} \quad \alpha\,|\downarrow\rangle - \beta\,|\uparrow\rangle \quad &\text{if } \omega_1 \text{ is detected}\end{aligned}$$

neglecting global phase. Note that an additional Pauli-Z operation is needed if ω_1 is detected.

Now, let us consider an imperfectly over-coupled single-sided cavity with waveguide-cavity coupling $\kappa_{\rm wg}/\kappa < 1$. We denote $r_{\rm off}$ and $r_{\rm on}$ as the off- and on-resonance cavity reflections, and r_m as the mirror reflection. Assuming the interferometric couplers are lossless in the add-drop filter, the photon-atom entangled state is then

$$|\psi\rangle = \alpha r_m |\omega_0, \downarrow\rangle + \alpha r_m |\omega_0, \uparrow\rangle + \beta r_{\rm off} |\omega_1, \downarrow\rangle + \beta r_{\rm on} |\omega_1, \uparrow\rangle \tag{D.9}$$

After the Hadamard on the photon, the state evolves to

$$\begin{aligned} |\psi\rangle &= \alpha r_m(|\omega_0\rangle + |\omega_1\rangle)(|\downarrow\rangle + |\uparrow\rangle) + \beta(|\omega_0\rangle - |\omega_1\rangle)(r_{\rm off}|\downarrow\rangle + r_{\rm on}|\uparrow\rangle) \\ &= |\omega_0\rangle \otimes [(\alpha r_m + \beta r_{\rm off})|\downarrow\rangle + (\alpha r_m + \beta r_{\rm on})|\uparrow\rangle] \\ &\quad + |\omega_1\rangle \otimes [(\alpha r_m - \beta r_{\rm off})|\downarrow\rangle + (\alpha r_m - \beta r_{\rm on})|\uparrow\rangle]. \end{aligned} \tag{D.10}$$

The additional Hadamard on the atom would yield

$$\begin{aligned} |\psi\rangle &= |\omega_0\rangle \otimes [(\alpha r_m + \beta r_{\rm off})(|\downarrow\rangle + |\uparrow\rangle) + (\alpha r_m + \beta r_{\rm on})(|\downarrow\rangle - |\uparrow\rangle)] \\ &\quad + |\omega_1\rangle \otimes [(\alpha r_m - \beta r_{\rm off})(|\downarrow\rangle + |\uparrow\rangle) + (\alpha r_m - \beta r_{\rm on})(|\downarrow\rangle - |\uparrow\rangle)] \\ &= |\omega_0\rangle \otimes [(2\alpha r_m + \beta(r_{\rm on} + r_{\rm off}))|\downarrow\rangle + \beta(-r_{\rm on} + r_{\rm off})|\uparrow\rangle] \\ &\quad + |\omega_1\rangle \otimes [(2\alpha r_m - \beta(r_{\rm on} + r_{\rm off}))|\downarrow\rangle + \beta(r_{\rm on} - r_{\rm off})|\uparrow\rangle]. \end{aligned} \tag{D.11}$$

If the register qubit is $|\psi_P\rangle = (|\downarrow\rangle + |\uparrow\rangle)/\sqrt{2}$ such that $\alpha = \beta = 1/\sqrt{2}$ and we assume $|r_m| = 1$, detection on the ω_0 port would herald the state

$$|\psi\rangle = (2 + r_{\rm on} + r_{\rm off})|\downarrow\rangle + (-r_{\rm on} + r_{\rm off})|\uparrow\rangle. \tag{D.12}$$

Since $\mathrm{sgn}(r_{\rm on}) = 1$ and $\mathrm{sgn}(r_{\rm off}) = -1$, we see that $|\psi\rangle \Rightarrow |\downarrow\rangle + |\uparrow\rangle$ requires $|r_{\rm on}| = |r_{\rm off}|$, which hints at the need to "balance" these two reflections. Eq. 2.17 dictates that $r_{\rm on} \propto \kappa_{\rm wg}(C-1)/(C+1)$ while $r_{\rm off} \propto \kappa_{\rm wg}/\kappa$ such that only a suitable regime of $\{g, \gamma, \kappa, \kappa_{\rm wg}\}$ would maximize the quantum state transfer fidelity as shown

in Figure 6-6.

D.2 Quantum state transfer: spin-to-photon

Once the bus qubit retrieves the data from the memory layer, we must extract the address out of the qRAM to obtain the correlated output state $\sum_j \alpha_j |j\rangle_a |D_j\rangle_b$. By sending additional photons, we can perform quantum state transfer that *maps the spin qubits onto the photonic qubits*. Similar to the heralding procedure for transferring the photonic states to spin qubits, the spins must undergo projective measurements to complete the spin-to-photon mapping. While it is feasible to perform single shot readout on one spin, it is experimentally difficult to simultaneously perform projective measurements on *multiple spins* within one layer. The issue can be circumvented by introducing an ancillary photon that is entangled with the spins for each layer, and heralding on such photon equates to performing projective readout on the spin qubits.

After data retrieval, the spin holds the routing state $|\psi_A\rangle = \alpha |\downarrow\rangle + \beta |\uparrow\rangle$. The incoming photon initialized in the superposition state (un-normalized) $|\psi_{P1}\rangle = |\omega_0\rangle_1 + |\omega_1\rangle_1$ interacts with the cavity, producing the output state

$$\begin{aligned} |\Psi\rangle &= -\alpha |\omega_0\rangle_1 |\downarrow\rangle - \alpha |\omega_1\rangle_1 |\downarrow\rangle - \beta |\omega_0\rangle_1 |\downarrow\rangle + \beta |\omega_1\rangle_1 |\uparrow\rangle \\ &= -\alpha(|\omega_0\rangle_1 + |\omega_1\rangle_1) |\downarrow\rangle - \beta(|\omega_0\rangle_1 - |\omega_1\rangle_1) |\uparrow\rangle . \end{aligned} \tag{D.13}$$

After a Hadamard operation on the spin qubit, the entangled state becomes

$$|\Psi\rangle = -\alpha(|\omega_0\rangle_1 + |\omega_1\rangle_1)(|\downarrow\rangle + |\uparrow\rangle) - \beta(|\omega_0\rangle_1 - |\omega_1\rangle_1)(|\downarrow\rangle - |\uparrow\rangle). \tag{D.14}$$

A subsequent Hadamard operation (via the frequency beam splitter) on the photon yields

$$\begin{aligned} |\Psi\rangle &= -\alpha |\omega_0\rangle_1 (|\downarrow\rangle + |\uparrow\rangle) - \beta |\omega_1\rangle_1 (|\downarrow\rangle - |\uparrow\rangle) \\ &= - |\downarrow\rangle \otimes (\alpha |\omega_0\rangle_1 + \beta |\omega_1\rangle_1) - |\uparrow\rangle \otimes (\alpha |\omega_0\rangle_1 - \beta |\omega_1\rangle_1). \end{aligned} \tag{D.15}$$

We then send a subsequent photon $|\Psi_{P2}\rangle = |\omega_0\rangle_2 + |\omega_1\rangle_2$ that will entangle with the spin qubit for performing the projective measurement. Similarly, the composite state undergoes a CZ operation upon cavity reflection, resulting in

$$\begin{aligned}|\Psi\rangle = |\downarrow\rangle\,(|\omega_0\rangle_2 + |\omega_1\rangle_2)(\alpha\,|\omega_0\rangle_1 + \beta\,|\omega_1\rangle_1) \\ + |\uparrow\rangle\,(|\omega_0\rangle_2 - |\omega_1\rangle_2)(\alpha\,|\omega_0\rangle_1 - \beta\,|\omega_1\rangle_1)\end{aligned} \tag{D.16}$$

Another Hadamard operation on the second photon would produce an entangled state

$$|\Psi\rangle = |\downarrow\rangle\,|\omega_0\rangle_2\,(\alpha\,|\omega_0\rangle_1 + \beta\,|\omega_1\rangle_1) + |\uparrow\rangle\,|\omega_1\rangle_2\,(\alpha\,|\omega_0\rangle_1 - \beta\,|\omega_1\rangle_1). \tag{D.17}$$

As a result, any projection on the frequency-encoded photon is a projective measurement on the spin as well. If $|\omega_0\rangle_2$ is detected, the effective projection onto $|\downarrow\rangle$ results in the transferred state onto the first photon. Instead, if $|\omega_1\rangle_2$ is detected, an additional π-pulse would be applied to the first photon to construct $\alpha\,|\omega_0\rangle_1 + \beta\,|\omega_1\rangle_1$. Imperfections in the cavity system would be treated in the same fashion as the previous section by taking account non-unity reflections: $r_{\text{on}}, r_{\text{off}}, r_m$.

D.3 Teleportation scheme

Essential to the setup of the teleportation scheme is to create a GHZ state for each layer prior to quantum teleportation. Below, we break down its creation process into 3 critical steps: photon-assisted Bell state creation, Bell state swap between nuclear (memory) and electron (broker) spins, and GHZ state creation by joining adjacent pairs. After which, we explain how a Bell state measurement can be made on two remotely entangled spins via the photon-assisted cavity interaction. Lastly, we provide an example of how teleportation enables transferring addresses onto the qRAM.

D.3.1 Photon-assisted Bell state creation

In order to create a Bell state between neighboring matter qubits, a photon is sent to reflect off each cavity consecutively. Importantly, the node is in the "setting" mode such that reflection off the cavity system generates a CZ gate. Here, we provide an example of how a photon interacting with two cavities aids construction of a Bell state between the two spin qubits. We begin with the photonic and the spin qubits prepared in the $|+\rangle$ state such that composite state is

$$|\psi\rangle = (|\omega_0\rangle + |\omega_1\rangle)(|\downarrow\rangle_1 + |\uparrow\rangle_1)(|\downarrow\rangle_2 + |\uparrow\rangle_2), \tag{D.18}$$

where the subscripts 1 and 2 denote different spins.

After the photon reflects off the first spin qubit coupled to the cavity, the state becomes an entangled state

$$\begin{aligned}|\psi\rangle = &-[(|\omega_0\rangle + |\omega_1\rangle)|\downarrow\rangle_1 + (|\omega_0\rangle - |\omega_1\rangle)|\uparrow\rangle_1](|\downarrow\rangle_2 + |\uparrow\rangle_2) \\ = &-[(|\omega_0\rangle|\downarrow\rangle_2 + |\omega_1\rangle|\downarrow\rangle_2 + |\omega_0\rangle|\uparrow\rangle_2 + |\omega_1\rangle|\uparrow\rangle_2)|\downarrow\rangle_1 \\ &+ (|\omega_0\rangle|\downarrow\rangle_2 - |\omega_1\rangle|\downarrow\rangle_2 + |\omega_0\rangle|\uparrow\rangle_2 - |\omega_1\rangle|\uparrow\rangle_2)|\uparrow\rangle_1].\end{aligned} \tag{D.19}$$

Upon reflecting off the second cavity system, it produces the state

$$\begin{aligned}|\psi\rangle = &[((|\omega_0\rangle + |\omega_1\rangle)|\downarrow\rangle_2 + (|\omega_0\rangle - |\omega_1\rangle)|\uparrow\rangle_2)|\downarrow\rangle_1 \\ &+ ((|\omega_0\rangle - |\omega_1\rangle)|\downarrow\rangle_2 + (|\omega_0\rangle + |\omega_1\rangle)|\uparrow\rangle_2)|\uparrow\rangle_1].\end{aligned} \tag{D.20}$$

A Hadamard operation on the photon leads to the final state

$$|\psi\rangle = |\omega_0\rangle(|\downarrow\downarrow\rangle + |\uparrow\uparrow\rangle) + |\omega_1\rangle(|\downarrow\uparrow\rangle + |\uparrow\downarrow\rangle). \tag{D.21}$$

If the ω_0 detection port clicks, the Bell state $|\Phi^+\rangle = |\downarrow\downarrow\rangle + |\uparrow\uparrow\rangle$ is heralded. On the other hand, if the ω_1 port registers a click, the Bell state $|\Psi^+\rangle = |\downarrow\uparrow\rangle + |\uparrow\downarrow\rangle$ is created. An Pauli X gate can be applied to the second spin qubit to transform $|\Psi^+\rangle$ to $|\Phi^+\rangle$.

Multiple pairs of adjacent tree nodes can simultaneously undergo the aforementioned evolution to create Bell states. Then, the entangled spin qubit pairs can be linked by the same procedure. As opposed to having a single photon reflecting off *all the nodes* across each layer to create a GHZ-like state, a process that inevitably suffers from exponentially decaying success probability, the pairwise creation protocol described here is much more efficient.

D.3.2 Bell state swap between electron and nuclear spins

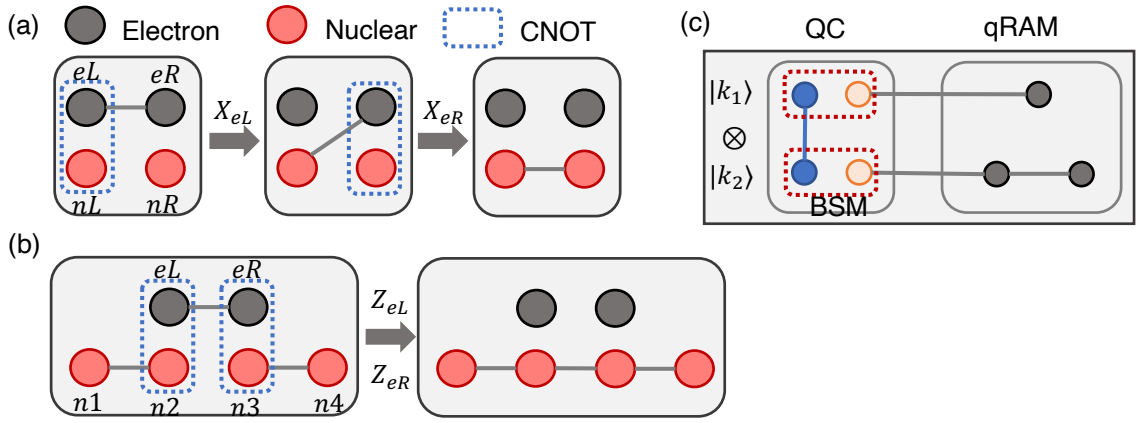

Figure D-1: Operations to: (a) swap a Bell state between a pair of entangled electron spins and a pair of nuclear spins; (b) entangle two pairs of Bell states to form a 4-qubit GHZ state in the nuclear spins. (c) A 2-level qRAM is first entangled with a remote QC. Local BSMs in the QC complete quantum teleportation of the query addresses onto the binary tree. The memory layer is not shown in the schematic for simplicity.

Figure D-1(a) shows two electron spins eL and eR entangled in a Bell state: $|00\rangle_e + |11\rangle_e$. Let the nuclear spins initialized in the ground state $|0\rangle_{nL/nR}$. A CNOT operation where eL acts as the control and nL as the target yields an effective GHZ state: $|0\rangle_{nL}|00\rangle_e + |1\rangle_{nL}|11\rangle_e$. Then, an X measurement on eL disentangles the electron spin from the GHZ state, leaving the final state $|\psi\rangle$

$$\begin{aligned} |\psi\rangle &= (\langle 0| \pm \langle 1|)_{eL} (|0\rangle_{nL}|00\rangle_e + |1\rangle_{nL}|11\rangle_e) \\ &= |0\rangle_{nL}|0\rangle_{eR} \pm |1\rangle_{nL}|1\rangle_{eR}\,. \end{aligned} \tag{D.22}$$

Similarly, a CNOT operation between eR and nR produces $|0\rangle_{nL}|0\rangle_{eR}|0\rangle_{nR} \pm |1\rangle_{nL}|1\rangle_{eR}|1\rangle_{nR}$. A subsequent X measurement on eR then leaves a Bell state between the nuclear spins, in the form of

$$|\psi\rangle = (\langle 0| \pm \langle 1|)_{eR}(|0\rangle_{eR}|00\rangle_n \pm |1\rangle_{eR}|11\rangle_n) = |00\rangle_n \pm |11\rangle_n . \tag{D.23}$$

D.3.3 GHZ state creation

Now, we assume two adjacent pairs of nuclear spins, $\{n1, n2\}$ and $\{n3, n4\}$ are entangled in a Bell state, as shown in Figure D-1(b). $n2$ and $n3$'s corresponding electron spins are also entangled in a Bell state via a photon-assisted interaction. We first consider the composite state including $n1, n2, eL, eR$ after a CNOT operation between $n2$ and eL, in which $n2$ is the control and eL is the target. It takes the form

$$\begin{aligned} |\psi\rangle &= |00\rangle_n|00\rangle_e + |00\rangle_n|11\rangle_e + |11\rangle_n|10\rangle_e + |11\rangle_n|01\rangle_e \\ &= (|00\rangle_n|0\rangle_{eR} + |11\rangle_n|1\rangle_{eR})|0\rangle_{eL} + (|00\rangle_n|1\rangle_{eR} + |11\rangle_n|0\rangle_{eR})|1\rangle_{eL} , \end{aligned} \tag{D.24}$$

where $|ij\rangle_e = |i\rangle_{eL}|j\rangle_{eR}$. A subsequent Z measurement on eL followed by a conditional Pauli transformation on eR yields a GHZ state: $|00\rangle_n|0\rangle_{eR} + |11\rangle|1\rangle_{eR}$.

Then, similarly, a CNOT operation between $n3$ and eR followed by a Z measurement on eR yields the final GHZ state (conditional Pauli transformation on the nuclear spins)

$$|\psi\rangle = |0000\rangle_n + |1111\rangle_n . \tag{D.25}$$

D.3.4 Teleportation

We present here an example of mapping 2-register addresses $\sum_j \alpha_j |k_{1,j}k_{2,j}\rangle$ onto a 2-level binary tree. Suppose the query addresses compose the superposition state, $\alpha|00\rangle + \beta|01\rangle + \gamma|10\rangle + \delta|11\rangle$, where each register represents the state of the corresponding node at each tree level. We consider the formalism that the atomic state $|0\rangle$ routes the subsequent qubit to the left branch, and $|1\rangle$ to the right. For an instance,

the address $|01\rangle$ means the root (level 1) node is in the state $|0\rangle$ and the left node of level 2 is in the state of $|1\rangle$.

Each layer in the qRAM is initialized as a GHZ state, e.g. $\left(|\tilde{0}\rangle + |\tilde{1}\rangle\right)/\sqrt{2}$ where $|\tilde{i}\rangle = |ii...i\rangle$. Importantly, the first register of each GHZ state belongs to an ancillary qubit in the QC, as shown in Figure D-1.

The un-normalized composite state would then be

$$|\Psi\rangle = (\alpha\,|00\rangle + \beta\,|01\rangle + \gamma\,|10\rangle + \delta\,|11\rangle) \otimes (|00\rangle + |11\rangle)_1(|000\rangle + |111\rangle)_2, \qquad \text{(D.26)}$$

where the subscripts 1 and 2 denote the layer number.

The state can be re-written as

$$\begin{aligned}
|\Psi\rangle = {} & \alpha\left[(|\Phi^+\rangle + |\Phi^-\rangle)\,|0\rangle + (|\Psi^+\rangle + |\Psi^-\rangle)\,|1\rangle\right]_1 \otimes \left[(|\Phi^+\rangle + |\Phi^-\rangle)\,|00\rangle + (|\Psi^+\rangle + |\Psi^-\rangle)\,|11\rangle\right]_2 \\
& + \beta\left[(|\Phi^+\rangle + |\Phi^-\rangle)\,|0\rangle + (|\Psi^+\rangle + |\Psi^-\rangle)\,|1\rangle\right]_1 \otimes \left[(|\Psi^+\rangle - |\Psi^-\rangle)\,|00\rangle + (|\Phi^+\rangle - |\Phi^-\rangle)\,|11\rangle\right]_2 \\
& + \gamma\left[(|\Psi^+\rangle - |\Psi^-\rangle)\,|0\rangle + (|\Phi^+\rangle - |\Phi^-\rangle)\,|1\rangle\right]_1 \otimes \left[(|\Phi^+\rangle + |\Phi^-\rangle)\,|00\rangle + (|\Psi^+\rangle + |\Psi^-\rangle)\,|11\rangle\right]_2 \\
& + \delta\left[(|\Psi^+\rangle - |\Psi^-\rangle)\,|0\rangle + (|\Phi^+\rangle - |\Phi^-\rangle)\,|1\rangle\right]_1 \otimes \left[(|\Psi^+\rangle - |\Psi^-\rangle)\,|00\rangle + (|\Phi^+\rangle - |\Phi^-\rangle)\,|11\rangle\right]_2 \\
= {} & |\Phi^+\rangle_1\,|\Phi^+\rangle_2\,(\alpha\,|0\rangle_1\,|00\rangle_2 + \beta\,|0\rangle_1\,|11\rangle_2\,\gamma\,|1\rangle_1\,|00\rangle_2 + \delta\,|1\rangle_1\,|11\rangle_2) + ... \qquad \text{(D.27)}
\end{aligned}$$

Bell state measurements for each layer would then project the composite state into one of the 16 possible combinations. Followed by conditional Pauli transformations, the query addresses are finally teleported onto the binary tree.

Bibliography

[1] T. Muller, C. Hepp, B. Pingault, E. Neu, S. Gsell, M. Schreck, H. Sternschulte, D. Steinmuller–Nethl, C. Becher, and M. Atature. Optical signatures of silicon-vacancy spins in diamond. *Nature Communications*, 5:3328, 2014.

[2] E. Pelucchi, G. Fagas, I. Aharonovich, D. Englund, E. Figueroa, Q. Gong, H. Hannes, J. Liu, C.-Y. Lu, N. Matsuda, J.-W. Pan, F. Schreck, F. Sciarrino, C. Silberhorn, J. Wang, and K. D. Joens. The potential and global outlook of integrated photonics for quantum technologies. *Nat. Rev. Phys.*, 4:pp.194–208, 2021.

[3] A. Reiserer and G. Rempe. Cavity-based quantum networks with single atoms and optical photons. *Rev. Mod. Phys.*, 87:1379, 2015.

[4] L. Li, T. Schroeder, E. H. Chen, M. Walsh, I. Bayn, J. Goldstein, O. Gaathon, M. E. Trusheim, M. Lu, J. Mower, M. Cotlet, M. L. Markham, D. J. Twitchen, and D. Englund. Coherent spin control of a nanocavity-enhanced qubit in diamond. *Nat. Commun.*, 6:6173, 2015.

[5] S. Pirandola, R. Laurenza, C. Ottaviani, and L. Banchi. Fundamental limits of repeaterless quantum communications. *Nat. Commun.*, 8:15043, 2017.

[6] E. N. Knall, C. M. Knaut, R. Bekenstein, D. R. Assumpcao, P. L. Stroganov, W. Gong, Y. Q. Huan, P.-J. Stas, B. Machielse, M. Chalupnik, D. Levonian, A. Suleymanzade, R. Riedinger, H. Park, M. Loncar, M. K. Bhaskar, and M. D. Lukin. Efficient source of shaped single photons based on an integrated diamond nanophotonic system. *Phys. Rev. Lett.*, 129:053603, 2022.

[7] S. Wehner, D. Elkouss, and R. Hanson. Quantum internet: a vision for the road ahead. *Science*, 362:6412, 2018.

[8] N. Gisin and R. Thew. Quantum communication. *Nat. Photon.*, 1:pp.165–171, 2007.

[9] V. Scarani, H. Bechmann–Pasquinucci, N. J. Cerf, M. Dusek, N. Lukenhaus, and M. Peev. The security of practical quantum key distribution. *Rev. Mod. Phys.*, 81:1301, 2009.

[10] H.-K. Lo, M. Curty, and K. Tamaki. Secure quantum key distribution. *Nat. Photon.*, 8:pp.595–604, 2014.

[11] J. I. Cirac, A. K. Ekert, S. F. Huelga, and C. Macchiavello. Distributed quantum computation over noisy channels. *Phys. Rev. A*, 59:4249, 1999.

[12] L. Jiang, J. M. Taylor, A. S. Sorensen, and M. D. Lukin. Distributed quantum computation based on small quantum registers. *Phys. Rev. A*, 76:062323, 2007.

[13] R. V. Meter, K. Nemoto, and W. Munro. Communication links for distributed quantum computation. *IEEE Trans. Comput.*, 56:pp.1643–1653, 2007.

[14] Q. Zhuang, Z. Zhang, and J. H. Shapiro. Distributed quantum sensing using continuous-variable multipartite entanglement. *Phys. Rev. A*, 97:032329, 2018.

[15] X. Guo, C. R. Breum, J. Borregaard, S. Izumi, M. V. Larsen, T. Gehring, M. Christandl, J. S. Neergaard–Nielsen, and U. L. Andersen. Distributed quantum sensing in a continuous-variable entangled network. *Nat. Phys.*, 16:pp.281–284, 2020.

[16] Z. Zhang and Q. Zhuang. Distributed quantum sensing. *Quantum Sci. Technol.*, 6:043001, 2021.

[17] C. W. Chou, H. de Riedmatten, D. Felinto, S. V. Polyakov, S. J. van Enk, and H. J. Kimble. Measurement-induced entanglement for excitation stored in remote atomic ensembles. *Nature*, 438:pp.828–832, 2005.

[18] M. Pompili, S. L. N. Hermans, S. Baier, H. K. C. Beukers, P. C. Humphreys, R. N. Schouten, R. F. L. Vermeulen, M. J. Tiggelman, L. dos Santos Martins, B. Dirkse, S. Wehner, and R. Hanson. Realization of a multinode quantum network ofremote solid-state qubits. *Science*, 372(6539):pp.259–264, 2021.

[19] S. Daiss, S. Langenfeld, S. Welte, E. Distante, P. Thomas, L. Hartung, O. Morin, and G. Rempe. A quantum-logic gate between distant quantum–network modules. *Science*, 371:pp.614–617, 2021.

[20] N. Leung, Y. Lu, S. Chakram, R. K. Naik, N. Earnest, R. Ma, K. Jacobs, A. N. Cleland, and D. I. Schuster. Deterministic bidirectional communication and remote entanglement generation between superconducting qubits. *npj Quant. Info.*, 5:18, 2019.

[21] M. A. Nielsen and I. L. Chuang. *Quantum computation and quantum information*. Cambridge University Press, 10 edition, 2010.

[22] K. C. Chen, P. Dhara, M. Heuck, Y. Lee, W. Dai, S. Guha, and D. Englund. Zero-added-loss entangled-photon multiplexing for ground- and space-based quantum networks. *Phys. Rev. Applied*, 19:054029, 2023.

[23] I. V. Inlek, C. Crocker, M. Lichtman, K. Sosnova, and C. Monroe. Multispecies trapped-ion node for quantum networking. *Phys. Rev. Lett.*, 118:250502, 2017.

[24] M. Atature, D. Englund, N. Vamivakas, S.–Y. Lee, and J. Wrachtrup. Material platforms for spin-based photonic quantum technologies. *Nat. Rev. Mater.*, 3:pp.38–51, 2018.

[25] M. H. Abobeih, J. Cramer, M. A. Bakker, N. Kalb, M. Markham, D. J. Twitchen, and T. H. Taminiau. One-second coherence for a single electron spincoupled to a multi-qubit nuclear-spin environment. *Nat. Commun.*, 9:2552, 2018.

[26] P. C. Humphreys, N. Kalb, J. J. Morits, R. N. Schouten, R. F. L. Vermeulen, D. J. Twitchen, M. Markham, and R. Hanson. Deterministic delivery of remote entanglement on a quantum network. *Nature*, 558:pp. 268–273, 2018.

[27] American Physical Society. *Spontaneous emission probabilities at ratio frequencies*, volume 69, 1946.

[28] S. B. van Dam, M. Walsh, M. J. Degen, E. Bersin, S. L. Mouradian, A. Galiullin, M. Ruf, M. IJspeert, T. H. Taminiau, R. Hanson, and D. R. Englund. Optical coherence of diamond nitrogen-vacancy centers formed by ion implantation and annealing. *Phys. Rev. B*, 99:161203, 2019.

[29] G. Thiering and A. Gali. Ab initio magneto-optical spectrum of group-iv vacancy color centers in diamond. *Phys. Rev. X*, 8:021063, 2018.

[30] C. Hepp, T. Muller, V. Waselowski, J. N. Becker, B. Pingault, H. Sternschulte, D. Steinmuller–Nethl, A. Gali, J. R. Maze, M. Atature, and C. Becher. Electronic structure of the silicon vacancy color center in diamond. *Phys. Rev. Lett.*, 112:036405, 2014.

[31] H. A. Jahn and E. Teller. Stability of polyatomic molecules in degenerate electronic states – i-orbital degeneracy. *Proc. R. Soc. A*, 161:905, 1937.

[32] K. D. Jahnke, A. Sipahigil, J. M. Binder, M. W. Doherty, M. Metsch, L. J. Rogers, N. B. Manson, M. D. Lukin, and F. Jelezko. Electron-phonon processes of the silicon-vacancy centre in diamond. *New. J. Phys.*, 17:043011, 2015.

[33] D. D. Sukachev, A. Sipahigil, C. T. Nguyen, M. K. Bhaskar, R. E. Evans, F. Jelezko, and M. D. Lukin. Silicon-vacancy spin qubit in diamond: a quantum memory exceeding 10 ms with single-shot state readout. *Phys. Rev. Lett.*, 119:223602, 2017.

[34] M. E. Trusheim, N. H. Wan, K. C. Chen, C. J. Ciccarino, J. Flick, R. Sundararaman, G. Malladi, E. Bersin, M. Walsh, B. Lienhard, H. Bakhru, P. Narang, and D. Englund. Lead-related quantum emitters in diamond. *Phys. Rev. B*, 99:075430, 2019.

[35] T. Iwasaki, Y. Miyamoto, T. Taniguchi, P. Siyushev, M. H. Metsch, F. Jelezko, and M. Hatano. Tin-vacancy quantum emitters in diamond. *Phys. Rev. Lett.*, 119:253601, 2017.

[36] M. E. Trusheim, B. Pingault, N. H. Wan, M. Gundogan, L. De Santis, K. C. Chen, M. Walsh, J. J. Rose, J. N. Becker, B. Lienhard, E. Bersin, G. Malladi, H. Bakhru, I. Walmsley, M. Atature, and D. Englund. Transform-limited photons from a coherent tin–vacancy spin in diamond. *Phys. Rev. Lett.*, 124:023602, 2020.

[37] J. Gorlitz, D. Herrmann, G. Thiering, P. Fuchs, M. Gandil, T. Iwasaki, T. Taniguchi, M. Kieschnick, J. Meijer, and M. Hatano. Spectroscopic investigations of negatively charged tin-vacancy centres in diamond. *New J. Phys.*, 22:013048, 2020.

[38] R. Debroux, C. P. Michaels, C. M. Purser, N. Wan, M. E. Trusheim, J. A. Martinez, R. A. Parker, A. M. Stramma, K. C. Chen, L. de Santis, E. M. Alexeev, A. C. Ferrari, D. Englund, D. A. Gangloff, and M. Atature. Quantum control of the tin-vacancy spin qubit in diamond. *Phys. Rev. X*, 11:041041, 2021.

[39] J. A. Martinez, R. A. Parker, K. C. Chen, C. M. Purser, L. Li, C. P. Michaels, A. M. Stramma, R. Debroux, I. B. Harris, M. H. Appel, E. C. Nichols, M. E. Trusheim, D. Gangloff, D. Englund, and M. Atature. Photonic indistinguishability of the tin-vacancy center in nanostructured diamond. *Phys. Rev. Lett.*, 129:173603, 2022.

[40] D. L. Moehring, P. Maunz, S. Olmschenk, K. C. Younge, D. N. Matsukevich, L.-M. Duan, and C. Monroe. Entanglement of single-atom quantum bits at a distance. *Nature*, 449:pp.68–71, 2007.

[41] H. Bernien, B. Hensen, W. Pfaff, G. Koolstra, M. S. Blok, L. Robledo, T. H. Taminiau, M. Markham, D. J. Twitchen, L. Childress, and R. Hanson. Heralded entanglement between solid-state qubits separated by three metres. *Nature*, 497:pp.86–90, 2013.

[42] B. Jing, X.-J. Wang, Y. Yu, P.-F. Sun, Y. Jiang, S.-J. Yang, W.-H. Jiang, X.-Y. Luo, J. Zhang, X. Jiang, X.-H. Bao, and J.-W. Pan. Entanglement of three quantum memories via interference of three single photons. *Nat. Photon.*, 13:pp.210–213, 2019.

[43] B. E. A. Saleh and M. C. Teich. *Fundamentals of photonics*. Wiley-Interscience, 2 edition, 2007.

[44] S. D. Barrett and P. Kok. Efficient high-fidelity quantum computation using matter qubits and linear optics. *Phys. Rev. A*, 71:060310(R), 2005.

[45] C. K. Hong, Z. Y. Ou, and L. Mandel. Measurement of subpicosecond time intervals between two photons by interference. *Phys. Rev. Lett.*, 59:2044, 1987.

[46] K. C. Chen, E. Bersin, and D. Englund. A polarization encoded photon-to-spin interface. *npj Quant. Info.*, 7:2, 2021.

[47] C. Pollock and M. Lipson. *Integrated photonics*. Springer, 2003.

[48] C. M. Natarajan, M. G. Tanner, and R. H. Hadfield. Superconducting nanowire single-photon detectors: physics and applications. *Supercond. Sci. Technol.*, 25:063001, 2012.

[49] F. Najafi, J. Mower, N. C. Harris, F. Bellei, A. Dane, C. Lee, X. Hu, P. Kharel, F. Marsili, S. Assefa, K. K. Berggren, and D. Englund. On-chip detection of non-classical light by scalable integration of single-photon detectors. *Nat. Commun.*, 6:5873, 2015.

[50] N. H. Wan, Tsung-Ju Lu, Kevin C. Chen, Michael P. Walsh, Matthew E. Trusheim, Lorenzo De Santis, Eric A. Bersin, Isaac B. Harris, Sara L. Mouradian, Ian R. Christen, Edward S. Bielejec, and Dirk Englund. Large-scale integration of near-indistinguishable artificial atoms in hybrid photonic circuits. *Nature*, 583:pp.226–231, 2020.

[51] C. Sorace–Agaskar, D. Kharas, S. Yegnanarayanan, R. T. Maxson, G. N. West, W. Loh, S. Bramhavar, R. J. Ram, J. Chiaverini, J. Sage, and P. Juodawlkis. Versatile silicon nitride and alumina integrated photonic platforms for the ultraviolet to short-wave infrared. *IEEE J. Quantum Electron.*, 25:5, 2019.

[52] D. J. Starling, K. Shtyrkova, I. Christen, R. Murphy, L. Li, K. C. Chen, D. Kharas, X. Zhang, J. Cummings, W. J. Nowak, E. Bersin, R. J. Niffenegger, M. Sutula, D. Englund, S. Hamilton, and P. B. Dixon. A fully packaged multi-channel cryogenic module for optical quantum memories. *Phys. Rev. Applied*, 19:064028, 2023.

[53] L.-M. Duan and H. J. Kimble. Scalable photonic quantum computation through cavity-assisted interactions. *Phys. Rev. Lett.*, 92:127902, March 2004.

[54] M. O. Scully and M. S. Zubairy. *Quantum Optics*. Cambridge University Press, 1997.

[55] D. F. Walls and G. J. Milburn. *Quantum Optics*. Springer, 2008.

[56] C. W. Gardiner and M. J. Collett. Input and output in damped quantum systems: quantum stochastic differential equations and the master equation. *Phys. Rev. A*, 31:3761, 1985.

[57] A. Faraon, P. E. Barclay, C. Santori, K.-M. C. Fu, and R. G. Beausoleil. Resonant enhancement of the zero-phonon emission from a colour centre in a diamond cavity. *Nat. Photon.*, 5:pp.301–305, 2011.

[58] M. J. Burek, Y. Chu, M. S. Z. Liddy, P. Patel, J. Rochman, S. Meesala, W. Hong, Q. Quan, M. D. Lukin, and M. Loncar. High quality-factor optical nanocavities in bulk single-crystal diamond. *Nat. Commun.*, 5:5718, 2014.

[59] B. Khanaliloo, M. Mitchell, A. C. Hryciw, and P. E. Barclay. High–q/v monolithic diamond microdisks fabricated with quasi-isotropic eetching. *Nano Lett.*, 15:pp. 5131–5136, 2015.

[60] S. Mouradian, N. H. Wan, T. Schroeder, and D. Englund. Rectangular photonic crystal nanobeam cavities in bulk diamond. *Appl. Phys. Lett.*, 111:021103, 2017.

[61] N. H. Wan, S. Mouradian, and D. Englund. Two-dimensional photonic crystal slab nanocavities on bulk single-crystal diamond. *Appl. Phys. Lett.*, 112:141102, 2018.

[62] R. Coccioli, M. Boroditsky, K. W. Kim, Y. Rahmat-Samii, and E. Yablonovitch. Smallest possible electromagnetic mode volume in a dielectric cavity. *IET Optoelectron.*, 145:pp.391–397, 1998.

[63] J. D. Joannopoulos, S. G. Johnson, J. N. Winn, and R. D. Meade. *Photonic crystals: molding the flow of light*. Princeton University Press, 2 edition, 2008.

[64] C. T. Nguyen, D. D. Sukachev, M. K. Bhaskar, B. Machielse, D. S. Levonian, E. N. Knall, P. Stroganov, R. Riedinger, H. Park, M. Loncar, and M. D. Lukin. Quantum network nodes based on diamond qubits with an efficient nanophotonic interface. *Phys. Rev. Lett.*, 123:183602, October 2019.

[65] L. Orphal–Kobin, K. Unterguggenberger, T. Pregnolato, N. Kemf, M. Matalla, R.-S. Unger, I. Ostermay, G. Pieplow, and T. Schroeder. Optically coherent nitrogen-vacancy defect centers in diamond nanostructures. *Phys. Rev. X*, 13:011042, 2023.

[66] M. K. Bhaskar, R. Riedinger, B. Machielse, D. S. Levonian, C. T. Nguyen, E. N. Knall, H. Park, D. Englund, M. Loncar, D. D. Sukachev, and M. D. Lukin. Experimental demonstration of memory-enhanced quantum communication. *Nature*, 580:pp.60–64, 2020.

[67] S. Fan, W. Suh, and J. D. Joannopoulos. Temporal coupled-mode theory for the fano resonance in optical resonators. *J. Opt. Soc. Am. A*, 20:3, 2003.

[68] T. G. Tiecke, J. D. Thompson, N. P. de Leon, L. R. Liu, V. Vuletic, and M. D. Lukin. Nanophotonic quantum phase switch with a single atom. *Nature*, 508:pp.241–244, April 2014.

[69] B. Desiatov, A. Shams-Ansari, M. Zhang, C. Wang, and M. Loncar. Ultra-low-loss integrated visible photonics using thin-film lithium niobate. *Optica*, 6:pp.380–384, 2019.

[70] Y.-I. Sohn, S. Meesala, B. Pingault, H. A. Atikian, J. Holzgrafe, M. Gundogan, C. Stavrakas, M. J. Stanley, A. Sipahigil, J. Choi, M. Zhang, J. L. Pacheco, J. Abraham, E. Bielejec, M. D. Lukin, M. Atature, and M. Loncar. Controlling the coherence of a diamond spin qubit through its strain environment. *Nat. Commun.*, 9:2012, May 2018.

[71] S. Maity, L. Shao, Y.-I. Sohn, S. Meesala, B. Machielse, E. Bielejec, M. Markham, and M. Loncar. Spectral alignment of single-photon emitters in diamond using strain gradient. *Phys. Rev. Appl.*, 10:024050, August 2018.

[72] R. E. Evans, M. K. Bhaskar, D. D. Sukachev, C. T. Nguyen, A. Sipahigil, M. J. Burek, B. Machielse, G. H. Zhang, A. S. Zibrov, E. Bielejec, H. Park, M. Loncar, and M. D. Lukin. Photon-mediated interactions between quantum emitters in a diamond nanocavity. *Science*, 362:pp.662–665, 2018.

[73] T. Grange, G. Hornecker, D. Hunger, J.-P. Poizat, J.-M. Gerard, P. Senellart, and A. Auffeves. Cavity-funneled generation of indistinguishable single photons from strongly dissipative quantum emitters. *Phys. Rev. Lett.*, 114:193601, 2015.

[74] H. Choi, D. Zhu, Y. Yoon, and D. Englund. Cascaded cavities boost the indistinguishability of imperfect quantum emitters. *Phys. Rev. Lett.*, 122:183602, 2019.

[75] T. Zhong, J. M. Kindem, E. Miyazono, and A. Faraon. Nanophotonic coherent light-matter interfaces based on rare-earth-doped crystals. *Nat. Commun.*, 6:8206, September 2015.

[76] A. M. Dibos, M. Raha, C. M. Phenicie, and J. D. Thompson. Atomic source of single photons in the telecom band. *Phys. Rev. Lett.*, 120:243601, June 2018.

[77] S. Dutta, E. A. Goldschmidt, S. Barik, U. Saha, and E. Waks. Integrated photonic platform for rare-earth ions in thin film lithium niobate. *Nano Lett.*, 20:pp.741–747, 2020.

[78] J. D. Thompson, T. G. Tiecke, N. P. de Leon, J. Feist, A. V. Akimov, M. gullans, A. S. Zibrov, V. Vuletic, and M. D. Lukin. Coupling a single trapped atom to a nanoscale optical cavity. *Science*, 340:pp.1202–1205, June 2013.

[79] X. Qiang, X. Zhou, J. Wang, C. M. Wilkes, T. Loke, S. O'Gara, L. Kling, G. D. Marshall, R. Santagati, T. C. Ralph, J. B. Wang, J. L. O'Brien, M. G. Thompson, and J. C. F. Matthews. Large-scale silicon quantum photonics implementing arbitrary two-qubit processing. *Nat. Photon.*, 12:pp.534–539, August 2018.

[80] Y.-F. Pu, N. Jiang, W. Chang, H. X. Yang, C. Li, and L.-M. Duan. Experimental realization of a multiplexed quantum memory with 225 individually accessible memory cells. *Nat. Commun.*, 8:15359, May 2017.

[81] K. Nemoto, M. Trupke, S. J. Devitt, A. M. Stephens, B. Scharfenberger, K. Buczak, T. Nobauer, M. S. Everitt, J. Schmiedmayer, and W. J. Munro. Photonic architecture for scalable quantum information processing in diamond. *Phys. Rev. X*, 4:031022, 2014.

[82] Y. Akahane, T. Asano, B.-S. Song, and S. Noda. High-q photonic nanocavity in a two-dimensional photonic crystal. *Nature*, 425:pp.944–947, 2003.

[83] S. Sangtawesin, B. L. Dwyer, S. Srinivasan, J. J. Allred, L. V. H. Rodgers, K. D. Greve, A. Stacey, N. Dontschuk, K. M. O'Donnell, D. Hu, D. A. Evans, C. Jaye, D. A. Fischer, M. L. Markham, D. J. Twitchen, H. Park, M. D. Lukin, and N. P. de Leon. Origins of diamond surface noise probed by correlating single-spin measurements with surface spectroscopy. *Phys. Rev. X*, 9:031052, 2019.

[84] M. Ruf, M. IJspeert, S. van Dam, N. de Jong, H. van den Berg, G. Evers, and R. Hanson. Optically coherent nitrogen-vacancy centers in micrometer-thin etched diamond membranes. *Nano Lett.*, 19:pp.3987–3992, 2019.

[85] S. Cui. *Near-surface nitrogen vacancy centers in diamond.* phdthesis, Harvard University, 2014.

[86] A. E. Rugar, H. Lu, C. Dory, S. Sun, P. J. McQuade, Z.-X. Shen, N. A. Melosh, and J. Vuckovic. Generation of tin-vacancy centers in diamond via shallow ion implantation and subsequent diamond overgrowth. *Nano Lett.*, 20:pp.1614–1619, 2020.

[87] P. Racke, L. Pietzonka, J. Meijer, D. Spemann, and R. Wunderlich. Vacancy diffusion and nitrogen-vacancy center formation near the diamond surface. *Appl. Phys. Lett.*, 118:204003, 2021.

[88] C. Bradac, W. Gao, J. Forneris, M. E. Trusheim, and I. Aharonovich. Quantum nanophotonics with group iv defects in diamond. *Nat. Commun.*, 10:5625, 2019.

[89] B. Khanaliloo, H. Jayakumar, A. C. Hryciw, D. P. Lake, H. Kaviani, and P. E. Barclay. Single-crystal diamond nanobeam waveguide optomechanics. *Phys. Rev. X*, 5:041051, 2015.

[90] M. J. Burek, N. P. de Leon, B. J. Shields, B. J. M. Hausmann, Y. Chu, Q. Quan, A. S. Zibrov, H. Park, M. D. Lukin, and M. Loncar. Free-standing mechanical and photonic nanostructures in single-crystal diamond. *Nano Lett.*, 12:pp.6084–6089, 2012.

[91] H. A. Atikian, P. Latawiec, M. J. Burek, Y.-I. Sohn, S. Meesala, N. Gravel, A. B. Kouki, and M. Loncar. Freestanding nanostructures via reactive ion beam angled etching. *APL Photonics*, 2:051301, 2017.

[92] C. Chia, B. MMachielse, A. Shams-Ansari, and M. Loncar. Development of hard masks for reactive ion beam angled etching of diamond. *Opt. Express*, 30:pp.14189–14201, 2022.

[93] M. Mitchell, D. P. Lake, and P. E. Barclay. Realizing q>300 000 in diamond microdisks for optomechanics via etch optimization. *APL Photonics*, 4:016101, 2019.

[94] I. Avrutsky, R. Gibson, J. Sears, G. Khitrova, H. M. Gibbs, and J. hendrickson. Linear systems approach to describing and classifying fano resonances. *Phys. Rev. B*, 87:125118, 2013.

[95] D. Englund, A. Faraon, I. Fushman, N. Stoltz, P. Petroff, and J. Vuckovic. Controlling cavity reflectivity with a single quantum dot. *Nature*, 450:pp.857–861, 2007.

[96] A. Gardill, I. Kemeny, M. C. Cambria, Y. Li, H. T. Dinani, A. Norambuena, J. R. Maze, V. Lordi, and S. Kolkowitz. Probing charge dynamics in diamond with an individual color center. *Nano Lett.*, 21:pp.6960–6966, 2021.

[97] J. Gorlitz, D. Herrmann, P. Fuchs, T. Iwasaki, T. Taniguchi, D. Rogalla, D. Hardeman, P.-O. Colard, M. Markham, M. Hatano, and C. Becher. Coherence of a charge stabilised tin-vacancy spin in diamond. *npj Quant. Info.*, 8:45, 2022.

[98] C. Cohen-Tannoudji, J. Dupont-Roc, and G. Grynberg. *Atom-photon interactions: basic processes and applications*. Wiley–VCH, 1998.

[99] R. E. K. Fishman, R. N. Patel, D. A. Hopper, T.-Y. Huang, and L. C. Bassett. Photon-emission-correlation spectroscopy as an analytical tool for solid-state quantum defects. *PRX Quantum*, 4:010202, 2023.

[100] A. E. Rugar, S. Aghaeimeibodi, D. Riedel, C. Dory, H. Lu, P. J. McQuade, Z.–X. Shen, N. A. Melosh, and J. Vuckovic. Quantum photonic interface for tin-vacancy centers in diamond. *Phys. Rev. X*, 11:031021, 2021.

[101] A. V. Inyushkin, A. N. Taldenkov, V. G. Ralchenko, A. P. Bolshakkov, and A. V. Khomich. Isotope effect in thermal conductivity of polycrystalline cvd-diamond: experiment and theory. *Crystals*, 11:322, 2021.

[102] N. A. Katcho, J. Carrete, W. Li, and N. Mingo. Effect of nitrogen and vacancy defects on the thermal conductivity of diamond: an ab initio green's function approach. *Phys. Rev. B*, 90:094117, 2014.

[103] Y. F. Gao, J. M. Lai, Z. Y. Li, P. H. Tan, C. X. Shan, and J. Zhang. Local laser heating effects in diamond probed by photoluminescence of siv centers at low temperature. *arXiv*, page 2306.06972, 2023.

[104] M. Stipcevic, B. G. Christensen, P. G. Kwiat, and D. J. Gauthier. Advanced active quenching circuit for ultra-fast quantum cryptography. *Opt. Express*, 25:pp.21861–21876, 2017.

[105] A. Faraon, C. Santori, Z. Huang, V. M. Acosta, and R. G. Beausoleil. Coupling of nitrogen-vacancy centers to photonic crystal cavities in monocrystalline diamond. *Phys. Rev. Lett.*, 109:033604, 2012.

[106] T. Schroder, M. E. Trusheim, M. Walsh, L. Li, J. Zheng, M. Schukraft, A. Sipahigil, R. E. Evans, D. D. Sukachev, C. T. Nguyen, J. L. Pacheco, R. M. Camacho, E. S. Bielejec, M. D. Lukin, and D. Englund. Scalable focused ion beam creation of nearly lifetime-limited single quantum emitters in diamond nanostructures. *Nat. Commun.*, 8:15376, 2017.

[107] C. T. Nguyen, D. D. Sukachev, M. K. Bhaskar, B. Machielse, D. S. Levonian, E. N. Knall, P. Stroganov, C. Chia, M. J. Burek, R. Riedinger, H. Park, M. Loncar, and M. D. Lukin. An integrated nanophotonic quantum register based on silicon-vacancy spins in diamond. *Phys. Rev. B*, 100:165428, October 2019.

[108] I. Christen, H. Raniwala, K. C. Chen, M. Colangelo, L. De Santis, C. Errando-Herranz, I. Harris, L. Li, Y. Song, O. Medeiros, M. Sutula, K. Berggren, M. Trusheim, P. B. Dixon, X. Zhang, D. Starling, K. Shtyrkova, D. Kharas, R. Murphy, E. Bersin, S. Hamilton, and D. Englund. Integrated quantum memories at 1.3 k with tin-vacancy centers and photonic circuits. In *Conference on Lasers and Electro-Optics*, 2023.

[109] A. Chanana, H. Larocque, R. Moreira, J. Carolan, B. Guha, E. G. Melo, V. Anant, J. Song, D. Englund, D. J. Blumenthal, K. Srinivasan, and M. Davanco. Ultra-low loss quantum photonic circuits integrated with single quantum emitters. *Nat. Commun.*, 13:7693, 2022.

[110] H. Raniwala, I. Christen, K. C. Chen, D. Starling, and D. Englund. Integrating nearly-indistinguishable quantum emitters onto a photonic interposer. In *Conference on Lasers and Electro-Optics*, 2023.

[111] R. A. Parker, J. A. Martinez, K. C. Chen, A. M. Stramma, I. B. Harris, C. P. Michaels, M. E. Trusheim, M. H. Appel, C. M. Purser, W. G. Roth, D. Englund, and M. Atature. A diamond nanophotonic interface with an optically accessible deterministic electronuclear spin register. *arXiv*, page 2305.18923, 2023.

[112] I. B. W. Harris, C. P. Michaels, K. C. Chen, R. A. Parker, M. Titze, J. A. Martinez, M. Sutula, I. R. Christen, A. M. Stramma, W. Roth, C. M. Purser, M. H. Appel, C. Li, M. E. Trusheim, N. L. Palmer, M. L. Markham, E. S. Bielejec, M. Atature, and D. Englund. Hyperfine spectroscopy of isotopically engineered group-iv color centers in diamond. *arXiv*, page 2306.00164, 2023.

[113] D. M. Lukin, M. A. Guidry, J. Yang, M. Ghezellou, S. D. Mishra, H. Abe, T. Ohshima, J. Ul-Hassan, and J. Vuckovic. Two-emitter multimode cavity quantum electrodynamics in thin-film silicon carbide photonics. *Phys. Rev. X*, 13:011005, 2023.

[114] K. Shang, S. Pathak, B. Guan, G. Liu, and S. J. B. Yoo. Low-loss compact multilayer silicon nitride platform for 3d photonic integrated circuits. *Opt. Express*, 23:pp.21334–21342, 2015.

[115] S. L. Mouradian. *A scalable quantum computation platform : solid state quantum memories coupled to photonic integrated circuits*. phdthesis, Massachusetts Institute of Technology, 2018.

[116] J. M. Bopp, M. Plock, T. Turan, G. Pieplow, S. Burger, and T. Schroeder. 'sawfish' photonic crystal cavity for near-unity emitter-to-fiber interfacing in quantum network applications. *arXiv*, page 2210.04702, 2022.

[117] K. C. Chen, W. Dai, C. Errando-Herranz, S. Lloyd, and D. Englund. Scalable and high-fidelity quantum random access memory in spin-photon networks. *PRX Quantum*, 2:030319, 2021.

[118] V. Giovannetti, S. Lloyd, and L. Maccone. Quantum random access memory. *Phys. Rev. Lett.*, 100:160501, 2008.

[119] V. Giovannetti, S. Lloyd, and L. Maccone. Architectures for a quantum random access memory. *Phys. Rev. A*, 78:052310, 2008.

[120] J. Biamonte, P. Wittek, N. Pancotti, P. Rebentrost, N. Wiebe, and S. Lloyd. Quantum machine learning. *Nature*, 549:pp.195–202, 2017.

[121] A. W. Harrow, A. Hassidim, and S. Lloyd. Quantum algorithm for linear systems of equations. *Phys. Rev. Lett.*, 103:150502, 2009.

[122] B. T. Kiani, A. Villanyi, and S. Lloyd. Quantum medical imaging algorithms. *arXiv*, page 2004.02036, 2020.

[123] L. K. Grover. A fast quantum mechanical algorithm for database search. In *Proceedings, 28th Annual ACM Symposium on the Theory of Computing*, number 212. ACM Press, 1996.

[124] F.-Y. Hong, Y. Xiang, Z.-Y. Zhu, L.-Z. Jiang, and L.-N. Wu. Robust quantum random access memory. *Phys. Rev. A*, 86:010306, 2012.

[125] E. S. Moiseev and S. A. Moiseev. Time-bin quantum ram. *J. Mod. Opt.*, 63:pp.2081–2092, 2016.

[126] C. T. Hann, C.-L. Zou, Y. Zhang, Y. Chu, R. J. Schoelkopf, S. M. Girvin, and L. Jiang. Hardware-efficient quantum random access memorywith hybrid quantum acoustic systems. *Phys. Rev. Lett.*, 123:250501, 2019.

[127] H.-H. Lu, J. M. Lukens, N. A. Peters, O. D. Odele, D. E. Leaird, A. M. Weiner, and P. Lougovski. Electro-optic frequency beam splitters and tritters for high-fidelity photonic quantum information processing. *Phys. Rev. Lett.*, 120:030502, 2018.

[128] C. Joshi, A. Farsi, A. Dutt, B. Y. Kim, X. Ji, Y. Zhao, A. M. Bishop, M. Lipson, and A. L. Gaeta. Frequency-domain quantum interference with correlated photons from an integrated microresonator. *Phys. Rev. Lett.*, 124:143601, 2020.

[129] H.-H. Lu, E. M. Simmerman, P. Lougovski, A. M. Weiner, and J. M. Lukens. Fully arbitrary control of frequency-bin qubits. *Phys. Rev. Lett.*, 125:120503, 2020.

[130] N. C. Harris, G. R. Steinbrecher, M. Prabhu, Y. Lahini, J. Mower, D. Bunandar, C. Chen, F. N. C. Wong, T. Baehr-Jones, M. Hochberg, S. Lloyd, and D. Englund. Quantum transport simulations in a programmable nanophotonic processor. *Nature Photon.*, 11:pp.447–452, 2017.

[131] G. Barbarossa, A. M. Matteo, and M. N. Armenise. Theoretical analysis of triple-coupler ring-based optical guided-wave resonator. *J. Lightwave Technol.*, 13:pp.148–157, 1995.

[132] M. D. Bowdrey, D. K. L. Oi, A. J. Short, K. Banaszek, and J. A. Jones. Fidelity of single qubit maps. *Phys. Lett. A*, 294:pp.258–260, 2002.

[133] C. Y. Hu, A. Young, J. L. O'Brien, W. J. Munro, and J. G. Rarity. Giant optical faraday rotation induced by a single-electron spin in a quantum dot: applications to entangling remote spins via a single photon. *Phys. Rev. B*, 78:085307, August 2008.

[134] C. T. Hann, G. Lee, S. M. Girvin, and L. Jiang. Resilience of quantum random access memory to generic noise. *PRX Quantum*, 2:020311, 2021.

[135] X. Rong, J. Geng, F. Shi, Y. Liu, K. Xu, W. Ma, F. Kong, Z. Jiang, Y. Wu, and J. Du. Experimental fault-tolerant universal quantum gates with solid-state spins under ambient conditions. *Nat. Commun.*, 6:8748, 2015.

[136] N. Kalb, A. A. Reiserer, P. C. Humphreys, J. J. W. Bakermans, S. J. Kamerling, N. H. Nickerson, S. C. Benjamin, D. J. Twitchen, M. Markham, and R. Hanson. Entanglement distillation between solid-state quantum network nodes. *Science*, 356:pp.928–932, 2017.

[137] M. Zhang, C. Wang, R. Cheng, A. Shams-Ansari, and M. Loncar. Monolithic ultra-high-q lithium niobate microring resonator. *Optica*, 4:pp.1536–1537, 2017.

[138] K. D. Jahnke, B. Naydenov, T. Teraji, S. Koizumi, T. Umeda, J. Isoya, and F. Jelezko. Long coherence time of spin qubits in 12c enriched polycrystalline chemical vapor deposition diamond. *Appl. Phys. Lett.*, 101:021405, 2012.

[139] N. H. Nickerson, J. F. Fitzsimons, and S. C. Benjamin. Freely scalable quantum technologies using cells of 5-to-50 qubits with very lossy and noisy photonic links. *Phys. Rev. X*, 4:041041, 2014.

[140] S. Meesala, Y.-I. Sohn, B. Pingault, L. Shao, H. A. Atikian, J. Holzgrafe, M. Gundogan, C. Stavrakas, A. Sipahigil, C. Chia, R. Evans, M. J. Burek, M. Zhang, L. Wu, J. L. Pacheco, J. Abraham, E. Bielejec, M. D. Lukin, M. Atature, and M. Loncar. Strain engineering of the silicon-vacancy center in diamond. *Phys. Rev. B*, 97:205444, 2018.

[141] Q. Quan, P. B. Deotare, and M. Loncar. Photonic crystal nanobeam cavity strongly coupled to the feeding waveguide. *Appl. Phys. Lett.*, 96:203102, 2010.

[142] A. Alajlan, I. Cojocaru, and A. V. Akimov. Compact design of a gallium phosphide nanobeam cavity for coupling to diamond germanium-vacancy centers. *Opt. Mater. Express*, 9:1678, 2019.

[143] J. P. Vasco, V. Savona, and D. Gerace. Optimized design of a silica encapsulated photonic crystal nanobeam cavity for integrated silicon-based nonlinear and quantum photonics. *Phys. Rev. Applied*, 13:034070, 2020.

[144] S. Sun, H. Kim, G. S. Solomon, and E. Waks. A quantum phase switch between a single solid-state spin and a photon. *Nat. Nanotechnol.*, 11:pp.539–544, February 2016.

[145] J. M. Kindem, A. Ruskuc, J. G. Bartholomew, J. Rochman, Y. Q. Huan, and A. Faraon. Control and single-shot readout of an ion embedded in a nanophotonic cavity. *Nature*, 580:pp.201–204, 2020.

[146] I. Pogorelov, T. Feldker, C. D. Marciniak, L. Postler, G. Jacob, O. Kriegelsteiner, V. Podlesnic, M. Meth, V. Negnevitsky, M. Stadler, B. Hofer, C. Wachter, K. Lakhmanskiy, R. Blatt, P. Schindler, and T. Monz. A compact ion-trap quantum computing demonstrator. *PRX Quantum*, 2:020343, 2021.

[147] A. Omran, H. Levine, A. Keesling, G. Semeghini, T. T. Wang, S. Ebadi, H. Bernien, A. S. Zibrov, H. Pichler, S. Choi, J. Cui, M. Rossignolo, P. Rembold, S. Montangero, T. Calarco, M. Endres, M. Greiner, V. Vuletic, and M. D. Lukin. Generation and manipulation of schrödinger cat states in rydberg atom arrays. *Science*, 365:pp.570–574, 2019.

[148] R. P. Feynman. Simulating physics with computers. *Int. J. Theor. Phys.*, 21:pp.467–488, 1982.

[149] S. J. Freedman and J. F. Clauser. Experimental test of local hidden-variable theories. *Phys. Rev. Lett.*, 28:938, 1972.

[150] A. Aspect, P. Grangier, and G. Roger. Experimental realization of einstein-podolsky-rosen-bohm gedankenexperiment: a new violation of bell's inequalities. *Phys. Rev. Lett.*, 49:91, 1982.

[151] D. Bouwmeester, J.-W. Pan, K. Mattle, M. Eibl, H. Weinfurter, and A. Zeilinger. Experimental quantum teleportation. *Nature*, 390:pp.575–579, 1997.

[152] P.–J. Stas, Y. Q. Huan, B. Machielse, E. N. Knall, A. Suleymanzade, B. Pingault, M. Sutula, S. W. Ding, C. M. Knaut, D. R. Assumpcao, Y.–C. Wei, M. K. Bhaskar, R. Riedinger, D. D. Sukachev, H. Park, M. Loncar, D. S. Levonian,

and M. D. Lukin. Robust multi-qubit quantum network node with integrated error detection. *Science*, 378:pp.557–560, 2022.

[153] R. Raussendorf, D. E. Browne, and H. J. Briegel. Measurement-based quantum computation on cluster states. *Phys. Rev. A*, 68:022312, 2003.

[154] J. Borregaard, H. Pichler, T. Schroeder, M. D. Lukin, P. Lodahl, and A. S. Sorensen. One-way quantum repeater based on near-deterministic photon-emitter interfaces. *Phys. Rev. X*, 10:021071, 2020.

[155] M. Dong, G. Clark, A. J. Leenheer, M. Zimmermann, D. Dominguez, A. J. Menssen, D. Heim, G. Gilbert, D. Englund, and M. Eichenfield. High-speed programmable photonic circuits in a cryogenically compatible, visible-near-infrared 200 mm cmos architecture. *Nat. Photon.*, 16:pp.59–65, 2022.

[156] D. M. Lukin, C. Dory, M. A. Guidry, K. Y. Yang, S. D. Mishra, R. Trivedi, M. Radulaski, S. Sun, D. Vercruysse, G. H. Ahn, and J. Vuckovic. 4h-silicon-carbide-on-insulator for integrated quantum and nonlinear photonics. *Nat. Photon.*, 14:pp.330–334, 2020.

[157] P. Lodahl. Quantum-dot based photonic quantum networks. *Quantum Sci. Technol.*, 3:013001, 2018.

[158] M. Raha, S. Chen, C. M. Phenicie, S. Ourari, A. M. Dibos, and J. D. Thompson. Optical quantum nondemolition measurement of a single rare earth ion qubit. *Nat. Commun.*, 11:1605, 2020.

[159] M. Prabhu, C. Errando-Herranz, L. De Santis, I. Christen, C. Chen, C. Gerlach, and D. Englund. Individually addressable and spectrally programmable artificial atoms in silicon photonics. *Nat. Commun.*, 14:2380, 2023.

[160] V. Saggio, C. Errando-Herranz, S. Gyger, C. Panuski, M. Prabhu, L. De Santis, I. Christen, D. Ornelas-Huerta, H. Raniwala, C. Gerlach, M. Colangelo, and D. Englund. Cavity-enhanced single artificial atoms in silicon. *arXiv*, page 2302.10230, 2023.

[161] L. Bischoff, P. Mazarov, L. Bruchhaus, and J. Gierak. Liquid metal alloy ion sources - an alternative for focussed ion beam technology. *Appl. Phys. Rev.*, 3:021101, 2016.

[162] M. P. Walsh. *Statistical metrology and process control of quantum devices.* phdthesis, Massachusetts Institute of Technology, 2020.

[163] M. Sutula, I. Christen, E. Bersin, M. P. Walsh, K. C. Chen, J. Mallek, A. Melville, M. Titze, E. S. Bielejec, S. Hamilton, D. Braje, P. B. Dixon, and D. R. Englund. Large-scale optical characterization of solid-state quantum emitters. *arXiv*, page 2210.13643, 2022.